Author:
Robbins, Joshua A D

Title:
Anomalous Phenomena in Chiral Superconductors

Anomalous Phenomena in Chiral Superconductors

By

JOSHUA ROBBINS

Department of Theoretical Physics
UNIVERSITY OF BRISTOL

A dissertation submitted to the University of Bristol in accordance with the requirements of the degree of PH.D. in the Faculty of Science.

OCTOBER 2018

Word count: 58,505

Abstract

The unconventional class of superconductivity comprises a broad range of materials with vast potential for applications in solid state devices. Unconventional superconducting states are capable of supporting a range of exotic properties, such as intrinsic magnetism, anomalous transport and non-trivial topology, making them ideal candidate materials for many fields, particularly those of spintronics and quantum computation. Harnessing these properties remains challenging as such materials are not yet fully understood, and thus the potential of this class remains largely untapped. The work presented here is focussed on chiral superconductors, a type of unconventional superconducting material in which the Cooper pairs form with an intrinsic magnetic moment. Interplay between the magnetisation associated with a chiral order parameter and the transport properties of superconductivity provides a rich platform for the emergence of unique and anomalous phenomena. The intent of this investigation is to derive a broad set of tools with which to study such phenomena in a general superconductor. Key among the results is the derivation of a modern theory to calculate the total orbital magnetic moment generated by the formation of a superconducting state with a chiral order parameter. Also presented are studies of the anomalous Hall and Kerr effects, which are phenomena deeply linked to the orbital moment. A comprehensive understanding of the shared origin of orbital magnetism and anomalous transport is developed through an analysis of the relation of these properties to the Berry curvature of the intrinsic bandstructure. As a physical platform on which to test and analyse these general theories, two distinct tight-binding models of the proposed p-wave superconductor Sr_2RuO_4 are presented and utilised for model calculations. The exact form of the order parameter in this material remains a source of fierce debate, and the comparison of the two models provides a method with which to study the origins of the key properties of the state from the structure of the gap. It is demonstrated that multi-band effects are essential in the description of the intrinsic phenomena in Sr_2RuO_4, and that the spin-orbit interaction plays a vital role in generating these properties. An outstanding issue in the identification of the order parameter in Sr_2RuO_4 is that p-wave symmetry is expected to induce large edge currents, which have not been observed experimentally. The results obtained here provide possible explanations for this perceived contradiction. Also shown are a range of factors which suppress the magnetisation associated with itinerant currents, such as the presence of superconducting gaps on multiple bands with inter-orbital pairing, the influence of the spin-orbit interaction and the addition of longer range pairing terms in the gap structure. Work remains to be done to irrefutably resolve these issues, but an essential foundation is established through the theoretical work presented here. Finally, the groundwork for a number of avenues for further study is laid, including the fine-tuning of the extended pairing model of Sr_2RuO_4, the study of anomalous phenomena in other chiral superconductors and the generalisation of the finite-temperature contributions to the orbital moment in a superconductor.

ACKNOWLEDGEMENTS

I would like to acknowledge the support and a guidance of a number of individuals and groups that have made this thesis possible. Firstly, many thanks must go to my supervisors Martin and James, whose advice, guidance and motivation were the launching point for the majority of my accomplishments over the past years. The calculations performed in this project were made through the Advanced Computing Research Centre at the University of Bristol, and financial support was provided by the Engineering and Physical Sciences Research Council.

The project was arranged as part of the Centre for Doctoral Training in Condensed Matter Physics, jointly run by the University of Bristol and the University of Bath. Many thanks are due to the administration and teaching staff involved with this enterprise, for their constant work in organising and running numerous lecture courses, training programs, industry trips, outreach programmes, social events and much more. All of these events have been a great benefit to my personal and professional development.

Finally, I would like to extend my heartfelt gratitude to my many friends and family, whose support and patience made it possible for me to complete this project. In particular, I would not have made it through this without Niamh, and she will have my love and gratitude always.

AUTHOR'S DECLARATION

I declare that the work in this dissertation was carried out in accordance with the requirements of the University's Regulations and Code of Practice for Research Degree Programmes and that it has not been submitted for any other academic award. Except where indicated by specific reference in the text, the work is the candidate's own work. Work done in collaboration with, or with the assistance of, others, is indicated as such. Any views expressed in the dissertation are those of the author.

SIGNED: ..... DATE: .....

Table of Contents

List of Tables

Table **Page**

List of Figures

CHAPTER 1

INTRODUCTION

The opening chapter introduces the reader to the phenomenon of superconductivity, charting the discovery of the effect in the early 1900's and the development of the theories currently in place to describe the extraordinary properties with which it is associated. A particular focus is placed on the distinction between the conventional and unconventional classes of superconducting materials, the latter of which is the basis of study in this thesis. The aim of this chapter is to develop a clear understanding of not only the fundamental properties of superconductors, but also the reasons that the anomalous phenomena investigated here are possible exclusively in unconventional configurations of the superconducting state.

1.1 Background and Motivation

1.1.1 Discovery and Applications of Superconductivity

In the early years of the 20th century, Heike Kamerlingh Onnes conducted a series of experiments exploring the electric transport properties of conducting materials at extremely low temperatures [1, 2]. A number of hypotheses had been proposed to predict the possible behaviour of the electrical resistivity as temperature approached absolute zero. It had been suggested that the resistivity may decrease linearly to zero (forming a hypothetical "perfect conductor" [3]), saturate at some finite value, or diverge exponentially [4]. In 1911, Kamerlingh Onnes made the startling discovery that all three of these proposals were false. He found instead that the resistivity of mercury did not persist near to 0 K, but dropped suddenly to zero at a finite temperature of 4.20 K (see Fig. 1.1) [5–7]. This process was shown to be reversible with respect to temperature [6], indicating a phase transition unlike any previously measured or predicted. Kamerlingh Onnes dubbed this phenomenon "superconductivity" and was awarded the 1913 Nobel Prize in recognition of his

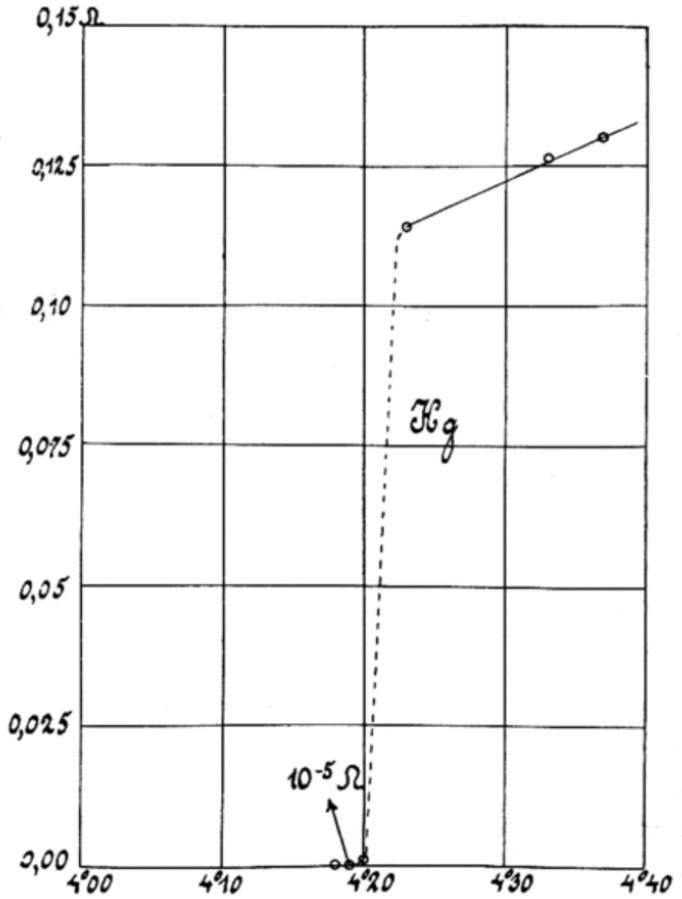

FIGURE 1.1. The plot displays the resistance (Ω) against temperature (K) for pure mercury approaching absolute zero, as measured by Kamerlingh Onnes in 1911 [5–7]. The sudden disappearance of the resistance at 4.20 K clearly indicates the superconducting transition. Figure reproduced from ref. [7].

achievement.

The key characteristics of the superconducting state were established over the following years [8–10]. Kamerlingh Onnes verified that the state does indeed display perfect conductance, demonstrating that a current generated by an induction magnet persists indefinitely after the magnet has been removed [8]. It was also found that superconductivity can not be sustained in the presence of arbitrarily large magnetic fields [9]. All superconducting materials have a well-defined, temperature-dependent critical field curve ($H_c(T)$). If a field exceeding H_c is applied to a sample at a temperature below its superconducting transition temperature (T_c), normal metallic behaviour is recovered. In contrast, small applied fields are completely expelled from within the bulk of a superconducting wire, demonstrating that the state is perfectly diamagnetic [10].

Decades of intense research followed Kamerlingh Onnes' discovery, and superconducting

transitions were identified in a vast range of elements and compounds as the community sought to understand and exploit the remarkable properties of the phase [11–13]. In 1954, the first successful superconducting magnet was engineered at the University of Illinois. This device utilised the persistent, zero resistance current (or "supercurrent") in a superconducting niobium wire to generate large, steady magnetic fields. A flurry of work in the 60's and 70's refined the design of the magnet, and technological applications of superconductivity became increasingly widespread [14]. In particular, superconducting magnets have found commercial use in magnetic resonance imaging devices and large-scale particle accelerators [14].

In addition to the zero resistance properties of the supercurrent, recent work has suggested that unique superconducting materials (known as "topological superconductors") may be able to support symmetry-protected transport modes [15–20]. The existence of such a mode would enable the design of highly efficient devices to perform quantum computations which are free from decoherence [21–23]. A particular state with non-trivial topology is the "chiral" superconducting phase, which is introduced more thoroughly in Section 1.1.2. In brief terms, a chiral superconducting phase is a state in which superconductivity is present in coexistence with an intrinsic magnetisation. Such a configuration presents an ideal platform for the emergence of novel and anomalous phenomena, many of which are discussed in detail in Section 1.3.2.

The investigation of the anomalous properties present in chiral superconducting states is the leading motivation for this thesis. It is the belief of the author that the calculation and discussion of these effects will lead to a greater understanding of a state which could have groundbreaking technological applications. Furthermore, it is hoped that the techniques developed and refined in the work presented here will ultimately become vital tools in the investigation of general superconducting states and in the wider field of condensed matter physics.

1.1.2 Magnetism in Superconductors

The anomalous phenomena which are the subject of this thesis arise from the interplay between superconductivity and magnetism. In 1933, Meissner and Ochsenfeld investigated the interaction between a superconducting state and an external magnetic field (H), and a final key property of the state was uncovered. Observations revealed that a material completely expels all internal magnetic fields upon transition into the superconducting state [10], provided that H_c has not been exceeded. This phenomenon is now commonly known as the "Meissner effect". A theoretical explanation of the effect was found by the London brothers, who showed that an externally applied field must decay exponentially from the surface of the sample to the interior in order to minimise the electromagnetic free energy of the state [24]. The decay is facilitated by a surface current induced by the applied field. An opposing field generated by the surface current negates the external field within the bulk of the sample, in a process known as "Meissner screening".

In technical terms, the Meissner effect can be described as the consequence of perfect diamagnetism (i.e. superconductors have a magnetic susceptibility $\chi_m = -1$). The coexistence of this

property with zero resistivity crucially distinguishes the superconducting state from that of the previously proposed perfect conductor [25]. For the case of a perfect conductor, flux contained within the bulk of a sample would be preserved as it is cooled through T_c. In contrast, for a superconductor, the flux is expelled regardless of whether the field is applied above or below the transition temperature. On the basis of this observation, the superconducting transition can be identified as a true thermodynamic phase transition, as the key properties of the superconductor are defined by independent thermodynamic properties (T and H) and are independent of its history [26].

The discovery of the Meissner effect, in addition to the previously observed critical field behaviour [9], established that there is some level of competition between superconductivity and magnetism. It could naturally be inferred from this that a general superconducting state would not display an intrinsic magnetisation. Experimental investigation of this hypothesis is challenging, however, as Meissner screening renders external magnetic probes ineffective. Further complicating the matter, superconductors fall into one of two possible classes: "conventional" or "unconventional", which have distinct origins and symmetry properties [26]. Conventional superconductors are well described by the Bardeen-Cooper-Schrieffer (BCS) theory (see Section 1.2.2 for further detail) and are indeed non-magnetic [27, 28]. The origins of unconventional states, and their resulting magnetic properties, remain a far more open problem [29–31].

Certain experimental and theoretical observations have indicated strongly that some unconventional states may form with chiral symmetry breaking properties, possibly resulting in a net internal magnetisation [32]. The primary motivation of this thesis is to explore the anomalous phenomena associated with a superconductor of this nature. Key among the results presented here is the derivation of a new formalism to calculate the net magnetisation arising from the finite orbital angular momentum carried by such a state (see Chapter 4). Further discussion is focussed on the anomalous Hall effect and the Kerr effect (Chapter 5) [33], which are driven by the appearance of a finite orbital magnetisation. These properties were calculated through tight-binding models of the proposed chiral superconductor Sr_2RuO_4, which are introduced in Chapter 3.

1.2 Conventional Superconductivity and Superfluidity

1.2.1 Occupation Statistics

In the five decades following Kamerlingh Onnes' initial discovery [5–7], understanding the origin of the superconducting state remained one of the leading challenges facing the physics community, attracting the attention of many of the world's most esteemed minds, such as Einstein [34] and Feynman [35]. To understand the microscopic theory that was eventually obtained, it is vital to first establish the distinction between the boson and fermion classes of particle. The key feature which distinguishes the two is that an ideal gas of bosons at low temperatures is governed by

different quantum statistical laws than an equivalent gas of fermions [36]. Bosons obey Bose-Einstein statistics, which dictate that an unlimited number of bosonic particles can occupy a single discrete energy state. In contrast, fermions are governed by Fermi-Dirac statistics, which adhere to Pauli's exclusion principle. This rule prevents any two indistinguishable fermions from occupying a single state (see App. A.1 for a demonstration of the exclusion principle on the statistics of paired fermions).

The distinction between Fermi-Dirac and Bose-Einstein statistics is of critical importance to the electrical conductivity of solid state materials, and consequently plays a key role in explaining the phenomenon of superconductivity. Charge currents are typically carried by spin-1/2 electrons, which obey Pauli's exclusion principle. For a conducting lattice at thermodynamic equilibrium, all energy states up to some cut off energy (known as the "Fermi energy") are occupied by itinerant electrons. Each of these states can be parametrised in terms of a reciprocal space vector ($\mathbf{k}$) which is proportional to the crystal momentum [36], and so we can define a "Fermi surface", which corresponds to the region in reciprocal space connecting the states with energy equal to the Fermi energy. The Fermi surface thus separates occupied electron states from unoccupied states. Consider now an external energy source, such as an electric voltage, applied to this conductor. Only those electrons in states near to the Fermi surface can be excited by the electric field as they are energetically close to unoccupied states to be scattered in to. This means only a small fraction of the total density of itinerant electrons can participate in the conduction of a current.

1.2.2 Discovery of Superfluidity and BCS Theory

In 1927, it was experimentally observed that liquid ^{4}He (a bosonic atom) undergoes a phase transition at 2.17 K [37, 38]. The low-temperature phase displays the extraordinary property of zero viscosity [39, 40]. It was later understood that the viscosity vanishes due to the formation of a Bose-Einstein condensate (BEC) [41], meaning that the transition corresponds to the temperature at which a macroscopic fraction of the ^{4}He atoms begin to occupy the single lowest energy state [42–45]. The frictionless transport of this state appears to be a clear analogue of the vanishing resistance observed in the superconducting state, and the phenomenon was consequently named "superfluidity". A key step in developing a microscopic theory of superconductivity was the hypothesis that the superconducting transition occurs due to some mechanism which allows the fermionic electrons to behave in a bosonic-like fashion [46, 47], enabling the formation of a charged equivalent of the Bose-Einstein condensate.

It should be noted that a degenerate, ground state Bose-Einstein condensate cannot display superfluidity in the absence of interactions [48]. The vanishing of viscosity occurs only in strongly correlated condensates, arising from a phase coherence induced by the overlap of wavefunctions occupying the same quantum state [48, 49]. In the coherent state, a single particle can not be scattered by a small external potential. Instead, scattering can only occur if the potential is large enough to deflect every particle in the condensate simultaneously. An excited, phase coherent state

can therefore be displaced without encountering resistance from common scattering potentials, leading to the property of zero viscosity observed in superfluids [42, 43].

Despite the discovery and understanding of the superfluid state developed towards the end of the 1930's [42–45], it was not until 1957 that a microscopic theory of superconductivity was finally developed [27]. The key breakthrough that laid the groundwork for this theory was made by Cooper [50]. He demonstrated that two free electrons, with energies above a filled "sea" of occupied electron states (i.e. above the Fermi surface), are able to become paired under an arbitrarily small attractive potential. The electron pairs (now known as "Cooper pairs") have a net spin which is integer, leading to the desired bosonic structure. Overlap and interaction between the bosonic wavefunctions is strong due to the large radius of a pair (~ 1000 Å for a typical superconductor [51]), resulting in the formation of a highly correlated condensate displaying the phase coherence observed in superfluids [27, 28, 52]. This theory successfully reproduced the key experimental properties of the superconducting state, including the Meissner effect, and is now known as the BCS theory of conventional superconductivity. Its authors; Bardeen, Cooper and Schrieffer; were rewarded with the 1972 Nobel Prize.

In the years following Bardeen, Cooper and Schrieffer's breakthrough, the BCS theory was generalised and refined [53–57], becoming the established theory of superconductivity. Despite its successes, the groundbreaking result did not irrefutably confirm the exact nature of the mechanism responsible for Cooper pairing. It relied only on the assumption that there is some attractive electron-electron interaction. The prime candidate for this interaction, however, was an attractive force mediated by the emission and absorption of phonons (lattice vibrations with quantised energy) [27, 28], a possible pairing mechanism which had been previously proposed by Fröhlich [58]. The phonon exchange originates from the Coulomb interaction between an itinerant electron and a lattice of positively charged ionic cores. Intuitively, it can be understood that the attractive force between the two leads to an increase in the positive charge density in the region surrounding the electron, which in turn leads to the attraction of an additional electron to that region of space. In this way, the two electrons become correlated and bound to one another. In the 1960's, McMillan demonstrated that phonon-mediated pairing was consistent with experimental measurements of electron-tunnelling spectra in a range of superconducting materials, providing convincing evidence that this mechanism enables the superconducting transition [59].

The BCS theory took the further assumption that the pairing interaction can be described in terms of a weak on-site potential [28, 60]. The proposed phonon-mediated interaction is viable in this respect since the lattice is far heavier than the electrons, meaning that the transmission of phonons is extremely slow with respect to the velocity of an electron [58]. When the temperature drops as low as T_c, phonon transmission becomes sufficiently slow that the exchange of a virtual phonon can take place at a single site. In this regime, the emission and absorption of the phonon occur at the same point in space but at different times and the retarded nature of the interaction thus allows the electrons to overcome their Coulomb repulsion. The temporal displacement

between emission and absorption leads to the requirement for the exchanged phonon to be below some cut-off energy ($\hbar\omega_D$, where ω_D is the Debye frequency) [27], which restricts Cooper pairing to only those electrons within a small interval around the Fermi surface. This also dictates the transition temperature for a particular lattice, as the Debye frequency is directly related to the atomic masses and lattice spacing.

Given that Pauli's exclusion principle prevents any two identical electrons from occupying the same site, the assumption of an on-site potential necessitates the pairing of electrons with opposite spin only. The pair therefore has a total spin quantum number $S = 0$, which is known as the singlet pairing configuration (see App. A.1 for a detailed discussion on the distinction between singlet and triplet pairing) [36]. The pairing mechanism is also governed by an isotropic potential, meaning that the interaction does not imbue the electrons with any orbital angular momentum [27]. Superconductivity thus forms with an s-wave symmetry, where the Cooper pair wavefunction carries no net spin or orbital angular momentum ($L = 0$). An s-wave state which conforms to the constraints of BCS theory is now commonly referred to as a conventional superconducting state.

A key success of the BCS theory was the prediction of a gap in the energy spectrum at the Fermi energy [61]. This Fermi surface gap corresponds to the binding energy associated with a Cooper pair and was consistent with the observed exponential behaviour of the specific heat below T_c. For the case of s-wave symmetry, the pairing interaction is isotropic in nature. Spherically symmetric pairing results in a gap which is isotropic in reciprocal space, i.e. a constant gap in energy is present at all points on the Fermi surface. As a result, the Cooper pair has no internal structure and can be described in terms of a single number (Δ), which determines the magnitude of the energy gap (equal to 2Δ).

For three decades following the development and refinement of the BCS theory, it was demonstrated that all known superconducting states displayed the key characteristics of phonon-mediated pairing and the conventional s-wave symmetry [11–14]. This includes the observation of the isotope effect in mercury, where the transition temperature of different isotopes were shown to share the same relationship with atomic mass as the temperature does with phonon energy [62, 63]. The dependence of the phonon-mediated pairing mechanism on the ionic masses restricts the possible transition temperature for this case, and it was widely believed for several decades that T_c could not exceed a value of approximately 28 K for a conventional superconductor [59].

It is now known that superconductivity is not restricted to the constraints of BCS theory [29, 30]. The Cooper pair phase is possible in more exotic pairing symmetries than the conventional s-wave structure, in some cases resulting in symmetry-protetcted "nodes" in reciprocal space where the energy gap is zero, and the transition is by no means limited to temperatures below 28 K [64]. In fact, it has been shown that T_c can reach as high as 203 K for a conventional superconductor at high pressure [65]. In the following section, the recent advancements of superconducting theory

beyond the initial assumptions of Bardeen, Cooper and Schrieffer are described, as well as the consequences and possibilities for Cooper pair wavefunctions with non-zero angular momentum, in either the spin channel, the orbital channel, or both.

1.3 Unconventional Superconductivity

1.3.1 Beyond BCS Theory

Any superconducting state in which the Cooper pairs form in a configuration other than the isotropic s-wave symmetry does not fall within the confines of BCS theory. Before unconventional superconductivity was proven to exist, however, the first instance of non-s-wave Cooper pairing was in fact found in superfluid ^{3}He. Studies of the low-temperature phase of ^{3}He were initially motivated by the debate concerning the origin of the superfluid state, which went on throughout the 1940's. London proposed that investigation of ^{3}He would provide a crucial test of the theory that superfluidity was a consequence of Bose-Einstein condensation [66]. A fermionic isotope of ^{4}He, such as ^{3}He, would not be subject to BEC, meaning that it should not display a phase transition in the temperature range near to 2.17 K (the transition temperature of ^{4}He). This proposal was verified in 1949, where it was shown that ^{3}He retains non-superfluid properties at temperatures as low as 1 K [67].

Several years on from these initial experiments, a series of theoretical investigations suggested that there may indeed be a superfluid phase in ^{3}He, and that such a phase would display a non-s-wave pair symmetry [68–70]. In 1972, a superfluid phase transition was identified, at the much lower temperature of 2.6 mK [71]. The transition into a non-viscous state in a fermionic liquid corresponds to some form of Cooper pairing. In this case, however, pairing occurs in a material without a lattice, indicating that phonons play no role and an exotic mechanism must be responsible. Further complicating the matter, liquid ^{3}He in fact displays two stable superfluid phases (see Fig. 1.2) [72]. The experimental properties of these phases were established in the following years [73, 74], and the exotic nature of this state was confirmed through observations of anisotropies in the pair wavefunction, which is not possible in the conventional, spin singlet configuration.

Different nodal structures are supported by the two gapped phases in superfluid ^{3}He, but both display a p-wave symmetry ($L = 1$) [72]. Pauli's exclusion principle states that a pair wavefunction must be antisymmetric under particle exchange (see App. A.1) [36]. Odd-parity pairing (i.e. a pair wavefunction with an odd orbital quantum number) thus necessitates that the spin part of the wavefunction must be symmetric. This corresponds to spin triplet pairing, where the total spin quantum number $S = 1$. The Cooper pairing mechanism to generate this odd-parity state is widely believed to arise from magnetic spin fluctuations, demonstrating that non-trivial magnetic properties can be prevalent in a non-s-wave paired state [74–76].

Although this exotic pairing was observed in a liquid rather than a lattice, it seemed natural to

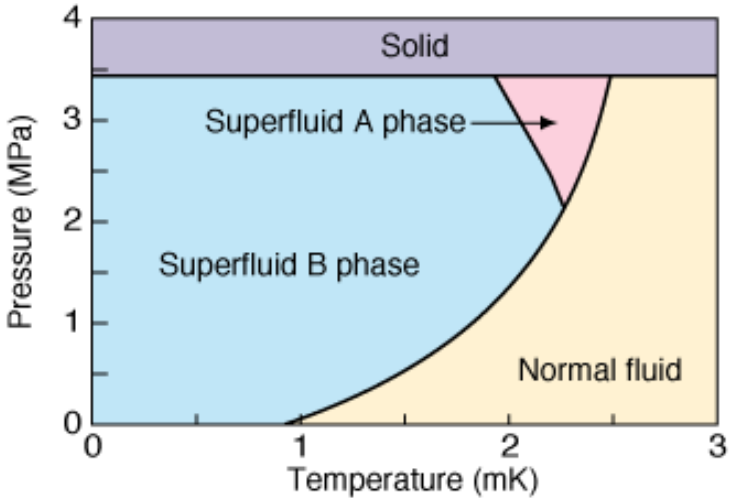

FIGURE 1.2. The plot displays the phase diagram of ^{3}He below its superfluid transition at 2.6 mK. Two distinct phases, A and B, can be formed. Figure courtesy of E. Thuneberg.

infer from these results that electron-phonon pairing is not the only mechanism possible to create a superconducting state. The first such unconventional superconducting state was identified in 1979, when a T_c of 0.5 K was found in $CeCu_2Si_2$ [77]. It was immediately highlighted that this particular compound can not be consistent with the requirements of the conventional phonon pairing theory due to the fact that the superconductivity arises from conduction electrons with an enhanced effective mass [78]. The conduction electrons in such a heavy-fermion material have a suppressed Fermi velocity (the velocity of electron states at the Fermi surface). In BCS Cooper pairing, screening of the Coulomb repulsion requires the Fermi velocity to greatly exceed the phonon velocity. A transition temperature of 0.5 K in this material was shown to be incompatible with this theory [77].

A raft of heavy-fermion compounds with different structures were identified as unconventional superconductors in the years following the initial discovery in $CeCu_2Si_2$ [79]. Materials in this class display signatures of anisotropy in the pair wavefunction, leading to nodes in the gap structure. There is, however, a wide variety of possible pairing symmetries, and so no universal microscopic theory has been established for heavy-fermion superconductivity [80]. Nevertheless, a general phase diagram for this class of materials exists, where superconductivity tends to occur in close proximity to a magnetic phase [81]. It is widely believed, therefore, that magnetic fluctuations play a key role in the formation of Cooper pairs, resulting in the observed anisotropic pairing wavefunctions [82].

Notable among the identified heavy-fermion compounds is UPt_3, which displays a phase diagram very similar to that of ^{3}He, including multiple superconducting phases [83]. Anisotropies

in the upper critical field [84], in conjunction with the coexistence of spin fluctuations and superconductivity, have led some to speculate that UPt_3 also displays a p-wave order parameter [85]. Spin triplet pairing and time-reversal symmetry breaking, consistent with p-wave symmetry, have been observed experimentally [86], yet attempts to transfer the spin-fluctuation models of Cooper pairing in ^{3}He to this supposed charged analogue have thus far been unsuccessful. The origin of superconductivity and the exact nature of the order parameter in this material therefore remain an open problem.

In 1986, the first instance of superconductivity above 28 K (the proposed upper limit of BCS superconductivity) was observed in a layered cuprate compound La_2BaCuO_4 [87], ushering in another class of unconventional superconductors now known as the cuprates [88]. The authors Bednorz and Müller recorded a transition temperature of 35 K in the material, and a record T_c of 134 K has since been found for a cuprate compound at ambient pressure [89]. A fascinating trait universal to the cuprate class of superconductors is the existence of a "pseudogap" regime in the phase diagram [90]. The pseudogap phenomenon is the appearance of a partial energy gap at the Fermi surface at temperatures above the superconducting transition, and its origin remains a widely controversial subject. Many distinct models have been proposed to explain the effect, and it is believed by some that Cooper pairs "preform" at a temperature $T^* > T_c$, forming a condensate which does not display the phase coherence required for superconductivity [91].

The discovery of high-temperature superconductivity in the cuprates instigated a large amount of research into methods to enhance the transition temperature. It has been shown that T_c can reach as high 203 K [65], albeit at a very high pressure of 150 GPa, with no upper limit currently established. Pressure remains the primary avenue for the enhancement of T_c, but other prospects include the use of infrared laser pulses [92]. The ultimate goal is to identify a material which can sustain a supercurrent at room-temperature and superconductivity would clearly become ubiquitous in solid state devices if this were to be achieved.

Given that it had been observed that high-temperature superconductivity was possible in layered perovskite cuprate structures, a natural avenue for further study was in other materials with the same layered structure. A compound which replicates this structure is Sr_2RuO_4, which is a perovskite material in which the copper atoms are replaced with ruthenium [93–95]. This material is of fundamental importance to this thesis. A T_c of 1.5 K was identified in 1994 [96], and investigations of the susceptibility [97] and measurements of time-reversal symmetry breaking [98–102] have since led to the suggestion that the pair wavefunction may display a spin-triplet p-wave symmetry analogous to that observed in the ^{3}He A phase (and possibly in UPt_3) [103–106]. A major theme of this thesis is the exploration of this hypothesis, and the properties of the proposed p-wave state are discussed at greater length in Chapter 3.

It should be reiterated that key questions raised here regarding the nature of the pairing mechanism in unconventional superconductors, the pseudogap phenomenon, and the ultimate goal of room temperature superconductivity are not major topics of discussion in this thesis.

These are all fiercely debated issues of huge importance in the condensed matter field, which tie to the classes of materials that are studied here. Rather, the focus of this work is placed on understanding the anomalous phenomena associated with anisotropic pair wavefunctions arising in unconventional superconducting states, and an introduction to these topics is given in Section 1.3.2 below.

1.3.2 Anomalous Phenomena in Chiral Superconductors

It has been firmly established that the transition into the superfluid phase of ^{3}He coincides with the formation of spin triplet Cooper pairs with p-wave symmetry [72–76]. This exotic symmetry results from the pairing of finite-size particles, which can not be facilitated by an on-site potential, crucially distinguishing the pairing in ^{3}He from that of the BCS-type pairing between point-like electrons. On-site pairing is prohibited in this case due to the strong repulsive core of helium atoms at short distances [68, 69]. The unconventional pairing requires the binding of atoms to occur via a long-range interaction, while the pair wavefunction must vanish at close distances. In a classical analogy, this could be equated to the case of two gravitational bodies orbiting one another, bound by the centrifugal force. As a result, the pair wavefunction must have a non-zero orbital angular momentum, in contrast to the conventional s-wave state.

A pair wavefunction with total spin equal to 1 has three possible spin projections ($S_z = -1, 0, 1$) [36]. In the case of p-wave pairing, there are then three possible orbital projections ($L_z = -1, 0, 1$) for each of these spin projections. As a result, this state must be parametrised in terms of an order parameter with 9 distinct components. It is immediately clear, then, that this unconventional state displays a far richer structure than the conventional s-wave superconducting states, for which there is a single order parameter only. The more complex structure of the condensate results in the multiple stable superfluid phases, each arising from different superpositions of the three spin wavefunctions (see Fig. 1.2) [26, 72, 74].

The discovery of p-wave pairing in ^{3}He was a groundbreaking result, demonstrating that it is possible to generate Cooper pairs with an internal structure. An equivalent exotic pairing of electrons to form an unconventional superconducting state takes on an added layer of significance due to the charged nature of the pair constituents. For any electron-electron Cooper pair wavefunction with symmetry lower than the s-wave order, the resulting structure is a charged bosonic particle with non-zero angular momentum. The pair would therefore carry an intrinsic magnetic moment. The question then arises as to whether the correlated moments in such an unconventional state would cancel or generate a net magnetisation. Such a state may seem like a contradictory result, given that the established Meissner effect and critical field properties suggest some level of antithesis between superconductivity and magnetism. Nevertheless, a wide variety of exotic and anomalous phenomena have been shown to arise in unconventional superconducting states with magnetic Cooper pairs, as discussed further below. It is this interplay between superconductivity and magnetism that is the driving force of this thesis.

The distinguishing feature of a magnetic state is the breaking of time-reversal symmetry (TRS), indicating that a particular handedness, or chirality, has been adopted. It is the property that the state is no longer symmetric under the reversal of all time-dependent quantities, such as velocity and momentum. This property is illustrated by the chirality of the Lorentz force ($\mathbf{F} \propto \mathbf{v} \times \mathbf{B}$). A charged particle moving perpendicularly to a magnetic field is subject to the Lorentz force, which deflects the particle in a transverse direction. The direction of this force changes upon a time-reversal transformation, demonstrating that the magnetic field breaks TRS. Time-reversal symmetry is broken in the transition to the superconducting state when Cooper pairs form with a finite angular momentum, in either the spin or orbital degree of freedom [29, 32, 98]. Returning to the classical analogy for this scenario, the pair can be viewed as a current loop. The loop must flow in either the clockwise or anti-clockwise direction, hence the state chooses a handedness at the transition.

For the case of Sr_2RuO_4, which is believed to replicate the nodal p-wave structure of the ^{3}He A phase [103, 104, 106], it has been predicted that the breaking of TRS should result in the formation of a finite loop of current confined to the surface of the sample, lying in the plane perpendicular to the direction of magnetisation [107–109]. The general idea behind this proposal is that, in regions near to the surface in the xy-plane, the boundary of the sample suppresses the component of the order parameter perpendicular to the surface. As a result, superconductivity only persists parallel to the boundary. The time-reversal symmetry breaking nature of the order parameter then results in currents which flow in opposite directions for parallel boundaries, thus resulting in a net flow of current around the sample surface. This prediction has proven highly controversial, however, as such an edge current has never been identified experimentally despite years of intense research [110–112].

To study the influence of magnetisation in superconducting states, and the possibility that a finite edge current exists, the central part of this thesis is the derivation of a new formalism to calculate the orbital magnetisation of a general superconductor. This corresponds to the magnetisation arising from both the intrinsic structure of the Cooper pair and that generated by itinerant currents (see Fig. 1.3). Attaining a framework of this nature is not trivial due to the difficulty of evaluating position-dependent quantities (such as the orbital angular momentum $\hat{\mathbf{r}} \times \hat{\mathbf{p}}$) for an infinite periodic lattice model. A formalism was developed to calculate this property for a normal state insulator [113, 114], and the extension of this theory to the general superconducting state is presented in detail in Chapter 4. The new formalism is then applied to two distinct models of Sr_2RuO_4, which are introduced in Chapter 3.

Following on from the measurement of the orbital magnetisation, the focus in Chapter 5 is the anomalous Hall effect (AHE), which is a direct consequence of chiral symmetry breaking. The conventional Hall effect is a phenomenon present in all conducting materials and is very commonly utilised in electronic devices such as magnetometers. This effect results from the application of a magnetic field to a material which is conducting a current. The applied field

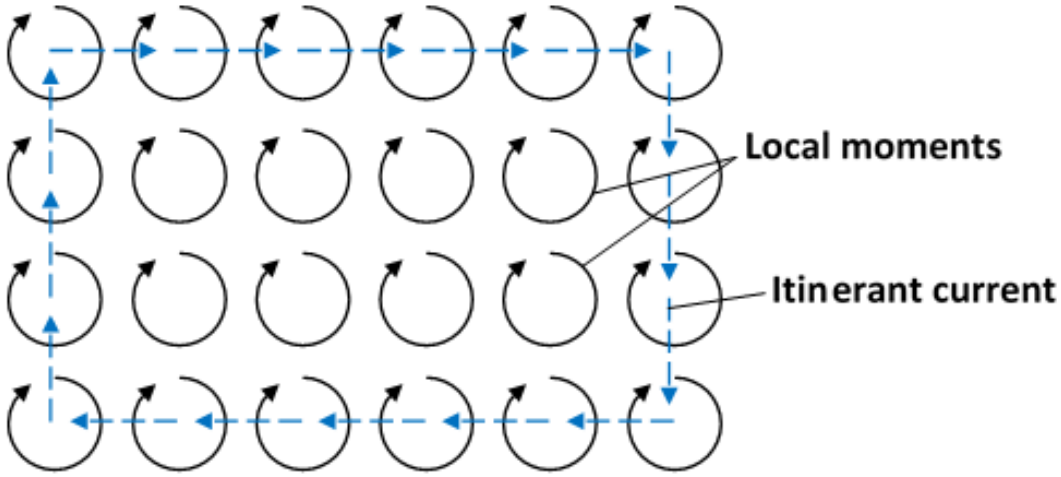

FIGURE 1.3. Chiral Cooper pairs form with a finite orbital angular momentum, and thus carry an intrinsic magnetic moment. The breaking of time-reversal symmetry coinciding with the transition into the chiral state leads to the formation of an itinerant edge current. The net flow of Cooper pairs near to the sample surface also generates a magnetic field.

exerts a Lorentz force on the charge carriers, deflecting them in the direction transverse to the current flow. As a result, a transverse voltage (referred to as the Hall voltage) is generated. For materials with an intrinsic magnetic field, a spontaneous Hall effect is observed in the absence of an external field. This is referred to as the anomalous Hall effect (see Fig. 1.4). Three distinct mechanisms are typically thought to be capable of generating an AHE [115], and the particular origin in Sr_2RuO_4 and many other unconventional superconductors remains a point of controversy [116, 117]. The disputes concerning this effect are addressed in Chapter 5.

Also introduced and analysed in Chapter 5 is the Kerr effect (see Fig. 1.5). This is an optical phenomenon driven by the same mechanism as the AHE [33, 102, 118]. The Kerr effect is a result of magnetic circular dichroism, a property associated with any state which breaks chiral symmetry. Circularly dichroic materials interact differently with incident circularly polarised radiation depending on its handedness. Given that a linearly polarised beam can be equated with the sum of two circularly polarised beams of opposite handedness, it is found that linearly polarised light reflected from a dichroic surface experiences a rotation of its plane of polarisation. This shift in the polarisation is referred to as the Kerr effect. Kerr rotations have been measured experimentally in a number of superconductors [33, 86, 102, 118, 119], and the investigation of this phenomenon provides a further avenue with which to discuss the possible origins of the AHE in unconventional superconductors.

Finally, the work presented here touches upon the topic of topology. This is a field of enormous interest in the current community, having been the basis of the study rewarded with the 2016

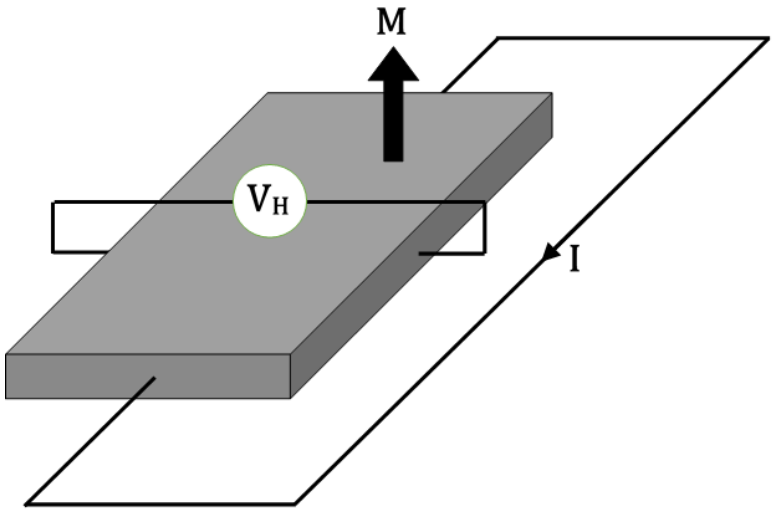

FIGURE 1.4. The conventional Hall effect occurs when a current is passed through a metal in an applied magnetic field, and results in the appearance of the transverse Hall voltage (V_H). Shown here is the spontaneous Hall effect which is observed in materials with an intrinsic magnetisation (**M**), even in the absence of an external field. This is referred to as the anomalous Hall effect.

Nobel Prize. Topological states of matter correspond to those which preserve a particular quantity under continuous transformation in some parameter space. In solid state materials, this quantity can be one of several possible topological invariants. An insulator with a non-zero invariant displays the extraordinary property of surface conductance occurring simultaneously with bulk insulating behaviour [120, 121]. This is known as a topological insulator, and has drawn great interest due to the fact that these surface currents are symmetry-protected, meaning that they transport charge without energy dissipation [122]. Dissipationless transport would be extremely valuable in devices which perform quantum computations [123]. The edge modes in topological insulators are further classified by spin-momentum locking, providing avenues for application in spintronics devices via the quantum spin Hall effect [124].

A particular class of topological invariant which is of fundamental importance is the Chern number [120]. Chern insulators display the quantum anomalous Hall effect, which results in the appearance of quantised edge currents. A non-zero Chern number arises in two-dimensional lattices in which the bandstructure is gapped at the Fermi surface and time-reversal symmetry is broken. These conditions may naturally be satisfied in chiral superconducting states [15, 16, 20]. The topology of unconventional superconductors thus provides an intriguing source of debate and analysis. Furthermore, it has been hypothesised that a topological superconductor would support the existence of Majorana fermions, exotic quasiparticles which are their own anti-particle [17–19]. These states are topologically-protected, quantised modes, making them ideal candidates to store quantum bits (or “qubits”) of information [21, 22]. Control of a Majorana mode would make

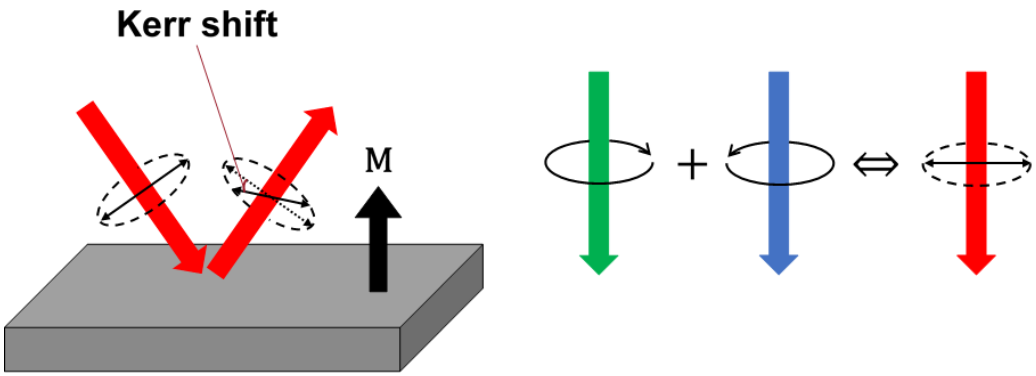

FIGURE 1.5. The incident linearly polarised beam is equivalent to the sum of two circularly polarised beams of opposite handedness. Due to the dichroism of the sample, it is found that the linearly polarised light reflected experiences a rotation of its plane of polarisation. This is known as the Kerr effect [33, 102, 118].

the tantalising prospect of realising quantum computation devices far more feasible [23].

In the work described here, the topology of the states modelled is not discussed at great length, and this work will be left to others more specialised in the topic. However, this insight into the ramifications of TRS breaking in a superconductor serves as a major motivation into studying the anomalous properties of chiral superconducting states, and indicates a further fundamental significance to the work carried out in this thesis.

CHAPTER 2

THEORETICAL BACKGROUND

This chapter lays the groundwork for the theoretical models that were used to perform the calculations in this project. The relevant background knowledge is split into two components: approaches to modelling the normal state electronic properties of a periodic lattice, and the modelling of a general superconducting state. Normal state properties were calculated through the tight-binding approximation, which is also used to describe superconductivity via the Bogoliubov-de Gennes framework. The general theoretical work discussed here is utilised in Chapter 3 to develop specific models of the proposed chiral superconductor Sr_2RuO_4. These models provide a platform on which to analyse the general theories developed in Chapters 4 and 5 for the study of the orbital magnetisation and anomalous Hall effect, respectively, in unconventional superconductors.

2.1 Modelling the Normal State

The principal challenge in the study of periodic crystalline structures is to accurately describe the physical properties of a many-body electronic state. The Hamiltonian for such a state includes a set of interactions which encompasses sums over all atoms and electrons associated with the lattice sites in an infinitely extended system. Clearly, a direct computation of the Schrödinger equation associated with this Hamiltonian is not feasible as a result. To bypass this problem, it is often assumed that the system of interacting particles can be approximated by non-interacting particles in an effective mean-field potential. By removing the many-body interactions, an effective Hamiltonian for a single particle can be obtained which is bi-linear in field operators. This can then be diagonalised to obtain approximations for the energy and wavefunction of an electron in a given system.

A commonly-used technique to describe an electronic state is the density functional theory (DFT) [125, 126]. DFT forgoes the mean-field approach, and instead the Schrödinger equation is solved in conjunction with a set of self-consistency conditions. These conditions are obtained by acknowledging that the ground state properties of the many-body state are uniquely described by the electron density. This approach is widely employed in part because it is readily applicable to cases of complex lattice symmetries and multi-atom bases. While DFT would be a technique well-suited to the study of the normal state of Sr_2RuO_4, knowledge of the density alone is not sufficient for the purpose of the calculations which are presented in this thesis. Rather, a more beneficial framework is one which generates an effective Hamiltonian which can be diagonalised analytically, without the need for a self-consistent computation.

Mean-field approaches utilise Landau-Fermi liquid theory [36]. This theory establishes that an interacting state can be equated to a non-interacting gas of fermions with a renormalised bandstructure. As such, the many-body Hamiltonian can be reduced to an effective, single-particle Hamiltonian. The technique which will be used here to obtain a single-particle Schrödinger equation is to expand the many-body wavefunction in the tight-binding basis and apply the Slater-Koster parametrisation [127, 128]. In this expanded basis, the interactions of the state are accounted for by a set of adjustable parameters, and a diagonalisable single-electron Hamiltonian can be constructed.

A key advantage of the tight-binding approach over DFT is that it facilitates the calculation of the gradient of the Hamiltonian. The derivative with respect to $\mathbf{k}$ of the effective, single-particle Hamiltonian obtained in the mean-field approximation can be determined by hand. This derivative becomes vitally important in the computation of the anomalous phenomena which are the subject of this thesis (see Chapters 4 and 5). The tight-binding method rapidly becomes unwieldy in multi-atom and multi-band bases, as highlighted in Section 2.1.2. Nevertheless, it is sufficient for the systems studied here and is a powerful tool to model the bandstructure and investigate the transport properties of a lattice.

In this section, the fundamental approximations which drive the tight-binding method are presented. A simple toy Hamiltonian for a one-dimensional lattice chain with a single-atom, single-orbital basis is then derived in this formalism. Finally, the approach to extending this model to higher dimensions and more complicated lattice structures is discussed. This extension is then performed in Chapter 3 to obtain a tight-binding Hamiltonian for Sr_2RuO_4.

2.1.1 Tight-Binding Approximation

Consider a periodic lattice of atoms, each occupied by n electrons, extending infinitely through space. By Bloch's theorem, the wavefunction for a electron in this system can be written as a Bloch state ($\psi_{n\mathbf{k}}(\mathbf{r})$) [36], which is parametrised in terms of a discrete set of bands (n) and a continuous set of crystal wavevectors ($\mathbf{k}$).

The effective single-particle Schrödinger equation for this electron is then

$$\hat{H}(\mathbf{r})\psi_{n\mathbf{k}}(\mathbf{r}) = \epsilon_{n\mathbf{k}}\psi_{n\mathbf{k}}(\mathbf{r}), \tag{2.1}$$

where $\hat{H}(\mathbf{r})$ is the lattice Hamiltonian and $\epsilon_{n\mathbf{k}}$ is the energy of an electron state. The Hamiltonian includes the kinetic energy of the electron, its interaction with the atomic lattice, and the interaction with the rest of the Fermi sea of electrons occupying the lattice sites.

The approach used here to find approximate solutions to equation (2.1) is the parametrised tight-binding method, which was first introduced in 1954 by Slater and Koster [128]. It was envisaged as a simplified method of applying Bloch's linear combination of atomic orbitals (LCAO) approach [127]. The LCAO method is driven by the assumption that electron states in a periodic lattice are highly localised on atomic sites. In this scenario, an electron interacts weakly with the lattice, and so it can be inferred that the stationary state wavefunction is very similar to that of an isolated atom.

Working under the assumption of tight-binding, it is natural to perform an expansion of the Bloch wavefunction in terms of the atomic wavefunctions of each lattice site. The wavefunctions of free atoms are given by atomic orbitals $\phi_j(\mathbf{r})$, which are well-defined mathematical functions for an electron state [36], where the index j contains both the spin and orbital quantum numbers of the basis. The atomic orbitals are orthogonal and localised on lattice sites, meaning that neighbouring orbitals do not overlap and

$$\int \mathrm{d}\mathbf{r}\, \phi^*_{j'}(\mathbf{r}+\mathbf{R}'_i)\phi_j(\mathbf{r}+\mathbf{R}_i) = \delta_{ii'}\delta_{jj'}, \tag{2.2}$$

where $\mathbf{R}$ are lattice vectors connecting atomic sites.

A general expansion of the wavefunction in the orbital basis takes the form

$$\psi_{n\mathbf{k}}(\mathbf{r}) = \sum_{i,j} c^{nj}_{\mathbf{k}}(\mathbf{R}_i)\phi_j(\mathbf{r}-\mathbf{R}_i), \tag{2.3}$$

where i sums over all lattice vectors. The coefficients $c_{\mathbf{k}}$ can be simplified by ensuring that the expanded wavefunction retains the properties of a Bloch state and is appropriately normalised.

A Bloch state is governed by the translational behaviour

$$\psi_{n\mathbf{k}}(\mathbf{r}+\mathbf{R}'_i) = \mathrm{e}^{\mathrm{i}\mathbf{k}\cdot\mathbf{R}'_i}\psi_{n\mathbf{k}}(\mathbf{r}). \tag{2.4}$$

Performing expansion (2.3) on equation (2.4) gives

$$\sum_{i,j} c^{nj}_{\mathbf{k}}(\mathbf{R}_i)\phi_j(\mathbf{r}-(\mathbf{R}_i-\mathbf{R}'_i)) = \mathrm{e}^{\mathrm{i}\mathbf{k}\cdot\mathbf{R}'_i}\sum_{i'',j'} c^{nj'}_{\mathbf{k}}(\mathbf{R}''_i)\phi_{j'}(\mathbf{r}-\mathbf{R}''_i). \tag{2.5}$$

The lattice sum over i on the left hand side can be replaced with a sum over i''', where $\mathbf{R}_i''' = \mathbf{R}_i - \mathbf{R}_i'$. Multiplying both sides of (2.5) by $\phi^*_{j''}(\mathbf{r})$, integrating over real space and applying (2.2), the coefficients can be shown to obey

$$c^{nj}_{\mathbf{k}}(\mathbf{R}_i) = \mathrm{e}^{\mathrm{i}\mathbf{k}\cdot\mathbf{R}_i} c^{nj}_{\mathbf{k}}(\mathbf{0}), \tag{2.6}$$

where lattice and band indices have been relabelled.

The full expansion in the tight-binding basis is now

$$\psi_{n\mathbf{k}}(\mathbf{r}) = \sum_{i,j} \mathrm{e}^{\mathrm{i}\mathbf{k}\cdot\mathbf{R}_i} c^{nj}_{\mathbf{k}}(\mathbf{0}) \phi_j(\mathbf{r} - \mathbf{R}_i). \tag{2.7}$$

For the sake of enforcing normalisation, it is necessary to temporarily restrict the expansion to a finite number of atoms. The infinitely extended lattice is instead approached through a finite-sized sample of N_c sites with periodic boundary conditions. Observables are then naturally defined in the thermodynamic limit by setting $N_c \to \infty$. To generate a tight-binding model for a particular lattice, this expansion is applied to equation (2.1) and the lattice and orbital sums enforce the considered symmetries and dimensionality of the system. The following subsection outlines this process for a simple toy model.

2.1.2 One-Dimensional Chain

A simple example of a one-dimensional chain extended along the x-direction is now considered. The lattice spacing is denoted a, and there is a single band consisting of the atomic s-orbital without spin. To calculate the energy dispersion (energy as a function of wavevector) of the band, the expectation value of the Hamiltonian is taken. Multiplying both sides of (2.1) by $\psi^*_{\mathbf{k}}$ and integrating in real space gives

$$\epsilon(\mathbf{k}) = \int dx\, \psi^*_{\mathbf{k}}(x) \hat{H}(x) \psi_{\mathbf{k}}(x), \tag{2.8}$$

where the index n has been suppressed for this single-band model. Applying the expansion (2.7), this becomes

$$\epsilon(\mathbf{k}) = |c_{\mathbf{k}}(\mathbf{0})|^2 \sum_{i,j} \mathrm{e}^{\mathrm{i}k_x(x_i - x_j)} \left[\int dx\, \phi^*(x - x_j) \hat{H}(x) \phi(x - x_i) \right]. \tag{2.9}$$

In the single-band case, the basis is normalised by setting $c_{\mathbf{k}}(\mathbf{0}) = 1/\sqrt{N_c}$. Inserting this and

shifting the lattice sum by $x \to x + x_i'$, the dispersion can be written as

$$\begin{aligned}\epsilon(k_x) &= \frac{1}{N_c}\sum_{i,j} \mathrm{e}^{\mathrm{i}k_x(x_i - x_j)}\left[\int dx\, \phi^*(x)\hat{H}(x + x_j)\phi(x - (x_i - x_j))\right] \\ &= \sum_i \mathrm{e}^{\mathrm{i}k_x x_i}\left[\int dx\, \phi^*(x)\hat{H}(x)\phi(x - x_i)\right], \end{aligned} \tag{2.10}$$

where, in the last line, the translational invariance of the lattice Hamiltonian has been applied and indices have been relabelled. The double sum over i, j is replaced with a single sum over $x_i' = x_i - x_j$, with a factor N_c introduced to account for repeated terms. The thermodynamic limit is now recovered and the lattice sum extends infinitely.

For the case that $x_i \neq 0$, the integral in the last line of (2.10) is referred to as a "transfer integral". In a purely localised regime, an electron would be confined to a lattice site by an infinite potential barrier, and only the on-site integral ($x_i = 0$) would be non-zero. In the tight-binding picture, this restriction is relaxed slightly, and the electron is instead shared among the lattice sites. It can be imagined the electron is able to "hop" to other sites. The lattice sum of transfer integrals can be simplified by placing constraints on which sites an electron can hop to.

In the simplest approximation, it is assumed that there is no hopping beyond nearest-neighbour atoms, and so transfer integrals for $|x_i| > a$ can be set to zero. The dispersion equation (2.10) then simplifies to

$$\epsilon(k_x) = \int dx\, \phi^*(x)\hat{H}(x)\phi(x) + \mathrm{e}^{\mathrm{i}k_x a}\int dx\, \phi^*(x)\hat{H}(x)\phi(x - a) + \mathrm{e}^{-\mathrm{i}k_x a}\int dx\, \phi^*(x)\hat{H}(x)\phi(x + a). \tag{2.11}$$

Note that the lattice Hamiltonian $\hat{H}(x)$ has remained unchanged thus far, and contains the full set of interactions with the atomic lattice and Fermi sea. The integrals above therefore can not be evaluated easily and explicitly. Slater and Koster proposed that, for a Landau-Fermi liquid, the transfer integrals can be replaced with adjustable constants while retaining the correct symmetry properties of the energy band [128]. This provides a computationally efficient method to obtain the dispersion for a particular lattice. Given that the lattice does not break mirror symmetry, and the s-orbital is isotropic, it can be inferred that the second and third integrals in (2.11) are equal. These are replaced with the hopping parameter t, while the on-site integral is denoted ϵ_0. The parameters encode the hopping and on-site atomic energies of the electron respectively.

Inserting the Slater-Koster parameters, the dispersion

$$\epsilon(k_x) = \epsilon_0 + 2t\cos(k_x a), \tag{2.12}$$

is obtained. Equation (2.12) represents the dispersion for a single electron band in a one-dimensional chain in the nearest-neighbour tight-binding approximation. The dispersion is

augmented by the parameters ϵ_0 and t, which dictate the occupation and bandwidth of the band respectively. A significant advantage of the tight-binding approach is that the interaction of a single electron with the lattice of atomic nuclei and the rest of the electrons is now completely hidden within these parameters and does not have to be computed directly. Parameters are instead typically determined through comparison with empirical data. This is a process whereby the fundamental electronic properties of the lattice (such as the bandstructure, density of states, heat capacity etc.) are calculated via equation (2.12), and the parameters are then tuned such that the calculations recreate experimental data.

It should be noted that, generally speaking, the convention is to define the nearest-neighbour hopping parameter as a positive value. In this case, the single-band dispersion (2.12) would be $\epsilon(k_x) = \epsilon_0 - 2t\cos(k_x a)$, displaying an energy minimum at $k_x = 0$. The reverse convention has been applied in this instance in order to be consistent with the relevant literature which utilises the normal state tight-binding Hamiltonian for Sr_2RuO_4 discussed in Chapter 3 [129].

It is observed that the structure of the lattice dictates the shape of the dispersion obtained. Increasing the lattice spacing a, for example, leads to a flatter dispersion in $\mathbf{k}$-space. This can be understood intuitively as the velocity and effective mass of an electron are directly related to the gradient of the dispersion. These properties are also dictated by the hopping parameter t, which is inversely proportional to the effective mass. A small effective mass reflects weak localisation, and so the tight-binding approximation breaks down when t becomes very large and the electron can travel freely through the lattice.

Deriving a tight-binding Hamiltonian for more complex systems requires equation (2.8) to be generalised to higher spatial dimensions and the required orbital basis. The determination of which transfer integrals must be retained in such a scenario requires careful consideration of the symmetry of the orbital basis and the shape of the lattice. For example, a p_x-type orbital is distributed primarily along the x-direction, and therefore has different hopping energies for the x and y-axes in a square lattice configuration. Similarly, an isotropic orbital acquires different x and y hopping parameters if the lattice breaks rotational symmetry.

For a multi-band, multi-orbital system, a number of additional parameters must be introduced to encode any inter-orbital hopping energies. The Hamiltonian in this case takes on a matrix form, where its dimension is given by the size of the orbital basis. Diagonalisation becomes increasingly inefficient with the number of bands, a problem which is exacerbated when moving to the Bogoliubov-de Gennes framework in which solutions must be obtained self-consistently (see Section 2.2 below). When tackling a superconducting state, the tight-binding approach is therefore best suited to single atom unit cells with small orbital bases, as is the case for the model of Sr_2RuO_4 introduced in Chapter 3.

2.2 Modelling the Superconducting State

The tight-binding method generates a single-particle Hamiltonian for an electron in a lattice. In this formalism, the Coulombic potential exerted by the lattice on a single charge carrier (via both the atoms and the Fermi sea) is encoded within the introduced Slater-Koster parameters for on-site and hopping energies. Superconductivity, however, is an intrinsically two-particle phenomenon [26]. Obtaining a mean-field approximation for the electron-electron interaction responsible for Cooper pairing requires a more advanced approach than the Slater-Koster parametrisation introduced in the previous section. The approach applied here is Bogoliubov's self-consistent field method [53, 130–132].

In Sections 2.2.1 and 2.2.2, a derivation of the mean-field Bogoliubov equation for a superconducting state is presented. The layout draws heavily from the detailed discussion in Ketterson and Song's textbook [26]. For clarity, this initial derivation is restricted to the case of the singlet, s-wave pairing expected in conventional BCS superconducting states. In Section 2.2.3, this formalism is generalised to be able to account for the exotic pairing symmetries relevant to chiral superconducting phases.

2.2.1 Bogoliubov-de Gennes Equation

The theory of superconductivity developed by Bardeen, Cooper and Schrieffer relies on the assumption of a homogeneous pairing potential, treating the electron cloud as a uniform Fermi gas [27, 28, 50]. While this is sufficient in the case of clean, bulk conventional superconducting states, consideration of a position-dependent mean-field Hamiltonian is required in order to account for boundaries, scattering centres and magnetic fields. A microscopic pairing theory which provides such a framework was developed by Bogoliubov [53, 130, 131] and refined by de Gennes [132]. This technique generalises the Cooper pairing problem to an inhomogeneous lattice. In addition to allowing the consideration of an inhomogeneous s-wave paired state, the more general framework provides a platform on which to investigate the anisotropic pairing symmetries of unconventional superconductors.

To begin the derivation of the Bogoliubov-de Gennes (BdG) equation, the position-dependent Hamiltonian must be introduced. This Hamiltonian must be able to account for the appearance of "anomalous averages", the fundamental feature which distinguishes a superconducting state from that of a normal metal or insulator [26]. The anomalous average is the expectation value for electron and hole pairs resulting from Cooper pairing, which breaks the particle number conserving symmetry of a typical electronic state. The requirement for pair amplitudes in the ground state density enforces the need for a two-particle potential in the Hamiltonian, in contrast to the single-particle operators discussed in Section 2.1.

A Hamiltonian for electrons within a general many-body system is now introduced, including a two-particle potential which is responsible for the formation of Cooper pairs. Introducing second

quantised notation (see App. A.2 for further details on this representation), the full Hamiltonian is

$$\hat{H} = \hat{H}^{(1)} + \hat{V}^{(2)}, \tag{2.13a}$$

$$\hat{H}^{(1)} = \int \mathrm{d}\mathbf{r}\, \hat{\psi}^{\dagger}_{\alpha}(\mathbf{r}) \hat{H}_0(\mathbf{r}) \hat{\psi}_{\beta}(\mathbf{r}), \quad \hat{H}_0(\mathbf{r}) = -\frac{\hbar^2}{2m}\left(\nabla - \frac{\mathrm{i}e}{\hbar}\mathbf{A}\right)^2 \delta_{\alpha\beta} + U^{(1)}_{\alpha\beta}(\mathbf{r}), \tag{2.13b}$$

$$\hat{V}^{(2)} = \frac{1}{2}\int \mathrm{d}\mathbf{r} \left[\int \mathrm{d}\mathbf{r}'\, \hat{\psi}^{\dagger}_{\delta}(\mathbf{r}) \hat{\psi}^{\dagger}_{\gamma}(\mathbf{r}') U^{(2)}_{\delta\gamma,\alpha\beta}(\mathbf{r},\mathbf{r}') \hat{\psi}_{\alpha}(\mathbf{r}') \hat{\psi}_{\beta}(\mathbf{r}) \right], \tag{2.13c}$$

where $\hat{H}^{(1)}$ is a one-electron Hamiltonian and $\hat{V}^{(2)}$ is the two-particle potential. In the second quantised language, $\hat{\psi}(\mathbf{r})$ ($\hat{\psi}^{\dagger}(\mathbf{r})$) are the Fermi field operators which destroy (create) a particle at position $\mathbf{r}$. The operator $\hat{H}_0$ generates the energy of a particle created by the operator $\hat{\psi}^{\dagger}$. Greek letter subscripts of the operators are spin indices, for which the general summation convention is implied. The inclusion of the vector potential $\mathbf{A}$ in the kinetic energy operator accounts for the interaction of the electron's orbital motion with an external magnetic field ($\mathbf{A}$ can be simply set to zero for the case of no external field).

Explicit diagonalisation of (2.13) is problematic due to the presence of a quartic operator in $\hat{V}^{(2)}$. The aim of the mean-field approach is to replace this quartic term with an effective single-particle operator and an associated set of eigenfunctions which approximate the behaviour of an electron within the many-body state. An effective Hamiltonian which will achieve this goal can be inferred from the following considerations. The aim is to obtain a state in which pairs of electrons can become bound spontaneously. Such an electron pair is generated by the operator $\hat{\psi}^{\dagger}\hat{\psi}^{\dagger}$. The Hamiltonian must be Hermitian, which means the Hermitian conjugate of this operator ($\hat{\psi}\hat{\psi}$, which creates hole-hole pairs) is also required. For now, the assumption of singlet pairing will be taken, meaning that only Cooper pairs containing two electrons of opposite spin are required. This removes the need for pair operators of the form $\hat{\psi}_{\downarrow}\hat{\psi}_{\downarrow}$ and $\hat{\psi}_{\uparrow}\hat{\psi}_{\uparrow}$ corresponding to equal spin pairs, which would be found only in a triplet configuration.

Under these considerations, it can be assumed that the effective Hamiltonian will take the form [26]

$$\hat{H}_e = \int \mathrm{d}\mathbf{r}\, \hat{\psi}^{\dagger}_{\alpha}(\mathbf{r}) \hat{H}_0(\mathbf{r}) \hat{\psi}_{\alpha}(\mathbf{r}) + \Delta(\mathbf{r}) \hat{\psi}^{\dagger}_{\uparrow}(\mathbf{r}) \hat{\psi}^{\dagger}_{\downarrow}(\mathbf{r}) + \Delta^{*}(\mathbf{r}) \hat{\psi}_{\downarrow}(\mathbf{r}) \hat{\psi}_{\uparrow}(\mathbf{r}). \tag{2.14}$$

The introduced function $\Delta(\mathbf{r})$ (often referred to as the pairing potential) is the amplitude for the creation of Cooper pairs. The presence of this term admits the appearance of non-vanishing anomalous averages ($\langle \hat{\psi}^{\dagger}_{\uparrow}\hat{\psi}^{\dagger}_{\downarrow}\rangle$ and $\langle \hat{\psi}_{\downarrow}\hat{\psi}_{\uparrow}\rangle$) whilst reducing the quartic terms in the two-particle

interaction to bi-linear forms. Formally, the presence of pair operators corresponds to the breaking of $U(1)$ symmetry (also referred to as gauge symmetry). This symmetry reflects the fermion number-conserving properties of a normal electronic state, which is broken when pairs of fermions become bound and form a Bose liquid [132].

For now, it is assumed that the effective Hamiltonian is a valid approximation for the superconducting ground state, and that the pairing potential originates from the mean-field approximation of the two-particle interaction appearing in the full many-body Hamiltonian. In Section 2.2.2, the variations of the minimised free energies of (2.13) and (2.14) are equated. Through this process, an expression for the pairing potential in terms of the two-particle potential and the field operators is generated. It is then possible to produce a set of self-consistent conditions for $\Delta(\mathbf{r})$ by expanding the field operators in terms of an introduced set of eigenfunctions which diagonalise the effective Hamiltonian. The assumption that (2.14) is a valid approximation can be verified in this way.

In the absence of quartic terms, the mean-field Hamiltonian (2.14) can be diagonalised through an appropriate expansion of the Fermi operators. To diagonalise the one-electron Hamiltonian for a non-superconductor, this expansion would be performed in terms of a single-component basis. However, due to the presence of pair amplitudes in the effective Hamiltonian, a general Bogoliubov-Valatin transformation must instead be applied, which takes the form [131, 133]

$$\hat{\psi}_{\uparrow}(\mathbf{r}) = \sum_{m} u_m(\mathbf{r})\hat{\gamma}_{m\uparrow} - v_m^*(\mathbf{r})\hat{\gamma}_{m\downarrow}^{\dagger}\,, \tag{2.15a}$$

$$\hat{\psi}_{\downarrow}(\mathbf{r}) = \sum_{m} u_m(\mathbf{r})\hat{\gamma}_{m\downarrow} + v_m^*(\mathbf{r})\hat{\gamma}_{m\uparrow}^{\dagger}\,. \tag{2.15b}$$

A two-component set of functions has been introduced, consisting of the pair of terms $u_m(\mathbf{r})$ and $v_m(\mathbf{r})$. The index m sums over all states, which are uniquely identified by the translational quantum numbers of the system. Rather than the single-particle states generated by the Fermi operators, the introduced operators $\hat{\gamma}_{m\alpha}$ and $\hat{\gamma}_{m\alpha}^{\dagger}$ produce quasiparticle states. The quasiparticles are collective excitations arising from the binding of two particles through the potential $\hat{V}^{(2)}$.

Equations for the introduced functions $u_m(\mathbf{r})$ and $v_m(\mathbf{r})$ are obtained under the condition that the transformation diagonalises the Hamiltonian, i.e.

$$\hat{H}_e = E_{0S} + \sum_{m\alpha} \epsilon_m \hat{\gamma}_{m\alpha}^{\dagger}\hat{\gamma}_{m\alpha}\,, \tag{2.16}$$

where E_{0S} is the superconducting ground state energy and ϵ_m is the energy associated with a quasiparticle state created by the operator $\gamma_m^{\dagger}$. Diagonalisation of the Hamiltonian implies that the Bogoliubov transformation recasts the interacting system of particles into a state of non-interacting quasiparticles. In Section 2.2.2, the free energy of the effective Hamiltonian is minimised in order to ensure that this quasiparticle state replicates the ground state of the interacting system.

The Fermi operators obey the anti-commutation relations given by equation (A.11) in App. A.2 [26]. Applying expansion (2.15) to those relations, a similar set of rules for the quasiparticle operators are obtained,

$$\hat{\gamma}_{m\alpha}\hat{\gamma}_{m'\beta} + \hat{\gamma}_{m'\beta}\hat{\gamma}_{m\alpha} = 0, \tag{2.17a}$$

$$\hat{\gamma}_{m\alpha}\hat{\gamma}^{\dagger}_{m'\beta} + \hat{\gamma}^{\dagger}_{m'\beta}\hat{\gamma}_{m\alpha} = \delta_{mm'}\delta_{\alpha\beta}. \tag{2.17b}$$

An equation which generates the quasiparticle energies ϵ_m in terms of the mean-field operators can now be obtained. This is achieved by evaluating the commutator of $\hat{H}_e$ with a Fermi operator via two different approaches. Firstly, starting from (2.14), the relations (A.11) can be applied to find

$$[\hat{H}_e, \hat{\psi}_{\uparrow}(\mathbf{r})] = -\hat{H}_0(\mathbf{r})\hat{\psi}_{\uparrow}(\mathbf{r}) - \Delta(\mathbf{r})\hat{\psi}^{\dagger}_{\downarrow}(\mathbf{r}). \tag{2.18}$$

This can then be expanded in terms of the quasiparticle operators via (2.15), giving the first result

$$[\hat{H}_e, \hat{\psi}_{\uparrow}(\mathbf{r})] = -\sum_m \left[\hat{H}_0(\mathbf{r})u_m(\mathbf{r}) + \Delta(\mathbf{r})v_m(\mathbf{r})\right]\hat{\gamma}_{m\uparrow} - \left[\hat{H}_0(\mathbf{r})v^*_m(\mathbf{r}) - \Delta(\mathbf{r})u^*_m(\mathbf{r})\right]\hat{\gamma}^{\dagger}_{m\downarrow}. \tag{2.19}$$

The second approach requires the commutator of the Hamiltonian with the quasiparticle operators to first be evaluated. Using equations (2.16) and (2.17), these relations are

$$[\hat{H}_e, \hat{\gamma}_{m\alpha}] = -\epsilon_m\hat{\gamma}_{m\alpha}, \tag{2.20a}$$

$$[\hat{H}_e, \hat{\gamma}^{\dagger}_{m\alpha}] = \epsilon_m\hat{\gamma}^{\dagger}_{m\alpha}. \tag{2.20b}$$

The required expression can be obtained directly from (2.16) by applying the relations (2.20), resulting in

$$[\hat{H}_e, \hat{\psi}_{\uparrow}(\mathbf{r})] = -\sum_m \epsilon_m\left[u_m(\mathbf{r})\hat{\gamma}_{m\uparrow} + v^*_m(\mathbf{r})\hat{\gamma}^{\dagger}_{m\downarrow}\right]. \tag{2.21}$$

Equating the coefficients of the quasiparticle operators in equations (2.19) and (2.21) generates a pair of coupled equations,

$$\epsilon_m u_m(\mathbf{r}) = \hat{H}_0(\mathbf{r})u_m(\mathbf{r}) + \Delta(\mathbf{r})v_m(\mathbf{r}), \tag{2.22a}$$

$$\epsilon_m v_m(\mathbf{r}) = -\hat{H}^*_0(\mathbf{r})v_m(\mathbf{r}) + \Delta^*(\mathbf{r})u_m(\mathbf{r}). \tag{2.22b}$$

Finally, equations (2.22) can be written in a more compact matrix form. The result is the Bogoliubov-de Gennes equation,

$$\begin{pmatrix} \hat{H}_0(\mathbf{r}) & \Delta(\mathbf{r}) \\ \Delta^\dagger(\mathbf{r}) & -\hat{H}_0^*(\mathbf{r}) \end{pmatrix} \begin{pmatrix} u_m(\mathbf{r}) \\ v_m(\mathbf{r}) \end{pmatrix} = \epsilon_m \begin{pmatrix} u_m(\mathbf{r}) \\ v_m(\mathbf{r}) \end{pmatrix}, \quad \underline{H}\boldsymbol{\psi}_m(\mathbf{r}) = \epsilon_m \boldsymbol{\psi}_m(\mathbf{r}). \tag{2.23}$$

Equation (2.23) is the final result for this subsection. The mean-field pairing potential $\Delta(\mathbf{r})$ becomes non-zero upon transition into the superconducting state. When $\Delta(\mathbf{r}) = 0$, equation (2.23) reduces to two decoupled equations for the bandstructure of a state with no pairing interaction. In this case, the function $u_m(\mathbf{r})$ becomes equivalent to a single-electron eigenfunction, while $v_m(\mathbf{r})$ becomes the equivalent eigenfunction for hole states (as $-\hat{H}_0^*$ is the time-reversed electron Hamiltonian). The appearance of a finite $\Delta(\mathbf{r})$ thus enforces mixing between the electron and hole states, leading to a gap in the energy spectrum at the Fermi energy.

The pairing potential is often referred to as the "gap function", and the method of structuring this term to reflect a particular state is discussed in more detail in Section 3.2. Assuming that Δ is very small, $\psi_m(\mathbf{r})$ are almost pure electron or hole wavefunctions (i.e. $|u_m| >> |v_m|$ or vice versa). The quasiparticle energies are approximately given by $\epsilon_m = \sqrt{E_{0m}^2 + |\Delta|^2}$, where E_{0m} is the energy eigenvalue for the one-electron Hamiltonian. The minimum excitation energy for the ground state of an electron is thus $\sim |\Delta|^2$. This reflects the binding energy of the Cooper pair, with $\Delta(\mathbf{r})$ corresponding to the energy required to break up a pair.

2.2.2 Self-Consistency Conditions

The Bogoliubov-de Gennes equation acts as an effective Schrödinger equation for a general superconducting state. It is obtained by introducing a mean-field approximation for the two-particle pairing interaction responsible for Cooper pairing. In this section, a method for calculating $\Delta(\mathbf{r})$ in a self-consistent manner is derived for a conventional singlet pairing state, again drawing from the textbook [26]. Bogoliubov's approach requires prior knowledge of the symmetry of the superconducting gap in $\mathbf{k}$-space and the resulting pair wavefunction [53, 130–132]. However, the exact nature of the mechanism responsible for the pairing interaction is not needed. This distinction will be of vital importance when moving on to more general unconventional superconducting symmetries in Section 2.2.3 as the pairing interaction is typically not known in such states.

The self-consistency conditions for the pairing potential are obtained by minimising the free energy of both the effective and full Hamiltonians with respect to the chosen expansion of the Fermi operators given in (2.15). Combining this minimisation with the condition given by equation (2.16), a set of optimised expressions for the functions $u_m(\mathbf{r})$ and $v_m(\mathbf{r})$ can be obtained. Calculation of the free energy can be simplified by excluding external interactions and by placing constraints on the lattice potential and pairing interaction.

A spin-independent form for the one-electron potential is taken, i.e.

$$U^{(1)}_{\alpha\beta} = U^{(1)}\delta_{\alpha\beta}\,. \tag{2.24}$$

$U^{(1)}$ represents the periodic potential associated with the lattice. A lattice potential which is diagonal in spin corresponds to the assumption that the lattice can not scatter an electron between its two possible spin states. This is a reasonable assumption if there are no magnetic impurities in the lattice and spin-orbit coupling is negligible.

For the conventional case of s-wave pairing, the inter-particle potential is also diagonal in the spin indices,

$$U^{(2)}_{\delta\gamma,\alpha\beta} = U^{(2)}\delta_{\alpha\gamma}\delta_{\delta\beta}\,. \tag{2.25}$$

A contact form for the inter-particle potential can also be assumed in abidance with BCS theory, which is enforced via

$$U^{(2)}(\mathbf{r},\mathbf{r}') = -V\delta(\mathbf{r}-\mathbf{r}')\,. \tag{2.26}$$

The phonon-mediated mechanism in this case can be described by an on-site interaction due to the retarded exchange of virtual phonons via the lattice, as discussed in Section 1.2.2. Under these constraints, the two-particle operator in (2.13) takes the form

$$\hat{V}^{(2)} = -\frac{V}{2}\int \mathrm{d}\mathbf{r}\;\hat{\psi}^{\dagger}_{\beta}(\mathbf{r})\hat{\psi}^{\dagger}_{\alpha}(\mathbf{r})\hat{\psi}_{\alpha}(\mathbf{r})\hat{\psi}_{\beta}(\mathbf{r})\,. \tag{2.27}$$

The free energy of the two Hamiltonians is now evaluated via the equation [36]

$$F = \langle\hat{H}\rangle - TS\,. \tag{2.28}$$

Note that the energy in a many-body state is typically measured with respect to the Fermi energy μ. To incorporate this, the one-electron Hamiltonian would be replaced with $\hat{H}^{(1)} - \mu\hat{N}$, where $\hat{N} = \int \mathrm{d}\mathbf{r}\,\hat{\psi}^{\dagger}_{\alpha}(\mathbf{r})\hat{\psi}_{\alpha}(\mathbf{r})$. For an explicit calculation of the free energy, consideration of the Fermi energy is essential. However, the purpose of this derivation is only to equate the minimised free energies of two Hamiltonians with the same Fermi energy and so μ can be neglected. Furthermore, the energy values in the tight-binding calculations presented throughout this thesis are computed relative to μ.

The full Hamiltonian (2.13) contains four Fermi operators due to the quartic nature of the inter-particle potential $\hat{V}^{(2)}$. Expectation values of such quartic terms can be replaced with the

product of expectation values of pairs of the individual operators via Wick's theorem [134]. The Gor'kov factorisation can then be applied to the expanded operators to calculate the free energy in the mean-field approximation [135, 136]. The result is that the quartic expectation value becomes

$$\begin{aligned}\langle\hat{\psi}^\dagger_\alpha(\mathbf{r}_1)\hat{\psi}^\dagger_\beta(\mathbf{r}_2)\hat{\psi}_\gamma(\mathbf{r}_3)\hat{\psi}_\delta(\mathbf{r}_4)\rangle &= \langle\hat{\psi}^\dagger_\alpha(\mathbf{r}_1)\hat{\psi}^\dagger_\beta(\mathbf{r}_2)\rangle\langle\hat{\psi}_\gamma(\mathbf{r}_3)\hat{\psi}_\delta(\mathbf{r}_4)\rangle - \langle\hat{\psi}^\dagger_\alpha(\mathbf{r}_1)\hat{\psi}_\gamma(\mathbf{r}_3)\rangle\langle\hat{\psi}^\dagger_\beta(\mathbf{r}_2)\hat{\psi}_\delta(\mathbf{r}_4)\rangle \\ &\quad + \langle\hat{\psi}^\dagger_\alpha(\mathbf{r}_1)\hat{\psi}_\delta(\mathbf{r}_4)\rangle\langle\hat{\psi}^\dagger_\beta(\mathbf{r}_2)\hat{\psi}_\gamma(\mathbf{r}_3)\rangle\,. \end{aligned} \tag{2.29}$$

The Gor'kov factorisation is applied to calculate the expectation value of the full Hamiltonian (which is quartic) with respect to states of the mean-field Hamiltonian (which is quadratic). Applying this factorisation, the free energy can be computed by inserting (2.13) into (2.28). Taking into account the explicit form (2.27), the variation in the free energy is given by

$$\begin{aligned}\delta F = -T\delta S + \int \mathrm{d}\mathbf{r}\, &\delta\langle\hat{\psi}^\dagger_\alpha(\mathbf{r})\hat{H}_0(\mathbf{r})\hat{\psi}_\alpha(\mathbf{r})\rangle \\ &- V\Big[\langle\hat{\psi}^\dagger_\beta(\mathbf{r})\hat{\psi}^\dagger_\alpha(\mathbf{r})\rangle\delta\langle\hat{\psi}_\alpha(\mathbf{r})\hat{\psi}_\beta(\mathbf{r})\rangle + \langle\hat{\psi}_\alpha(\mathbf{r})\hat{\psi}_\beta(\mathbf{r})\rangle\delta\langle\hat{\psi}^\dagger_\beta(\mathbf{r})\hat{\psi}^\dagger_\alpha(\mathbf{r})\rangle\Big] = 0\,. \end{aligned} \tag{2.30}$$

The free energy is minimised when $\delta F = 0$, i.e. when the free energy is stationary.

Moving on to the effective Hamiltonian, the free energy is found by evaluating the expectation value $\langle\hat{H}_e\rangle$. Assuming that condition (2.16) is fulfilled, $\hat{H}_e$ is diagonalised by the Bogoliubov expansion (2.15) and the expectation value can be written in terms of the eigenvalues and eigenfunctions of the chosen expansion. Again, the optimised expansion corresponds to the set of eigenfunctions which minimise the free energy and so F_e must be stationary, i.e.

$$\delta F_e = -T\delta S + \int \mathrm{d}\mathbf{r}\,\delta\langle\hat{\psi}^\dagger_\alpha(\mathbf{r})\hat{H}_0(\mathbf{r})\hat{\psi}_\alpha(\mathbf{r})\rangle + \big[\Delta(\mathbf{r})\delta\langle\hat{\psi}^\dagger_\uparrow(\mathbf{r})\hat{\psi}^\dagger_\downarrow(\mathbf{r})\rangle + \Delta^*(\mathbf{r})\delta\langle\hat{\psi}_\downarrow(\mathbf{r})\hat{\psi}_\uparrow(\mathbf{r})\rangle\big] = 0\,. \tag{2.31}$$

Equating the coefficients of (2.30) and (2.31) demonstrates that the mean-field pairing potential is given by

$$\Delta(\mathbf{r}) = -V\langle\hat{\psi}_\downarrow(\mathbf{r})\hat{\psi}_\uparrow(\mathbf{r})\rangle = V\langle\hat{\psi}_\uparrow(\mathbf{r})\hat{\psi}_\downarrow(\mathbf{r})\rangle\,. \tag{2.32}$$

The potential is thus antisymmetric under particle exchange, which is consistent with Pauli's exclusion principle [36]. An equation for the gap function in terms of $u_m(\mathbf{r})$ and $v_m(\mathbf{r})$ can be obtained by performing the Bogoliubov expansion (2.15) on (2.32) and applying the quasiparticle operator identities [26]

$$\langle\hat{\gamma}^\dagger_{m\alpha}\hat{\gamma}_{m'\beta}\rangle = \delta_{\alpha\beta}\delta_{mm'}f_m\,, \tag{2.33a}$$

$$\langle\hat{\gamma}_{m'\beta}\hat{\gamma}^\dagger_{m\alpha}\rangle = \delta_{\alpha\beta}\delta_{mm'}(1-f_m)\,, \tag{2.33b}$$

$$\langle\hat{\gamma}_{m\alpha}\hat{\gamma}_{m'\beta}\rangle = 0\,, \tag{2.33c}$$

where f_m is the Fermi factor,

$$f_m = \frac{1}{\mathrm{e}^{\epsilon_m/(k_B T)} + 1}. \tag{2.34}$$

Note that the energy is has again been defined relative to μ in stating definition (2.34). The resulting expression for the mean-field potential is

$$\Delta(\mathbf{r}) = V \sum_m u_m(\mathbf{r}) v_m^*(\mathbf{r})(1 - 2f_m). \tag{2.35}$$

Equation (2.35) and the previously defined BdG equation (2.23) are coupled via the functions $u_m(\mathbf{r})$ and $v_m(\mathbf{r})$. Position-dependent values for the mean-field potentials of a conventional superconducting state can be calculated through this set of equations in a self-consistent process, provided that an appropriate single-particle Hamiltonian $\hat{H}_0$ for the normal state excluding the presence of pairs has first been obtained. In Section 2.2.3 below, this approach is generalised to be able to account for exotic pairing interactions.

2.2.3 Spin-Dependent Pairing Generalisation

To proceed from the conventional formalism developed in Sections 2.2.1 and 2.2.2, a spin-dependent pairing interaction is required. The lattice potential can be made spin-dependent to account for magnetic lattice defects and spin-orbit coupling but remains spin-diagonal here. An additional spin-orbit term is added to the normal state tight-binding Hamiltonian in Chapter 3, but that does not influence the derivation of the pairing potential presented here.

The inclusion of spin-dependent pairing is necessary in order to generate spin-triplet Cooper pairs. To incorporate this, a more general form for the effective Hamiltonian [26],

$$\begin{aligned} \hat{H}_e = \int \mathrm{d}\mathbf{r} \Big\{ & \hat{\psi}_\alpha^\dagger(\mathbf{r}) \hat{H}_0(\mathbf{r}) \hat{\psi}_\alpha(\mathbf{r}) \\ & + \int \mathrm{d}\mathbf{r}' \left[\Delta_{\alpha\beta}(\mathbf{r}, \mathbf{r}') \hat{\psi}_\alpha^\dagger(\mathbf{r}) \hat{\psi}_\beta^\dagger(\mathbf{r}') + \Delta_{\alpha\beta}^*(\mathbf{r}, \mathbf{r}') \hat{\psi}_\beta(\mathbf{r}') \hat{\psi}_\alpha(\mathbf{r}) \right] \Big\}, \end{aligned} \tag{2.36}$$

is required. This Hamiltonian is now able to account for anomalous averages of the form $\langle \hat{\psi}_\uparrow^\dagger \hat{\psi}_\uparrow^\dagger \rangle$ and $\langle \hat{\psi}_\downarrow^\dagger \hat{\psi}_\downarrow^\dagger \rangle$.

The derivation from this point follows very closely to the spin-independent potential case. The Gor'kov factorisation is again applied to the generalised two-body operator to obtain the variation in the free energy of the full Hamiltonian,

$$\begin{aligned}\delta F = -T\delta S + \int \mathrm{d}\mathbf{r} \Big\{ & \delta\langle\hat{\psi}^\dagger_\alpha(\mathbf{r})\hat{H}_0(\mathbf{r})\hat{\psi}_\alpha(\mathbf{r})\rangle \\ & + \frac{1}{2}\int \mathrm{d}\mathbf{r}' \Big[U^{(2)}_{\delta\gamma,\alpha\beta}(\mathbf{r},\mathbf{r}')\Big(- \langle\hat{\psi}^\dagger_\delta(\mathbf{r})\hat{\psi}_\alpha(\mathbf{r}')\rangle\delta\langle\hat{\psi}^\dagger_\gamma(\mathbf{r}')\hat{\psi}^\dagger_\beta(\mathbf{r})\rangle - \langle\hat{\psi}^\dagger_\gamma(\mathbf{r}')\hat{\psi}^\dagger_\beta(\mathbf{r})\rangle\delta\langle\hat{\psi}^\dagger_\delta(\mathbf{r})\hat{\psi}_\alpha(\mathbf{r}')\rangle \\ & \qquad + \langle\hat{\psi}^\dagger_\delta(\mathbf{r})\hat{\psi}_\beta(\mathbf{r})\rangle\delta\langle\hat{\psi}^\dagger_\gamma(\mathbf{r}')\hat{\psi}_\alpha(\mathbf{r}')\rangle + \langle\hat{\psi}^\dagger_\gamma(\mathbf{r}')\hat{\psi}_\alpha(\mathbf{r}')\rangle\delta\langle\hat{\psi}^\dagger_\delta(\mathbf{r})\hat{\psi}_\beta(\mathbf{r})\rangle \\ & \qquad + \langle\hat{\psi}^\dagger_\delta(\mathbf{r})\hat{\psi}^\dagger_\gamma(\mathbf{r}')\rangle\delta\langle\hat{\psi}_\alpha(\mathbf{r}')\hat{\psi}_\beta(\mathbf{r})\rangle + \langle\hat{\psi}_\alpha(\mathbf{r}')\hat{\psi}_\beta(\mathbf{r})\rangle\delta\langle\hat{\psi}^\dagger_\delta(\mathbf{r})\hat{\psi}^\dagger_\gamma(\mathbf{r}')\rangle\Big)\Big]\Big\}. \end{aligned} \tag{2.37}$$

The variation in the free energy of the effective Hamiltonian is now

$$\begin{aligned}\delta F_e = -T\delta S + \int \mathrm{d}\mathbf{r} \Big\{ & \delta\langle\hat{\psi}^\dagger_\alpha(\mathbf{r})\hat{H}_0(\mathbf{r})\hat{\psi}_\alpha(\mathbf{r})\rangle \\ & + \int \mathrm{d}\mathbf{r}' \Big[\Delta_{\alpha\beta}(\mathbf{r},\mathbf{r}')\delta\langle\hat{\psi}^\dagger_\alpha(\mathbf{r})\hat{\psi}^\dagger_\beta(\mathbf{r}')\rangle + \Delta^*_{\beta\alpha}(\mathbf{r},\mathbf{r}')\delta\langle\hat{\psi}_\alpha(\mathbf{r}')\hat{\psi}_\beta(\mathbf{r})\rangle\Big]\Big\}, \end{aligned} \tag{2.38}$$

where the dummy spin indices in the last term inside the square brackets have been relabelled.

Equating expressions (2.37) and (2.38) generates relationships between the gap function and the two-particle potential,

$$\Delta_{\alpha\beta}(\mathbf{r},\mathbf{r}') = \frac{1}{2}U^{(2)}_{\alpha\beta,\delta\gamma}(\mathbf{r},\mathbf{r}')\langle\hat{\psi}_\delta(\mathbf{r}')\hat{\psi}_\gamma(\mathbf{r})\rangle\,, \tag{2.39a}$$

$$\Delta^*_{\beta\alpha}(\mathbf{r},\mathbf{r}') = \frac{1}{2}U^{(2)}_{\delta\gamma,\alpha\beta}(\mathbf{r},\mathbf{r}')\langle\hat{\psi}^\dagger_\delta(\mathbf{r})\hat{\psi}^\dagger_\gamma(\mathbf{r}')\rangle\,. \tag{2.39b}$$

The two-particle potential is identical under particle exchange, i.e. $U^{(2)}_{\gamma\delta,\beta\alpha}(\mathbf{r}',\mathbf{r}) = U^{(2)}_{\delta\gamma,\alpha\beta}(\mathbf{r},\mathbf{r}')$. Applying this to the relations above, it can be shown that the gap function is antisymmetric under particle exchange as before,

$$\Delta_{\alpha\beta}(\mathbf{r},\mathbf{r}') = -\Delta_{\beta\alpha}(\mathbf{r}',\mathbf{r})\,. \tag{2.40}$$

Obtaining the Bogoliubov-de Gennes equation in this case again relies upon deriving the commutator of the effective Hamiltonian with a Fermi field operator. Applying (A.11) and the antisymmetric property of the gap function gives

$$[\hat{H}_e,\hat{\psi}_\alpha(\mathbf{r})] = -\hat{H}_0(\mathbf{r})\hat{\psi}_\alpha(\mathbf{r}) - \int \mathrm{d}\mathbf{r}'\,\Delta_{\alpha\beta}(\mathbf{r},\mathbf{r}')\hat{\psi}^\dagger_\beta(\mathbf{r}')\,. \tag{2.41}$$

The spin-generalised Bogoliubov-Valatin transformation is defined by

$$\hat{\psi}_\alpha(\mathbf{r}) = \sum_j u_{j\alpha}(\mathbf{r})\hat{\gamma}_j - v^*_{j\alpha}(\mathbf{r})\hat{\gamma}^\dagger_j\,, \tag{2.42}$$

where the sum index j now includes both the spin and translational quantum numbers of the system, in contrast to the spin-independent expansion (2.15). A careful distinction must be drawn between the spin quantum number and the index α, which can be referred to as a spin coordinate. The spin quantum number identifies discrete energy states, while the coordinate distinguishes between up and down projections of an electron wavefunction. By including these spin projections, it is possible to account for effects dependent on the spin of the electron and hole wavefunctions which correlate to form the quasiparticle excitations. For the spin-independent treatment in Sections 2.2.1 and 2.2.2, these effects are not included and only the spin quantum number is required.

Proceeding through the remainder of the steps outlined in equations (2.18)-(2.23), the spin-dependent generalised BdG equations are obtained,

$$\epsilon_j u_{j\alpha}(\mathbf{r}) = \hat{H}_0(\mathbf{r}) u_{j\alpha}(\mathbf{r}) + \int \mathrm{d}\mathbf{r}'\, \Delta_{\alpha\beta}(\mathbf{r},\mathbf{r}') v_{j\beta}(\mathbf{r}'), \tag{2.43a}$$

$$-\epsilon_j v_{j\alpha}(\mathbf{r}) = \hat{H}_0^*(\mathbf{r}) v_{j\alpha}(\mathbf{r}) + \int \mathrm{d}\mathbf{r}'\, \Delta^*_{\alpha\beta}(\mathbf{r},\mathbf{r}') u_{j\beta}(\mathbf{r}'). \tag{2.43b}$$

To find the generalised self-consistency conditions, the Bogoliubov transformation is enforced on the Fermi operators in equation (2.39), and the rules (2.33) are then applied giving

$$\Delta_{\alpha\beta}(\mathbf{r},\mathbf{r}') = \frac{1}{2} U^{(2)}_{\alpha\beta,\delta\gamma}(\mathbf{r},\mathbf{r}') \sum_j v^*_{j\delta}(\mathbf{r}') u_{j\gamma}(\mathbf{r}) f_j + v^*_{j\gamma}(\mathbf{r}) u_{j\delta}(\mathbf{r}')(1-f_j). \tag{2.44}$$

Applying the antisymmetric property of the gap function (2.40) and exchanging indices, this becomes

$$\Delta_{\alpha\beta}(\mathbf{r},\mathbf{r}') = -\frac{1}{2} U^{(2)}_{\alpha\beta,\delta\gamma}(\mathbf{r},\mathbf{r}') \sum_j v^*_{j\gamma}(\mathbf{r}) u_{j\delta}(\mathbf{r}') f_j + v^*_{j\delta}(\mathbf{r}') u_{j\gamma}(\mathbf{r})(1-f_j). \tag{2.45}$$

Finally, taking the sum of equations (2.44) and (2.45), an expression for the pairing potential in terms of the set of particle-hole functions which minimise the free energy is obtained,

$$\Delta_{\alpha\beta}(\mathbf{r},\mathbf{r}') = \frac{1}{4} U^{(2)}_{\alpha\beta,\delta\gamma}(\mathbf{r},\mathbf{r}') \sum_j (v^*_{j\gamma}(\mathbf{r}) u_{j\delta}(\mathbf{r}') - v^*_{j\delta}(\mathbf{r}') u_{j\gamma}(\mathbf{r}))(1-2f_j). \tag{2.46}$$

The pair of equations (2.43) and (2.46) represent the equivalent set of self-consistency conditions for the fully generalised superconducting state. The exact form of the two-particle potential $U^{(2)}$ depends on the symmetry of the particular superconducting gap which is to be modelled. In Section 3.2, the form this potential takes for the chiral superconducting symmetries studied in Sr_2RuO_4 is discussed in more detail.

CHAPTER 3

MODELS OF Sr_2RuO_4

The purpose of this chapter is to introduce the reader to the proposed chiral superconductor Sr_2RuO_4. Superconductivity in this material displays a number of anomalous phenomena, but the classification of its order parameter remains a source of controversy. Outlined here is the process of applying the theoretical methods discussed in Chapter 2 to generate a functioning model of the material, capable of recreating its key electronic and superconducting properties. Two distinct approaches were utilised for the purpose of calculations: a fully three-dimensional model, including inter-plane hybridisation, and a two-dimensional structure with an extended pairing regime.

3.1 Normal State

The primary focus of this thesis is the study of anomalous phenomena in the putative chiral superconductor Sr_2RuO_4. In order to study the properties of the superconducting state, a firm grasp on the normal state structure of the material is required. In this section, an overview of the lattice and electronic properties of Sr_2RuO_4 is given, leading on to the derivation of a normal state tight-binding Hamiltonian.

3.1.1 Lattice and Electronic Properties

The conduction of a current in the Sr_2RuO_4 normal metallic state occurs via electron charge carriers in the $4d$-shell of the ruthenium atom [137]. Ruthenium atoms within the material lie on a body-centred tetragonal (BCT) lattice with parameters $a = 0.3862$ nm and $c = 1.2722$ nm (see Fig. 3.1) [93–95, 138, 139]. The compound forms in a layered-perovskite structure with $I4/mmm$ space-group symmetry, similar to that of many cuprate superconductors. No indications of a

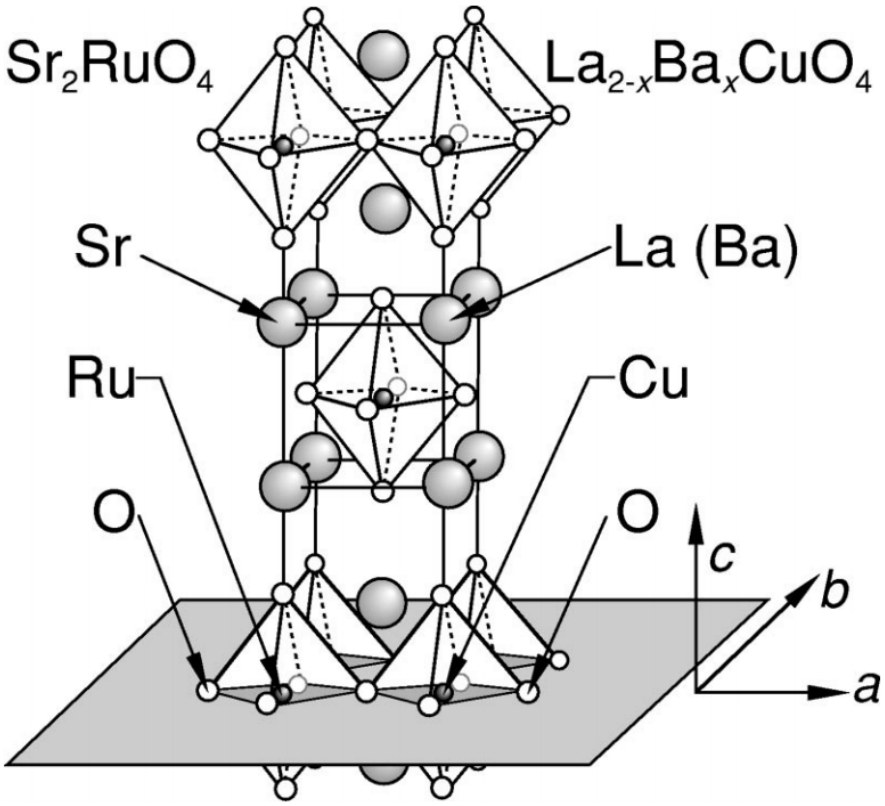

FIGURE 3.1. The body-centred tetragonal lattice of Sr_2RuO_4 alongside that of $La_{2-x}Ba_xCuO_4$. Superconductivity was discovered in Sr_2RuO_4 due to the similarity in its composition to that of the cuprate superconductors. Figure reproduced from ref. [106].

structural transition or lattice distortion have been found at low temperatures in this material [93, 94, 140–143].

The metallic state is a well-described two-dimensional Fermi liquid confined primarily to the Ru planes [138, 144, 145]. Electrons in a Fermi liquid behave very similarly to free electrons in a gas of non-interacting particles. In the liquid case, the interacting state is approximated by a system of non-interacting particles where the Coulombic potential experienced by an electron is accounted for by introducing an effective mass. The state in Sr_2RuO_4 is thus well described in the mean-field approximation, meaning the material is ideally suited for study through the tight-binding method and Bogoliubov's approach to the superconducting interaction. In addition, the structural stability of the lattice benefits the tight-binding approach. The absence of a transition admits the use of temperature-independent lattice constants and Slater-Koster parameters, which simplifies the process of calculating the temperature evolution of the superconducting gap.

Quantum oscillation measurements have established that the metallic Fermi surface consists of three approximately cylindrical sheets (see Fig. 3.2) [146]. Electronic structure calculations

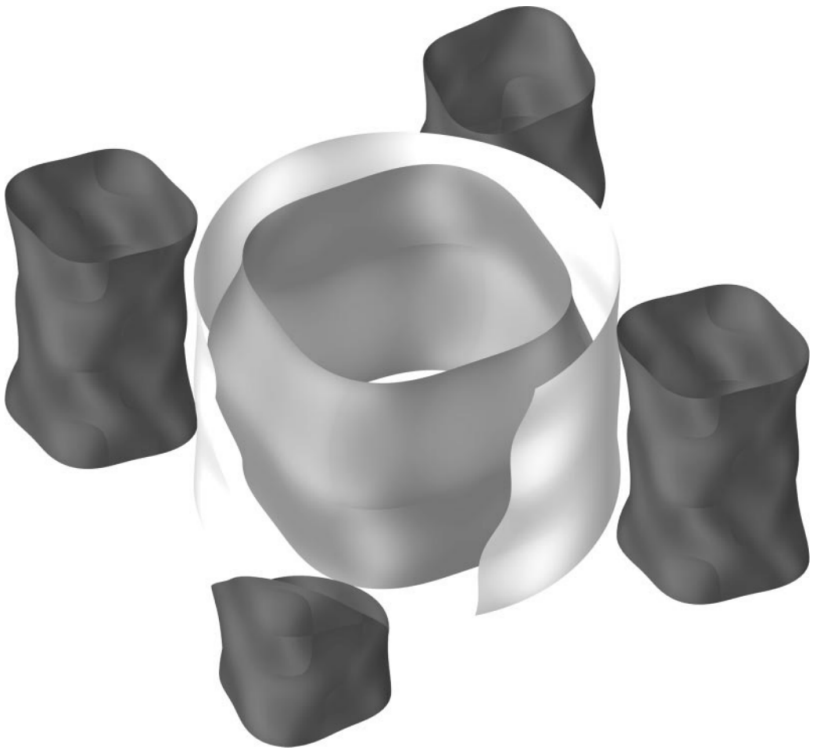

FIGURE 3.2. The three Fermi surface sheets of Sr_2RuO_4, as seen in quantum oscillation measurements. All three sheets are roughly cylindrical in the k_z-direction. The central sheets correspond to the electron-like β (innermost sheet) and γ (outermost) bands, while the 4 pockets in the corner of the Brillouin zone arise from the hole-like α band. Corrugation along the k_z-axis has been magnified by a factor of 15 for visibility. Figure is by C. Bergemann [154].

have also been utilised to show that the three sheets arise mainly from the Ru 4d d_{xy}, d_{xz} and d_{yz} orbitals (depicted in Fig. 3.3) [137, 147, 148]. The sheets are roughly cylindrical in the k_z-direction, with slight corrugations arising from weak inter-plane coupling [148–153], and will be referred to by α, β and γ respectively, which is the commonly used nomenclature in studies of this material (first introduced in ref. [154]). Bands derived from the d_{xz} and d_{yz} orbitals are dispersed almost exclusively in the x and y-directions of the Ru planes respectively, and are thus referred to as the "quasi-1D" bands. The d_{xy} band, in contrast, is isotropic in the plane and forms a 2D band. Hybridisation between the 1D bands drives the formation of the α and β sheets, while the γ sheet arises primarily from the 2D band.

3.1.2 Tight-Binding Hamiltonian: 3D

The three-orbital basis, in addition to spin, forms a 6×6 tight-binding Hamiltonian matrix. Despite the fact that the metallic state of Sr_2RuO_4 is very strongly two-dimensional [138, 144, 145], with

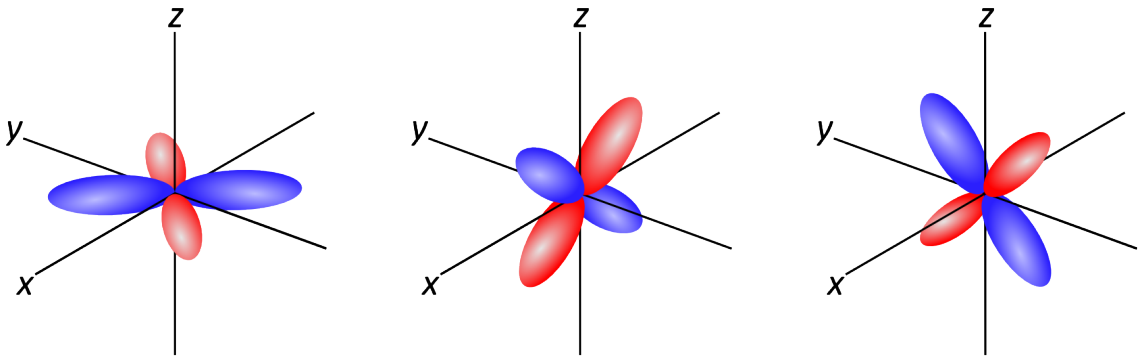

FIGURE 3.3. Pictorial representation of the spatial distributions of the three orbital wavefunctions d_{xy}, d_{xz} and d_{yz} (from left to right). This is the basis of the tight-binding Hamiltonian for Sr_2RuO_4. The blue and red lobes refer to positive and negative phases of the wavefunction respectively. It should be noted that the orbitals displayed here most closely resemble those in the $3d$ electron shell. The $4d$ orbitals which contribute to the Fermi surface in Sr_2RuO_4 abide the same symmetry considerations, rather with more complex geometries.

only weak out-of-plane hybridisation, a fully three-dimensional approach to modelling the normal state is taken here. The motivation for this lies in the observation that the superconducting gap likely displays line nodes [155–158]. Taking a p-wave order parameter and enforcing out-of-plane pairing naturally generates the required nodal gap structure (see Section 3.2 for a more detailed discussion of the gap structure) [159]. This three-dimensional superconducting state requires a three-dimensional normal state model as a foundation.

Before adapting the matrix to the specific considerations of the orbital basis, the toy tight-binding Hamiltonian derived in Section 2.1.2 must be generalised to the case of a BCT lattice. Transfer integrals for next-nearest neighbour in-plane and nearest neighbour out-of-plane hopping are included in addition to nearest neighbour hopping. This particular form of the Hamiltonian is well-established in the literature, having been refined and utilised to perform calculations for a number of properties of Sr_2RuO_4 [129, 160–166].

Nearest neighbour integrals are described by the parameter t as usual. For the in-plane next-nearest neighbours, lattice sites are separated by a vector $(\pm a, \pm a, 0)$, leading to hopping integrals of the form

$$\begin{aligned} &e^{i(k_x a+k_y a)}\int d\mathbf{r}\,\phi^*(\mathbf{r})\hat{H}(\mathbf{r})\phi(x-a,y-a,z)+e^{-i(k_x a+k_y a)}\int d\mathbf{r}\,\phi^*(\mathbf{r})\hat{H}(\mathbf{r})\phi(x+a,y+a,z)\\ &+e^{i(k_x a-k_y a)}\int d\mathbf{r}\,\phi^*(\mathbf{r})\hat{H}(\mathbf{r})\phi(x-a,y+a,z)+e^{-i(k_x a-k_y a)}\int d\mathbf{r}\,\phi^*(\mathbf{r})\hat{H}(\mathbf{r})\phi(x+a,y-a,z). \end{aligned} \tag{3.1}$$

These additional transfer integrals are denoted by t'. Summing the four terms in equation (3.1), and adding to the nearest neighbour dispersion (2.12) derived in 2.1.2, the dispersion for the base

plane of a reciprocal-space tetragonal lattice is obtained,

$$\epsilon_{||}(\mathbf{k}) = \epsilon_0 + 2t\left[\cos(k_x a) + \cos(k_y a)\right] + 4t'\cos(k_x a)\cos(k_y a). \tag{3.2}$$

Nearest neighbour atoms in the out-of-plane direction for a BCT structure are separated by a vector of the form $(\pm a/2, \pm a/2, \pm c/2)$. Summing over the eight possible hopping directions given by these vectors, the dispersion along the c-axis is

$$\epsilon_{\perp}(\mathbf{k}) = 8t''\cos\left(k_x\frac{a}{2}\right)\cos\left(k_y\frac{a}{2}\right)\cos\left(k_z\frac{c}{2}\right), \tag{3.3}$$

where an out-of-plane hopping parameter t'' has been introduced.

The general form of the tight-binding dispersion for a BCT lattice must now be adapted to conform to the specific symmetry considerations of the adopted orbital basis. The d-orbital basis (which has orbital quantum number $l = 2$) contains wavefunctions which have C_4 rotational symmetry (see Fig. 3.3), in contrast to the isotropic s-orbital case. Henceforth, the d_{xy}, d_{xz} and d_{yz} orbitals will be referred to by a, b and c respectively.

To construct the Hamiltonian matrix in the 6×6 basis, consideration must be given to both intra-orbital and inter-orbital hopping integrals, in addition to intra-spin and inter-spin processes. In the absence of a magnetic exchange splitting and spin-orbit coupling, intra-spin hopping is the same for both spin projections, meaning the up and down spin blocks of the Hamiltonian are identical ($H^{\uparrow\uparrow}_{mm'} = H^{\downarrow\downarrow}_{mm'}$). Furthermore, for the case of no magnetic defects and again neglecting spin-orbit coupling, spin scattering via the lattice is not possible, and so $H^{\uparrow\downarrow}_{mm'} = H^{\downarrow\uparrow}_{mm'} = 0$. Finite contributions to these off-diagonal blocks of the normal state Hamiltonian are incorporated through the addition of a spin-orbit coupling Hamiltonian derived in Section 3.1.3.

The a-orbital has mirror symmetry about the $y = x$ direction, meaning that its dispersion in the base plane is identical in the x and y-directions. However, as this wavefunction is confined primarily to the xy-plane, there is very little dispersion for the a-orbital in the z-direction, and it is found that this contribution can be neglected entirely. As a result, the intra-orbital $a - a$ dispersion is given by

$$H_{aa}(\mathbf{k}) = \epsilon_a + 2t\left[\cos(k_x a) + \cos(k_y a)\right] + 4t'\cos(k_x a)\cos(k_y a), \tag{3.4}$$

where the spin indices have been suppressed temporarily.

The b and c-orbitals are rotations of the a-orbital, being confined to the xz and yz-planes respectively. They therefore hybridise strongly in the out-of-plane direction, but break rotational symmetry in the base plane, leading to negligible next-nearest hopping contributions. Distinct parameters for hopping in the x and y-directions respectively are required here. The remaining diagonal elements of the tight-binding Hamiltonian thus take the form

$$H_{bb}(\mathbf{k}) = \epsilon_b + 2\left[t_b^x \cos(k_x a) + t_b^y \cos(k_y a)\right] + 8t_b'' \cos\left(k_x \frac{a}{2}\right)\cos\left(k_y \frac{a}{2}\right)\cos\left(k_z \frac{c}{2}\right), \tag{3.5}$$

$$H_{cc}(\mathbf{k}) = \epsilon_c + 2\left[t_c^x \cos(k_x a) + t_c^y \cos(k_y a)\right] + 8t_c'' \cos\left(k_x \frac{a}{2}\right)\cos\left(k_y \frac{a}{2}\right)\cos\left(k_z \frac{c}{2}\right). \tag{3.6}$$

Off-diagonal elements within each spin block of the Hamiltonian relate to the various inter-orbital hopping terms. In the base plane, the b and c-orbitals are confined primarily to the x and y-directions respectively, meaning there is negligible nearest neighbour inter-orbital $b-c$ hopping. Significant hybridisation between the b and c-orbitals occurs through next-nearest neighbour and out-of-plane hopping however, and so matrix elements of the form H_{bc} are non-zero.

An important consideration must be made concerning the spatial asymmetry of the d-orbitals when determining the inter-orbital contribution to the dispersion. Adjacent lobes of a d-orbital wavefunction are out-of-phase with respect to one another (see Fig. 3.3). This results in anti-symmetric inter-orbital hopping. As a specific example, next-nearest in-plane hopping from b to c along the (a,a,0) vector incurs a phase difference with respect to hopping in the ($-a$,$-a$,0)-direction. The antisymmetric hopping is accounted for by replacing the even cosine terms in the Hamiltonian with odd sine terms.

Under the relevant symmetry considerations, the inter-orbital tight-binding elements for the b and c-orbitals are deduced to be

$$H_{bc}(\mathbf{k}) = 4t_{bc}' \sin(k_x a)\sin(k_y a) + 8t_{bc}'' \sin\left(k_x \frac{a}{2}\right)\sin\left(k_y \frac{a}{2}\right)\cos\left(k_z \frac{c}{2}\right). \tag{3.7}$$

The a-orbital only hybridises significantly with the other orbital characters via the z-direction. Again taking into account the phase considerations of the orbital wavefunctions, the final inter-orbital matrix elements are

$$H_{ab}(\mathbf{k}) = 8t_{ab}'' \cos\left(k_x \frac{a}{2}\right)\sin\left(k_y \frac{a}{2}\right)\sin\left(k_z \frac{c}{2}\right), \tag{3.8}$$

$$H_{ac}(\mathbf{k}) = 8t_{ac}'' \sin\left(k_x \frac{a}{2}\right)\cos\left(k_y \frac{a}{2}\right)\sin\left(k_z \frac{c}{2}\right). \tag{3.9}$$

The tight-binding Hamiltonian is real and Hermitian, meaning that $H_{mm\prime} = H_{m\prime m}$. The introduced tight-binding parameters are constrained by again considering the rotational symmetry of the orbital basis, giving [129, 164]

$$\epsilon_b = \epsilon_c, \quad t_b^x = t_c^y, \quad t_b^y = t_c^x, \quad t_b'' = t_c'', \quad t_{ab}'' = t_{ac}''. \tag{3.10}$$

With these constraints in place, the Schrödinger equation for the normal state can be written as

$$\underline{H}(\mathbf{k})\,\boldsymbol{\psi}_n(\mathbf{k}) = \epsilon_n(\mathbf{k})\,\boldsymbol{\psi}_n(\mathbf{k}), \tag{3.11a}$$

$$\underline{H}(\mathbf{k}) = \begin{pmatrix} H_{aa}^{\uparrow\uparrow}(\mathbf{k}) & H_{ab}^{\uparrow\uparrow}(\mathbf{k}) & H_{ac}^{\uparrow\uparrow}(\mathbf{k}) & 0 & 0 & 0 \\ H_{ab}^{\uparrow\uparrow}(\mathbf{k}) & H_{bb}^{\uparrow\uparrow}(\mathbf{k}) & H_{bc}^{\uparrow\uparrow}(\mathbf{k}) & 0 & 0 & 0 \\ H_{ac}^{\uparrow\uparrow}(\mathbf{k}) & H_{bc}^{\uparrow\uparrow}(\mathbf{k}) & H_{cc}^{\uparrow\uparrow}(\mathbf{k}) & 0 & 0 & 0 \\ 0 & 0 & 0 & H_{aa}^{\downarrow\downarrow}(\mathbf{k}) & H_{ab}^{\downarrow\downarrow}(\mathbf{k}) & H_{ac}^{\downarrow\downarrow}(\mathbf{k}) \\ 0 & 0 & 0 & H_{ab}^{\downarrow\downarrow}(\mathbf{k}) & H_{bb}^{\downarrow\downarrow}(\mathbf{k}) & H_{bc}^{\downarrow\downarrow}(\mathbf{k}) \\ 0 & 0 & 0 & H_{ac}^{\downarrow\downarrow}(\mathbf{k}) & H_{bc}^{\downarrow\downarrow}(\mathbf{k}) & H_{cc}^{\downarrow\downarrow}(\mathbf{k}) \end{pmatrix}, \quad \boldsymbol{\psi}_n(\mathbf{k}) = \begin{pmatrix} u_{na}^{\uparrow}(\mathbf{k}) \\ u_{nb}^{\uparrow}(\mathbf{k}) \\ u_{nc}^{\uparrow}(\mathbf{k}) \\ u_{na}^{\downarrow}(\mathbf{k}) \\ u_{nb}^{\downarrow}(\mathbf{k}) \\ u_{nc}^{\downarrow}(\mathbf{k}) \end{pmatrix}. \tag{3.11b}$$

This represents the structure of the tight-binding Hamiltonian for a BCT lattice in a multi-orbital basis. In order to adapt this model to the normal state of Sr_2RuO_4, the subsequent step is to fine-tune the introduced parameters to recreate the experimentally observed bandwidths [167, 168], Fermi surface [146] and cyclotron masses [169]. Table. 3.1 presents the obtained parameters to achieve these constraints and plots of the resultant bandstructure (Fig. 3.4) and Fermi surface (Fig. 3.5) are also displayed. See App. B.1 for an overview of the formulae used to calculate the electronic structure properties of the tight-binding Hamiltonian.

ϵ_a	ϵ_b	t	t'	t_b^x	t_c^x	t_b''	t_{ab}''	t_{bc}'	t_{bc}''
-131.82	-116.15	-81.62	-36.73	-109.37	-6.56	0.26	-1.05	-8.75	-1.05

TABLE 3.1. Table of tight-binding parameters tuned to the bandstructure properties of Sr_2RuO_4 above 1.5 K, given in units of meV [129, 164, 166] (note there an error in the value given for ϵ_b in ref. [129], but the corrected value is reported in [164]).

3.1.3 Spin-Orbit Interaction

The spin-orbit interaction is a relativistic coupling of the magnetic moments associated with the orbital and spin components of an electron's angular momentum. To gain an intuitive understanding of the origin of this effect, consider the rest frame of an electron orbiting a charged nucleus. In this frame, the nucleus tracks out an orbiting path, thus generating a magnetic field. The spin magnetic moment of the electron couples to the magnetic field, meaning that the electron experiences an energy shift which will be dependent on the direction of its spin angular momentum. This effect leads to the splitting of energy lines between up and down electron spins in atomic spectra.

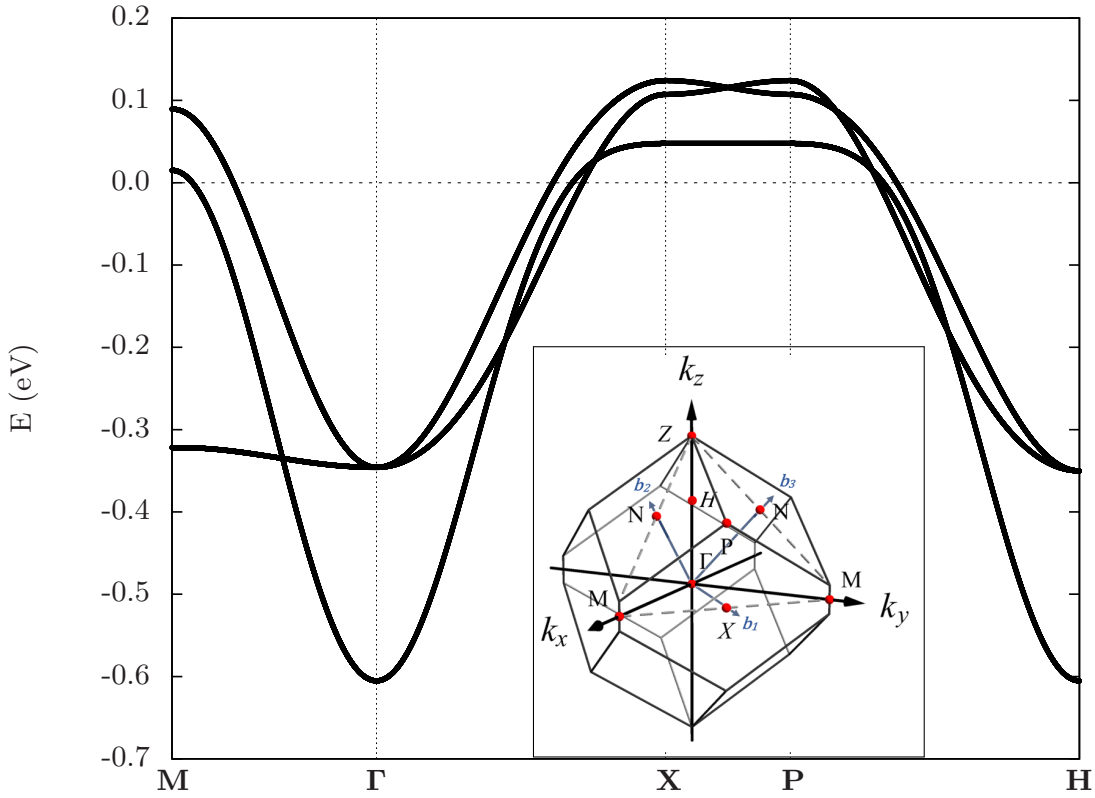

FIGURE 3.4. The diagram shows the three spin-degenerate bands of Sr_2RuO_4 in the normal state in the absence of SOC. Dispersions are calculated through diagonalisation of the tight-binding Hamiltonian (3.11) with the Slater-Koster parameters given in Table 3.1. The inset is recreated from ref. [170], and shows the Brillouin zone for the BCT lattice with symmetry points and reciprocal primitive vectors labelled. In **k**-space, the path taken to generate the plot is $(\pi/a,0,0)$-$(0,0,0)$-$(\pi/a,\pi/a,0)$-$(\pi/a,\pi/a,\pi/c)$-$(0,0,\pi/c)$.

Spin-orbit coupling plays a key role in driving anomalous transport properties arising from time-reversal symmetry breaking. For a normal state ferromagnet, TRS is broken in the spin channel. In the absence of spin-dependent lattice scattering or impurities, this symmetry breaking will not induce a transverse current. The presence of significant SOC, however, provides an intrinsic mechanism with which to generate a spontaneous Hall voltage [171, 172]. It can be imagined intuitively that the spin-orbit interaction transfers magnetisation from the spin degree of freedom to the orbital channel, generating a finite orbital magnetisation. Ordering in the orbital channel then results in a net transverse conductivity in response to an applied voltage. A more detailed discussion of the possible origins of the anomalous Hall effect, and the role that SOC plays in these, is given in Section 5.1.1. It can be inferred from this brief introduction, however, that SOC plays a significant role in the anomalous phenomena arising in a superconducting state which breaks chiral symmetry. Furthermore, for the quantitative consideration of edge currents

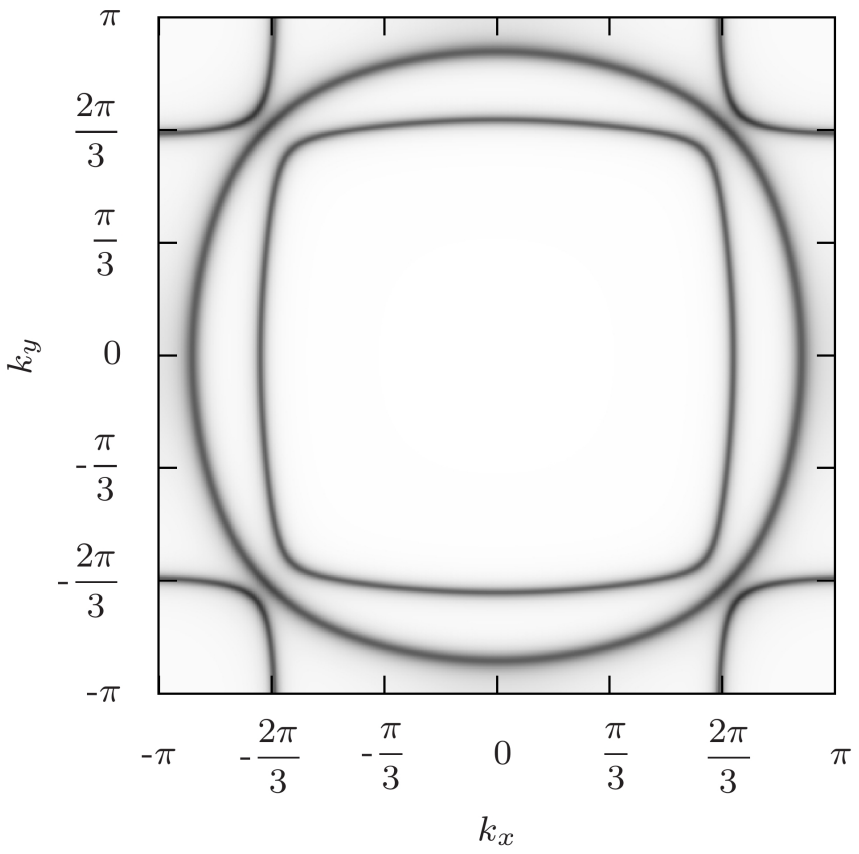

FIGURE 3.5. The diagram shows the three spin-degenerate Fermi surface sheets of Sr_2RuO_4 in the tight-binding formalism, excluding spin-orbit coupling. It is plotted from [-π,-π] to [π,π] in the $k_x k_y$-plane for $k_z = 0$. The circular sheet is the γ band, the inner electron-like sheet is the β band and the outer hole pockets represent the α band.

and the orbital moment, the incorporation of SOC appears to be vital [164, 173].

In this subsection the spin-orbit contribution to the Hamiltonian in the tight-binding approximation is derived for the required orbital basis. Spin-orbit coupling is here introduced in an on-site approximation, where any momentum-dependent contributions are neglected. The operator for the on-site contribution to SOC is [164, 174]

$$\hat{H}_{so} = \lambda' \hat{\mathbf{l}} \cdot \hat{\mathbf{s}} = \lambda' \left[\hat{l}_z \hat{s}_z + \frac{1}{2} \left(\hat{l}_+ \hat{s}_- + \hat{l}_- \hat{s}_+ \right) \right], \tag{3.12}$$

where λ' is a parameter determining the strength of the coupling. $\hat{s}_z$ and $\hat{l}_z$ are the z-components of the quantum mechanical operators for the spin and orbital angular momentum respectively, while $\hat{s}_\pm$ and $\hat{l}_\pm$ are the ladder operators (see App. A.3 for an introduction to the operators).

The magnitude of the effective magnetic field experienced by an orbiting electron is dictated primarily by two factors. Firstly, the mass of the atom is proportional to its charge, and is

accounted for by the spin-orbit coupling parameter λ'. An approximate value for this parameter is obtained through comparison with empirical and first-principles data. The second consideration is the orbital angular momentum of the electron, which is generated by the orbital angular momentum operator.

In expanding the eigenfunctions in the tight-binding basis, the SOC contribution to the Hamiltonian becomes a matrix in the orbital basis ($\underline{H}_{so}$). The matrix elements are determined by considering the angular momentum carried by each of the orbital wavefunctions in the basis. Such a wavefunction consists of a component which describes its orbital angular momentum and a spin component. The orbital part of the wavefunction comprises a radial distribution function ($f_l(r)$) and an angular distribution constructed from spherical harmonic functions ($Y_l^{m_l}(\theta,\phi)$).

Quantum mechanical operators $\hat{l}$ and $\hat{s}$ generate the orbital and spin angular momentum of a state respectively. The angular momentum operators act on states which have clearly defined projection quantum numbers m_l and m_s. Such a state can be written in Dirac notation in the form $|l,m_l\rangle$ (see A.2 for details). A compact notation for the orbital wavefunctions can be obtained by introducing Dirac states of the form

$$|m_l,m_s\rangle = |l,m_l\rangle|s,m_s\rangle\,, \tag{3.13}$$

where the orbital and spin quantum numbers can be suppressed in this instance as the used wavefunctions all have $l=2$ and $s=1/2$. The spherical harmonic functions which contribute to the orbitals in the basis are obtained by projecting the $|l,m_l\rangle$ states onto the angular component of the position basis $|\mathbf{r}\rangle$. Similarly, the spin component of the orbital wavefunctions results from the projection of $|s,m_s\rangle$ onto spin space $|\sigma\rangle$. The orbital basis can thus be written as

$$\phi^{\sigma}_{d\alpha}(\mathbf{r}) = f_l(r)\langle\mathbf{r},\sigma|d,\alpha\rangle\,, \tag{3.14}$$

where d sums over the three orbital projections which contribute to superconductivity in Sr_2RuO_4 ($d=a,b,c$). Adding the two spin projections ($\alpha=\uparrow,\downarrow$), this results in an orbital basis made up of 6 wavefunctions.

Within this notation, the Dirac states which generate the two spin projections of the d_{xy}, d_{xz} and d_{yz} orbitals are [175]

$$\begin{aligned}
|a\uparrow\rangle &= \frac{\mathrm{i}}{\sqrt{2}}\big(|-2,1/2\rangle - |2,1/2\rangle\big), \quad |a\downarrow\rangle = \frac{\mathrm{i}}{\sqrt{2}}\big(|-2,-1/2\rangle - |2,-1/2\rangle\big),\\
|b\uparrow\rangle &= \frac{1}{\sqrt{2}}\big(|-1,1/2\rangle - |1,1/2\rangle\big), \quad |b\downarrow\rangle = \frac{1}{\sqrt{2}}\big(|-1,-1/2\rangle - |1,-1/2\rangle\big),\\
|c\uparrow\rangle &= \frac{\mathrm{i}}{\sqrt{2}}\big(|-1,1/2\rangle + |1,1/2\rangle\big), \quad |c\downarrow\rangle = \frac{\mathrm{i}}{\sqrt{2}}\big(|-1,-1/2\rangle + |1,-1/2\rangle\big).
\end{aligned} \tag{3.15}$$

It should be highlighted that, for the orbital basis, wavefunctions are constructed by a superposition of different spherical harmonic states (see (3.15)). It is expedient to write the functions in this way so that they depend on states with definite values of m_l and m_s. This allows one to evaluate the matrix elements of the spin-orbit coupling operator via the standard set of angular momentum operator rules (see equations (A.12) and (A.15)). However, in order to obtain the spin-orbit contribution to the tight-binding Hamiltonian, the matrix elements must then be transformed from the definite-m basis to the orbital basis. This process is outlined below.

In the definite-m basis (where m refers to both m_l and m_s), there are 10 possible configurations of the angular momentum components, given by $m_l = 0$, ± 1 or ± 2, in addition to $m_s = \pm 1/2$. The spin-orbit Hamiltonian in this basis is calculated by applying operator (3.12) to the 10 possible combinations of (3.13), resulting in

$$\tilde{H}_{so}^{mm\prime} = \langle m_l, m_s | \left[\hat{l}_z \hat{s}_z + \frac{1}{2}\left(\hat{l}_+ \hat{s}_- + \hat{l}_- \hat{s}_+ \right) \right] | m_l', m_s' \rangle ,$$

$$\underline{\tilde{H}}_{so} = \begin{pmatrix} -1 & 0 & 0 & 0 & 0 & 0 & 1 & 0 & 0 & 0 \\ 0 & -1/2 & 0 & 0 & 0 & 0 & 0 & \sqrt{3/2} & 0 & 0 \\ 0 & 0 & 0 & 0 & 0 & 0 & 0 & 0 & \sqrt{3/2} & 0 \\ 0 & 0 & 0 & 1/2 & 0 & 0 & 0 & 0 & 0 & 1 \\ 0 & 0 & 0 & 0 & 1 & 0 & 0 & 0 & 0 & 0 \\ 0 & 0 & 0 & 0 & 0 & 1 & 0 & 0 & 0 & 0 \\ 1 & 0 & 0 & 0 & 0 & 0 & 1/2 & 0 & 0 & 0 \\ 0 & \sqrt{3/2} & 0 & 0 & 0 & 0 & 0 & 0 & 0 & 0 \\ 0 & 0 & \sqrt{3/2} & 0 & 0 & 0 & 0 & 0 & -1/2 & 0 \\ 0 & 0 & 0 & 1 & 0 & 0 & 0 & 0 & 0 & -1 \end{pmatrix} , \tag{3.16}$$

where $\hbar$ has been set to 1 and the rows and columns of the matrix are ordered by $(m_l, m_s) = (-2,1/2), (-1,1/2), (0,1/2), (1,1/2), (-2,-1/2), (-2,-1/2), (-1,-1/2), (0,-1/2), (1,-1/2), (-2,-1/2)$.

The matrix which performs the required transformation to the orbital basis is found by taking a contraction of the m-basis with the basis given in (3.15). The states in the definite-m basis are orthogonal, and so the matrix takes the form

$$A^{jm} = \langle d, \alpha | m_l, m_s \rangle ,$$

$$\underline{A} = \begin{pmatrix} -\mathrm{i} & 0 & 0 & 0 & \mathrm{i} & 0 & 0 & 0 & 0 & 0 \\ 0 & 1 & 0 & -1 & 0 & 0 & 0 & 0 & 0 & 0 \\ 0 & -\mathrm{i} & 0 & -\mathrm{i} & 0 & 0 & 0 & 0 & 0 & 0 \\ 0 & 0 & 0 & 0 & 0 & -\mathrm{i} & 0 & 0 & 0 & \mathrm{i} \\ 0 & 0 & 0 & 0 & 0 & 0 & 1 & 0 & -1 & 0 \\ 0 & 0 & 0 & 0 & 0 & 0 & -\mathrm{i} & 0 & -\mathrm{i} & 0 \end{pmatrix} , \tag{3.17}$$

where the rows are ordered by $a^{\uparrow}$, $b^{\uparrow}$, $c^{\uparrow}$, $a^{\downarrow}$, $b^{\downarrow}$, $c^{\downarrow}$ to be consistent with the tight-binding Hamiltonian written in equation (3.11).

Finally, the spin-orbit Hamiltonian in the tight-binding basis is given by

$$\underline{H}_{so} = \lambda \underline{A} \underline{\tilde{H}}_{so} \underline{A}^T = \lambda \begin{pmatrix} 0 & 0 & 0 & 0 & -\mathrm{i} & 1 \\ 0 & 0 & -\mathrm{i} & \mathrm{i} & 0 & 0 \\ 0 & \mathrm{i} & 0 & -1 & 0 & 0 \\ 0 & -\mathrm{i} & -1 & 0 & 0 & 0 \\ \mathrm{i} & 0 & 0 & 0 & 0 & \mathrm{i} \\ 1 & 0 & 0 & 0 & -\mathrm{i} & 0 \end{pmatrix}, \tag{3.18}$$

where the adjusted coupling parameter is

$$\lambda = \lambda' \int \mathrm{d}\mathbf{r} \, |f(\mathbf{r})|^2 . \tag{3.19}$$

The index of the function $f(r)$ has been suppressed as all three orbital characters have the same radial distributions.

In order to incorporate this perturbation into the tight-binding model, the magnitude of the parameter λ must be discussed. In the literature, there is an extended controversy on this subject. Some authors have proposed that $\lambda \sim 50$ meV [176, 177], while orbital excitation spectra suggest a value as high as 200 meV [178]. This debate is further complicated by the contrasts in results obtained by tight-binding and *ab initio* approaches. In the first-principles case, the SOC parameter within the notation introduced here (i.e. including the radial contribution to the wavefunctions as in (3.19)) can be inferred to be $\lambda \sim 50$ meV. However, for the tight-binding models that have been used previously in studies of Sr_2RuO_4, SOC has been neglected, and so a discussion of the size of λ in this approximation has not been made at length.

To estimate a reasonable value for λ in this formalism, the magnitude of the induced energy splitting in the bandstructure will be assessed. The tight-binding parameters presented in Table 3.1 produce a bandwidth of roughly 0.7 eV (see Fig. 3.4), in agreement with the Fermi surface measured in de Haas-van Alphen experiments [168], as well as direct ARPES results giving a bandwidth of ~1 eV [167]. Furthermore, it agrees with other tight-binding fits [179, 180]. This is in stark contrast to *ab initio* results [181, 182], where the bandwidth is significantly larger than in experiments [167]. This comparison leads to a band renormalisation by a factor of about 1/4 (see Fig. 3.6).

A value of $\lambda = 50$ meV in first-principles calculations leads to an effective splitting of 100 meV at the Γ-point [182]. Taking the set of tight-binding parameters which recreate the *ab initio* bandwidth, the tight-binding model including SOC with $\lambda = 50$ meV recovers the same splitting, as can be seen in Fig. 3.7. However, in the case of the experimentally found bandwidth (corresponding to the parameters given in Table 3.1), spin-orbit coupling of that size leads to

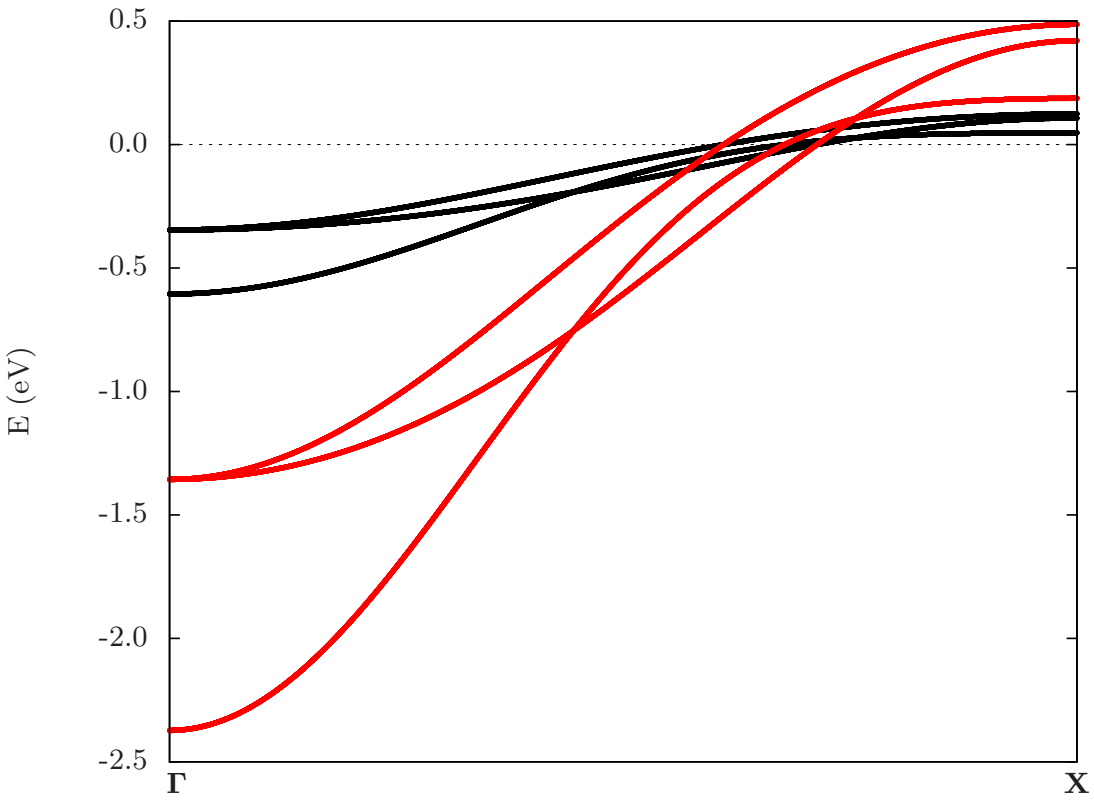

FIGURE 3.6. Tight-binding band structure along the [110] direction without spin-orbit coupling, comparing the large bandwidth obtained from first principles calculations (red) to the renormalized bandwidth which has been fitted to experimental data (black).

a complete rearrangement of the Fermi surface. It is impossible to reconcile such a large SOC parameter with the experimentally found Fermi surface. This is due to the significant band renormalisation, which increases the effective SOC on the energy scale set by the hopping parameter t. In light of this, it appears natural to apply the same renormalisation to the SOC constant λ as for the hopping parameters. This scaling gives λ = 12.5 meV, which provides a Fermi surface and effective masses in reasonable agreement to experiment. The resulting band structure is shown in Fig. 3.8.

It is important to highlight here the dominant implications of SOC on the electronic structure of the normal state in Sr_2RuO_4. The three Fermi surface sheets have been recreated in Fig. 3.9 through a series of orbitally-resolved Bloch spectra (see App. B.1). This represents the individual contributions of each orbital wavefunction to the bands at the Fermi surface. It is observed that hybridisation between the 2D band and the 1D bands is minimal in the absence of SOC, despite the inclusion of inter-orbital hopping terms H_{ac} and H_{ac}. The b and c-orbitals contribute negligibly to the γ sheet, while entirely forming the α and β sheets.

The addition of SOC does not significantly alter the Fermi surface obtained, and thus the

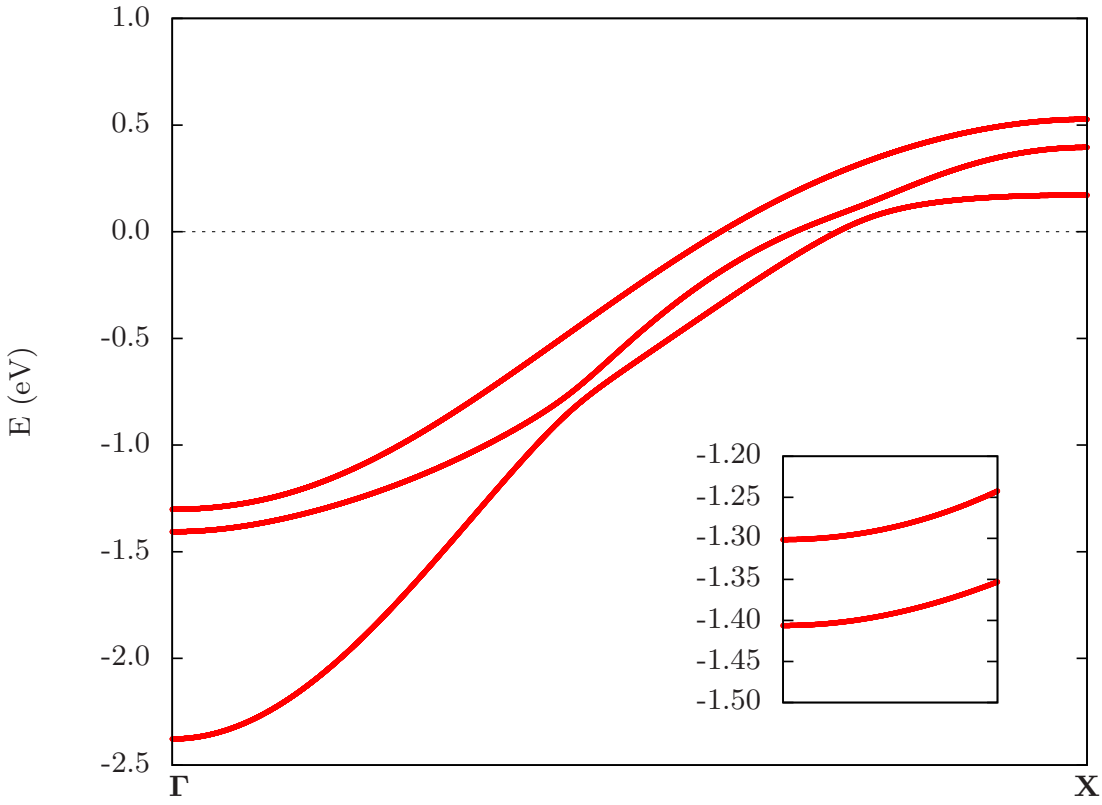

FIGURE 3.7. Tight-binding bandstructure along the [110] direction including SOC for the bandwidth obtained from first-principles calculation. The inset shows the Γ-point splitting induced by SOC.

tight-binding bandstructure accurately recreates empirical data with and without spin-orbit coupling. However, the individual contributions of each orbital to the electronic states are strongly affected, leading to a significant mixing of the orbital character within the different bands. This effect is most prominent at the near degeneracies along the [110] direction, where all orbitals contribute similarly to the three bands. When SOC is included, the α-orbital is no longer confined to only the circular γ band but also contributes to the α pockets and central β band. Similar mixing occurs for the 1D bands and has been reported previously [183]. In agreement with the results presented here, the addition of SOC and the subsequent orbital mixing were reported to have a negligible influence on the band crossings. The orbital mixing induced by spin-orbit coupling has a vital impact on the anomalous properties studied in this thesis, and is a key topic of discussion in Chapters 4 and 5.

3.1.4 Tight-Binding Hamiltonian: 2D

It is alluded to in Section 3.1.2 that certain unique experimental properties of the superconducting state in Sr_2RuO_4 can be recovered by including out-of-plane coupling terms in the gap structure.

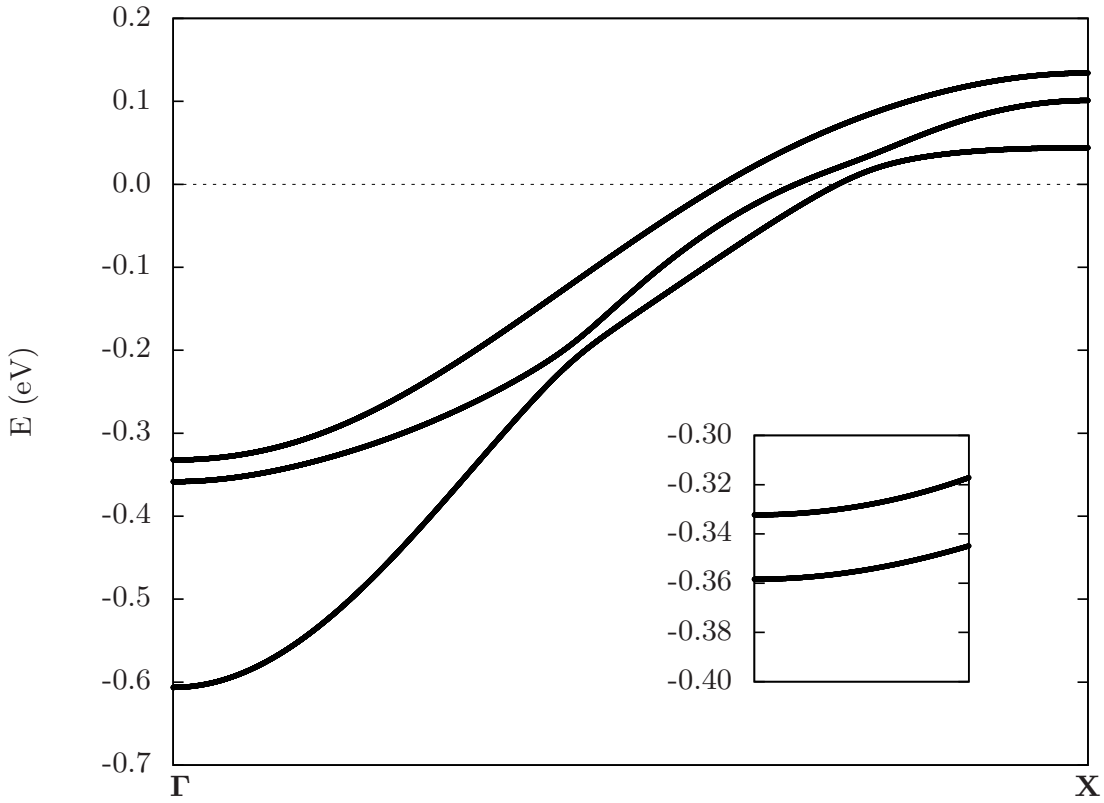

FIGURE 3.8. Tight-binding bandstructure along the [110] direction including SOC for the renormalized bandstructure. The inset shows the Γ-point splitting induced by SOC.

While this offers an elegant solution to the heat capacity and intrinsic anomalous transport properties of the state, some may argue that the influence of such terms should be minimal due to the strongly two-dimensional nature of the normal state Fermi liquid (as evidenced by the weak corrugations in the Fermi surface sheets along the k_z-direction). With this in mind, it is interesting to compare the results obtained from this approach with a model in which the superconducting state is described by a purely two-dimensional structure.

A gap structure without out-of-plane pairing was recently proposed by Scaffidi and Simon [184, 185]. It was suggested that by including longer-range in-plane pairing terms, it may be possible to generate the correct specific heat power law in addition to causing a suppression of edge currents, which would be consistent with experiment. The specific details of the gap structure are outlined in Section 3.2.3. The purpose of this section is simply to note the slight difference in the Slater-Koster parameters required to generate the Fermi surface without inter-plane hybridisation.

The tight-binding Hamiltonian used in this approach was introduced in ref. [185]. It shares the same structure as that given by equation (3.11), where the out-of-plane hopping terms t''_b, t''_{bc} and t''_{ab} are now neglected (note however the difference in the nomenclature of the a, b and c

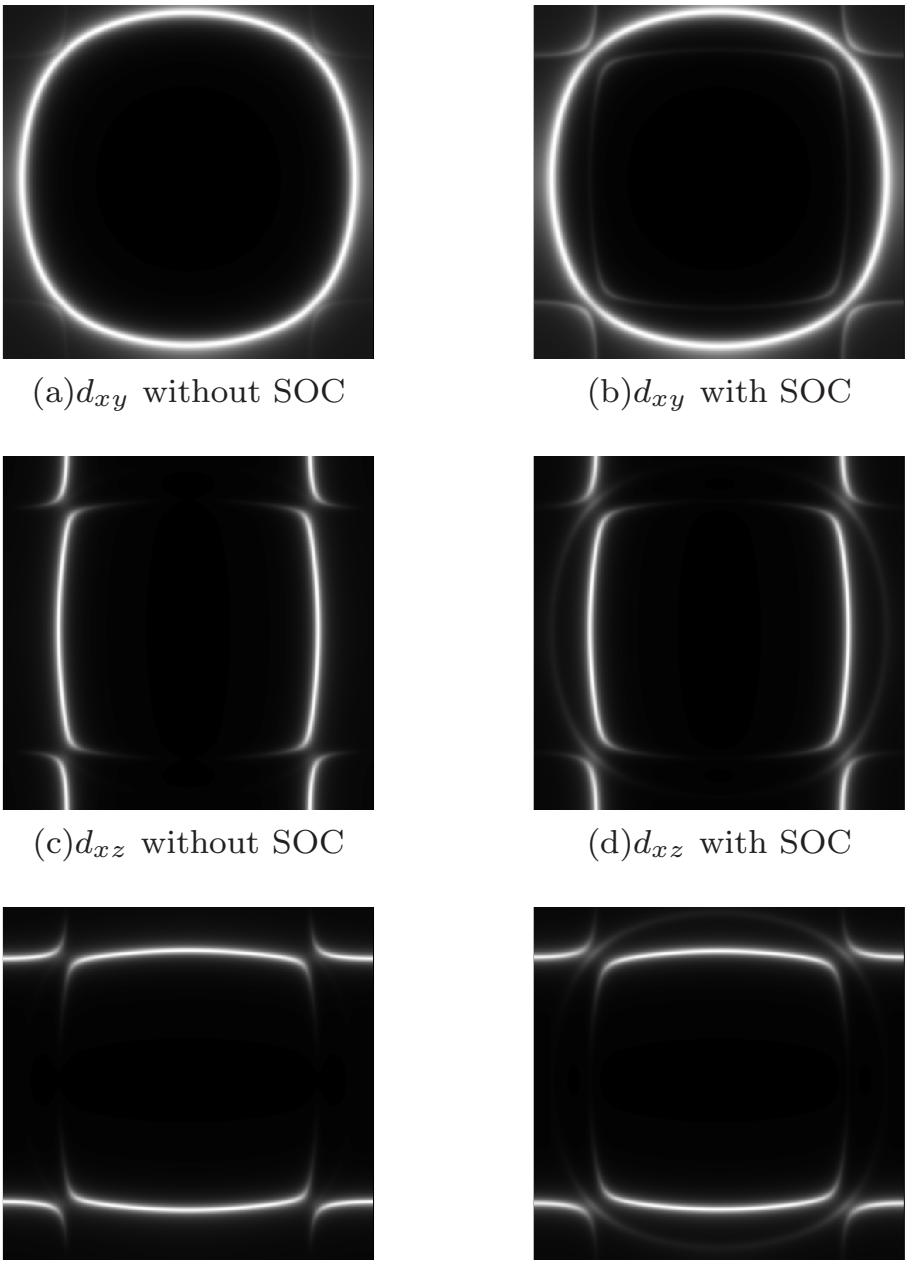

(a)d_{xy} without SOC (b)d_{xy} with SOC

(c)d_{xz} without SOC (d)d_{xz} with SOC

(e)d_{yz} without SOC (f)d_{yz} with SOC

FIGURE 3.9. Displayed are the orbitally-resolved Bloch spectral functions depicting the individual contributions of the a, b and c orbitals, respectively, to the Fermi surface. These are obtained by projecting the distinct components of the eigenvectors onto the Fermi surface density of states, with (right) and without (left) the inclusion of SOC.

orbitals in the cited literature). Generating the correct Fermi surface areas while maintaining the parameter ratios cited in [185] requires the parameters laid out in Table 3.2. Note also that the spin-orbit coupling term taken here is found to be 10.9 meV within this notation, of a very similar magnitude to that deduced in Section 3.1.3.

ϵ_a	ϵ_b	t	t'	t_b^x	t_c^x	t'_{bc}
-120.31	-109.37	-87.50	-32.81	-109.37	-10.94	-1.09

TABLE 3.2. Table of tight-binding parameters tuned to the bandstructure properties of Sr_2RuO_4 above 1.5 K, while conforming to the ratios laid out in ref. [185]. Parameters are given in units of meV.

3.2 Superconducting State

The symmetry properties of a particular superconducting state are embodied by the structure of the energy gap which appears upon the formation of Cooper pairs. The gap is representative of the binding energy associated with a pair, and a particular pairing interaction places constraints on the allowed wavevectors for two paired electrons. Conventional superconducting states comprise Cooper pairs of equal and opposite wavevector and spin. As a result, every electron at the Fermi surface has an equal chance of pairing, and so the energy gap is constant. For unconventional superconducting states, however, the symmetry of the pair wavefunction is more complex and the gap is a position-dependent (or equivalently **k**-dependent) function. Modelling an unconventional superconducting state thus requires careful consideration of the structure of the mean-field pairing potential to reflect the correct pair wavefunction symmetry.

In this section, an overview of the experimental and theoretical studies of the superconducting gap in Sr_2RuO_4 is given. It has been proposed by many that the pair wavefunction has a p-wave symmetry, although this hypothesis remains heavily debated. The structure of the pairing potential required to reflect a p-wave gap is presented, in addition to the self-consistent conditions used to perform calculations with this symmetry within the tight-binding framework.

3.2.1 Gap Properties

Superconductivity was discovered in Sr_2RuO_4 as a result of a search for materials with a similar structure to that of the cuprates (see Fig. 3.3). It was naturally expected that this superconducting state also displays an unconventional symmetry, a conjecture which was verified by the observation that the superconducting state can be destroyed via elastic impurity scattering [186, 187]. Suppression of the superconducting state by non-magnetic impurities is not possible in a conventional s-wave symmetry according to Anderson's theorem [188]. The theorem states

that the mixing of **k**-states induced by elastic scattering will have negligible influence on a **k**-independent gap, but will average the gap to zero for all **k** in a non-s-wave structure.

The cuprate superconducting state typically displays a d-wave, singlet pairing configuration [88]. In contrast, early investigations of the gap in Sr_2RuO_4 suggested that superconductivity in this state may be triplet in nature [103–105]. The primary evidence supporting this hypothesis is the observation that the spin susceptibility remains temperature-independent deep into the superconducting state [97], contrary to spin singlet superconductors in which the spin susceptibility goes to zero with temperature. This parity-dependent behaviour is a consequence of the Fermi surface polarisation which occurs when the spin susceptibility is finite. In a polarised state, there are no pairs of Fermi surface states with opposite momenta in addition to opposite spin, negating the formation of singlet Cooper pairs, meaning the susceptibility must vanish in a conventional superconductor.

A large amount of evidence suggests that the superconducting gap in Sr_2RuO_4 exhibits line nodes, although the origin and location of these nodes remains fiercely debated [162, 189, 190]. Low-temperature measurements have shown that the specific heat (C/T) is linear with respect to T [155–158, 191, 192], consistent with nodal lines in the gap. Further supporting pieces of evidence include the T^3 variation in the NMR spin-relaxation rate [97], a T^2 dependence of the penetration depth at low temperatures [193, 194], and linear temperature dependence of the thermal conductivity [195–198]. It is also believed, however, that the nodal structure observed in these experiments could be recovered if there are gaps with deep minima on all three bands [185, 189].

Time-reversal symmetry breaking has also been observed at the superconducting transition, indicating the presence of an intrinsic magnetisation in the state. The clearest direct measurement of this is through the appearance of a Kerr shift at T_c [102]. The Kerr effect is an optical phenomenon revealing the breaking of chiral symmetry [33], and is discussed and computed for the two models of Sr_2RuO_4 in Chapter 5. In addition, TRS breaking has been shown via muon spin-resonance experiments [98] and through the demonstration that the vortex lattice below T_c forms in a square configuration [99–101], which is predicted to occur in chiral superconductors [199, 200].

The observation of spin triplet pairing indicates that the pair wavefunction has an odd-parity symmetry, i.e. the pair exhibits an odd orbital quantum number. For a superconductor, this can correspond to p-wave symmetry ($L = 1$), f-wave symmetry ($L = 3$) etc. (note that, strictly speaking, L is not a good quantum number for a crystal, but this convention is typically retained on the basis that the wavefunction can still be classified by the number of nodes on the Fermi surface). A triplet state can be comprised of a superposition of three possible independent spin configurations, related to the three spin projections ($S_z = -1, 0, 1$). The structure of the superconducting state must therefore be defined in terms of three distinct gap functions. This spin-dependence means that the pairing potential of a triplet state is comprehensively defined using the formalism

$$\underline{\Delta}(\mathbf{k}) = \begin{pmatrix} \Delta^{\uparrow\uparrow}(\mathbf{k}) & \Delta^{\uparrow\downarrow}(\mathbf{k}) \\ \Delta^{\downarrow\uparrow}(\mathbf{k}) & \Delta^{\downarrow\downarrow}(\mathbf{k}) \end{pmatrix}, \tag{3.20}$$

where the matrix element indices refer to the spins of the paired electrons. A more compact notation is found by introducing a complex vector $\mathbf{d}(\mathbf{k})$ [70], defined by

$$\begin{pmatrix} \Delta^{\uparrow\uparrow}(\mathbf{k}) & \Delta^{\uparrow\downarrow}(\mathbf{k}) \\ \Delta^{\downarrow\uparrow}(\mathbf{k}) & \Delta^{\downarrow\downarrow}(\mathbf{k}) \end{pmatrix} = \begin{pmatrix} -d_x(\mathbf{k}) + \mathrm{i}d_y(\mathbf{k}) & d_z(\mathbf{k}) \\ d_z(\mathbf{k}) & d_x(\mathbf{k}) + \mathrm{i}d_y(\mathbf{k}) \end{pmatrix}. \tag{3.21}$$

In this notation, the $\mathbf{d}$-vector transforms like a vector under a rotation of spins. The pairing symmetry and nodal structure of the gap, in addition to the orbital and spin angular momentum of the Cooper pairs, are defined uniquely by $\mathbf{d}$.

The $\mathbf{d}$-vector describing a spin triplet superconductor points in the direction in spin space normal to the plane in which equal spin pairs form. Application of a field in the direction perpendicular to $\mathbf{d}$ should not therefore affect the spin susceptibility of the superconducting state, as triplet pairs can form in the presence of Fermi surface polarisation. For the case of Sr_2RuO_4, it has been shown experimentally that the susceptibility is constant with respect to fields in the ab-plane, suggesting that $\mathbf{d}$ aligns with the c-axis [105, 201]. The measurements confirm that $\mathbf{d}$ has a uniform direction in space, but spins will typically align with any applied magnetisation and so it is feasible that the $\mathbf{d}$-vector simply rotates in the presence of an external field. However, it is believed that spin-orbit coupling in Sr_2RuO_4 is sufficiently large to pin $\mathbf{d}$ to the c-axis [177]. In this case, an order parameter of the form $\mathbf{d} = d_z\hat{\mathbf{z}}$ is expected.

The derivation in Section 2.2.3 generates a non-local pairing potential for a general superconducting state ($\Delta(\mathbf{r}, \mathbf{r}')$). Conversion to the $\mathbf{k}$-dependent basis consistent with the triplet framework shown in (3.20) must be performed in order to proceed. The index $\{j, \alpha\}$ identifying the functions $u_{j\alpha}$ and $v_{j\alpha}$ in Chapter 2 refers to the state (enumerated by the spin and translational quantum numbers) and the spin coordinate of the wavefunction respectively. For a periodic lattice, the translational quantum number of a state can be numbered by $\mathbf{k}$, assuming that momentum-dependent SOC is negligible. In the $\mathbf{k}$-dependent framework, states are numbered by the band index n and the indices can thus be re-written as $\{n, \mathbf{k}, \alpha\}$.

A further slight alteration in the notation will be made when converting to the $\mathbf{k}$-dependent framework. In addition to re-writing the variables to be consistent with lattice states, the functions u and v will be henceforth be renamed θ and χ respectively, i.e. $(u_{j\alpha}, v_{j\alpha}) \equiv (\theta^{\alpha}_{n\mathbf{k}}, \chi^{\alpha}_{n\mathbf{k}})$. The reason for this is that the term $u_{n\mathbf{k}}(\mathbf{r})$ is conventionally used to describe the cell-periodic component of a Bloch wavefunction $\psi_{n\mathbf{k}}(\mathbf{r})$. In contrast, the functions $u_{j\alpha}(\mathbf{r})$ and $v_{j\alpha}(\mathbf{r})$ (the notation conventionally used in the derivation of the BdG equation) refer to electron and hole wavefunctions which are extended in real space. This distinction is of vital importance throughout the derivation of a theory for the orbital magnetisation in a superconductor, which is presented in Chapter 4.

Once the conversion to **k**-space has been performed, an expansion of the eigenfunctions in the tight-binding basis is required in order to carry out model calculations. As outlined in Section 2.1.1, a general expansion of a Bloch wavefunction in the orbital basis takes the form of equation (2.7). For the case of the BdG equation, however, the eigenfunctions are two-component eigenvectors in the electron-hole basis, rather than the single-component electron basis. An adapted tight-binding expansion compliant with the particle-hole basis can be written in the general form

$$\boldsymbol{\psi}^{\alpha}_{n\mathbf{k}}(\mathbf{r}) = \begin{pmatrix} \theta^{\alpha}_{n\mathbf{k}}(\mathbf{r}) \\ \chi^{\alpha}_{n\mathbf{k}}(\mathbf{r}) \end{pmatrix} = \mathrm{e}^{\mathrm{i}\mathbf{k}\cdot\mathbf{r}} \begin{pmatrix} u^{\alpha}_{n\mathbf{k}}(\mathbf{r}) \\ v^{\alpha}_{n\mathbf{k}}(\mathbf{r}) \end{pmatrix} = \sum_{i,d} \mathrm{e}^{\mathrm{i}\mathbf{k}\cdot\mathbf{R}_i} \begin{pmatrix} u^{\alpha}_{nd}(\mathbf{k}) \\ v^{\alpha}_{nd}(\mathbf{k}) \end{pmatrix} \phi^{\alpha}_{d}(\mathbf{r}-\mathbf{R}_i), \tag{3.22}$$

where the index d again sums over the orbital character (a,b,c).

Inserting expansion (3.22) into the generalised BdG equation (2.43), the tight-binding form of the equation is obtained,

$$\begin{pmatrix} \underline{H}^{\uparrow\uparrow}(\mathbf{k}) & \underline{H}^{\uparrow\downarrow}(\mathbf{k}) & \underline{\Delta}^{\uparrow\uparrow}(\mathbf{k}) & \underline{\Delta}^{\uparrow\downarrow}(\mathbf{k}) \\ \underline{H}^{\downarrow\uparrow}(\mathbf{k}) & \underline{H}^{\downarrow\downarrow}(\mathbf{k}) & \underline{\Delta}^{\downarrow\uparrow}(\mathbf{k}) & \underline{\Delta}^{\downarrow\downarrow}(\mathbf{k}) \\ (\underline{\Delta}^{\uparrow\uparrow}(\mathbf{k}))^* & (\underline{\Delta}^{\downarrow\uparrow}(\mathbf{k}))^* & -(\underline{H}^{\uparrow\uparrow}(\mathbf{k}))^* & -(\underline{H}^{\uparrow\downarrow}(\mathbf{k}))^* \\ (\underline{\Delta}^{\uparrow\downarrow}(\mathbf{k}))^* & (\underline{\Delta}^{\downarrow\downarrow}(\mathbf{k}))^* & -(\underline{H}^{\downarrow\uparrow}(\mathbf{k}))^* & -(\underline{H}^{\downarrow\downarrow}(\mathbf{k}))^* \end{pmatrix} \begin{pmatrix} \mathbf{u}^{\uparrow}_n(\mathbf{k}) \\ \mathbf{u}^{\downarrow}_n(\mathbf{k}) \\ \mathbf{v}^{\uparrow}_n(\mathbf{k}) \\ \mathbf{v}^{\downarrow}_n(\mathbf{k}) \end{pmatrix} = \epsilon_n(\mathbf{k}) \begin{pmatrix} \mathbf{u}^{\uparrow}_n(\mathbf{k}) \\ \mathbf{u}^{\downarrow}_n(\mathbf{k}) \\ \mathbf{v}^{\uparrow}_n(\mathbf{k}) \\ \mathbf{v}^{\downarrow}_n(\mathbf{k}) \end{pmatrix}. \tag{3.23}$$

The normal state Hamiltonian and gap function have now been written as 3×3 matrices in the orbital basis, while the 12-component eigenfunctions also comprise four 3-component vectors of the form $\mathbf{u}^{\uparrow}_n = (u^{\uparrow}_{na}, u^{\uparrow}_{nc}, u^{\uparrow}_{nc})$. The matrix elements of these operators are given respectively by

$$H^{\alpha\alpha'}_{dd'}(\mathbf{k}) = \sum_i \mathrm{e}^{\mathrm{i}\mathbf{k}\cdot\mathbf{R}_i} \int \mathrm{d}\mathbf{r}\, (\phi^{\alpha}_{d}(\mathbf{r}))^* \hat{H}_0(\mathbf{r})\, \phi^{\alpha'}_{d'}(\mathbf{r}-\mathbf{R}_i), \tag{3.24}$$

and

$$\Delta^{\alpha\alpha'}_{dd'}(\mathbf{k}) = \sum_i \mathrm{e}^{\mathrm{i}\mathbf{k}\cdot\mathbf{R}_i} \int \mathrm{d}\mathbf{r} \left[\int \mathrm{d}\mathbf{r}'\, (\phi^{\alpha}_{d}(\mathbf{r}))^* \, \Delta^{\alpha\alpha'}(\mathbf{r},\mathbf{r}')\, \phi^{\alpha'}_{d'}(\mathbf{r}'-\mathbf{R}_i) \right], \tag{3.25}$$

where the real space integrals extend over the lattice unit cell only. These elements are obtained under the assumption of no overlap of basis functions given in equation (2.2).

3.2.2 Pairing Potential Structure: 3D

The tight-binding Hamiltonian derived in Section 3.1 establishes a method to model the normal Fermi liquid state of Sr_2RuO_4 in the absence of a pair condensate. To proceed to modelling its superconducting properties, the BdG equation (3.23) must be solved. The tight-binding

Hamiltonian matrix elements (3.24) are given by (3.4)-(3.9) plus the SOC Hamiltonian (3.18). To complete the model, the orbital-dependent form of the pairing potential (3.25) is now introduced.

An understanding of the structure of the superconducting order parameter ($\mathbf{d}(\mathbf{k})$) is required for this step. This function encodes the chiral symmetry breaking associated with the unconventional superconducting transition in addition to the breaking of gauge symmetry. Many different gap symmetries have been proposed to explain the various experimental properties outlined in Section 3.2.1 [106, 202]. The approach taken here is to use a p-wave order parameter, which is widely believed to be the most likely structure [97, 103, 104, 161, 162].

The formation of the gap function used here to abide p-wave symmetry whilst conforming to the specific experimental properties of Sr_2RuO_4 was introduced in detail previously by Annett *et al* [161, 162]. The introduced structure is a minimal model which has been shown to recreate the line nodal gap behaviour in addition to being used in calculations of the Berry curvature [163] and the Kerr effect [129]. Note, however, that spin-orbit coupling was neglected in previous calculations made with this gap configuration. The influence of SOC on these results is a key topic of discussion in Chapters 4 and 5.

An order parameter of the form $\mathbf{d} = d_z\hat{\mathbf{z}}$ is enforced by taking the $S_z = 0$ projection of the spin triplet state, meaning that $\Delta^{\downarrow\uparrow} = \Delta^{\uparrow\downarrow}$ is finite, while $\Delta^{\uparrow\uparrow} = \Delta^{\downarrow\downarrow} = 0$. Laid out in textbook [26] is an approach whereby the inter-particle potential $U^{(2)}$ is split into density and spin-dependent components (which is a reasonable technique if the influence of SOC on the pairing interaction is negligible [203]) and the pairing potential is separated into components depending on triplet and singlet interactions. Applying this method to the spin-dependent pairing potential derived in equation (2.45), and extracting the relevant triplet contribution, the pairing potential can be written as

$$\begin{aligned}\Delta^{\downarrow\uparrow}(\mathbf{r},\mathbf{r}') = \frac{1}{2}\sum_{n,\mathbf{k}}\tilde{V}(\mathbf{r},\mathbf{r}')\left[1-2f_{n\mathbf{k}}\right] \\ \times\left[\left(\chi^{\downarrow}_{n\mathbf{k}}(\mathbf{r}')\right)^{*}\theta^{\uparrow}_{n\mathbf{k}}(\mathbf{r})+\left(\chi^{\uparrow}_{n\mathbf{k}}(\mathbf{r}')\right)^{*}\theta^{\downarrow}_{n\mathbf{k}}(\mathbf{r})-\left(\chi^{\downarrow}_{n\mathbf{k}}(\mathbf{r})\right)^{*}\theta^{\uparrow}_{n\mathbf{k}}(\mathbf{r}')-\left(\chi^{\uparrow}_{n\mathbf{k}}(\mathbf{r})\right)^{*}\theta^{\downarrow}_{n\mathbf{k}}(\mathbf{r}')\right],\end{aligned} \tag{3.26}$$

noting that the functions $u_{j\alpha}, v_{j\alpha}$ in equation (2.45) have been renamed $\theta^{\alpha}_{n\mathbf{k}}, \chi^{\alpha}_{n\mathbf{k}}$ as discussed in Section 3.2.1. Performing the tight-binding expansion (3.22) upon this function, and inserting into (3.25), the potential can be written in its $\mathbf{k}$-dependent form as

$$\Delta^{\downarrow\uparrow}_{dd\prime}(\mathbf{k}) = \sum_{n,\mathbf{k}\prime} V^{\downarrow\uparrow}_{dd\prime}(\mathbf{k},\mathbf{k}')\left[\left(v^{\downarrow}_{nd}(\mathbf{k}')\right)^{*}u^{\uparrow}_{nd\prime}(\mathbf{k}')+\left(v^{\uparrow}_{nd\prime}(\mathbf{k}')\right)^{*}u^{\downarrow}_{nd}(\mathbf{k}')\right]\left[1-2f_n(\mathbf{k}')\right], \tag{3.27}$$

where the antisymmetric property of the pair potential (2.40) has been applied in addition to $V^{\downarrow\uparrow}_{dd\prime} = V^{\uparrow\downarrow}_{dd\prime}$. The orbital-dependent interaction parameter is given by

$$V_{dd'}^{\alpha\alpha'}(\mathbf{k},\mathbf{k}') = \int \mathrm{d}\mathbf{r} \int \mathrm{d}\mathbf{r}'\, \tilde{V}(\mathbf{r},\mathbf{r}') \times \sum_{i,i',i''} \mathrm{e}^{\mathrm{i}\mathbf{k}\mathbf{R}_i} \mathrm{e}^{\mathrm{i}\mathbf{k}'(\mathbf{R}_i'-\mathbf{R}_i'')} \left(\phi_d^{\alpha}(\mathbf{r})\right)^* \left(\phi_d^{\alpha}(\mathbf{r}'-\mathbf{R}_i'')\right)^* \phi_{d'}^{\alpha'}(\mathbf{r}-\mathbf{R}_i')\phi_{d'}^{\alpha'}(\mathbf{r}'-\mathbf{R}_i). \tag{3.28}$$

The approach taken here, whereby the superconducting interaction is converted to an orbital-dependent framework, has been laid out previously for the p-wave order parameter considered in Sr_2RuO_4 [190, 204]. The parameter $V_{dd'}$ (referred to as the "scattering potential" in the literature) corresponds to the electron-electron interaction responsible for Cooper pairing between two orbital wavefunctions. Parametrisation of the scattering potential can now be performed by considering the underlying orbital and lattice symmetries of the structure, generating a tight-binding form for the superconducting order parameter. It is assumed that pairing is dominated by next-nearest neighbours, with on-site pairing not considered (as this would correspond to s-wave pairs).

In the base plane, nearest neighbour pairing requires that $\mathbf{R}_i = (\pm a, 0, 0)$ or $\mathbf{R}_i = (0, \pm a, 0)$ and that $\mathbf{R}_i'$ and $\mathbf{R}_i''$ are also separated by a single lattice spacing. Summing the non-zero contributions, the resulting vertex is

$$\begin{aligned} V_{dd'}^{\alpha\alpha'}(\mathbf{k},\mathbf{k}') = &\left[\sin(k_x a)\sin(k_x' a)\int \mathrm{d}\mathbf{r}\int \mathrm{d}\mathbf{r}'\, \tilde{V}(\mathbf{r},\mathbf{r}')\left(\phi_d^{\alpha}(\mathbf{r})\right)^*\left(\phi_d^{\alpha}(\mathbf{r}')\right)^*\phi_{d'}^{\alpha'}(x'-a,y',z')\phi_{d'}^{\alpha'}(x-a,y,z)\right] \\ &+\left[\sin(k_y a)\sin(k_y' a)\int \mathrm{d}\mathbf{r}\int \mathrm{d}\mathbf{r}'\, \tilde{V}(\mathbf{r},\mathbf{r}')\left(\phi_d^{\alpha}(\mathbf{r})\right)^*\left(\phi_d^{\alpha}(\mathbf{r}')\right)^*\phi_{d'}^{\alpha'}(x',y'-a,z')\phi_{d'}^{\alpha'}(x,y-a,z)\right], \end{aligned} \tag{3.29}$$

where the lattice sum has been shifted by setting $\mathbf{R}_i'' = \mathbf{0}$.

The double integrals in (3.29) are replaced with tunable constants. Enforcing p-wave symmetry requires that there is a relative phase difference between pairing in the x and y-directions. This is accomplished in the presented formalism by inserting a factor i between the two directions, resulting in an order parameter of the form

$$d_z(\mathbf{k}) \propto \sin(k_x a) + \mathrm{i}\sin(k_y a). \tag{3.30}$$

In-plane pairing will be enforced for the a-orbital only. Inserting (3.29) into (3.27), the structure for the in-plane component of the pairing potential is found,

$$\Delta_{aa}^{\uparrow\downarrow}(\mathbf{k}) = V_a(T)\left(\sin(k_x a) + \mathrm{i}\sin(k_y a)\right), \tag{3.31}$$

$$V_a(T) = U_{||}\sum_n \int \mathrm{d}\mathbf{k}\left[u_{na}^{\uparrow}(\mathbf{k})\left(v_{na}^{\downarrow}(\mathbf{k})\right)^* + u_{na}^{\downarrow}(\mathbf{k})\left(v_{na}^{\uparrow}(\mathbf{k})\right)^*\right]\sin(k_x a)\left[1-2f\left(\epsilon_n(\mathbf{k}),T\right)\right], \tag{3.32}$$

where the introduced constant $U_{||}$ is tuned to replicate the experimentally observed transition temperature (1.5 K). Note that the temperature dependence of parameter V_a has now been

highlighted explicitly. This dependence arises from the Fermi factor $f(\epsilon_n(\mathbf{k}))$ in the integration.
$V_a(T)$
the generalised BdG equation (3.23).

The order parameter is written in the **d**-vector notation as $\mathbf{d}(\mathbf{k}) = \Delta_0(T)(\sin k_x + \mathrm{i}\sin k_y)\hat{z}$. Chiral symmetry-breaking of the transition arises from the factor i in this state, which enforces a relative phase difference between pairing of electrons in the x and y-directions of the lattice. As a result of this pairing structure, the Cooper pairs gain a handedness, driving the formation of the anomalous properties which are the core focus of this investigation. The transition temperature is defined by $\Delta_0(T > T_c) = 0$.

In addition to pairing along the x and y-axes, out-of-plane pairing is considered. This is a method which naturally generates the nodal gap structure consistent with a linear heat capacity [159], which would not be present in a purely two-dimensional p-wave gap of the form (3.31). Nearest neighbour out-of-plane pairing occurs via sites separated by vectors $(\pm a/2, \pm a/2, \pm c/2)$. Applying this to the lattice sum in the scattering potential (3.28), and again enforcing p-wave symmetry, the equivalent out-of-plane order parameter is obtained,

$$d_z'(\mathbf{k}) \propto \left[\sin\left(k_x\frac{a}{2}\right)\cos\left(k_y\frac{a}{2}\right) + \mathrm{i}\cos\left(k_x\frac{a}{2}\right)\sin\left(k_y\frac{a}{2}\right)\right]\cos\left(k_z\frac{c}{2}\right). \tag{3.33}$$

The out-of-plane pairing occurs in the b and c-orbital channels, as inter-plane hybridisation is negligible for the a-orbital. Line nodes which are horizontal with respect to the k_z-axis are evident in this order parameter, as d_z' vanishes for $k_z = \pm\pi/c$.

Out-of-plane pairing can be formed in both intra-orbital and inter-orbital configurations,

$$\Delta_{bb}^{\uparrow\downarrow}(\mathbf{k}) = V_b^x(T)\sin\left(k_x\frac{a}{2}\right)\cos\left(k_y\frac{a}{2}\right)\cos\left(k_z\frac{c}{2}\right) + \mathrm{i}V_b^y(T)\cos\left(k_x\frac{a}{2}\right)\sin\left(k_y\frac{a}{2}\right)\cos\left(k_z\frac{c}{2}\right), \tag{3.34}$$

$$\Delta_{cc}^{\uparrow\downarrow}(\mathbf{k}) = V_c^x(T)\sin\left(k_x\frac{a}{2}\right)\cos\left(k_y\frac{a}{2}\right)\cos\left(k_z\frac{c}{2}\right) + \mathrm{i}V_c^y(T)\cos\left(k_x\frac{a}{2}\right)\sin\left(k_y\frac{a}{2}\right)\cos\left(k_z\frac{c}{2}\right), \tag{3.35}$$

$$\Delta_{bc}^{\uparrow\downarrow}(\mathbf{k}) = V_{bc}^x(T)\sin\left(k_x\frac{a}{2}\right)\cos\left(k_y\frac{a}{2}\right)\cos\left(k_z\frac{c}{2}\right) + \mathrm{i}V_{bc}^y(T)\cos\left(k_x\frac{a}{2}\right)\sin\left(k_y\frac{a}{2}\right)\cos\left(k_z\frac{c}{2}\right), \tag{3.36}$$

$$\begin{aligned} V_b^x(T) = 4U_\perp \sum_n \int \mathrm{d}\mathbf{k} \left[u_{nb}^{\uparrow}(\mathbf{k})\left(v_{nb}^{\downarrow}(\mathbf{k})\right)^* + u_{nb}^{\downarrow}(\mathbf{k})\left(v_{nb}^{\uparrow}(\mathbf{k})\right)^*\right]\sin\left(k_x\frac{a}{2}\right)\cos\left(k_y\frac{a}{2}\right)\cos\left(k_z\frac{c}{2}\right) \\ \times\left[1 - 2f\left(\epsilon_n(\mathbf{k}), T\right)\right], \end{aligned} \tag{3.37}$$

$$\begin{aligned} V_c^x(T) = 4U_\perp \sum_n \int \mathrm{d}\mathbf{k} \left[u_{nc}^{\uparrow}(\mathbf{k})\left(v_{nc}^{\downarrow}(\mathbf{k})\right)^* + u_{nc}^{\downarrow}(\mathbf{k})\left(v_{nc}^{\uparrow}(\mathbf{k})\right)^*\right]\sin\left(k_x\frac{a}{2}\right)\cos\left(k_y\frac{a}{2}\right)\cos\left(k_z\frac{c}{2}\right) \\ \times\left[1 - 2f\left(\epsilon_n(\mathbf{k}), T\right)\right], \end{aligned} \tag{3.38}$$

$$V_{bc}^{x}(T) = 4U_{\perp}\sum_{n}\int \mathrm{d}\mathbf{k}\left[u_{nb}^{\uparrow}(\mathbf{k})\left(v_{nc}^{\downarrow}(\mathbf{k})\right)^{*} + u_{nc}^{\downarrow}(\mathbf{k})\left(v_{nb}^{\uparrow}(\mathbf{k})\right)^{*}\right]\sin\left(k_x\frac{a}{2}\right)\cos\left(k_y\frac{a}{2}\right)\cos\left(k_z\frac{c}{2}\right)$$
$$\times\left[1-2f\left(\epsilon_n(\mathbf{k}),T\right)\right]. \tag{3.39}$$

The inclusion of pairing on the 1D bands via an out-of-plane interaction represents a key feature of the approach taken here. Most previous studies of this material have generated superconductivity primarily on the 2D pairing parameter [107, 190, 191, 204] or the 1D pairing terms [205, 206], while here both are implemented on an equal footing. Taking into consideration the symmetry of the orbital wavefunctions within the basis and the symmetry of the pair wavefunction, the interaction parameters are constrained by [129, 161, 162, 164]

$$V_b^y = V_c^x, \quad V_c^y = V_b^x, \quad V_{bc}^y = -V_{bc}^x. \tag{3.40}$$

Two distinct tunable constants ($U_{||}$ and $U_{\perp}$) have been introduced to account for pairing in the in-plane and out-of-plane directions. This approach to modelling the superconducting state is distinct from a typical multi-band BCS-like model. In that case, pairing on each band via different coupling constants would lead to multiple transition temperatures. However, experimental studies of Sr_2RuO_4 indicate that there is only a single superconducting phase transition. Here, the model is instead built in terms of real space bonds between electrons occupying specific orbitals, centered on specific lattice sites. Through investigation of a number of models constructed in this way, it was found that two non-zero coupling constants $U_{||}$ and $U_{\perp}$ form a useful minimal set [161]. These two constants must then be tuned separately such that both pairing channels display simultaneous transitions at T_c.

The physics implied by this approach should be commented on further. Typically, the instability leading to a superconducting transition corresponds to an irreducible representation of the point group of the crystal. In such a case, the transition temperatures associated with pairing in different bands naturally coincide, as there is only one transition for a given representation. For the real space bond approach taken here, it is implied that the model has a higher symmetry than the crystal, so an irreducible representation of the crystal corresponds to the superposition of two distinct representations of the model. The coupling constants are then adjusted such that model is fine-tuned to represent the crystal. Pairing via a particular distinct irreducible representation will henceforth be referred to as a "pairing channel" for convenience.

It was found that, for zero spin-orbit coupling, the required values for the tunable constants are $U_{||} = 37.63$ and $U_{\perp} = 50.69$ meV. The band splitting induced by the spin-orbit perturbation to the tight-binding Hamiltonian, however, has a significant influence on the formation of the spin-dependent gaps in the multi-orbital structure, resulting in the requirement for different interaction constants to maintain the correct transition behaviour. In this case, it was found that $U_{||} = 41.99$ and $U_{\perp} = 52.69$ meV [164]. The increase in the required constants to maintain the

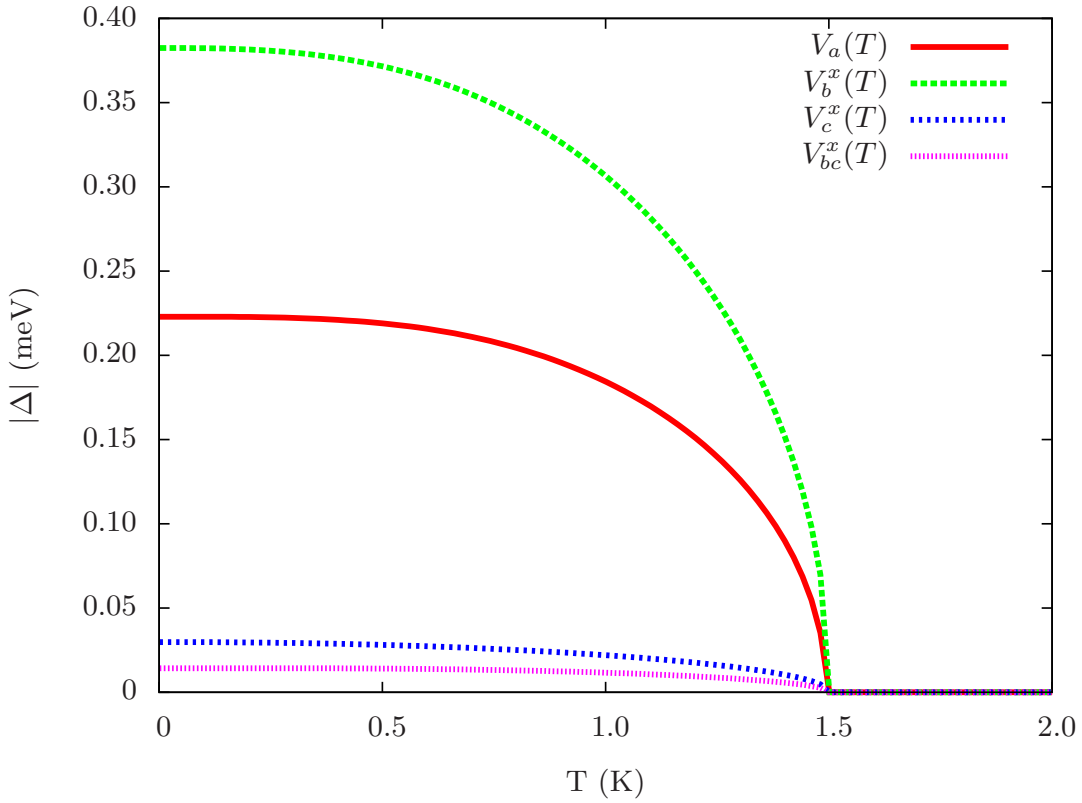

FIGURE 3.10. Computed values of the in-plane and out-of-plane gap parameters for the model of Sr_2RuO_4 without spin-orbit coupling. The values are calculated self-consistently through the Bogoliubov framework with an enforced p-wave symmetry.

correct T_c indicates that the spin-orbit interaction inhibits superconductivity in this case to some extent.

The components of the gap parameter are plotted against temperature, for the model with and without the spin-orbit interaction (see Fig. 3.10 and Fig. 3.11). Shown clearly is the appearance of a non-zero gap at the required temperature of 1.5 K. The addition of SOC does not qualitatively alter the temperature dependence of the various components of the gap parameters. However, the additional interaction causes a reduction in the relative difference in the magnitude of the parameters at zero temperature. The primary out-of-plane term V_b^x is suppressed by the addition of SOC, while V_{bc}^x approximately doubles. The in-plane gap also increases, becoming closer in magnitude to the out-of-plane pairing term.

Overall, the addition of a spin-orbit Hamiltonian causes the different components of the gap structure to become more closely correlated. This behaviour is expected as the SOC Hamiltonian enforces further inter-orbital hybridisation. Hybridisation between the distinct channels is essential, given that the model here requires the superposition of two representations to recreate an irreducible representation of the crystal, and thus the addition of spin-orbit coupling appears to

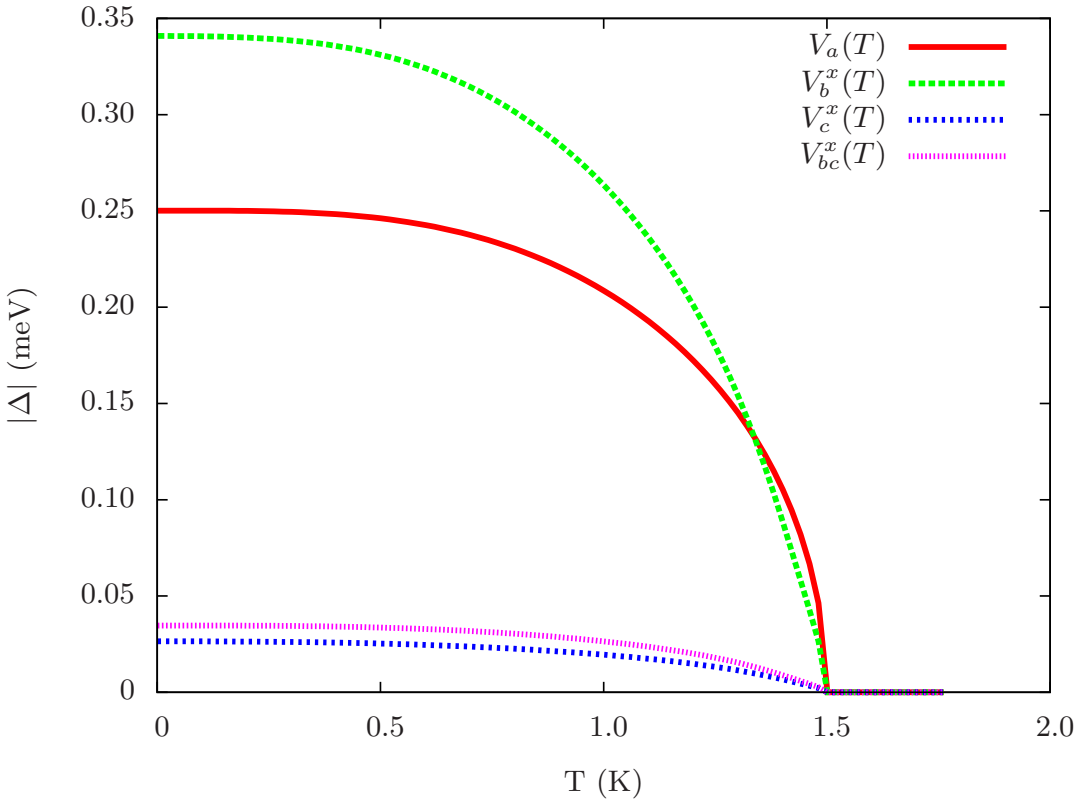

FIGURE 3.11. Computed values of the in-plane and out-of-plane gap parameters for the model of Sr_2RuO_4 with spin-orbit coupling included. The values are calculated self-consistently through the Bogoliubov framework with an enforced p-wave symmetry.

be vital. To emphasise this assessment, shown in Fig. 3.12 is the behaviour of the gap components near to T_c, for the model including SOC, with imperfect fine-tuning of the interaction constants. This calculation is performed for constants $U_{||} = 42.00$ and $U_{\perp} = 52.68$ meV, which are obtained by slightly altering those used to produce Fig. 3.12. The distinct components of the gap are here clearly converging toward distinct transition temperatures, as would be expected for pairing via different representations. However, the hybridisation in the system causes the gaps to converge to a single T_c, demonstrating the superposition of representations required in this approach.

The enforced gap structure also clearly replicates the correct line nodal structure, as evidenced by comparison of the model's heat capacity with experiment (see Fig. 3.13). Linear temperature dependence in C/T arises from the line nodes at $k_z = \pi/c$, while the correct gradient of the model calculation indicates that the magnitude of the gap at zero temperature is a reasonable approximation. In addition, the constant normal state value coincides well with experiment, reiterating that the Fermi surface and bandwidth are accurately recovered by the tight-binding Hamiltonian. The equation used to calculate the heat capacity is presented in App. B.1, and a discussion of the required unit conversion is given in B.2.

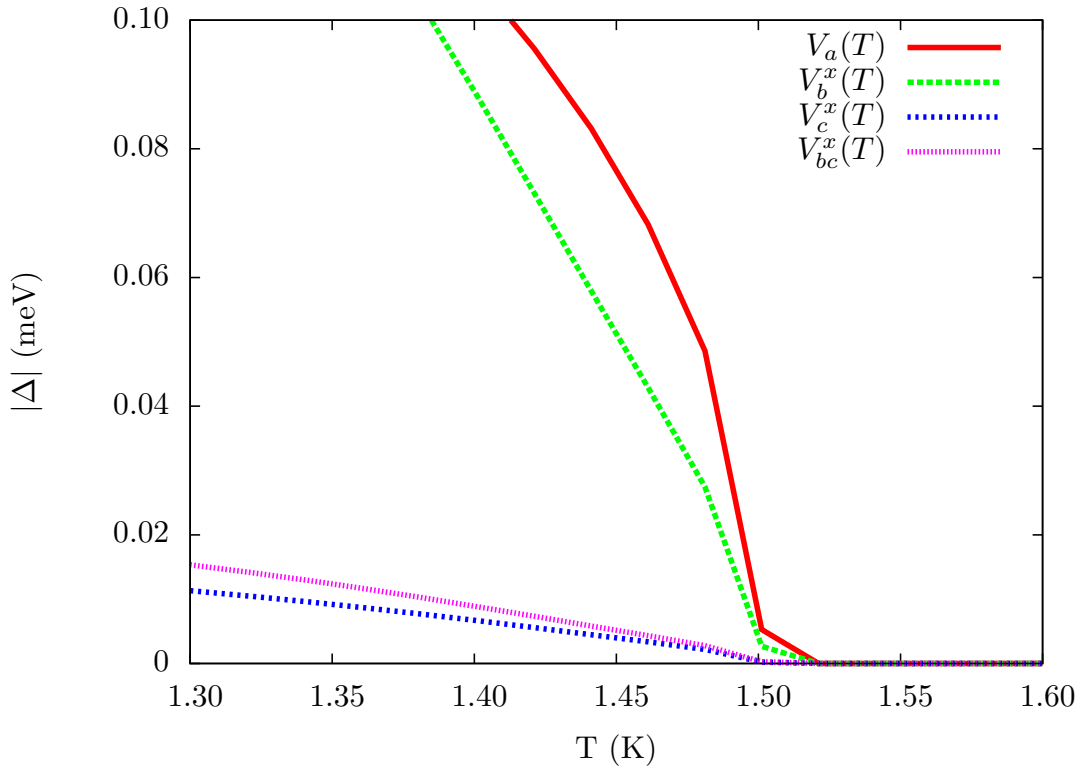

FIGURE 3.12. Computed values of the in-plane and out-of-plane gap parameters for the model of Sr_2RuO_4 with spin-orbit coupling included. The region near to T_c is shown with imperfect fine-tuning of the interaction constants. The four components of the gap converge to a single transition.

Finally, Fig. 3.14 shows k_x-k_y resolved plots of the finite contributions to the heat capacity throughout the Brillouin zone. It is observed that the introduction of spin-orbit coupling has negligible influence here. The increased inter-band hybridisation thus does not alter the nodal structure of the gap, while the changes in the magnitudes of the gap parameters has a minimal impact on the observed heat capacity. Low-temperature excitations are limited primarily to the α and β bands, which display line nodes, along the [110] direction in both cases. Small contributions arise also from deep minima on the γ band in the [±1 0 0] and [0 ±1 0] directions.

3.2.3 Pairing Potential Structure: 2D

Outlined here is an alternative approach to modelling the superconducting gap in Sr_2RuO_4. This formalism was motivated by the desire to reconcile a TRS breaking superconducting symmetry with the lack of observed edge currents in Sr_2RuO_4 while retaining a purely two-dimensional Fermi liquid. The 2D model was initially proposed by Scaffidi and Simon [184, 185], but the purpose of that investigation was to study the topological properties of the gapped bands for zero temperature only. Here, the temperature dependence of the gap will be analysed by adapting the

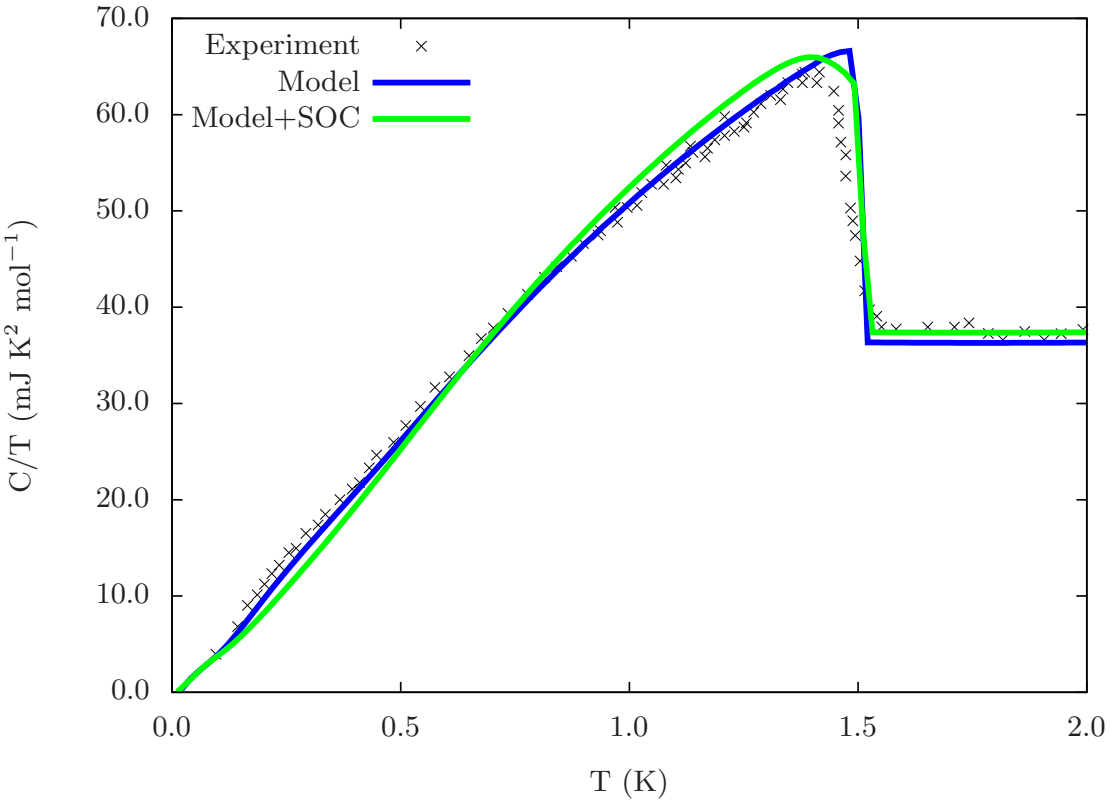

FIGURE 3.13. The plot shows the experimentally measured heat capacity alongside model calculations. The model clearly replicates the line nodal structure of the superconducting gap observed experimentally, with or without the inclusion of SOC. Experimental results were obtained from ref. [157].

order parameter to the Bogoliubov-de Gennes self-consistent framework.

The initial motivation behind this approach was to develop a model in which all three bands have gaps of a similar order. The reasoning was that a dominant p-wave gap on the γ band exhibits a topological number $C = 1$, which is believed to necessitate the appearance of large edge currents [109, 207–209]. An alternative picture sees superconductivity driven by anitferromagnetic nesting between the 1D bands, leading to an overall Chern number of 0, which would be consistent with the null result in magnetometry-based searches for edge currents. This model is also problematic, however, as thermodynamic measurements indicate that the gap should be approximately equal on all three bands [157, 191, 192, 210].

To reconcile these seemingly contradictory results, the authors performed functional renormalisation group (RG) calculations on the Fermi surface. This technique was initially developed by Raghu *et al* [211]. It generates the possible order parameters for a given superconducting Hubbard model with adjustable pairing interaction parameters. By including SOC and multi-band effects, it was found that the chiral order parameter obtained included additional terms, which correspond to effective longer-ranged pairing terms when transformed to real space [185].

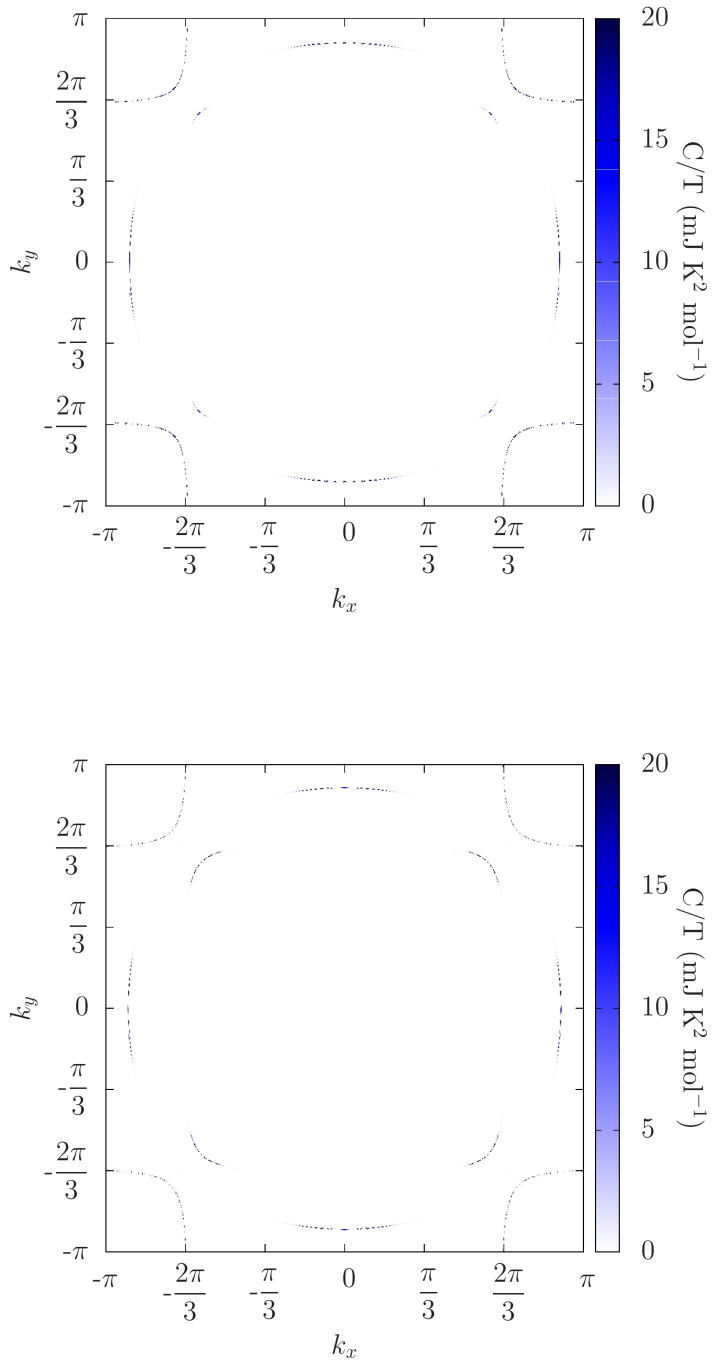

FIGURE 3.14. Brillouin zone heat map of the contributions to the heat capacity, for the 3D model without (upper) and with (lower) spin-orbit coupling. Calculations are performed for $k_z = 0$ and $T = 0.16$ K.

It was later shown that this extended order parameter displays a total Chern number of -7, which may result in a suppression of topological edge currents arising in the superconducting state [184]. In the model used here, the interaction terms deduced to be relevant through the RG investigation will be recreated by hand in the real space bond approach demonstrated in Section 3.2.2. Self-consistent calculations of the orbital moment and anomalous Hall effect obtained through this gap configuration will then provide a new avenue with which to study the effects of this structure on the state's topological and anomalous properties.

Within the notation used here, the derived gap has the form

$$\begin{aligned}\Delta_{aa}(\mathbf{k}) =& V_a(T)\left[\sin(k_x a)+\mathrm{i}\sin(k_y a)\right]+V_a'(T)\left[\sin(k_x a)\cos(k_y a)+\mathrm{i}\sin(k_y a)\cos(k_x a)\right]\\ &+V_a''(T)\left[\sin(3k_x a)+\mathrm{i}\sin(3k_y a)\right], \qquad (3.41a)\end{aligned}$$

$$\Delta_{bb}(\mathbf{k}) = V_b'(T)\sin(k_x a)\cos(k_y a)+V_b''(T)\sin(3k_x a), \qquad (3.41b)$$

$$\Delta_{cc}(\mathbf{k}) = \mathrm{i}\left[V_c'(T)\sin(k_y a)\cos(k_x a)+V_c''(T)\sin(k_y a)\right]. \qquad (3.41c)$$

Through comparison with the orbital-dependent framework outlined in Section 3.2.2, it is clear that the pairing terms introduced in this approach correspond to three distinct pairing channels. The standard nearest neighbour p-wave interaction (with order parameter given by (3.30)) is enforced again on the a-orbital only. However, given that there are no out-of-plane interactions in this model, the additional terms arise from different order parameters. Firstly, next-nearest pairing in the $(\pm a,\pm a,0)$ directions is included, incurring an order parameter of the form

$$d_z'(\mathbf{k}) \propto \sin(k_x a)\cos(k_y a)+\mathrm{i}\sin(k_y a)cos(k_x a). \qquad (3.42)$$

In addition, pairing between atoms separated by three lattice spacings is enforced,

$$d_z''(\mathbf{k}) \propto \sin(3k_x)+\mathrm{i}\sin(3k_y). \qquad (3.43)$$

By following the approach laid out in 3.2.2, it is possible to deduce the equivalent self-consistent equations for the extended pairing terms,

$$\begin{aligned}V_d'(T) = 4U_d' \sum_n \int \mathrm{d}\mathbf{k}\left[u_{nd}^{\uparrow}(\mathbf{k})\left(v_{nd}^{\downarrow}(\mathbf{k})\right)^* + u_{nd}^{\downarrow}(\mathbf{k})\left(v_{nd}^{\uparrow}(\mathbf{k})\right)^*\right]\sin\left(k_x a\right)\cos\left(k_y a\right)\\ \times\left[1-2f\left(\epsilon_n(\mathbf{k}),T\right)\right], \qquad (3.44)\end{aligned}$$

$$\begin{aligned}V_d''(T) = 4U_d'' \sum_n \int \mathrm{d}\mathbf{k}\left[u_{nd}^{\uparrow}(\mathbf{k})\left(v_{nd}^{\downarrow}(\mathbf{k})\right)^* + u_{nd}^{\downarrow}(\mathbf{k})\left(v_{nd}^{\uparrow}(\mathbf{k})\right)^*\right]\sin\left(3k_x a\right)\\ \times\left[1-2f\left(\epsilon_n(\mathbf{k}),T\right)\right]. \qquad (3.45)\end{aligned}$$

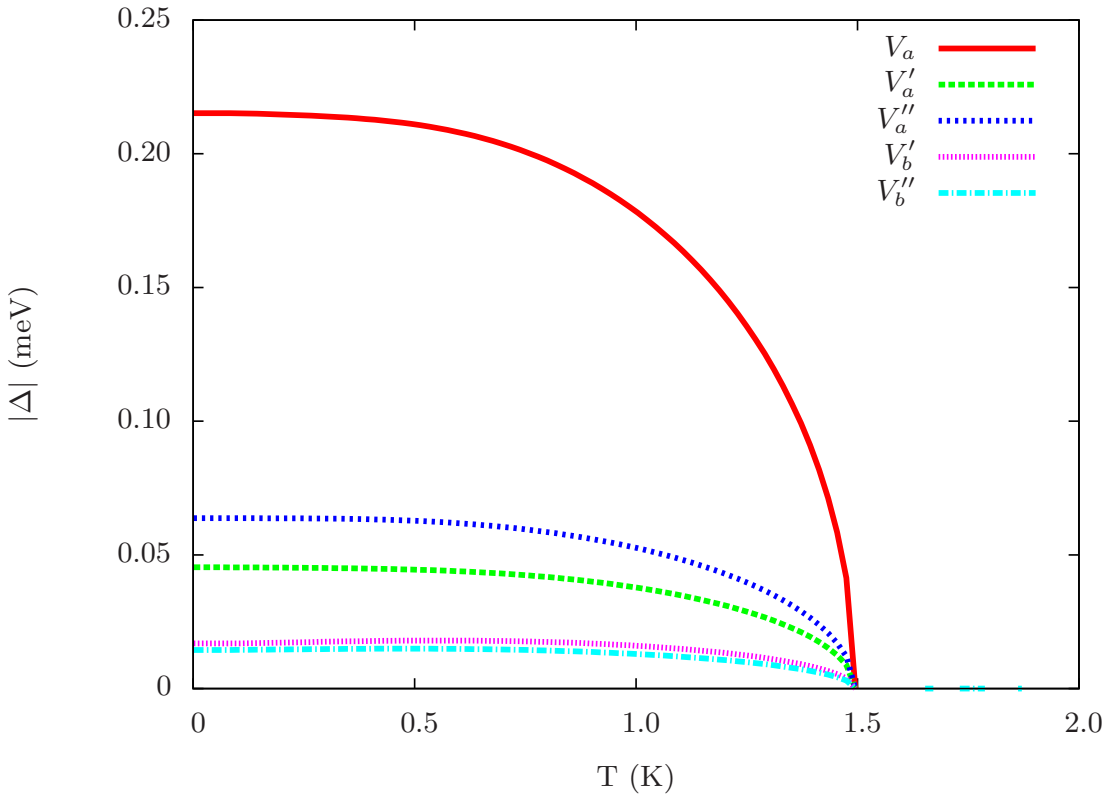

FIGURE 3.15. Computed values of the in-plane gap parameters in the extended pairing regime for the 2D model of Sr_2RuO_4. The values are calculated self-consistently through the Bogoliubov framework with an enforced p-wave symmetry.

The gap parameter V_a is again computed via equation (3.32), while the parameters for the 1D bands are related by $V_b' = V_c'$ and $V_b'' = V_c''$ [185]. Three distinct parameters are required for the pairing channels on the γ band, meaning that there are in total 5 adjustable interaction constants which must be tuned to obtain the single transition temperature at 1.5 K. The required parameters were found to be $U_a = 45.44$, $U_a' = 5.953$, $U_a'' = 6.200$, $U_b' = 67.02$ meV and $U_b'' = 97.62$ eV, and the results of the self-consistent calculation are displayed in Fig. 3.15.

It should be noted here that there will be no comparison with the model excluding SOC for the 2D case. This is due to the fact SOC is essential to obtain gaps of similar magnitude on all three pairing channels in this approach. The extended pairing is driven by distinct nesting regions on the α and β bands, with superconductivity arising on the γ band only through coupling to these bands. Preliminary calculations verified that the removal of spin-orbit coupling in this model led to a complete suppression of Δ_{aa}, which is consistent with the initial RG calculations made for a model excluding SOC [211].

In the original analysis of this pairing structure, it was shown that this gap can produce a reasonable estimate of the heat capacity jump at T_c [185]. It was also claimed by the authors

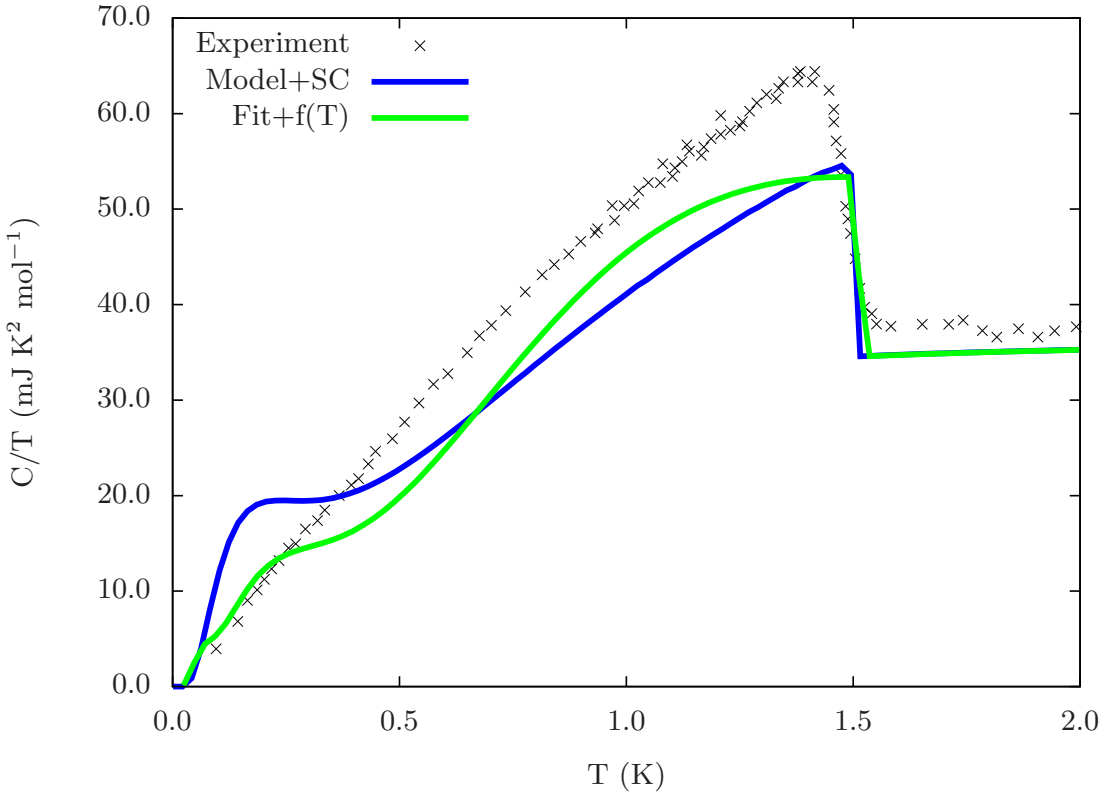

FIGURE 3.16. The plot shows the experimentally measured heat capacity alongside model calculations. The two model plots correspond respectively to the self-consistent Bogoliubov-de Gennes approach and the renormalisation group calculation fit with an enforced temperature dependence $f(T) = \Delta(0)\sqrt{1 - T/T_c}$.

that the linear behaviour of the specific heat below T_c was recreated. However, given that the temperature dependence of the gap was not calculated, this power law behaviour was not shown explicitly and it is unclear how this conclusion was reached.

In order to assess the specific heat properties of this model, the temperature dependence of the gap is modelled through two different approaches. Firstly, the specific heat corresponding to the self-consistent gap is shown alongside experimental data in Fig. 3.16. While this approach supports the claim that the linear behaviour is recovered near to T_c, it is clear that the low temperature region is not able to maintain the correct dependence as C/T goes exponentially to zero, indicating that the state becomes fully gapped at approximately 0.5 K. The second approach is to take the values of the gap parameter obtained through RG calculations at $T = 0$ and enforce an approximate temperature dependence given by $f(T) = \Delta(0)\sqrt{1 - T/T_c}$. In contrast, this approach appears to give the correct nodal structure near to zero temperature, but deviates significantly as T approaches the transition.

It is currently unclear whether the low temperature behaviour of the fitted approach can be recovered in the self-consistent framework. The 2D order parameters clearly do not generate the

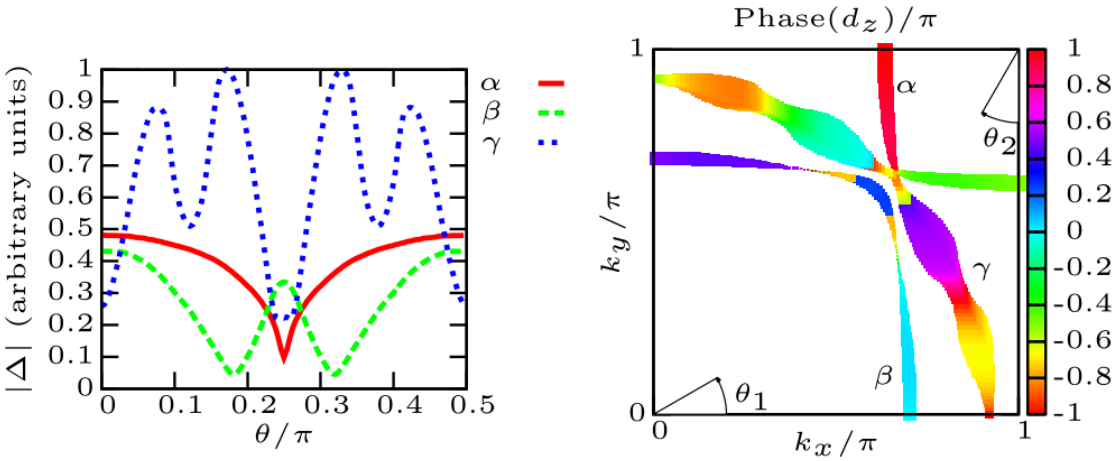

FIGURE 3.17. Gap magnitudes of the three band gaps (left) alongside the phase of the order parameter (right) obtained through renormalisation group calculations. Deep minima appear in close proximity on all three bands in the [110] direction. Figure is recreated from ref. [185].

expected line nodes, but it is also possible to obtain a T-linear heat capacity if there are deep minima on all three bands [185, 189]. The problem therefore most likely lies in the considerable differences in the relative ratios of the gap magnitudes obtained in the two approaches. The renormalisation calculation produced gaps on the 1D bands of magnitudes approximately three times larger than $|\Delta_a|$ [184], in contrast to the self-consistent calculation giving $|\Delta_a| > |\Delta_b'|$ (see Fig. 3.15). Comparison with the gap magnitudes plotted in ref. [185] (see Fig. 3.17) strongly suggests that this enhancement of the relative size of $|\Delta_a|$ will result in gap minima for the 2D band which are considerably larger than those on the 1D bands. As a result of this, it can be inferred that the self-consistent calculation is generating a low-temperature gap structure in which there are deep minima on the α and β bands, but not on the γ band, and so the required linear behaviour in C/T is not reproduced near to $T = 0$.

The distinctly different nodal structures of the two approaches are highlighted by Brillouin zone plots of the k_x-k_y resolved heat capacity (Fig. 3.18). These calculations are performed at a temperature of 0.16 K, within the temperature range where the self-consistent result appears to be fully gapped according to the temperature-resolved plot (Fig. 3.16). In the upper heat map, the **k**-resolved plot for the self-consistent solution is shown. Observed are contributions to the heat capacity from all states in the electron-like β band, in contrast to the 3D model in which this band contributes only in the [110] direction (Fig. 3.14). Given that there are no line nodes in the 2D case, the excitations observed uniformly here on the α and β bands are reflective of the small size of the 1D gaps relative to the gap on the γ band. In contrast, the localised low-temperature excitations throughout the Brillouin zone for the renormalised fit (lower plot of

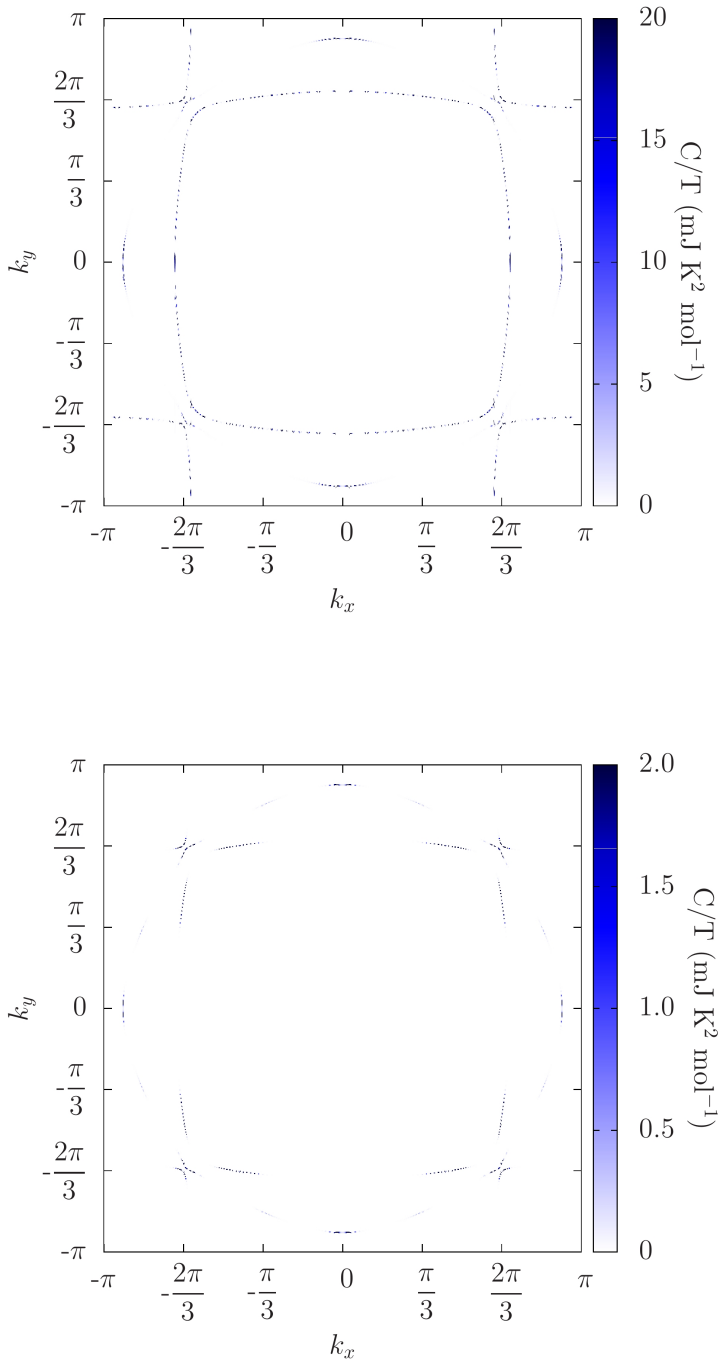

FIGURE 3.18. Brillouin zone heat map of the contributions to the heat capacity, for the 2D model solved self-consistently (upper) and through renormalised fitting (lower). Calculations are performed for $k_z = 0$ and T=0.16 K.

Fig. 3.18) correspond to the specific minima on each band, as all three bands have deep minima resulting in the linear temperature dependence of the superconducting heat capacity. It can be clearly seen that the regions contributing to the heat capacity here coincide with the gap minima displayed in Fig. 3.17.

For the Slater-Koster parameters utilised here, a suppression of $|\Delta_a|$ to recover the low-temperature nodal structure within the BdG approach would likely lead to distinct transition temperatures for each pairing channel, which is not observed in experiment. If this is the case, then the extended pairing regime would not represent a physical system for this particular material. However, given that the magnitude of the 2D gap in this model is directly related to the spin-orbit interaction, it could be speculated that the relative gap magnitudes consistent with the RG calculation could be recreated through the appropriate fine-tuning of the SOC parameter. It may therefore be possible to obtain the correct heat capacity through this model by shifting the normal state properties such that the fitted gap magnitudes are found. For the purpose of calculations presented through this model here though, the results can be considered non-physical and purely of qualitative interest, at least in the region $T < 0.5$ K.

A further interesting comment can be made regarding the contrasting temperature dependences of the gap parameters and heat capacity. The smooth linear evolution of the heat capacity observed experimentally indicates that the superconducting band gap also changes smoothly with respect to temperature. Intuitively, it would be expected that the gap parameters plotted in Fig. 3.15 should lead to a smooth heat capacity plot as a result. However, the crucial distinction which must be made is that the gap parameters here are written in an orbitally-resolved form. When strong inter-orbital hybridisation is present, via SOC and inter-orbital hopping, the band picture is significantly different from the orbital structure. This result is in fact partially observed in the 3D model calculations (see Fig. 3.13), where the introduction of SOC causes the gradient to deviate slightly from the near perfect linear temperature dependence computed in the absence of strong hybridisation.

The presence of additional pairing channels in the 2D model appears to strongly influence the effect of hybridisation on the gap evolution. In this case, it is possible that the band gap evolution is not smooth despite the smooth orbital evolution. Therefore, another approach worth considering would be to adjust the superconducting interaction terms to obtain the correct zero temperature magnitudes, but without further tuning of the SOC parameter. Through preliminary calculations made following this approach, it was found that it is possible to obtain a picture in which the gap parameters all display a T_c of 1.5 K, but without the smooth temperature evolution observed in Fig. 3.15. Kinks in the low-temperature regions of the orbital plots are induced, in a manner similar to that shown in Fig. 3.12. It is possible that this may result in the required smooth evolution in the low-temperature region of the heat capacity calculation due to the influence of inter-orbital hybridisation on the band gaps.

CHAPTER 4

ORBITAL MAGNETISATION

A key signature of the chiral superconducting state is the appearance of an orbital magnetisation. Each unit cell generates a net magnetic moment due to the finite orbital angular momentum carried by the chiral Cooper pairs. In addition, chiral symmetry breaking facilitates the formation of itinerant edge currents, which are a further source of magnetisation. In this chapter, the derivation of a modern method to calculate these distinct sources of magnetism in a general superconducting state is presented. The formalism presented here is then applied to the models of Sr_2RuO_4 developed in Chapter 3, followed by a discussion of the sources of the various components of the magnetic moment, the influence of spin-orbit coupling and the significance of the results with respect to the search for edge currents in this material.

4.1 Theoretical and Experimental Background

In this section, an overview of the existing theory and experimental techniques for the measurement of the orbital magnetisation is given. Section 4.1.1 details the methods of measuring the magnetisation in both normal state and superconducting lattices, in addition to discussing the technique for distinguishing the orbital component of the magnetisation from the spin part. A fundamental theory for the orbital component of the magnetisation in a periodic lattice was developed relatively recently and is introduced in Section 4.1.2, which also includes an outline of the pre-existing methods to estimate the property. Finally, Section 4.1.3 introduces the reader to the intriguing problem of itinerant edge currents in the superconducting state of Sr_2RuO_4. Such currents have been predicted to exist in this material as a result of the proposed p-wave structure but have never been identified experimentally.

4.1.1 Experimental Techniques

The magnetisation of an electronic state consists of two components, the spin part and the orbital part. A technique to distinguish between the two has been well-established for many decades. This depends on the measurement of the gyromagnetic factor (g'), a dimensionless property representing the ratio of magnetic moment to angular momentum for a particular system. The total magnetic moment (μ_{tot}) is related to g' via [212]

$$g' = \frac{2\mu_{tot}}{\mu_{tot} + \mu_{orb}}, \tag{4.1}$$

where μ_{orb} is the magnetic moment associated with the orbital component of the angular momentum and $\mu_{tot} = \mu_{orb} + \mu_{spin}$.

The gyromagnetic factor of a normal state ferromagnet can be determined through magneto-mechanical techniques. An example is the Einstein-de Haas effect, which relates to the rotation of a magnetic body under the application of an external field along the magnetisation axis [213]. As a consequence of the conservation of angular momentum, any change in the total magnetisation induced by this field (ΔM) is accompanied by a proportional change in angular momentum (ΔJ). The gyromagnetic ratio ($\gamma = \Delta M/\Delta J$) can be measured from this process, which then relates to the gyromagentic factor by $g' = 2m\gamma/e$. An alternative approach is to apply the inverse process, i.e. by inducing a mechanical rotation of the body a change in the total moment is observed, which is known as the Barnett effect [214].

A number of standard magnetometry methods, such as SQUID and Hall probes, are widely employed to discern the total magnetic moment of general solid state materials. Knowledge of μ_{tot} and g' can then be used to determine the orbital contribution to the magnetic moment via equation (4.1). Measurement of an intrinsic magnetisation in a superconductor is problematic, however, as the Meissner effect screens any internal fields, meaning the total moment visible to external probes is highly suppressed [107]. The bulk fields can be probed instead through muon spin resonance (μSR) experiments. In this technique, a muon is implanted in the lattice and the presence of local fields is determined through observation of the direction in which constituent particles are emitted when the muon decays. Although this provides a bulk probe which is not subject to surface effects, the presence of an impurity in the superconducting lattice has a significant influence on the local itinerant currents, and it is believed that the muon suppresses the superconducting order parameter in this region [215].

More modern approaches to extracting the orbital part of the magnetisation include the use of sum rules on circular dichroism spectra (which will be introduced in more detail in Section 5.2) [216], and x-ray diffraction measurements [217]. The magnetisation in normal state ferromagnets is typically dominated by the spin component [212]. However, the orbital component has been shown to be of a similar order to the spin part in certain systems, and has even been demonstrated to fully compensate the spin magnetisation [216, 217]. Of course, a key motivation of the work

presented here is that the orbital component is also believed to play a vital role in anomalous and topological transport properties [218–220]. A complete theory to compute the orbital magnetic moment elucidates the influence of different order parameters on these properties in chiral superconducting states.

4.1.2 Modern Theories

The calculation of the orbital moment in an isolated atom is a relatively straightforward task. The quantity is proportional to the expectation value of the quantum mechanical operator for orbital angular momentum ($\hat{\mathbf{l}} = \hat{\mathbf{r}} \times \hat{\mathbf{p}}$), which is evaluated with respect to the atomic wavefunctions. As described in Section 3.1.3, atomic wavefunctions are well-described in terms of spherical harmonic functions, which have a well-defined position-dependence and definite values of orbital angular momentum. The operator $\hat{\mathbf{l}}$ can be evaluated trivially in this case, and this process extends easily to molecules and finite-sized lattices.

Solid state materials are described by periodic lattices in the thermodynamic limit. Evaluation of the orbital angular momentum becomes problematic upon extension to infinite lattices, and thus obtaining a fundamental theory for the total magnetic moment in a crystal is challenging. A rough approximation can be made by calculating the on-site orbital moment carried by each atom in the unit cell [160]. Extending this method, an improved estimation can made through DFT calculations with atom-centered orbital basis sets, wherein the lattice potential is segregated into finite regions surrounding each atomic site and the total moment in these areas is computed. Both of these approaches crucially neglect any itinerant magnetisation arising from interstitial movement of electrons, and are thus inappropriate for the discussion of transport properties and edge currents. Linear-response theory can also be applied to the problem, but this technique is limited to the calculation of finite changes in the magnetisation, and not the total moment itself [221, 222].

Until fairly recently, no fundamental theory for orbital magnetism in solids existed [113]. The lack of a complete theory presented a serious problem, particularly as the orbital moment is believed to play a key role in anomalous transport phenomena. Since such a theory for the normal state was established, it has been shown that many solid-state phenomena commonly utilised in technological applications are directly related to the orbital magnetisation. For example, the solid-state NMR shielding tensors can be defined in terms of the derivative of the magnetisation with respect to an applied magnetic dipole [223]. Other properties such as the orbital magnetoelectric coupling and response [224, 225], and the spin Hall conductivity [226], can also be obtained from derivatives of the orbital magnetisation.

The problem of computing the orbital momentum in a periodic lattice originates from the fact that the position operator is ill-defined when acting on Bloch states. Electron wavefunctions formulated in the Bloch representation are extended in real space, and thus the position of an occupied wavefunction is not associated with a clearly defined quantum number. In general terms,

the expectation value of the position operator (and thus $\hat{\mathbf{l}}$) is not bounded, meaning that it is difficult to obtain a closed formula for the orbital moment in an extended periodic system.

To be more specific, the position operator becomes problematic due to two complications. Firstly, there is a freedom in how the cell-periodic components of the Bloch wavefunctions ($u_{\mathbf{k}}(\mathbf{r})$) can be constructed, provided that they are constrained by the translational symmetry of the lattice ($u_{\mathbf{k}}(\mathbf{r}+\mathbf{R}) = u_{\mathbf{k}}(\mathbf{r})$). The set of wavevectors $\mathbf{k}$ which parametrise these functions are defined relative to the unit cell, but the unit cell is not unique. Any local evaluation of the orbital angular momentum operator in the Bloch representation would hypothetically be achieved via an expectation value of the form $\langle u_{\mathbf{k}}|\hat{\mathbf{l}}|u_{\mathbf{k}}\rangle$, where the angle brackets here correspond to a real space integral over the unit cell. However, this calculation clearly depends on the chosen definition of the cell-periodic functions. The freedom in the Bloch basis thus leads to a non-unique solution for the local orbital moment.

Any observable quantity must of course have a unique solution for the entire lattice. To avoid the problem associated with freedom of choice in the unit cell, it would be natural to instead evaluate the unbound $\langle\mathbf{r}\rangle$ by integrating over the entire lattice, rather than the unit cell. However, this approach leads to a second obstacle. In the thermodynamic limit, the lattice extends infinitely in real space. The position operator thus becomes infinite at the boundaries of the integral, and so the expectation value becomes undefined and the solution can not be obtained.

The coexistence of these two factors means that the position expectation values of Bloch wavefunctions cannot be evaluated directly. In order to compute the orbital magnetisation, an equivalent $\mathbf{k}$-space operator is instead required to replace the position-dependent operator $\hat{\mathbf{l}}$. Deriving a general theory of this form for the orbital magnetisation in a bulk periodic lattice remained a serious problem for many years. This difficulty in describing the orbital magnetisation in a lattice is identical to the longstanding problem of calculating the electric polarisation, which suffers the same obstacles as it depends on operator $e\hat{\mathbf{r}}$, where e is the electric charge.

It was eventually demonstrated that a change in polarisation of a lattice is directly related to the Berry curvature of the bandstructure (see Section 5.1.2 for a detailed discussion of Berry phase effects) [227, 228]. The reciprocal-space equation for polarisation changes was derived by reformulating the problem in a localised basis. In this approach, the cell-periodic functions $u_{\mathbf{k}}(\mathbf{r})$ are replaced with Wannier orbitals ($W_{\mathbf{R}}$), which are related to Bloch states by

$$W_{\mathbf{R}}(\mathbf{r}) = \Omega \int_{BZ} \frac{d\mathbf{k}}{(2\pi)^3}\, \mathrm{e}^{\mathrm{i}\mathbf{k}\cdot\mathbf{r}}\, u_{\mathbf{k}}(\mathbf{r}). \tag{4.2}$$

Wannier functions are instead parametrised in terms of the real-space lattice vectors and have clearly defined position quantum numbers [114, 229]. They form a complete orthogonal set of wavefunctions and have a gauge freedom due to the freedom in the Bloch basis. This freedom allows the definition of Wannier orbitals which are exponentially localised in real space, and so can be directly evaluated with respect to the position operator. In the transformed basis, the

expectation value of any position-dependent operator is then a clearly defined quantity, written as

$$A(\mathbf{r}) = \sum_{\mathbf{R}} W^*_{\mathbf{R}}(\mathbf{r}) \hat{A}(\mathbf{r}) W_{\mathbf{R}}(\mathbf{r}) . \tag{4.3}$$

A rigorous normal state theory for the orbital magnetisation was eventually developed through an analogous approach [113, 114]. Beginning from an expression written in the Wannier basis, the group were able to remove the dependence of the equation on $\hat{\mathbf{r}}$. They subsequently performed a lattice Fourier transform to derive a clearly defined reciprocal-space equation for the orbital magnetisation written in terms of Bloch functions. This derivation was carried out initially for the specific case of a normal state, single-band insulating lattice [113], before being generalised to multi-band configurations, metals and Chern insulators [114].

Equation (4.3) produces a clearly defined solution as the wavefunctions are localised. However, the Wannier orbitals are simply a proposed set of basis functions which are not uniquely defined. Unitary mixing between Wannier orbitals leads to a gauge freedom and so there is no associated Hamiltonian. Instead, the derivation uses equation (4.3) as a solid, clearly-defined platform from which to convert to the reciprocal-space set of equations. The Bloch wavefunctions in the $\mathbf{k}$-space expression can then be expanded in the tight-binding basis in order to re-write the equation in terms of solutions to the tight-binding Hamiltonian.

The process of converting the expression to $\mathbf{k}$-space has been discussed at great length in refs. [113, 114]. In Section 4.2, this derivation is extended to incorporate the particle-hole basis eigenfunctions required to be consistent with the Bogoliubov-de Gennes formalism. The steps required to obtain the normal sate expressions will become clear when working through Section 4.2. Here, the normal state result is simply stated as a point of reference, and as a means to introduce the distinct components of the magnetisation introduced in the literature [113, 114],

$$\mathbf{M}_{\mathrm{LC}} = \frac{\gamma m}{\hbar} \mathrm{Im} \left[\int_{BZ} \frac{d\mathbf{k}}{(2\pi)^3} \sum_n \left(\langle \partial_{\mathbf{k}} u_{n\mathbf{k}} | \times \hat{H}_{\mathbf{k}} | \partial_{\mathbf{k}} u_{n\mathbf{k}} \rangle f_{n\mathbf{k}} \right) \right] , \tag{4.4a}$$

$$\mathbf{M}_{\mathrm{IC}} = \frac{\gamma m}{\hbar} \mathrm{Im} \left[\int_{BZ} \frac{d\mathbf{k}}{(2\pi)^3} \sum_n E_{n\mathbf{k}} \left(\langle \partial_{\mathbf{k}} u_{n\mathbf{k}} | \times | \partial_{\mathbf{k}} u_{n\mathbf{k}} \rangle f_{n\mathbf{k}} \right) \right] , \tag{4.4b}$$

$$\mathbf{M} = \mathbf{M}_{\mathrm{LC}} + \mathbf{M}_{\mathrm{IC}} . \tag{4.4c}$$

where $\gamma = -e/(2m)$ is the gyromagnetic ratio for the orbital magnetic moment.

The normal state derivation introduced two distinct contributions to the total moment, referred to as the "local" and "itinerant" circulations, denoted $\mathbf{M}_{\mathrm{LC}}$ and $\mathbf{M}_{\mathrm{IC}}$ respectively. These terms correspond to orbital moments generated by the movement of the centres of mass of orbital

wavefunctions (itinerant), and the moment due to self-rotation about their centres of mass (local). Equation (4.4) thus incorporates the complete set of contributions to the orbital moment in an extended lattice, including the on-site atomic moment generated by the orbital basis and the magnetisation due to surface circulation.

A caveat to the formalism laid out here must now be made. Although the sum $\mathbf{M}$ represents the physically observable magnetisation, the individual components $\mathbf{M}_{\mathrm{LC}}$ and $\mathbf{M}_{\mathrm{IC}}$ are not separately gauge-invariant and thus do not uniquely define the local and itinerant sources of the orbital moment. The fundamental problem with the way in which these equations are formulated is that $\mathbf{M}_{\mathrm{LC}}$ is not the true self-rotation of orbitals and in fact includes a contribution arising from intra-cell movement of wavefunctions [230]. The assignment of Wannier functions to specific unit cells is not unique, resulting in a gauge freedom in the definition of $\mathbf{M}_{\mathrm{LC}}$ and subsequently $\mathbf{M}_{\mathrm{IC}}$.

Following the initial derivation of equation (4.4), a paper by Souza and Vanderbilt showed that this set of formulae could be converted into distinct, measurable quantities [230]. By separating $\mathbf{M}_{\mathrm{LC}}$ into contributions from the occupied and unoccupied bands, a gauge-invariant equation for the self-rotation of Wannier orbitals can be extracted. This term refers then only to the magnetic moment of an occupied orbital and can be thought of as the intra-orbital magnetisation. The remaining itinerant contribution then comes from inter-orbital sources, i.e. the current generated through hopping of electrons between orbitals. A total orbital magnetic moment is measurable through the techniques outlined in Section 4.1.1, while the self-rotation component can be identified individually via circular dichroism measurements and the sum-rule [230]. The derivation presented in Section 4.2, however, draws heavily from the approach employed to formulate equations (4.4a) and (4.4b) as extraction of the gauge-invariant components becomes exceeding difficult when working with particle-hole wavefunctions of a Cooper pair condensate (see Section 4.3 for a further discussion on this problem).

Equations (4.4a) and (4.4b) are dependent on cell-periodic functions which are limited to a single-component electron states, and are thus inappropriate for the discussion of the magnetisation in a pair condensate. Despite the lack of an appropriate fundamental theory, the orbital moment carried by a pair condensate has been highly studied since the discovery of unconventional pairing in the superfluid phase of ^{3}He [72–74]. Given that each Cooper pair in the p-wave state carries an orbital angular momentum of $\hbar$, an intuitive estimation would give a total angular momentum of $N\hbar/2$ for a condensate of N paired particles [231]. This approximation is problematic, however, as it does not account for the influence of pair correlations occurring on a length scale set by the coherence length ξ_0.

The landmark paper by Anderson and Morel, which initially predicted the existence of a chiral superfluid state in ^{3}He, estimated that pair correlation effects would reduce the total orbital moment by a factor $|\Delta|/\epsilon_F$, where ϵ_F is the Fermi energy [69]. This reduction was expected as the result of the cancellation of orbital currents carried by neighbouring Cooper pairs within the range of the coherence length. Within a distance ξ_0 of the sample surface in this picture, cancellation

of local currents does not occur, and a finite current remains, resulting in the suppressed total moment.

Further reduction in the total moment was later predicted by consideration of the respective orbital currents carried by electron and hole constituents of the Cooper pair condensate [232]. Due to the particle-hole symmetry of the paired state, these contributions would be expected to cancel, leaving only finite angular momentum arising from a small fraction of the condensate near to the Fermi surface. A total orbital angular momentum predicted in this case was $(|\Delta|/\epsilon_F)^2$ smaller than the initial prediction of $N\hbar/2$.

More recent theoretical work has argued, however, that the effect of pair correlations on the total moment carried by the condensate should not be as drastic [108, 109, 207, 209]. It is believed by many that the topologically-protected edge modes of the state may be able to carry the full orbital angular momentum of the condensate, which leads to a result giving an orbital moment of $N\hbar/2$ at zero temperature, in agreement with the earliest predictions. The magnitude of this moment is then expected to evolve as the superfluid density in the temperature range 0 K - T_c.

For superfluid ^{3}He, $(|\Delta|/\epsilon_F)^2$ is approximately equal to 10^{-6}. The various estimations outlined above thus range by 6 orders of magnitude for this particular condensate, clearly reiterating the need for a fundamental theory to calculate the total orbital moment carried by a Cooper pair condensate. In the work presented in Section 4.2, equations (4.4a) and (4.4b) are extended to account for the wavefunctions of a general BdG Hamiltonian, such that they are appropriate for the study of the intrinsic orbital magnetisation in unconventional superconductors and superfluids.

4.1.3 Edge Currents in Sr_2RuO_4

For the case of a chiral p-wave superconducting state, it has been predicted that the appearance of a finite orbital magnetisation should result in the existence of spontaneous edge currents (see Section 5.1.2 for a description of the origin of this current) [17, 107–109, 207–209]. The initial theoretical models proposed to describe the superconducting state of Sr_2RuO_4 enforced a p-wave gap only on the γ band with the order parameter given by (3.30) [107, 190, 191, 204]. Through a series of self-consistent Green's function calculations on such a model, it was estimated that the local magnetisation near to a surface in a state of this configuration should generate a magnetic field of approximately 100 G [107]. The total magnetisation near to a boundary is complicated, however, by the presence of a Meissner screening current which will be induced by the intrinsic field. Accounting for the opposing field associated with this current, it was estimated that the net local magnetisation at the surface of Sr_2RuO_4 should be of the order of 10 G. This calculation was made in a quasi-classical approximation, without the benefit of a fundamental quantum mechanical theory which is developed in Section 4.2. Nevertheless, it has been assumed that the approximation at least roughly predicts the magnitude of the edge currents in the single-band

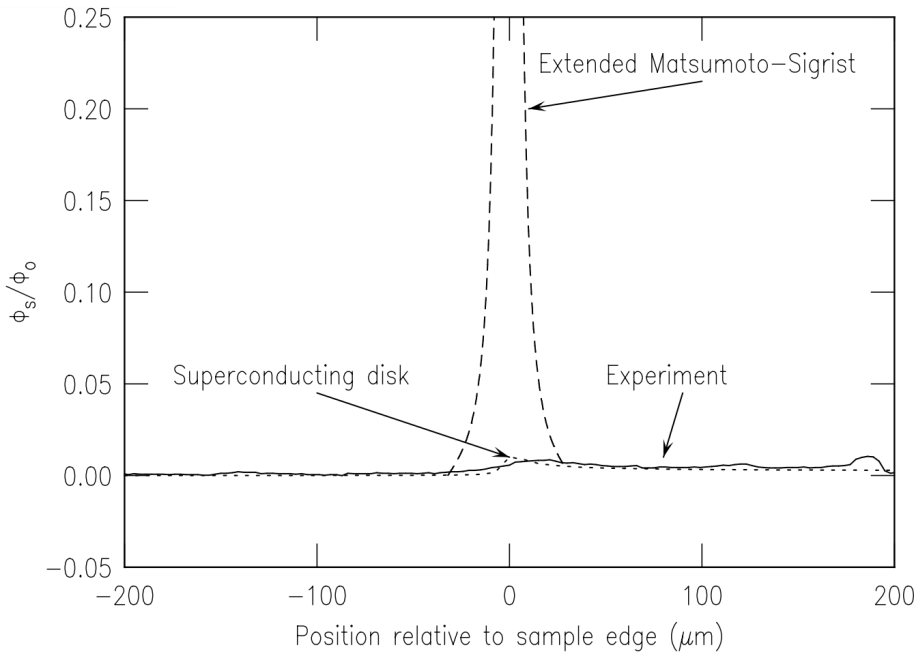

FIGURE 4.1. Experimental search for edge currents in Sr_2RuO_4 via scanning SQUID magnetometry. The three edge magnetisation curves correspond to the measurement for Sr_2RuO_4 ("Experiment"), the theoretical prediction for Sr_2RuO_4 given by ref. [107] ("Extended Matsumoto-Sigrist"), and the prediction for an ideal superconducting disk in a uniform residual field of 3 nT ("Superconducting disk"). No indication of a local magnetisation is discerned at the sample surface, in contrast to the theoretical prediction. The vertical axis is given in dimensionless units, where Φ_s is the measured magnetic flux and $\Phi_0 = h/2e$ is the superconducting flux quantum. Figure is recreated from ref. [110].

p-wave state.

Following the prediction of a large edge current in Sr_2RuO_4, many experimental probes have been applied to the material utilising the various techniques outlined in Section 4.1.1. Scanning SQUID magnetometry and Hall bar probes have been used [110–112], in addition to cantilever magnetometry [233], but all approaches have failed to identify any discernible edge magnetisation. Enhancement of the experimental set-up has enabled measurements with resolution as small as ±2.5 mG [112]. Fig. 4.1 displays the results from ref. [110] alongside the predictions made from the single band p-wave model (referred to as the "Extended Matsumoto-Sigrist" approximation), clearly demonstrating that this theory does not replicate experiment.

If the experimental results are to be reconciled with a p-wave configuration, either the magnitude of the predicted edge current or domain sizes must be drastically different. The

results outlined above established that any edge current existing in Sr_2RuO_4 must be at least 3 orders of magnitude smaller than that predicted through quasi-classical methods. Alternatively, a magnetisation of this size could be present without being detected if the domain sizes are significantly small (< 300 Å) as to not be visible through magnetometry techniques. This latter scenario seems unlikely, however, as such a small domain size would contradict the experimentally observed Kerr effect (see 5.2 for further detail).

In the work presented in this chapter, a general theory for the orbital magnetisation in a superconductor is derived and applied to the models of Sr_2RuO_4 developed in Chapter 3. This allows a fully inclusive estimation of the itinerant magnetisation to be made, without the shortcomings of previous approximations. Furthermore, the models used here are not limited to the single-band configuration initially proposed, and so the effects of multiple gaps with inter-band hybridisation and nodes can be discussed in addition to the impact of extended pairing channels on the total moment.

4.2 Orbital Magnetisation of a Superconductor

The derivation of a set of equations to compute the total orbital magnetisation in a general superconductor is presented in this section. This approach draws from the Wannier-based normal state derivations laid out in refs. [113, 114, 223]. The key distinction here is the introduction of a set of two-component Wannier wavefunctions to describe the particle-hole superconducting state. Expansion of the Bloch-dependent equations in the tight-binding basis is also performed, resulting in the extraction of a purely on-site contribution to the orbital magnetic moment. The on-site term is only a single component of the total orbital magnetisation, but it can be easily compared with previous approximations [160].

4.2.1 Conversion to Particle-Hole Basis

The orbital moment is related to the expectation value of the orbital angular momentum operator. In second quantised form, the general many-body operator for the total orbital angular momentum in the $\hat{z}$-direction is given by

$$\hat{L}_z = \sum_\alpha \int d\mathbf{r}\, \hat{\psi}^\dagger_\alpha(\mathbf{r}) \hat{l}_z \hat{\psi}_\alpha(\mathbf{r}), \tag{4.5}$$

where $\hat{\psi}^\dagger$, $\hat{\psi}$ are Fermi creation and annihilation operators respectively, α is the spin index, and $\hat{l}_z = [\hat{\mathbf{l}} = \hat{\mathbf{r}} \times \hat{\mathbf{p}}]_{\hat{z}}$ is the single-particle angular momentum operator. The total orbital magnetic moment is then given by $\gamma \langle \hat{L}_z \rangle$, where $\gamma = -e/(2m)$ is the gyromagnetic ratio. Angle brackets here correspond to the expectation value taken with respect to a generic many-body state.

In order to account for the superconducting state, the Bogoliubov-Valatin transformation is performed on the creation and annihilation operators, as is carried out when generating the

superconducting Hamiltonian in Section 2.2. The spin-generalised expansion given in equation (2.42) is applied to (4.5). Taking the **k**-dependent form of the wavefunctions introduced in Section 3.2.1, this transformation gives

$$\begin{aligned}\hat{L}_z = \sum_{n,n\prime,\mathbf{k},\mathbf{k}\prime,\alpha} \int d\mathbf{r}\, &\left(\theta^{\alpha}_{n\mathbf{k}}(\mathbf{r})\right)^* \hat{l}_z\, \theta^{\alpha}_{n\prime\mathbf{k}\prime}(\mathbf{r})\, \hat{\gamma}^{\dagger}_{n\mathbf{k}} \hat{\gamma}_{n\prime\mathbf{k}\prime} + \chi^{\alpha}_{n\mathbf{k}}(\mathbf{r})\, \hat{l}_z \left(\chi^{\alpha}_{n\prime\mathbf{k}\prime}(\mathbf{r})\right)^* \hat{\gamma}_{n\mathbf{k}} \hat{\gamma}^{\dagger}_{n\prime\mathbf{k}\prime} \\ &- \left(\theta^{\alpha}_{n\mathbf{k}}(\mathbf{r})\right)^* \hat{l}_z \left(\chi^{\alpha}_{n\prime\mathbf{k}\prime}(\mathbf{r})\right)^* \hat{\gamma}^{\dagger}_{n\mathbf{k}} \hat{\gamma}^{\dagger}_{n\prime\mathbf{k}\prime} - \chi^{\alpha}_{n\mathbf{k}}(\mathbf{r})\, \hat{l}_z\, \theta^{\alpha}_{n\prime\mathbf{k}\prime}(\mathbf{r})\, \hat{\gamma}_{n\mathbf{k}} \hat{\gamma}_{n\prime\mathbf{k}\prime}. \end{aligned} \tag{4.6}$$

The important effect of performing the Bogoliubov-Valatin transformation is that the system of interacting electrons can be rewritten as an equivalent non-interacting quasiparticle basis. In the transformed quasiparticle system, the superconducting gap explicitly separates the states at the Fermi energy, leading to a gapped excitation spectrum.

To compute the total moment, the expectation value of operator (4.6) must be taken. Applying the identities for the quasiparticle operators displayed in equation (2.33), the total orbital moment is found to be

$$\gamma\langle\hat{L}_z\rangle = \gamma \sum_{n,\mathbf{k},\alpha} \int d\mathbf{r} \left(\theta^{\alpha}_{n\mathbf{k}}(\mathbf{r})\right)^* \hat{l}_z\, \theta^{\alpha}_{n\mathbf{k}}(\mathbf{r}) f_{n\mathbf{k}} + \chi^{\alpha}_{n\mathbf{k}}(\mathbf{r})\, \hat{l}_z \left(\chi^{\alpha}_{n\mathbf{k}}(\mathbf{r})\right)^* (1 - f_{n\mathbf{k}}), \tag{4.7}$$

where $f_{n\mathbf{k}}$ is the Fermi factor, as defined in equation (2.34). This equation includes both the electron and hole contributions to the orbital moment, which is essential in the mixed hole/electron state which forms when a gap is induced on the bandstructure.

The hole-dependent contribution to (4.7) can be replaced with its complex conjugate via

$$\begin{aligned}\int d\mathbf{r}\, \chi^{\alpha}_{n\mathbf{k}}(\mathbf{r})\, \hat{l}_z \left(\chi^{\alpha}_{n\mathbf{k}}(\mathbf{r})\right)^* &= \int d\mathbf{r} \left(\chi^{\alpha}_{n\mathbf{k}}(\mathbf{r})\right)^* \hat{l}^*_z\, \chi^{\alpha}_{n\mathbf{k}}(\mathbf{r}) \\ &= \int d\mathbf{r} \left[\chi^{\alpha}_{n\mathbf{k}}(\mathbf{r})\, \hat{l}_z \left(\chi^{\alpha}_{n\mathbf{k}}(\mathbf{r})\right)^*\right]^*, \end{aligned} \tag{4.8}$$

where the first line can be obtained as $\hat{l}_z$ is a Hermitian operator, and thus the integral is a real expectation value. Equation (4.7) can then be written in the more compact form

$$\gamma\langle\hat{L}_z\rangle = \gamma \sum_{n,\mathbf{k},\alpha} \int d\mathbf{r} \left(\boldsymbol{\psi}^{\alpha}_{n\mathbf{k}}(\mathbf{r})\right)^{\dagger} \underline{L_z}\, \boldsymbol{\psi}^{\alpha}_{n\mathbf{k}}(\mathbf{r}), \quad \underline{L_z} = \begin{pmatrix} \hat{l}_z f_{n\mathbf{k}} & 0 \\ 0 & \hat{l}^*_z (1 - f_{n\mathbf{k}}) \end{pmatrix}. \tag{4.9}$$

This equation represents the total orbital moment for a superconducting state in the Bloch representation. However, as discussed in Section 4.1.2, this expression is insufficient for the purpose of evaluating the orbital angular momentum operator as the electron and hole amplitudes are extended Bloch-type wavefunctions. It will be important for further steps in this derivation to emphasise the distinction between single-particle operators (e.g. $\hat{\mathbf{r}}$, $\hat{l}_z$) and particle-hole operators

(such as $\underline{L_z}$). Particle-hole operators have matrix forms and operate on two-component Bogoliubov eigenfunctions, as opposed to single-particle operators which act on single-particle states.

The next step in the derivation is to re-write expression (4.9) in an effective real-space Wannier representation. Due to the invariance of the trace, the sum over the complete basis set $\boldsymbol{\psi}_{n\mathbf{k}}$ can be transformed to any representation defined by a complete basis set of orbitals. The transformation to the Wannier basis is achieved via

$$\boldsymbol{\psi}_{n\mathbf{k}}(\mathbf{r}) = \sum_{\mathbf{R}} \mathrm{e}^{\mathrm{i}\mathbf{k}\cdot\mathbf{R}} \mathbf{W}_{n\mathbf{R}}(\mathbf{r}), \tag{4.10}$$

where $\mathbf{W}_{n\mathbf{R}}$ are the Wannier eigenstates and $\mathbf{R}$ sums over all real-space lattice vectors. The index α has now been temporarily suppressed as the spin projection of the electron and hole wavefunctions plays no part in the subsequent derivation.

At this point, the derivation carried out here diverges significantly from the approach taken to obtain the normal state orbital magnetisation expressions. In this case, the Wannier eigenstates are now two-component vectors, of the form

$$\mathbf{W}_{n\mathbf{R}}(\mathbf{r}) = \begin{pmatrix} \tilde{u}_{n\mathbf{R}}(\mathbf{r}) \\ \tilde{v}_{n\mathbf{R}}(\mathbf{r}) \end{pmatrix} = \Omega \int_{BZ} \frac{d\mathbf{k}}{(2\pi)^3} \, \mathrm{e}^{\mathrm{i}\mathbf{k}\cdot(\mathbf{r}-\mathbf{R})} \begin{pmatrix} u_{n\mathbf{k}}(\mathbf{r}) \\ v_{n\mathbf{k}}(\mathbf{r}) \end{pmatrix}, \tag{4.11}$$

where Ω is the unit cell volume. In the transformed basis, equation (4.7) thus becomes

$$\begin{aligned} \gamma\langle \hat{L}_z \rangle &= \gamma \sum_{n,\mathbf{R}} \int d\mathbf{r} \, \left[\tilde{u}^*_{n\mathbf{R}}(\mathbf{r}) \hat{l}_z \, \tilde{u}_{n\mathbf{R}}(\mathbf{r}) f_{n\mathbf{R}} + \tilde{v}^*_{n\mathbf{R}}(\mathbf{r}) \hat{l}^*_z \, \tilde{v}_{n\mathbf{R}}(\mathbf{r})(1 - f_{n\mathbf{R}}) \right] \\ &= \gamma \sum_{n,\mathbf{R}} \int d\mathbf{r} \, \mathbf{W}^\dagger_{n\mathbf{R}}(\mathbf{r}) \underline{L_z} \mathbf{W}_{n\mathbf{R}}(\mathbf{r}), \end{aligned} \tag{4.12}$$

and it can be observed that the form of equation (4.9) has been retained.

The total moment must now be split into the local and itinerant contributions introduced in ref. [113]. The local contribution can be described as the intrinsic moment carried by each Wannier orbital. It is calculated by evaluating $\langle \hat{\mathbf{r}} \times \hat{\mathbf{v}} \rangle$ for the localised orbitals at each lattice site, and then summing over the lattice. The itinerant component accounts for the interstitial movement of orbitals and can be thought of as the extrinsic moment carried by each Wannier function. This is found by instead evaluating $\langle \hat{\mathbf{r}} \rangle \times \langle \hat{\mathbf{v}} \rangle$ in the surface region of a finite-sized sample.

4.2.2 Local Magnetisation

Henceforth, the discussion will refer the magnetisation rather than the moment, as this is the appropriate quantity for discussion in solids. Each component of the magnetisation is calculated by summing the orbital moment contributions from all unit cells and then dividing by the total sample volume ΩN_c, where Ω is the unit cell volume and N_c is the total number of unit cells.

Ultimately, the aim is to derive expressions which describe fully extended, infinite lattices, but the initial working system is a finite-size sample. To recover the extended lattice, the thermodynamic limit is taken before Fourier transforming to reciprocal space.

The local magnetisation can now be defined formally. First, consider the intrinsic moment of a single unit cell, which is found by taking expression (4.12) and reducing the integral over all position space to one unit cell at lattice position $\mathbf{R}$. Taking the sum over all cells, and then dividing by the total volume, generates the local magnetisation,

$$\begin{aligned}\mathbf{M}_{\mathrm{LC}} = \frac{\gamma m}{\Omega N_c} \sum_{n,\mathbf{R}} \int_{UC} d\mathbf{r} \Big\{ &\tilde{u}^*_{n\mathbf{R}}(\mathbf{r}) [(\hat{\mathbf{r}} - \mathbf{R}) \times \hat{\mathbf{v}}] \, \tilde{u}_{n\mathbf{R}}(\mathbf{r}) f_{n\mathbf{R}} \\ &+ \tilde{v}^*_{n\mathbf{R}}(\mathbf{r}) \left[(\hat{\mathbf{r}} - \mathbf{R}) \times \hat{\mathbf{v}}^*\right] \tilde{v}_{n\mathbf{R}}(\mathbf{r}) (1 - f_{n\mathbf{R}}) \Big\}. \end{aligned} \tag{4.13}$$

The standard definition for the single-particle velocity operator is

$$\hat{\mathbf{v}} = \frac{\hat{\mathbf{p}}}{m} = \frac{\mathrm{i}}{\hbar} [\hat{H}(\mathbf{r}), \hat{\mathbf{r}}] = \frac{\mathrm{i}}{\hbar} [\hat{H}(\mathbf{r}), (\hat{\mathbf{r}} - \mathbf{R})], \tag{4.14}$$

where $\hat{H}(\mathbf{r})$ is the normal state Hamiltonian. Substituting this into (4.13) gives

$$\begin{aligned}\mathbf{M}_{\mathrm{LC}} = \frac{\mathrm{i}\gamma m}{\hbar \Omega N_c} \sum_{n,\mathbf{R}} \int_{UC} d\mathbf{r} \Big\{ &\tilde{u}^*_{n\mathbf{R}}(\mathbf{r}) \left[(\hat{\mathbf{r}} - \mathbf{R}) \times \hat{H}(\mathbf{r}) (\hat{\mathbf{r}} - \mathbf{R})\right] \tilde{u}_{n\mathbf{R}}(\mathbf{r}) f_{n\mathbf{R}} \\ &- \tilde{v}^*_{n\mathbf{R}}(\mathbf{r}) \left[(\hat{\mathbf{r}} - \mathbf{R}) \times \hat{H}^*(\mathbf{r}) (\hat{\mathbf{r}} - \mathbf{R})\right] \tilde{v}_{n\mathbf{R}}(\mathbf{r}) (1 - f_{n\mathbf{R}}) \Big\}, \end{aligned} \tag{4.15}$$

where the second term from the commutator in (4.14) disappears as $(\hat{\mathbf{r}} - \mathbf{R}) \times (\hat{\mathbf{r}} - \mathbf{R}) = 0$. Given that the lattice is invariant with respect to translations by $\mathbf{R}$, the intrinsic moment of all bulk unit cells is identical. As such, the expression can be recreated by evaluating only the moment at the origin $\mathbf{0}$ and then replacing the sum over lattice sites with the multiplicative factor N_c,

$$\begin{aligned}\mathbf{M}_{\mathrm{LC}} = \frac{\mathrm{i}\gamma m}{\hbar \Omega} \sum_{n} \int_{UC} d\mathbf{r} \Big\{ &\tilde{u}^*_{n\mathbf{0}}(\mathbf{r}) \left[\hat{\mathbf{r}} \times \hat{H}(\mathbf{r}) \hat{\mathbf{r}}\right] \tilde{u}_{n\mathbf{0}}(\mathbf{r}) f_{n\mathbf{0}} \\ &- \tilde{v}^*_{n\mathbf{0}}(\mathbf{r}) \left[\hat{\mathbf{r}} \times \hat{H}^*(\mathbf{r}) \hat{\mathbf{r}}\right] \tilde{v}_{n\mathbf{0}}(\mathbf{r}) (1 - f_{n\mathbf{0}}) \Big\}. \end{aligned} \tag{4.16}$$

Equation (4.16) thus represents the local contribution to the orbital magnetisation in the thermodynamic limit, as the expression does not depend on the number of lattice sites.

It is now beneficial to insert the cell-periodic components of the Bloch wavefunction, which are related to the Wannier functions by

$$\begin{pmatrix} u_{n\mathbf{k}}(\mathbf{r}) \\ v_{n\mathbf{k}}(\mathbf{r}) \end{pmatrix} = \mathrm{e}^{-\mathrm{i}\mathbf{k}\cdot\mathbf{r}} \begin{pmatrix} \theta_{n\mathbf{k}}(\mathbf{r}) \\ \chi_{n\mathbf{k}}(\mathbf{r}) \end{pmatrix} = \sum_{\mathbf{R}} \mathrm{e}^{\mathrm{i}\mathbf{k}\cdot(\mathbf{R}-\mathbf{r})} \begin{pmatrix} \tilde{u}_{n\mathbf{R}}(\mathbf{r}) \\ \tilde{v}_{n\mathbf{R}}(\mathbf{r}) \end{pmatrix}. \tag{4.17}$$

This allows the following identities to be used,

$$\begin{pmatrix} \partial_{\mathbf{k}} u_{n\mathbf{k}}(\mathbf{r}) \\ \partial_{\mathbf{k}} v_{n\mathbf{k}}(\mathbf{r}) \end{pmatrix} = -\mathrm{i} \sum_{\mathbf{R}} \mathrm{e}^{\mathrm{i}\mathbf{k}\cdot(\mathbf{R}-\mathbf{r})} (\hat{\mathbf{r}} - \mathbf{R}) \begin{pmatrix} \tilde{u}_{n\mathbf{R}}(\mathbf{r}) \\ \tilde{v}_{n\mathbf{R}}(\mathbf{r}) \end{pmatrix}, \tag{4.18a}$$

$$\hat{H}_{\mathbf{k}}(\mathbf{r}) \begin{pmatrix} \partial_{\mathbf{k}} u_{n\mathbf{k}}(\mathbf{r}) \\ \partial_{\mathbf{k}} v_{n\mathbf{k}}(\mathbf{r}) \end{pmatrix} = -\mathrm{i} \sum_{\mathbf{R}} \mathrm{e}^{\mathrm{i}\mathbf{k}\cdot(\mathbf{R}-\mathbf{r})} \hat{H}(\mathbf{r}) (\hat{\mathbf{r}} - \mathbf{R}) \begin{pmatrix} \tilde{u}_{n\mathbf{R}}(\mathbf{r}) \\ \tilde{v}_{n\mathbf{R}}(\mathbf{r}) \end{pmatrix}, \tag{4.18b}$$

where $\partial_{\mathbf{k}} = \partial/\partial\mathbf{k}$ and $\hat{H}_{\mathbf{k}}(\mathbf{r})$ is the $\mathbf{k}$-dependent Hamiltonian which acts on the cell-periodic components of the Bloch functions ($\hat{H}_{\mathbf{k}}(\mathbf{r}) = \mathrm{e}^{-\mathrm{i}\mathbf{k}\cdot\mathbf{r}} \hat{H}(\mathbf{r}) \mathrm{e}^{\mathrm{i}\mathbf{k}\cdot\mathbf{r}}$).

Using equations (4.18), it is possible to show that (4.15) is equivalent to [114]

$$\begin{aligned} \mathbf{M}_{\mathrm{LC}} = \frac{\mathrm{i}\gamma m}{\hbar} \sum_{n} \int_{BZ} \frac{d\mathbf{k}}{(2\pi)^3} \int_{UC} d\mathbf{r} \Big\{ \Big[\partial_{\mathbf{k}} \big(u_{n\mathbf{k}}(\mathbf{r})\big)^* \times \hat{H}_{\mathbf{k}}(\mathbf{r}) \partial_{\mathbf{k}} u_{n\mathbf{k}}(\mathbf{r}) \Big] f_{n\mathbf{k}} \\ - \Big[\partial_{\mathbf{k}} \big(v_{n\mathbf{k}}(\mathbf{r})\big)^* \times \hat{H}^*_{\mathbf{k}}(\mathbf{r}) \partial_{\mathbf{k}} v_{n\mathbf{k}}(\mathbf{r}) \Big] (1 - f_{n\mathbf{k}}) \Big\}. \end{aligned} \tag{4.19}$$

It is clear that the transformation between equations (4.19) and (4.15) must introduce a factor of $1/(\Omega N_c)$. The factor $1/\Omega$ is cancelled out by the Brillouin zone integral in (4.19), while the $1/N_c$ factor is necessary to normalise the Wannier functions in (4.15).

The expression (4.19) can be written in a more compact form by introducing Dirac notation, making the spin of the wavefunctions and operators implicit,

$$\mathbf{M}_{\mathrm{LC}} = \frac{\gamma m}{\hbar} \mathrm{Im} \left\{ \int_{BZ} \frac{d\mathbf{k}}{(2\pi)^3} \sum_{n} \Big[\langle \partial_{\mathbf{k}} u_{n\mathbf{k}} | \times \hat{H}_{\mathbf{k}} | \partial_{\mathbf{k}} u_{n\mathbf{k}} \rangle f_{n\mathbf{k}} - \langle \partial_{\mathbf{k}} v_{n\mathbf{k}} | \times \hat{H}^*_{\mathbf{k}} | \partial_{\mathbf{k}} v_{n\mathbf{k}} \rangle (1 - f_{n\mathbf{k}}) \Big] \right\}. \tag{4.20}$$

This expression denotes the first major result of this chapter: the local magnetisation in a superconducting state. Comparison with the analogous normal state equation (4.4a) shows that the contribution to the moment arising from the electrons is identical, but an additional hole-dependent term is necessary in order to fully describe a Cooper pair condensate. Equation (4.20) is written in terms of an integration over the Brillouin zone, and contains only Bloch wavefunctions, meaning that it accurately describes an extended periodic system in the thermodynamic limit. All dependence of the expression on the position operator has been removed and so the equation contains only clearly-defined quantum mechanical terms.

4.2.3 Itinerant Magnetisation

The itinerant contribution $\mathbf{M}_{\mathrm{IC}}$ relates to the moment generated by the circulation of Wannier functions. In the absence of external fields, the bulk bands of a crystal carry no net current. If time-reversal symmetry is broken, however, a net flow of current arises on the surface on the sample, leading to the itinerant magnetisation [113]. Intuitively, it can be understood that this extrinsic moment arises from an expectation value of the form $\langle \hat{\mathbf{r}} \rangle \times \langle \hat{\mathbf{v}} \rangle$, where the expectation

values are computed with respect to Wannier functions. Explicitly, the distinction between the local and itinerant contributions can be demonstrated by writing the magnetisation in the form

$$\mathbf{M} = \gamma \sum_{n,\mathbf{R}} \langle (\hat{\mathbf{r}} - \hat{\mathbf{r}}_R) \times \hat{\mathbf{v}} \rangle + \hat{\mathbf{r}}_R \times \langle \hat{\mathbf{v}} \rangle \,. \tag{4.21}$$

where $\hat{\mathbf{r}}_R = \langle \hat{\mathbf{r}} \rangle$. The second part of (4.21) is non-zero only for lattice sites near to the surface. This makes a negligible contribution to the bulk magnetisation in the thermodynamic limit, and so $\mathbf{M}_{\mathrm{LC}}$ is defined by the first part (as shown in equation (4.13)). In contrast, the first part of equation (4.21) is zero near to the surface, so the itinerant magnetisation is defined by the second part.

The quantity $\langle \hat{\mathbf{v}} \rangle$ is described by evaluating velocity matrix elements with respect to the two-component wavefunctions in the particle-hole basis. Following the procedure used to obtain $\underline{L_z}$ (see (4.5)-(4.9)), and inserting identity (4.14), an equivalent particle-hole form of the velocity operator can be obtained,

$$\underline{\mathbf{v}} = \frac{\mathrm{i}}{\hbar} \begin{pmatrix} [\hat{H}(\mathbf{r}), \hat{\mathbf{r}}] f_{n\mathbf{R}} & 0 \\ 0 & -[\hat{H}^*(\mathbf{r}), \hat{\mathbf{r}}](1 - f_{n\mathbf{R}}) \end{pmatrix}. \tag{4.22}$$

Wannier matrix elements evaluated with respect to the velocity operator (4.22) take the form

$$\begin{aligned} \mathbf{W}^{\dagger}_{n\mathbf{R}}(\mathbf{r}) \underline{\mathbf{v}} \mathbf{W}_{n\mathbf{R}}(\mathbf{r}) &= -2\frac{\mathrm{i}}{\hbar} \left\{ \begin{pmatrix} \tilde{u}_{n\mathbf{R}}(\mathbf{r}) \\ \tilde{v}_{n\mathbf{R}}(\mathbf{r}) \end{pmatrix}^{\dagger} \begin{pmatrix} \hat{\mathbf{r}}\hat{H}(\mathbf{r}) f_{n\mathbf{R}} & 0 \\ 0 & -\hat{\mathbf{r}}\hat{H}^*(\mathbf{r})(1 - f_{n\mathbf{R}}) \end{pmatrix} \begin{pmatrix} \tilde{u}_{n\mathbf{R}}(\mathbf{r}) \\ \tilde{v}_{n\mathbf{R}}(\mathbf{r}) \end{pmatrix} \right\} \\ &= -2\frac{\mathrm{i}}{\hbar} \Bigg\{ \sum_{n\prime,\mathbf{R}\prime} \left[\tilde{u}^*_{n\mathbf{R}}(\mathbf{r}) \hat{\mathbf{r}} \tilde{u}_{n\prime\mathbf{R}\prime}(\mathbf{r}) f_{n\mathbf{R}} + \tilde{v}^*_{n\mathbf{R}}(\mathbf{r}) \hat{\mathbf{r}} \tilde{v}_{n\prime\mathbf{R}\prime}(\mathbf{r})(1 - f_{n\mathbf{R}}) \right] \\ &\qquad \times \left[\tilde{u}^*_{n\prime\mathbf{R}\prime}(\mathbf{r}) \hat{H}(\mathbf{r}) \tilde{u}_{n\mathbf{R}}(\mathbf{r}) - \tilde{v}^*_{n\prime\mathbf{R}\prime}(\mathbf{r}) \hat{H}^*(\mathbf{r}) \tilde{v}_{n\mathbf{R}}(\mathbf{r}) \right] \Bigg\}, \end{aligned} \tag{4.23}$$

where a complete Wannier set has been inserted (summed over indices n' and $\mathbf{R}'$) between the operators $\hat{\mathbf{r}}$ and $\hat{H}(\mathbf{r})$ to obtain the second line. The expression can be simplified by introducing the shorthand notation

$$\begin{aligned} v_{\langle n\prime\mathbf{R}\prime, n\mathbf{R}\rangle} &= -2\frac{\mathrm{i}}{\hbar} \Bigg\{ \left(\tilde{u}^*_{n\mathbf{R}}(\mathbf{r}) \hat{\mathbf{r}} \tilde{u}_{n\prime\mathbf{R}\prime}(\mathbf{r}) f_{n\mathbf{R}} + \tilde{v}^*_{n\mathbf{R}}(\mathbf{r}) \hat{\mathbf{r}} \tilde{v}_{n\prime\mathbf{R}\prime}(\mathbf{r})(1 - f_{n\mathbf{R}}) \right) \\ &\qquad \times \left[\tilde{u}^*_{n\prime\mathbf{R}\prime}(\mathbf{r}) \hat{H}(\mathbf{r}) \tilde{u}_{n\mathbf{R}}(\mathbf{r}) - \tilde{v}^*_{n\prime\mathbf{R}\prime}(\mathbf{r}) \hat{H}^*(\mathbf{r}) \tilde{v}_{n\mathbf{R}}(\mathbf{r}) \right] \Bigg\}. \end{aligned} \tag{4.24}$$

This notation has been introduced here in order to draw comparison to the normal state derivation [113, 114], which is drawn upon heavily throughout this subsection.

Initially, a finite-size lattice with dimensions $L_x \times L_y \times L_z$ is considered, before extending the expression to the thermodynamic limit. The focus is placed on a region at the surface of the

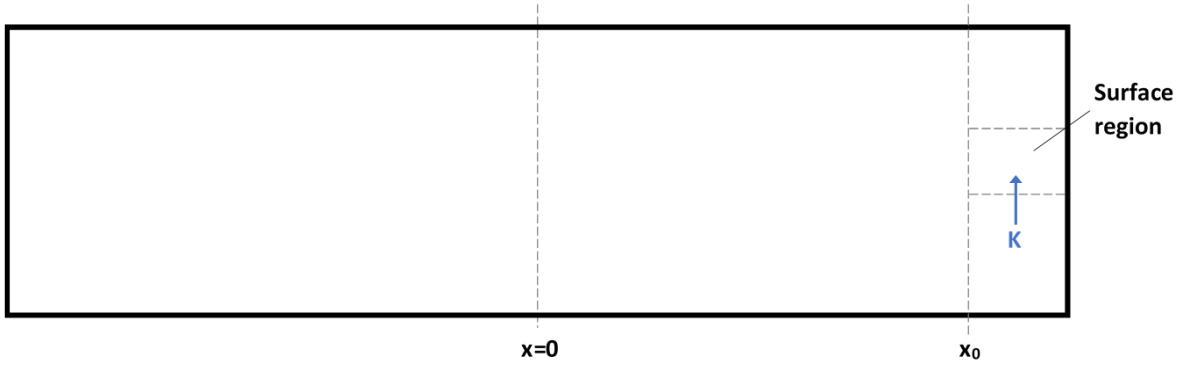

FIGURE 4.2. Shown is the xy-plane of a finite-sized lattice. To determine the itinerant magnetisation in the thermodynamic limit, the current per unit area ($\mathbf{K}$) flowing into a finite region near to the surface of the sample is considered.

sample for x larger than some arbitrary value x_0, which has a surface area in the yz-plane given by the lattice unit cell surface area A (see Fig. 4.2). To derive the orbital moment associated with the itinerant circulation of wavefunctions, it is beneficial to consider the current per unit area flowing through the surface region, which is given by

$$\begin{aligned}\mathbf{K} &= -\frac{e}{A}\sum_{n\prime,\mathbf{R}\prime}{}' \boldsymbol{W}^{\dagger}_{n\prime,\mathbf{R}\prime}(\mathbf{r})\underline{\mathbf{v}}\boldsymbol{W}_{n\prime,\mathbf{R}\prime}(\mathbf{r}) \\ &= -\frac{e}{A}\sum_{n,\mathbf{R}}\sum_{n\prime,\mathbf{R}\prime}{}' \upsilon_{\langle n\mathbf{R},n\prime\mathbf{R}\prime\rangle}\,, \end{aligned} \tag{4.25}$$

where the primed sum refers to the sum over only those Wannier functions within the finite surface region being considered. The second line of equation (4.25) can be interpreted as the current flowing from outside the surface region to inside this region. As a result, the sum over $\mathbf{R}$ is equivalent to the sum over only functions lying outside of the finite surface region as those inside would not contribute to the overall current. The sum limits can therefore be re-written as $R_x < x_0$ and $R'_x > x_0$ respectively.

Exploiting the translational invariance of the lattice, the current donated from some function at an arbitrary lattice position $\mathbf{R}$ to one at $\mathbf{R}'$ is equivalent to the current flowing from the origin to $\mathbf{R}'-\mathbf{R}$, where the origin is taken to be the centre of the lattice. As such, the surface current is equivalent to [113, 114]

$$\mathbf{K} = -\frac{e}{A}\sum_{n,n\prime}\sum_{R_x<x_0}\sum_{R_x\prime>x_0}{}' \upsilon_{\langle n\mathbf{0},n\prime(\mathbf{R}\prime-\mathbf{R})\rangle}\,. \tag{4.26}$$

In the double lattice sum, the total number of terms which correspond to a given displacement of $\mathbf{R}'-\mathbf{R}$ from the origin is $(R'_x-R_x)A/\Omega$ for $R_x<R'_x$, and zero otherwise. The double sum can

therefore be simplified to a single sum over all $\mathbf{R}' - \mathbf{R}$, including the above multiplying factor to account for repeated terms, resulting in

$$\begin{aligned}\mathbf{K} &= -\frac{e}{\Omega}\sum_{\substack{n,n\prime,\\(\mathbf{R}\prime-\mathbf{R})}}(R'_x - R_x)\,v_{\langle n\mathbf{0},n\prime(\mathbf{R}\prime-\mathbf{R})\rangle} \\ &= -\frac{e}{2\Omega}\sum_{n,n\prime,\mathbf{R}} R_x\,v_{\langle n\mathbf{0},n\prime\mathbf{R}\rangle}\,, \end{aligned} \tag{4.27}$$

where the last line has been obtained by relabelling indices. The additional factor of 1/2 has been introduced so that the sum can be extended to all lattice vectors $\mathbf{R}$. This accounts for the inclusion of lattice vectors for which $R_x > R'_x$, which do not contribute to the total current, but is necessary to facilitate the Fourier transform implemented below.

The expression for the surface current can be generalised such that it is valid for any given surface with unit normal vector $\hat{n}$,

$$\begin{aligned}K_\alpha &= -\frac{e}{2\Omega}\sum_\beta\sum_{n,n\prime,\mathbf{R}} R_\beta\,v_{\langle n\mathbf{0},n\prime\mathbf{R}\rangle,\alpha}\,\hat{n}_\beta \\ &= \sum_\beta G_{\alpha\beta}\hat{n}_\beta\,, \end{aligned} \tag{4.28}$$

where α denotes the direction of current flow and the velocity matrix elements have been encoded into a Cartesian tensor quantity $G_{\alpha\beta}$. The notation developed thus far can now be converted into the magnetisation generated by an itinerant current. Taking a surface which extends along the y-direction, with constant x, the total current flowing is $L_yL_zG_{yx}$ (for $x>0$) and $-L_yL_zG_{yx}$ (for $x<0$), with the surfaces separated by the distance L_x. The magnetic moment associated with a current loop is $1/2\oint(\mathbf{r}\times\mathbf{I})\cdot\mathrm{d}\mathbf{l}$, leading to a magnetic moment in the z-direction (m_z) of $L_xL_yL_zG_{yx}/2$.

The equivalent currents in the x-direction for constant y are found by permutation of indices, contributing to m_z via $-L_xL_yL_zG_{xy}/2$. Summing these contributions and converting to magnetisation by dividing by the total volume ($L_xL_yL_z$), the z-component of the itinerant magnetisation is obtained,

$$\begin{aligned}[\mathbf{M}_{\mathrm{IC}}]_{\hat{z}} &= \frac{1}{2}(G_{yx}-G_{xy}) \\ &= -\frac{e}{4\Omega}\left\{\left[\sum_{n,n\prime,\mathbf{R}} R_x\,v_{\langle n\mathbf{0},n\prime\mathbf{R}\rangle,\hat{y}}\right] - \left[\sum_{n,n\prime,\mathbf{R}} R_y\,v_{\langle n\mathbf{0},n\prime\mathbf{R}\rangle,\hat{x}}\right]\right\}. \end{aligned} \tag{4.29}$$

Generalising to three dimensions, the total itinerant magnetisation in terms of Wannier functions is

$$\mathbf{M}_{\mathrm{IC}} = \frac{\gamma m}{2\Omega}\sum_{n,n\prime,\mathbf{R}} \mathbf{R}\times v_{\langle n\mathbf{0},n\prime\mathbf{R}\rangle}\,. \tag{4.30}$$

The final part of the proof is performed in reverse, i.e. the reciprocal-space result is stated and then converted to the Wannier basis to demonstrate that it reproduces the real-space equation (4.30). The final equation written in terms of Bloch functions is [173]

$$\mathbf{M}_{\mathrm{IC}} = \frac{\gamma m}{\hbar}\mathrm{Im}\Bigg\{\int_{BZ}\frac{d\mathbf{k}}{(2\pi)^3}\sum_{n,n\prime}\int d\mathbf{r}\,\epsilon_{nn\prime\mathbf{k}}\Big[\big(\partial_{\mathbf{k}}u_{n\mathbf{k}}(\mathbf{r})\big)^*\times\partial_{\mathbf{k}}u_{n\prime\mathbf{k}}(\mathbf{r})f_{n\mathbf{k}} + \big(\partial_{\mathbf{k}}v_{n\mathbf{k}}(\mathbf{r})\big)^*\times\partial_{\mathbf{k}}v_{n\prime\mathbf{k}}(\mathbf{r})(1-f_{n\mathbf{k}})\Big]\Bigg\}. \tag{4.31}$$

where $\epsilon_{nn\prime\mathbf{k}} = \langle\boldsymbol{\psi}_{n\prime\mathbf{k}}|\underline{H}|\boldsymbol{\psi}_{n\mathbf{k}}\rangle$ and $\underline{H}$ is the BdG Hamiltonian, which takes the general form given by (2.23). Expanding the Bloch wavefunctions in this expectation value in terms of the Wannier basis, the identity

$$\langle\mathbf{W}_{n\prime\mathbf{R}\prime}|\underline{H}|\mathbf{W}_{n\mathbf{R}}\rangle = \frac{\Omega}{(2\pi)^3}\int_{BZ}\mathrm{e}^{\mathrm{i}\mathbf{k}\cdot(\mathbf{R}-\mathbf{R}\prime)}\epsilon_{nn\prime\mathbf{k}}, \tag{4.32}$$

can be obtained. In the Hamiltonian gauge, where $\boldsymbol{\psi}_{n\mathbf{k}}$ are eigenstates of $\underline{H}$, this simplifies to $\epsilon_{nn\prime\mathbf{k}} = \epsilon_{n\mathbf{k}}\delta_{nn\prime}$.

Equation (4.31) can be converted to the Wannier basis by applying (4.18a),

$$\mathbf{M}_{\mathrm{IC}} = \frac{\gamma m}{\hbar}\mathrm{Im}\Bigg\{\sum_{n,n\prime,\mathbf{R},\mathbf{R}\prime}\int_{BZ}\frac{d\mathbf{k}}{(2\pi)^3}\,\epsilon_{nn\prime\mathbf{k}}\,\mathrm{e}^{\mathrm{i}\mathbf{k}\cdot(\mathbf{R}\prime-\mathbf{R})}\int d\mathbf{r}\,\Big[(\mathbf{R}'-\mathbf{R})\times\big(\tilde{u}^*_{n\mathbf{R}}(\mathbf{r})\hat{\mathbf{r}}\,\tilde{u}_{n\prime\mathbf{R}\prime}(\mathbf{r})f_{n\mathbf{R}} + \tilde{v}^*_{n\mathbf{R}}(\mathbf{r})\hat{\mathbf{r}}\,\tilde{v}_{m\mathbf{R}\prime}(\mathbf{r})\big(1-f_{n\mathbf{R}}\big)\big)\Big]\Bigg\}. \tag{4.33}$$

The Brillouin zone integral in (4.33) can now be replaced with (4.32). Applying translational invariance once more ($\mathbf{R}'\to\mathbf{0}$, $\mathbf{R}\to(\mathbf{R}'-\mathbf{R})$) and relabelling indices, it is found that

$$\mathbf{M}_{\mathrm{IC}} = \frac{\gamma m}{\hbar\Omega}\mathrm{Im}\left\{\sum_{n,n\prime,\mathbf{R}}\mathbf{R}\times\Big[\tilde{u}^*_{n\mathbf{R}}(\mathbf{r})\hat{\mathbf{r}}\,\tilde{u}_{n\prime\mathbf{0}}(\mathbf{r})f_{n\mathbf{R}} + \tilde{v}^*_{n\mathbf{R}}(\mathbf{r})\hat{\mathbf{r}}\,\tilde{v}_{n\prime\mathbf{0}}(\mathbf{r})\big(1-f_{n\mathbf{R}}\big)\Big]\langle\mathbf{W}_{n\prime\mathbf{0}}|\mathbf{H}|\mathbf{W}_{n\mathbf{R}}\rangle\right\}. \tag{4.34}$$

Multiplying out the expectation value term above,

$$\begin{aligned}\mathbf{M}_{\mathrm{IC}} &= \frac{\gamma m}{\hbar\Omega}\mathrm{Im}\Bigg\{\sum_{n,n\prime,\mathbf{R}}\mathbf{R}\times\begin{pmatrix}\tilde{u}_{n\mathbf{R}}(\mathbf{r})\\ \tilde{v}_{n\mathbf{R}}(\mathbf{r})\end{pmatrix}^\dagger\begin{pmatrix}\hat{\mathbf{r}}f_{n\mathbf{R}} & 0\\ 0 & \hat{\mathbf{r}}(1-f_{n\mathbf{R}})\end{pmatrix}\begin{pmatrix}\tilde{u}_{n\prime\mathbf{0}}(\mathbf{r})\\ \tilde{v}_{n\prime\mathbf{0}}(\mathbf{r})\end{pmatrix}\\ &\qquad\times\begin{pmatrix}\tilde{u}_{n\mathbf{R}}(\mathbf{r})\\ \tilde{v}_{n\mathbf{R}}(\mathbf{r})\end{pmatrix}^\dagger\begin{pmatrix}\hat{H}(\mathbf{r}) & \Delta_{nn\prime}(\mathbf{r})\\ \Delta^*_{n\prime n}(\mathbf{r}) & -\hat{H}^*(\mathbf{r})\end{pmatrix}\begin{pmatrix}\tilde{u}_{n\prime\mathbf{0}}(\mathbf{r})\\ \tilde{v}_{n\prime\mathbf{0}}(\mathbf{r})\end{pmatrix}\Bigg\}\\ &= \frac{\gamma m}{2\Omega}\sum_{n,n\prime,\mathbf{R}}\mathbf{R}\times\Bigg\{v_{\langle m\mathbf{0},n\mathbf{R}\rangle} + \frac{2}{\hbar}\mathrm{Im}\Big[\big(\tilde{u}^*_{n\mathbf{R}}(\mathbf{r})\hat{\mathbf{r}}\,\tilde{u}_{n\prime\mathbf{0}}(\mathbf{r})f_{n\mathbf{R}} + \tilde{v}^*_{n\mathbf{R}}(\mathbf{r})\hat{\mathbf{r}}\,\tilde{v}_{n\prime\mathbf{0}}(\mathbf{r})(1-f_{n\mathbf{R}})\big)\\ &\qquad\times\big(\tilde{u}^*_{n\mathbf{R}}(\mathbf{r})\Delta_{nn\prime}(\mathbf{r})\tilde{v}_{n\prime\mathbf{0}}(\mathbf{r}) + \tilde{v}^*_{n\mathbf{R}}(\mathbf{r})\Delta^*_{n\prime n}(\mathbf{r})\tilde{u}_{n\prime\mathbf{0}}(\mathbf{r})\big)\Big]\Bigg\}.\end{aligned} \tag{4.35}$$

The final part of the proof is to demonstrate that the term in square brackets in equation (4.35) cancels to zero, such that the **k**-space result is equivalent to the real-space expression (4.30). Firstly, extracting the sum in the square brackets from (4.35), ignoring the multiplicative constants, and multiplying out the brackets gives

$$\begin{aligned}\sum_{n,n\prime,\mathbf{R}} \mathrm{Im}\Big\{&\big[\tilde{u}^*_{n\mathbf{R}}(\mathbf{r})\hat{\mathbf{r}}\,\tilde{u}_{n\prime\mathbf{0}}(\mathbf{r})f_{n\mathbf{R}}\big]\big[\tilde{u}^*_{n\mathbf{R}}(\mathbf{r})\Delta_{nn\prime}(\mathbf{r})\tilde{v}_{n\prime\mathbf{0}}(\mathbf{r})\big] + \big[\tilde{u}^*_{n\mathbf{R}}(\mathbf{r})\hat{\mathbf{r}}\,\tilde{u}_{n\prime\mathbf{0}}(\mathbf{r})f_{n\mathbf{R}}\big]\big[\tilde{v}^*_{n\mathbf{R}}(\mathbf{r})\Delta^*_{n\prime n}(\mathbf{r})\tilde{u}_{n\prime\mathbf{0}}(\mathbf{r})\big] \\ &+ \big[\tilde{v}^*_{n\mathbf{R}}(\mathbf{r})\hat{\mathbf{r}}\,\tilde{v}_{n\prime\mathbf{0}}(\mathbf{r})(1-f_{n\mathbf{R}})\big]\big[\tilde{u}^*_{n\mathbf{R}}(\mathbf{r})\Delta_{nn\prime}(\mathbf{r})\tilde{v}_{n\prime\mathbf{0}}(\mathbf{r})\big] \\ &+ \big[\tilde{v}^*_{n\mathbf{R}}(\mathbf{r})\hat{\mathbf{r}}\,\tilde{v}_{n\prime\mathbf{0}}(\mathbf{r})(1-f_{n\mathbf{R}})\big]\big[\tilde{v}^*_{n\mathbf{R}}(\mathbf{r})\Delta^*_{n\prime n}(\mathbf{r})\tilde{u}_{n\prime\mathbf{0}}(\mathbf{r})\big]\Big\}. \end{aligned} \tag{4.36}$$

Each of the terms in square brackets in (4.36) is a complex value. To simplify the sum, the identity

$$\mathrm{Im}\left[z_1 z_2\right] = \mathrm{Im}\left[z_1\right]\mathrm{Re}\left[z_2\right] + \mathrm{Re}\left[z_1\right]\mathrm{Im}\left[z_2\right], \tag{4.37}$$

can be applied. Expression (4.36) then becomes

$$\begin{aligned}&\sum_{n,n\prime,\mathbf{R}} \Big\{\mathrm{Im}\big[\tilde{u}^*_{n\mathbf{R}}(\mathbf{r})\hat{\mathbf{r}}\,\tilde{u}_{n\prime\mathbf{0}}(\mathbf{r})f_{n\mathbf{R}}\big]\mathrm{Re}\big[\tilde{u}^*_{n\mathbf{R}}(\mathbf{r})\Delta_{nn\prime}(\mathbf{r})\tilde{v}_{n\prime\mathbf{0}}(\mathbf{r})\big] \\ &\qquad +\mathrm{Im}\big[\tilde{u}^*_{n\mathbf{R}}(\mathbf{r})\hat{\mathbf{r}}\,\tilde{u}_{n\prime\mathbf{0}}(\mathbf{r})f_{n\mathbf{R}}\big]\mathrm{Re}\big[\tilde{v}^*_{n\mathbf{R}}(\mathbf{r})\Delta^*_{n\prime n}(\mathbf{r})\tilde{u}_{n\prime\mathbf{0}}(\mathbf{r})\big]\Big\} \\ &+\sum_{n,n\prime,\mathbf{R}} \Big\{\mathrm{Re}\big[\tilde{u}^*_{n\mathbf{R}}(\mathbf{r})\hat{\mathbf{r}}\,\tilde{u}_{n\prime\mathbf{0}}(\mathbf{r})f_{n\mathbf{R}}\big]\mathrm{Im}\big[\tilde{u}^*_{n\mathbf{R}}(\mathbf{r})\Delta_{nn\prime}(\mathbf{r})\tilde{v}_{n\prime\mathbf{0}}(\mathbf{r})\big] \\ &\qquad +\mathrm{Re}\big[\tilde{u}^*_{n\mathbf{R}}(\mathbf{r})\hat{\mathbf{r}}\,\tilde{u}_{n\prime\mathbf{0}}(\mathbf{r})f_{n\mathbf{R}}\big]\mathrm{Im}\big[\tilde{v}^*_{n\mathbf{R}}(\mathbf{r})\Delta^*_{n\prime n}(\mathbf{r})\tilde{u}_{n\prime\mathbf{0}}(\mathbf{r})\big]\Big\} \\ &+\sum_{n,n\prime,\mathbf{R}} \Big\{\mathrm{Im}\big[\tilde{v}^*_{n\mathbf{R}}(\mathbf{r})\hat{\mathbf{r}}\,\tilde{v}_{n\prime\mathbf{0}}(\mathbf{r})(1-f_{n\mathbf{R}})\big]\mathrm{Re}\big[\tilde{u}^*_{n\mathbf{R}}(\mathbf{r})\Delta_{nn\prime}(\mathbf{r})\tilde{v}_{n\prime\mathbf{0}}(\mathbf{r})\big] \\ &\qquad +\mathrm{Im}\big[\tilde{v}^*_{n\mathbf{R}}(\mathbf{r})\hat{\mathbf{r}}\,\tilde{v}_{n\prime\mathbf{0}}(\mathbf{r})(1-f_{n\mathbf{R}})\big]\mathrm{Re}\big[\tilde{v}^*_{n\mathbf{R}}(\mathbf{r})\Delta^*_{n\prime n}(\mathbf{r})\tilde{u}_{n\prime\mathbf{0}}(\mathbf{r})\big]\Big\} \\ &+\sum_{n,n\prime,\mathbf{R}} \Big\{\mathrm{Re}\big[\tilde{v}^*_{n\mathbf{R}}(\mathbf{r})\hat{\mathbf{r}}\,\tilde{v}_{n\prime\mathbf{0}}(\mathbf{r})(1-f_{n\mathbf{R}})\big]\mathrm{Im}\big[\tilde{u}^*_{n\mathbf{R}}(\mathbf{r})\Delta_{nn\prime}(\mathbf{r})\tilde{v}_{n\prime\mathbf{0}}(\mathbf{r})\big] \\ &\qquad +\mathrm{Re}\big[\tilde{v}^*_{n\mathbf{R}}(\mathbf{r})\hat{\mathbf{r}}\,\tilde{v}_{n\prime\mathbf{0}}(\mathbf{r})(1-f_{n\mathbf{R}})\big]\mathrm{Im}\big[\tilde{v}^*_{n\mathbf{R}}(\mathbf{r})\Delta^*_{n\prime n}(\mathbf{r})\tilde{u}_{n\prime\mathbf{0}}(\mathbf{r})\big]\Big\}. \end{aligned} \tag{4.38}$$

The next step is to use the identities

$$\mathrm{Im}\left[z_1\right] = -\mathrm{Im}\left[z_1^*\right], \quad \mathrm{Re}\left[z_1\right] = \mathrm{Re}\left[z_1^*\right]. \tag{4.39}$$

Taking the first sum in (4.38), and applying (4.39) results in

$$
\begin{aligned}
&\sum_{n,n\prime,\mathbf{R}} \Big\{ \mathrm{Im}\big[\tilde{u}^*_{n\mathbf{R}}(\mathbf{r})\hat{\mathbf{r}}\,\tilde{u}_{n\prime\mathbf{0}}(\mathbf{r}) f_{n\mathbf{R}}\big] \mathrm{Re}\big[\tilde{u}^*_{n\mathbf{R}}(\mathbf{r})\Delta_{nn\prime}(\mathbf{r})\tilde{v}_{n\prime\mathbf{0}}(\mathbf{r})\big] \Big\} \\
&+ \sum_{n,n\prime,\mathbf{R}} \Big\{ \mathrm{Im}\big[\tilde{u}^*_{n\mathbf{R}}(\mathbf{r})\hat{\mathbf{r}}\,\tilde{u}_{n\prime\mathbf{0}}(\mathbf{r}) f_{n\mathbf{R}}\big] \mathrm{Re}\big[\tilde{v}^*_{n\mathbf{R}}(\mathbf{r})\Delta^*_{n\prime n}(\mathbf{r})\tilde{u}_{n\prime\mathbf{0}}(\mathbf{r})\big] \Big\} \\
&= \sum_{n,n\prime,\mathbf{R}} \Big\{ \mathrm{Im}\big[\tilde{u}^*_{n\mathbf{R}}(\mathbf{r})\hat{\mathbf{r}}\,\tilde{u}_{n\prime\mathbf{0}}(\mathbf{r}) f_{n\mathbf{R}}\big] \mathrm{Re}\big[\tilde{u}^*_{n\mathbf{R}}(\mathbf{r})\Delta_{nn\prime}(\mathbf{r})\tilde{v}_{n\prime\mathbf{0}}(\mathbf{r})\big] \Big\} \\
&- \sum_{n,n\prime,\mathbf{R}} \Big\{ \mathrm{Im}\big[\tilde{u}^*_{n\prime\mathbf{0}}(\mathbf{r})\hat{\mathbf{r}}\,\tilde{u}_{n\mathbf{R}}(\mathbf{r}) f_{n\mathbf{R}}\big] \mathrm{Re}\big[\tilde{u}^*_{n\prime\mathbf{0}}(\mathbf{r})\Delta_{n\prime n}(\mathbf{r})\tilde{v}_{n\mathbf{R}}(\mathbf{r})\big] \Big\} . \qquad (4.40)
\end{aligned}
$$

By relabelling indices and utilising translational invariance in the last line of (4.40), the two sums can be shown to be identical and thus cancel. The remaining sums in (4.38) can be cancelled through the same procedure, and thus the real and reciprocal-space expressions for the itinerant magnetisation are identical as required.

The conversion of the normal state formalism for the orbital magnetisation in a periodic lattice to the particle-hole basis of a superconductor has now been completed, for both the local and itinerant components. The complete set of equations for the total orbital magnetisation in a superconductor are

$$
\mathbf{M}_{\mathrm{LC}} = \frac{\gamma m}{\hbar}\mathrm{Im}\left\{ \int_{BZ} \frac{d\mathbf{k}}{(2\pi)^3} \sum_n \Big[\langle \partial_{\mathbf{k}} u_{n\mathbf{k}}| \times \hat{H}_{\mathbf{k}} |\partial_{\mathbf{k}} u_{n\mathbf{k}}\rangle f_{n\mathbf{k}} - \langle \partial_{\mathbf{k}} v_{n\mathbf{k}}| \times \hat{H}^*_{\mathbf{k}} |\partial_{\mathbf{k}} v_{n\mathbf{k}}\rangle (1 - f_{n\mathbf{k}}) \Big] \right\} , \qquad (4.41a)
$$

$$
\mathbf{M}_{\mathrm{IC}} = \frac{\gamma m}{\hbar}\mathrm{Im}\left\{ \int_{BZ} \frac{d\mathbf{k}}{(2\pi)^3} \sum_n \epsilon_{n\mathbf{k}} \Big[\langle \partial_{\mathbf{k}} u_{n\mathbf{k}}| \times |\partial_{\mathbf{k}} u_{n\mathbf{k}}\rangle f_{n\mathbf{k}} + \langle \partial_{\mathbf{k}} v_{n\mathbf{k}}| \times |\partial_{\mathbf{k}} v_{n\mathbf{k}}\rangle (1 - f_{n\mathbf{k}}) \Big] \right\} , \qquad (4.41b)
$$

$$
\mathbf{M} = \mathbf{M}_{\mathrm{LC}} + \mathbf{M}_{\mathrm{IC}} . \qquad (4.41c)
$$

The final form of $\mathbf{M}_{\mathrm{IC}}$ has been obtained by again introducing Dirac notation, and by taking the Hamiltonian gauge. Both contributions derived for the superconducting state incur an additional hole-dependent term. Note that in the itinerant component, however, the hole term is now added rather than subtracted, as the conjugate of the complex Hamiltonian has been replaced with a real expectation value.

4.2.4 Tight-Binding Expansion and On-Site Contribution

The orbital magnetisation formalism developed in this chapter is not currently written in a basis which is consistent with the tight-binding models of Sr_2RuO_4 presented in Chapter 3. In order to perform practical computations, the Bloch wavefunctions in the reciprocal-space expressions (4.41) of the magnetisation must be recast into the tight-binding representation. The general

expansion of the particle-hole Bloch wavefunction in the orbital basis given by equation (3.22) is used again here.

Beginning with the expression for $\mathbf{M}_{\mathrm{IC}}$ (4.41b), the equation must be re-written in terms of the solutions to the tight-binging Bogoliubov-de Gennes equation (3.23). Focussing initially on the electron component, the $\mathbf{k}$-derivative required to compute (4.41b) is expanded as

$$\partial_{\mathbf{k}} u_{n\mathbf{k}}(\mathbf{r}) = \mathrm{e}^{-\mathrm{i}\mathbf{k}\cdot\mathbf{r}}\left[\partial_{\mathbf{k}}\theta_{n\mathbf{k}}(\mathbf{r}) - \mathrm{i}\mathbf{r}\theta_{n\mathbf{k}}(\mathbf{r})\right]. \tag{4.42}$$

The vector products in (4.41b) then take the form

$$\begin{aligned}\langle\partial_{\mathbf{k}} u_{n\mathbf{k}}| \times |\partial_{\mathbf{k}} u_{n\mathbf{k}}\rangle =& \langle\theta_{n\mathbf{k}}|\hat{\mathbf{r}}\times\hat{\mathbf{r}}|\theta_{n\mathbf{k}}\rangle + \langle\partial_{\mathbf{k}}\theta_{n\mathbf{k}}| \times |\partial_{\mathbf{k}}\theta_{n\mathbf{k}}\rangle \\ &+ \mathrm{i}\left(\langle\theta_{n\mathbf{k}}|\hat{\mathbf{r}}\times|\partial_{\mathbf{k}}\theta_{n\mathbf{k}}\rangle - \langle\partial_{\mathbf{k}}\theta_{n\mathbf{k}}|\times\hat{\mathbf{r}}|\theta_{n\mathbf{k}}\rangle\right).\end{aligned} \tag{4.43}$$

The first term from the right hand side of (4.43) disappears simply as $\mathbf{r}\times\mathbf{r} = 0$, while the third term also vanishes, leaving only a finite contribution from the second term.

Tight-binding solutions can be substituted into the Brillouin zone integral by taking the partial derivative of (3.22), giving

$$\partial_{\mathbf{k}}\theta_{n\mathbf{k}}(\mathbf{r}) = \sum_{i,j}\mathrm{e}^{\mathrm{i}\mathbf{k}\cdot\mathbf{R}_i}\phi_j(\mathbf{r}-\mathbf{R}_i)\left[\mathrm{i}\mathbf{R}_i u_{nj}(\mathbf{k}) + \partial_{\mathbf{k}} u_{nj}(\mathbf{k})\right]. \tag{4.44}$$

where the index j has been re-introduced to denote the sum over both the orbital character (d) and the spin projection (α) of the orbital wavefunctions. Substituting (4.44) into (4.43) yields

$$\begin{aligned}\langle\partial_{\mathbf{k}} u_{n\mathbf{k}}| \times |\partial_{\mathbf{k}} u_{n\mathbf{k}}\rangle &= \langle\partial_{\mathbf{k}}\theta_{n\mathbf{k}}| \times |\partial_{\mathbf{k}}\theta_{n\mathbf{k}}\rangle \\ &= \sum_{i,i',j,j'}\mathrm{e}^{\mathrm{i}\mathbf{k}\cdot(\mathbf{R}_i-\mathbf{R}'_i)}\left\{\int_{UC} d\mathbf{r}\,\phi^*_{j'}(\mathbf{r}-\mathbf{R}'_i)\phi_j(\mathbf{r}-\mathbf{R}_i)\right\} \\ &\quad\times\left\{(u_{nj'}(\mathbf{k}))^*\left[\mathbf{R}_i\times\mathbf{R}'_i\right]u_{nj}(\mathbf{k}) + \left[(\partial_{\mathbf{k}}u_{nj'}(\mathbf{k}))^*\times\partial_{\mathbf{k}}u_{nj}(\mathbf{k})\right]\right. \\ &\quad\left.+\,\mathrm{i}\left[\left((\partial_{\mathbf{k}}u_{nj'}(\mathbf{k}))^*\times\mathbf{R}_i u_{nj}(\mathbf{k})\right) - \left((u_{nj'}(\mathbf{k}))^*\mathbf{R}_i\times\partial_{\mathbf{k}}u_{nj}(\mathbf{k})\right)\right]\right\}.\end{aligned} \tag{4.45}$$

The condition that neighbouring basis functions do not overlap (given in equation (2.2)) is applied, simplifying equation (4.45) to

$$\begin{aligned}\langle\partial_{\mathbf{k}} u_{n\mathbf{k}}| \times |\partial_{\mathbf{k}} u_{n\mathbf{k}}\rangle = \sum_{i,j}&\left\{u^*_{nj}(\mathbf{k})\left[\mathbf{R}_i\times\mathbf{R}_i\right]u_{nj}(\mathbf{k}) + \left[\partial_{\mathbf{k}}u^*_{nj}(\mathbf{k})\times\partial_{\mathbf{k}}u_{nj}(\mathbf{k})\right]\right. \\ &\left.+\,\mathrm{i}\left[\left(\partial_{\mathbf{k}}u^*_{nj}(\mathbf{k})\times\mathbf{R}_i u_{nj}(\mathbf{k})\right) - \left(u^*_{nj}(\mathbf{k})\mathbf{R}_i\times\partial_{\mathbf{k}}u_{nj}(\mathbf{k})\right)\right]\right\}.\end{aligned} \tag{4.46}$$

As was the case with equation (4.43), the first and third terms on the right hand side of (4.46) vanish. Inserting this result, and the equivalent expansion of $|\chi_{n\mathbf{k}}\rangle$, into (4.41b) gives the final expression for the itinerant magnetisation in the tight-binding basis,

$$\mathbf{M}_{\mathrm{IC}} = \frac{\gamma m}{\hbar}\mathrm{Im}\Big\{\sum_{n,j}\int_{BZ}\frac{d\mathbf{k}}{(2\pi)^3}\,\epsilon_n(\mathbf{k})\Big[\partial_{\mathbf{k}}u^*_{nj}(\mathbf{k})\times\partial_{\mathbf{k}}u_{nj}(\mathbf{k})f_{n\mathbf{k}} + \partial_{\mathbf{k}}v^*_{nj}(\mathbf{k})\times\partial_{\mathbf{k}}v_{nj}(\mathbf{k})(1-f_{n\mathbf{k}})\Big]\Big\}. \tag{4.47}$$

To transform the $\mathbf{M}_{\mathrm{LC}}$ component (4.41a), the expansion performed in (4.43) must be applied to the term $\langle\partial_{\mathbf{k}}u_{n\mathbf{k}}|\times\hat{H}_{\mathbf{k}}|\partial_{\mathbf{k}}u_{n\mathbf{k}}\rangle$. The equivalent expansion results in

$$\langle\partial_{\mathbf{k}}u_{n\mathbf{k}}|\times\hat{H}_{\mathbf{k}}|\partial_{\mathbf{k}}u_{n\mathbf{k}}\rangle = \mathrm{e}^{\mathrm{i}\mathbf{k}\cdot\mathbf{r}}\Big\{\langle\theta_{n\mathbf{k}}|\hat{\mathbf{r}}\times\hat{H}_{\mathbf{k}}\hat{\mathbf{r}}|\theta_{n\mathbf{k}}\rangle + \langle\partial_{\mathbf{k}}\theta_{n\mathbf{k}}|\times\hat{H}_{\mathbf{k}}|\partial_{\mathbf{k}}\theta_{n\mathbf{k}}\rangle + \mathrm{i}\big(\langle\theta_{n\mathbf{k}}|\hat{\mathbf{r}}\hat{H}_{\mathbf{k}}\times|\partial_{\mathbf{k}}\theta_{n\mathbf{k}}\rangle - \langle\partial_{\mathbf{k}}\theta_{n\mathbf{k}}|\times\hat{H}_{\mathbf{k}}\hat{\mathbf{r}}|\theta_{n\mathbf{k}}\rangle\big)\Big\}\mathrm{e}^{-\mathrm{i}\mathbf{k}\cdot\mathbf{r}}. \tag{4.48}$$

Taking the second term in (4.48) and following the same procedure as (4.42)-(4.46), it is found that

$$\mathrm{e}^{\mathrm{i}\mathbf{k}\cdot\mathbf{r}}\langle\partial_{\mathbf{k}}\theta_{n\mathbf{k}}|\times\hat{H}_{\mathbf{k}}|\partial_{\mathbf{k}}\theta_{n\mathbf{k}}\rangle\mathrm{e}^{-\mathrm{i}\mathbf{k}\cdot\mathbf{r}} = \sum_{j,j\prime}\partial_{\mathbf{k}}u^*_{nj\prime}(\mathbf{k})\times\Big[\sum_{i,i\prime}\mathrm{e}^{\mathrm{i}\mathbf{k}\cdot(\mathbf{R}_i-\mathbf{R}'_i)}\int_{UC}d\mathbf{r}\;\phi^*_{j\prime}(\mathbf{r}-\mathbf{R}'_i)\hat{H}(\mathbf{r})\phi_j(\mathbf{r}-\mathbf{R}_i)\Big]\partial_{\mathbf{k}}u_{nj}(\mathbf{k}). \tag{4.49}$$

The term in the square brackets above reduces to the matrix element of the normal state tight-binding Hamiltonian (3.24). Thus, a first local contribution to the magnetisation can be written in the tight-binding basis as

$$\mathbf{M}^{(1)}_{\mathrm{LC}} = \frac{\gamma m}{\hbar}\mathrm{Im}\Big\{\sum_{n,j,j\prime}\int_{BZ}\frac{d\mathbf{k}}{(2\pi)^3}\Big[\partial_{\mathbf{k}}u^*_{nj\prime}(\mathbf{k})\times H_{jj\prime}(\mathbf{k})\partial_{\mathbf{k}}u_{nj}(\mathbf{k})f_{n\mathbf{k}} - \partial_{\mathbf{k}}v^*_{nj\prime}(\mathbf{k})\times H^*_{jj\prime}(\mathbf{k})\partial_{\mathbf{k}}v_{nj}(\mathbf{k})(1-f_{n\mathbf{k}})\Big]\Big\}. \tag{4.50}$$

Again, the third component in (4.48) vanishes. However, the first term is non-zero and takes the form

$$\begin{aligned}\mathrm{e}^{\mathrm{i}\mathbf{k}\cdot\mathbf{r}}\langle\theta_{n\mathbf{k}}|\hat{\mathbf{r}}\times\hat{H}_{\mathbf{k}}\hat{\mathbf{r}}|\theta_{n\mathbf{k}}\rangle\mathrm{e}^{-\mathrm{i}\mathbf{k}\cdot\mathbf{r}} &= \langle\theta_{n\mathbf{k}}|\hat{\mathbf{r}}\times\hat{H}\hat{\mathbf{r}}|\theta_{n\mathbf{k}}\rangle \\ &= \int_{UC}d\mathbf{r}\sum_{i,i\prime,j,j\prime}\mathrm{e}^{\mathrm{i}\mathbf{k}\cdot(\mathbf{R}_i-\mathbf{R}'_i)}\times \\ &\qquad \phi^*_{j\prime}(\mathbf{r}-\mathbf{R}'_i)u^*_{nj\prime}(\mathbf{k})\left[\hat{\mathbf{r}}\times\hat{H}(\mathbf{r})\hat{\mathbf{r}}\right]u_{nj}(\mathbf{k})\phi_j(\mathbf{r}-\mathbf{R}_i).\end{aligned} \tag{4.51}$$

Using identity (4.14), it can be shown that

$$\hat{\mathbf{r}} \times \hat{H}(\mathbf{r})\hat{\mathbf{r}} = -\mathrm{i}\hbar(\hat{\mathbf{r}} \times \hat{\mathbf{v}}) = -\frac{\mathrm{i}\hbar}{m}\hat{\mathbf{l}}, \tag{4.52}$$

as can be seen in equation (4.16). Substituting (4.52) into (4.51), the final local contribution is generated by the integral

$$\langle \theta_{n\mathbf{k}} | \hat{\mathbf{r}} \times \hat{H}\hat{\mathbf{r}} | \theta_{n\mathbf{k}} \rangle = -\frac{\mathrm{i}\hbar}{m} \int_{UC} d\mathbf{r} \sum_{n,i,i',j,j'} \mathrm{e}^{\mathrm{i}\mathbf{k}\cdot(\mathbf{R}_i - \mathbf{R}'_i)} \phi^*_{j'}(\mathbf{r} - \mathbf{R}'_i) u^*_{nj'}(\mathbf{k}) \hat{\mathbf{l}} u_{nj}(\mathbf{k}) \phi_j(\mathbf{r} - \mathbf{R}_i). \tag{4.53}$$

The angular momentum operator acts on the $\mathbf{r}$-dependent orbital wavefunctions, but not the $\mathbf{k}$-dependent BdG amplitudes $u_{nj}(\mathbf{k})$ and $v_{nj}(\mathbf{k})$. An exact form of component (4.53) thus relies on the specific orbital basis of the working model. The magnetisation associated with this expansion can be written in the general form

$$\mathbf{M}^{(2)}_{\mathrm{LC}} = \gamma \mathrm{Re}\left[\sum_{n,j,j'} \int_{BZ} \frac{d\mathbf{k}}{(2\pi)^3} u^*_{nj'}(\mathbf{k}) l_{jj'} u_{nj}(\mathbf{k}) f_{n\mathbf{k}} + v^*_{nj'}(\mathbf{k}) l^*_{jj'} v_{nj}(\mathbf{k})(1 - f_{n\mathbf{k}}) \right], \tag{4.54}$$

where the terms $l_{jj'}$ refer to the matrix elements obtained by evaluating the orbital angular momentum operator with respect to the orbital wavefunctions,

$$l_{jj'} = \int \mathrm{d}\mathbf{r}\, \phi^*_j(\mathbf{r}) \hat{l}_z \phi_{j'}(\mathbf{r}). \tag{4.55}$$

Condition (2.2) has again been applied to obtain (4.55). Equation (4.54) is a purely on-site contribution to the magnetic moment, meaning it is dependent only on the composition of the atomic basis of the lattice. It is equivalent to that derived previously in ref. [160].

Equation (4.54) represents the final result of this section. A fully generalised set of equations to compute the orbital magnetisation in a superconductor or superfluid has been derived, and is broken down as

$$\mathbf{M} = \mathbf{M}^{(1)}_{\mathrm{LC}} + \mathbf{M}^{(2)}_{\mathrm{LC}} + \mathbf{M}_{\mathrm{IC}}. \tag{4.56}$$

All three contributions have also been converted to the tight-binding basis for ease of computation. In the next section, the results obtained by evaluating these expressions with respect to the self-consistent solutions of the models for Sr_2RuO_4 are presented.

4.3 Model Calculations

Equations (4.47) and (4.50) were evaluated by inserting the self-consistent solutions to the BdG equation obtained for the p-wave models of Sr_2RuO_4. In order to perform these calculations, a method to determine the $\mathbf{k}$-derivatives of the eigenfunctions was required. These functions can be written in terms of the $\mathbf{k}$-dependent Hamiltonian, in a process which is particularly convenient for use in tight-binding computations as it requires a sum over only the band index, rather than any numerical differentiation. This relation is well-established for normal state eigenfunctions [234, 235], but it is important to verify here that this process remains valid for a superconducting Hamiltonian.

Firstly, the expectation value for the BdG Hamiltonian is taken with respect to two unequal eigenstates. In the Hamiltonian gauge, this produces a null result. Taking the derivative of this and applying the product rule,

$$\begin{aligned} 0 &= \nabla_{\mathbf{k}} \langle \boldsymbol{\psi}_{n\prime\mathbf{k}} | \underline{H} | \boldsymbol{\psi}_{n\mathbf{k}} \rangle \\ 0 &= \epsilon_{n\mathbf{k}} \langle \nabla_{\mathbf{k}} \boldsymbol{\psi}_{n\prime\mathbf{k}} | \boldsymbol{\psi}_{n\mathbf{k}} \rangle + \epsilon_{n\prime\mathbf{k}} \langle \boldsymbol{\psi}_{n\prime\mathbf{k}} | \nabla_{\mathbf{k}} \boldsymbol{\psi}_{n\mathbf{k}} \rangle + \langle \boldsymbol{\psi}_{n\prime\mathbf{k}} | \nabla_{\mathbf{k}} \underline{H} | \boldsymbol{\psi}_{n\mathbf{k}} \rangle \,. \end{aligned} \tag{4.57}$$

It should be noted that the components of the particle-hole wavefunctions $u_{n\mathbf{k}}$ and $v_{n\mathbf{k}}$ do not individually denote complete sets of eigenstates. However, the two-component solutions of the BdG equation do form a complete, normalised set, meaning that $\sum_n |\boldsymbol{\psi}_{n\mathbf{k}}\rangle\langle\boldsymbol{\psi}_{n\mathbf{k}}| = \hat{I}$ [26]. This completeness relation can be applied to (4.57) to isolate the derivatives of the eigenstates, resulting in

$$\begin{aligned} (\epsilon_{n\mathbf{k}} - \epsilon_{n\prime\mathbf{k}}) \langle \boldsymbol{\psi}_{n\prime\mathbf{k}} | \nabla_{\mathbf{k}} \boldsymbol{\psi}_{n\mathbf{k}} \rangle &= \langle \boldsymbol{\psi}_{n\prime\mathbf{k}} | \nabla_{\mathbf{k}} \underline{H} | \boldsymbol{\psi}_{n\mathbf{k}} \rangle \\ |\nabla_{\mathbf{k}} \boldsymbol{\psi}_{n\mathbf{k}} \rangle &= \sum_{n\prime \neq n} |\boldsymbol{\psi}_{n\prime\mathbf{k}}\rangle \frac{\langle \boldsymbol{\psi}_{n\prime\mathbf{k}} | \nabla_{\mathbf{k}} \underline{H} | \boldsymbol{\psi}_{n\mathbf{k}} \rangle}{\epsilon_{n\mathbf{k}} - \epsilon_{n\prime\mathbf{k}}} \\ &= \begin{pmatrix} |\nabla_{\mathbf{k}} u_{n\mathbf{k}} \rangle \\ |\nabla_{\mathbf{k}} v_{n\mathbf{k}} \rangle \end{pmatrix} . \end{aligned} \tag{4.58}$$

The derivative of $\underline{H}$ with respect to $\mathbf{k}$ is determined by hand for the two models, using the explicit matrix elements written in Chapter 3 for the normal state Hamiltonians and the gap functions. The right-hand side of equation (4.58) is then evaluated with respect to the eigenvalues and eigenvectors obtained from the corresponding self-consistent Bogoliubov calculations for each model. It should be stressed that the energies are thus the quasiparticle energy eigenvalues of the BdG equation associated with Hamiltonian $\underline{H}$, rather than the electron energies related to the normal state Hamiltonian.

The form of the on-site magnetisation (4.54) for the orbital basis of Sr_2RuO_4 can also be discussed. Inner products of the orbitals can be evaluated using the known properties of the spherical harmonics of the basis, which are written in equation (3.15). Taking the a, b and c

notation of the basis, and applying the rules given in equations (A.15), the matrix elements are deduced to be

$$\begin{aligned}\langle b|\hat{l}_z|c\rangle &= \int_{UC} d\mathbf{r}\left(\phi_b^{\alpha\prime}(\mathbf{r}-\mathbf{R}')\right)^* \hat{l}_z\,\phi_c^{\alpha}(\mathbf{r}-\mathbf{R}) = -\mathrm{i}\hbar\delta_{\mathbf{R}\mathbf{R}\prime}\delta_{\alpha\alpha\prime},\\ \langle c|\hat{l}_z|b\rangle &= \int_{UC} d\mathbf{r}\left(\phi_c^{\alpha\prime}(\mathbf{r}-\mathbf{R}')\right)^* \hat{l}_z\,\phi_b^{\alpha}(\mathbf{r}-\mathbf{R}) = \mathrm{i}\hbar\delta_{\mathbf{R}\mathbf{R}\prime}\delta_{\alpha\alpha\prime},\end{aligned} \tag{4.59}$$

with all other matrix elements going to zero. Applying this to (4.53), the final magnetisation is then

$$\begin{aligned}\mathbf{M}_{\mathrm{LC}}^{(2)} = \hbar\gamma\,\mathrm{Im}\Big\{\sum_n \int_{BZ}\frac{d\mathbf{k}}{(2\pi)^3}\,&[u_{nc}^*(\mathbf{k})u_{nb}(\mathbf{k})f_{n\mathbf{k}} + v_{nc}(\mathbf{k})v_{nb}^*(\mathbf{k})(1-f_{n\mathbf{k}})]\\ &-[u_{nb}^*(\mathbf{k})u_{nc}(\mathbf{k})f_{n\mathbf{k}} + v_{nb}(\mathbf{k})v_{nc}^*(\mathbf{k})(1-f_{n\mathbf{k}})]\Big\}.\end{aligned} \tag{4.60}$$

An interesting observation regarding this component is that the on-site moment is driven entirely by inter-orbital hybridisation between the α and β bands. There would be no source of on-site moment in a single-band chiral p-wave state in which the gap is enforced on the γ band only. Again highlighted here is the importance of accounting for the full set of of inter-band couplings at the Fermi surface for any quantitative consideration of the superconducting state in Sr_2RuO_4.

4.3.1 Orbital Magnetisation: 3D

The results obtained from computations of the distinct contributions to the magnetisation for the three-dimensional p-wave model are presented here. Shown in Fig. 4.3 is the total magnetic moment per unit cell associated with the sum of the itinerant contributions $\mathbf{M}_{\mathrm{IC}}$ and $\mathbf{M}_{\mathrm{LC}}^{(1)}$, for the three-dimensional gap structure of Sr_2RuO_4. The results obtained with and without the inclusion of spin-orbit coupling are compared. It should be noted that these contributions diverge to plus and minus infinity respectively as T approaches T_c. This problem arises due to the fact that these components are not separately gauge-invariant, as they are formulated in an analogous way to the non-unique normal state equations (4.4a) and (4.4b). The sum of the two must therefore be taken, and the imperfect cancellation between the two divergent contributions near to the transition results in the small region in which the total moment drops below zero, for the model including SOC.

It has been shown previously that gauge-invariant forms of the normal state equations for $\mathbf{M}_{\mathrm{LC}}$ and $\mathbf{M}_{\mathrm{IC}}$ can be obtained [230], as discussed in Section 4.1.2. This process requires an absolute distinction between the occupied and unoccupied states in the electron bandstructure. Making such a distinction here is complicated by the Bogoliubov transformation, which enforces mixing of the electron and hole states. This mixing is essential to recover the quasiparticle

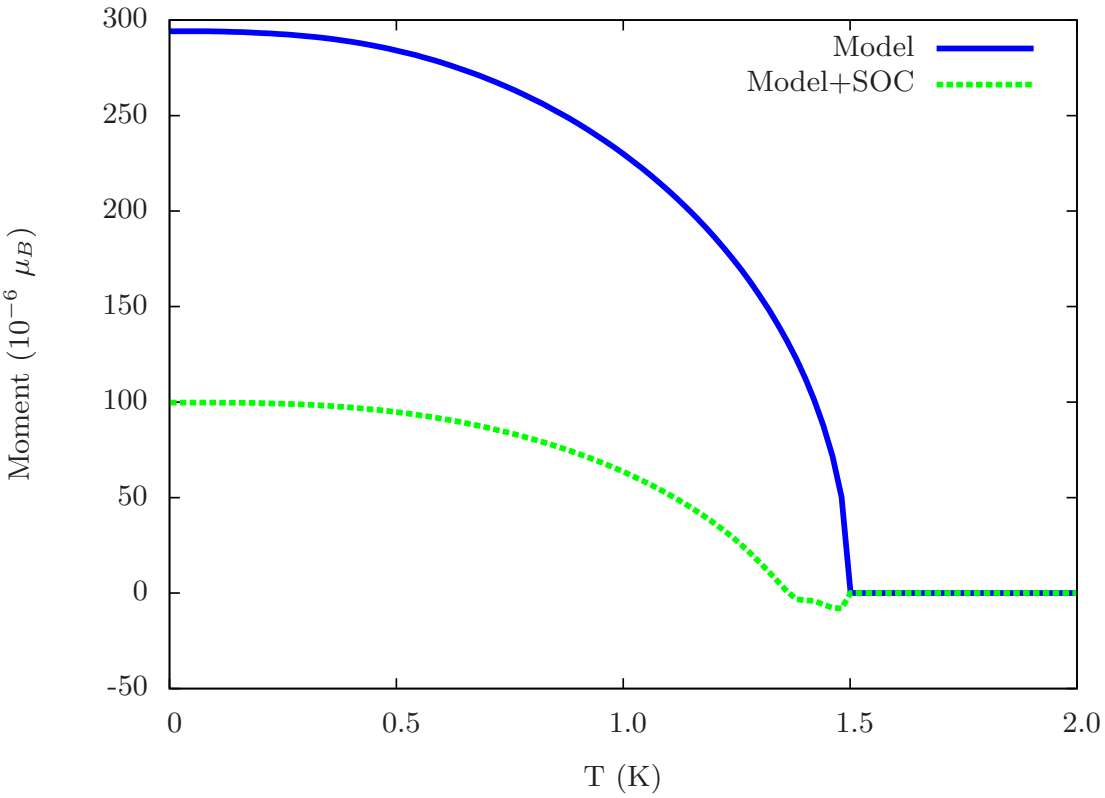

FIGURE 4.3. The sum of the itinerant and local magnetic moments carried by the unit cell associated with the components $\mathbf{M}_{\mathrm{IC}} + \mathbf{M}^{(1)}_{\mathrm{LC}}$, with and without spin-orbit coupling. This calculation was made via the 3D, p-wave model of Sr_2RuO_4. The orbital moment is given in units of Bohr magneton ($\mu_B = e\hbar/(2m)$).

bandstructure of the superconducting state, but prevents any attempts to project excitations onto occupied states and thus it is difficult to compare the generalised particle-hole expressions with the separately gauge-invariant formalism introduced in ref. [230]. Given that the term $\mathbf{M}^{(2)}_{\mathrm{LC}}$ is purely based on the atomic orbital basis, however, it is speculated that this term closely resembles the moment due to self-rotation defined by Souza and Vanderbilt, in which case $\mathbf{M}_{\mathrm{IC}} + \mathbf{M}^{(1)}_{\mathrm{LC}}$ would incorporate the inter-orbital itinerant contributions.

The sum of the components $\mathbf{M}_{\mathrm{IC}}$ and $\mathbf{M}^{(1)}_{\mathrm{LC}}$ is thus very closely related to the magnetisation associated with edge currents. There is not, however, a one-to-one correspondence between these two quantities. $\mathbf{M}_{\mathrm{IC}} + \mathbf{M}^{(1)}_{\mathrm{LC}}$ is in fact the contribution to the inter-orbital magnetisation which survives when extending the sample in the thermodynamic limit. In a finite sample, this remaining term may be distinguishable from the edge currents, which could include some finite contribution from $\mathbf{M}^{(2)}_{\mathrm{LC}}$.

In Fig. 4.4, the on-site magnetic moment for the model with and without SOC is displayed. Comparison of this with Fig. 4.3 reveals that the itinerant contributions are around two orders of magnitude larger than the on-site component. Converting the zero temperature values to units

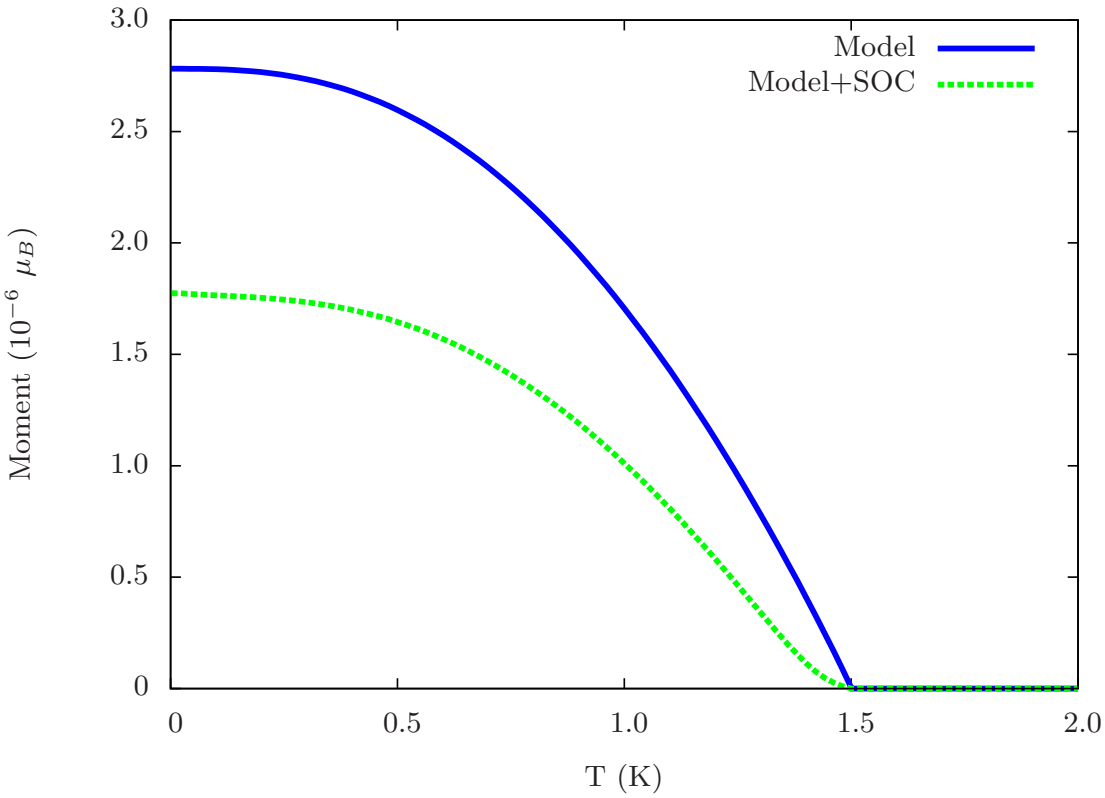

FIGURE 4.4. The on-site magnetic moment carried by the unit cell associated with the magnetisation $\mathbf{M}^{(2)}_{\mathrm{LC}}$, with and without spin-orbit coupling. This calculation was made via the 3D, p-wave model of Sr_2RuO_4. The moment is given in units of Bohr magneton ($\mu_B = e\hbar/(2m)$).

of magnetic field gives an itinerant magnetisation of the order of 100-300 mG, compared to an approximate field of around 2-3 mG for the on-site part (see App. B.2 for a detailed discussion on the conversion of units for the distinct components). The on-site magnetisation is similar to the resolution of the most recent attempts to experimentally identify an edge current in Sr_2RuO_4 via magnetometry measurements ($\sim$ 2.5 mG [112]), and it would therefore be feasible that this would be missed. However, the itinerant magnetisation, which includes that arising from edge currents, is still very large with respect to the detection limit of the experimental techniques.

There are a number of complications which should be taken into account when drawing conclusions from this result. Firstly, this value is computed as a bulk property, and so the influence of a boundary on the magnetisation is not accounted for. This is of particular significance for a superconductor as Meissner screening will induce a counter-propagating current at the surface which heavily suppresses the value computed through $\mathbf{M}_{\mathrm{IC}} + \mathbf{M}^{(1)}_{\mathrm{LC}}$ [107]. Furthermore, as has been discussed already, this sum is not the gauge-invariant value corresponding to the itinerant edge current and likely contains contributions from numerous sources within the lattice, notably the moment due to intra-cell movement of electrons. The reported value of 300 mG therefore

includes contributions to the field which are localised within the bulk unit cell. The value reported here agrees well with the result from μSR measurements, which gave a value of 500 mG for the local field [98]. This comparison further elucidates the strongly bulk-dependent nature of the calculation.

Despite the fact that the results reported here do not clearly reconcile the theory of a p-wave order parameter with results from magnetometry experiments, a large supression in the orbital moment in comparison to other theoretical approaches is keenly observed, as quasi-classical estimations give a screened edge current of the order of 10 G [107]. This reduction likely lies in the multi-band, nodal nature of the tight-binding model and gap structure implemented here. Significantly, this result agrees with other experimental and theoretical observations which support the idea that multi-band superconductivity is prevalent in this material. It has been shown previously that inter-orbital transitions are necessary in order for the Kerr effect to arise intrinsically in the superconducting state [129, 164], as elaborated upon in Chapter 5. In order to see the effect in a single-band picture, extrinsic mechanisms such as skew scattering must be considered [116]. The inclusion of the additional 1D, line nodal bands also leads to the correct specific heat below T_c [164], as discussed in Section 3.2. The nodeless 2D band would not produce the experimentally observed power laws in heat capacity [155–158, 191, 192], NMR spin relaxation rate [97] or thermal conductivity [195–198].

The discussion now proceeds to the influence of spin-orbit coupling. In principle, it would be expected that SOC plays a significant role in the generation of a magnetic moment in the chiral state, given that the interaction is essential for the generation of a spontaneous Hall voltage in the normal state [171, 236–238]. It is clear through observation of Figs. 4.3 and 4.4 that the addition of SOC results in a suppression of the total orbital moment. A significant quantitative reduction in all contributions to the magnetisation in observed, with only minor qualitative differences in the temperature-dependence displayed in the itinerant part. This suppression is also of similar order to that seen in the Kerr effect under the influence of SOC as reported in ref. [164], which is displayed in greater detail in Chapter 5.

In order to fully assess the influence of SOC, it is informative to also compute the spin moment of the chiral state. The relevant expression arises from the equation for the spin expectation value in the orbital basis,

$$\langle \hat{S}_z \rangle = \sum_{d,d\prime,\alpha,\alpha\prime} \langle d,\alpha | \frac{\hbar}{2}\sigma_z | d',\alpha' \rangle n^{\alpha\alpha\prime}_{dd\prime}, \tag{4.61}$$

where d,α are the orbital character and spin projections of the orbital basis respectively and $n^{\alpha\alpha\prime}_{dd\prime}$ are the single-particle density matrices. Due to the orthonormality of the orbital basis functions, the σ_z matrix elements are ± 1 for $\alpha = \alpha' = \pm 1/2$ and $d = d'$. The final expression is then

$$\langle \hat{S}_z \rangle = \sum_d \frac{\hbar}{2}\left(n^{\uparrow\uparrow}_{dd} - n^{\downarrow\downarrow}_{dd} \right), \tag{4.62}$$

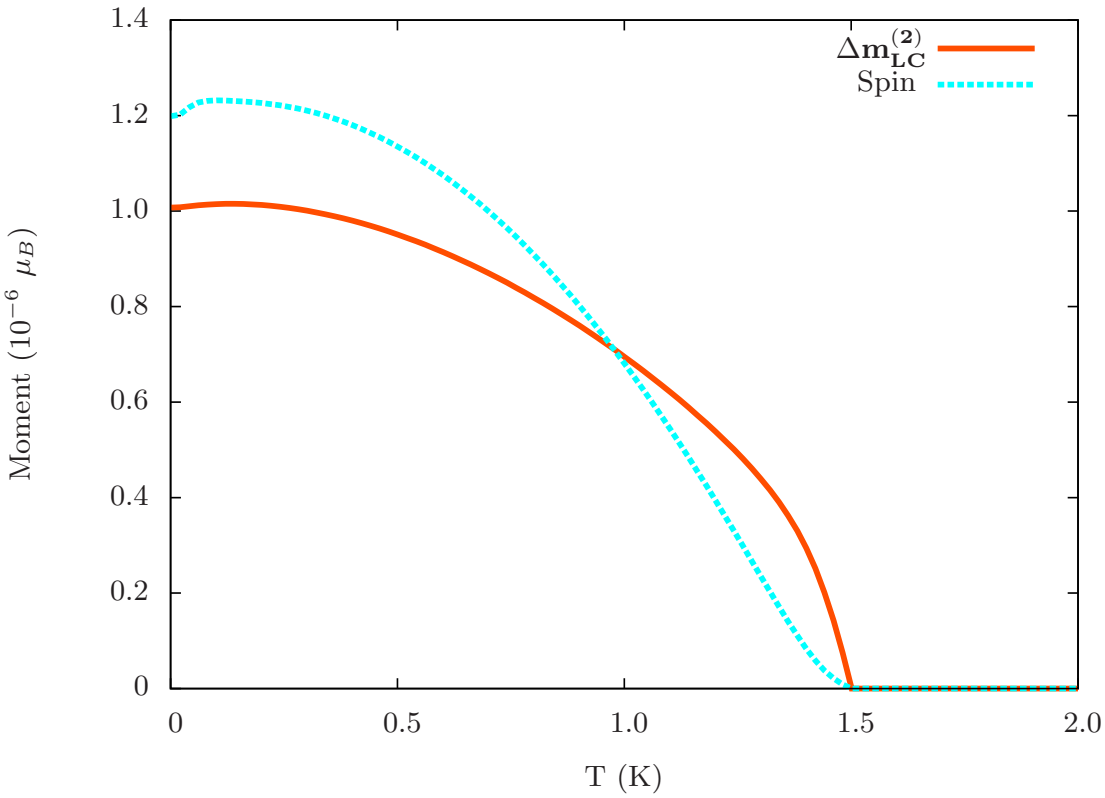

FIGURE 4.5. Spin moment in the 3D model including SOC, compared with the difference in the on-site orbital moment induced by the addition of SOC.

where the denisty matrices are given by [160]

$$n_{dd}^{\alpha\alpha} = \frac{1}{N}\sum_{n\mathbf{k}} |u_{n\mathbf{k}}^{\alpha}|^2 f_{n\mathbf{k}} + |v_{n\mathbf{k}}^{\alpha}|^2 \left(1 - f_{n\mathbf{k}}\right). \tag{4.63}$$

The spin magnetic moment is then $\gamma_s \langle \hat{S}_z \rangle$, where $\gamma_s = -eg/(2m_e)$ and g is the spin gyromagnetic ratio ($g \approx 2$).

It is interesting to note here that the spin moment in this context becomes non-zero when SOC is included (see Fig. 4.5), but is zero otherwise. The spin moment in the SOC regime is of similar order to the reduction in the on-site orbital moment induced by the spin-orbit interaction (which has been denoted $\Delta\mathbf{m}_{\mathrm{LC}}^{(2)}$). This would suggest that the spin-orbit interaction mediates a transfer of magnetic moment from the orbital degrees of freedom (where it arises from the chiral order parameter) to the spin degrees (which are otherwise disordered). It should also be noted that the in-plane components of the spin moment ($\langle \hat{S}_x \rangle$ and $\langle \hat{S}_y \rangle$) remain zero, with and without SOC.

This observation provides an interesting insight into the origin of the Kerr effect, a phenomenon which is driven by the anomalous Hall conductivity present in systems with a finite

orbital moment. The microscopic origin of this effect in unconventional superconductors has been extensively debated [116, 117]. The current controversy concerns whether the origin is extrinsic (i.e. arising from disorder [239–241]) or an intrinsic mechanism arising from coupling of the pair state to orbital degrees of freedom at the Fermi level [129, 164, 165].

In the normal state ferromagnet, the intrinsic mechanism facilitating the Kerr effect is induced by coupling of the ordered spins to the orbital component via SOC [171]. Namely, the symmetry breaking in the spin degree of freedom is transferred to the orbital component via the spin-orbit interaction. This is a clear analogue to the results reported here, where orbital order arises naturally due to the chiral superconducting order parameter and is then reduced via coupling to the disordered spin component. These results coincide with the observations reported in ref. [164], where the magnitude of the Kerr shift in the same chiral superconducting model was also shown to be suppressed by a similar order following the introduction of SOC. The model is thus able to effectively describe an intrinsic origin of the anomalous phenomena observed in Sr_2RuO_4.

This analysis of the influence of SOC is further supported by assessing the regions of the Brillouin zone in which the spin moment arises (see Fig. 4.6). It is observed that the spin moment is present in regions of near-degeneracies between the orbital degrees of freedom in the bandstructure. These regions on the Brillouin zone contribute strongly to the Berry curvature, which gives rise to an anomalous Hall conductivity [163]. In this structure, the Berry curvature originates from time-reversal symmetry breaking associated with the intrinsic magnetic field (see Section 5.1.2 for a further explanation on the origin of the Berry curvature), which implies that these regions contain the highest density of ordered orbital moments. From this it can be inferred that the spin magnetisation is arising directly as a result of coupling of the spins to the orbital degree of freedom.

Also displayed is a normalised plot of total magnetisation for the cases with and without SOC alongside the temperature evolution of the gap (see Fig. 4.7). Under the addition of SOC, the gap tends to evolve as $|\Delta(T)/\Delta(0)|^2$, which agrees with the observed development of the μSR [98] and Kerr effect signals [102]. These anomalous phenomena are closely linked to the bulk magnetic moment, and the so the equal temperature-dependence is expected. While the dependence of the μSR signal on the moment is obvious, the shared origin of the orbital moment and the Kerr effect will be formalised in Section 5.2. Note, however, that the temperature dependence of the gap including SOC is impaired somewhat by the numerical inaccuracy of this calculation near to $T = 0$, so these comparisons should be taken tentatively. In contrast, the model excluding SOC displays a temperature-dependence more in line with $|\Delta(T)/\Delta(0)|$.

4.3.2 Orbital Magnetisation: 2D

The calculations performed to obtain the results presented in Section 4.3.1 were replicated using the alternative two-dimensional pairing structure outlined in Section 3.2.3. The primary

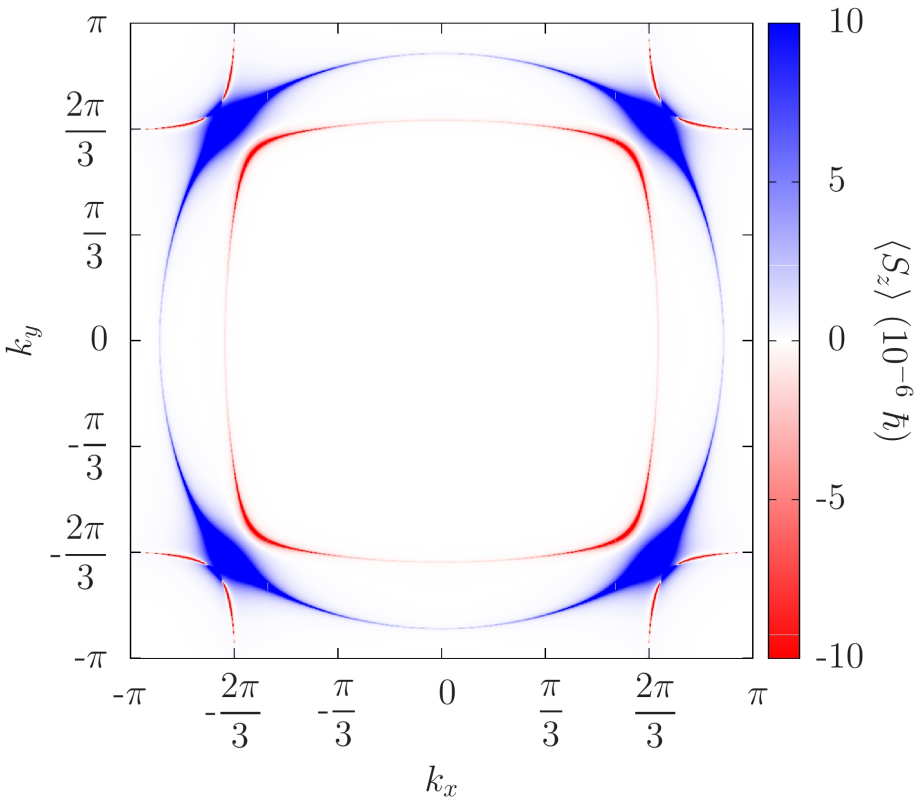

FIGURE 4.6. $k_x - k_y$ resolved plot of the spin moment in the Brillouin zone, for $k_z = 0$ and $T = 0$, calculated via the 3D model of Sr_2RuO_4 with the inclusion of spin-orbit coupling.

motivation behind performing orbital moment calculations with this model is that, according to the work carried out by Scaffidi and Simon, the extended pairing regime may result in a suppressed total magnetisation [184, 185]. Finite spin-orbit coupling is essential here as this interaction drives the formation of the multi-gap structure in the longer-range pairing channels. Figs. 4.8 and 4.9 display the itinerant and on-site contributions to the magnetic moment respectively for this model. The plots show the results obtained from the self-consistent solution alongside the renormalised fit with an approximate temperature-dependence $f(T) = \Delta(0)\sqrt{1 - T/T_c}$.

In both figures, it is observed that the moment in the self-consistent result corresponds well with the smooth temperature evolution expected, at least for temperatures above 0.5 K. Kinks in the self-consistent curves occur in the same temperature region that the state becomes fully gapped according to the specific heat (see Fig. 3.16). It is immediately clear that the inclusion of additional pairing channels causes a suppression of the total moment by approximately an order of magnitude relative to that calculated for the two-gap three-dimensional model. This result supports the observations made by Scaffidi and Simon that the extended model has a

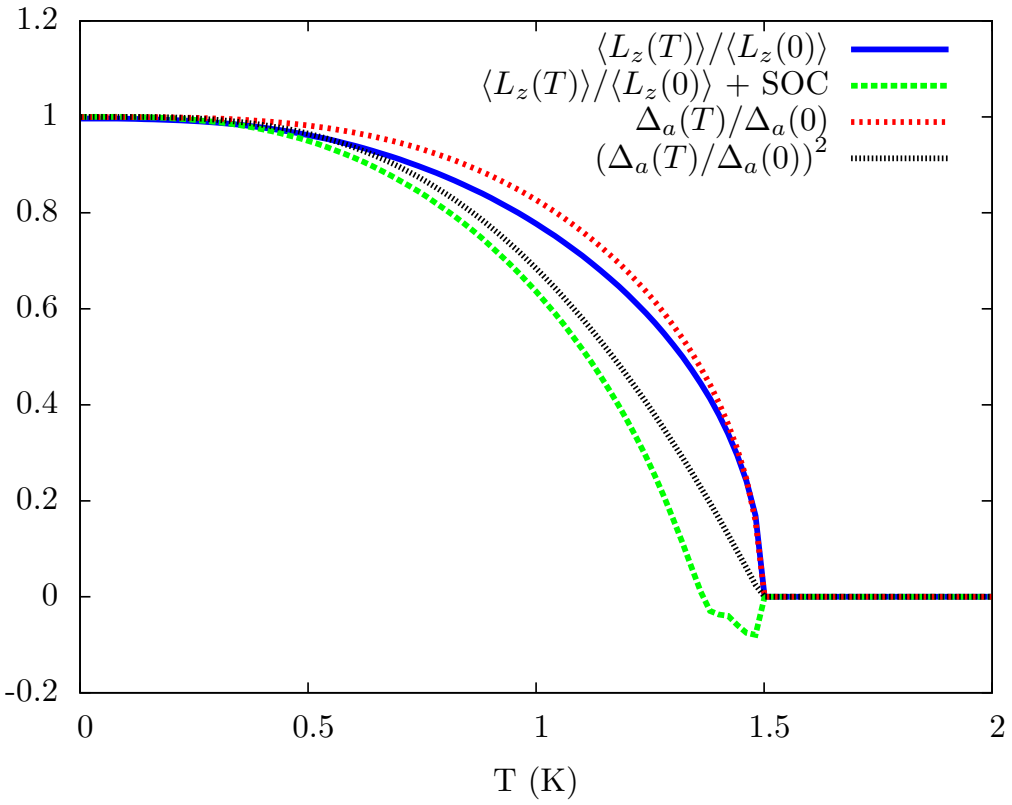

FIGURE 4.7. Normalised, total orbital moment per unit cell for the 3D model with and without SOC, against temperature. Also plotted is the normalised, in-plane component of the gap, computed without SOC. The inclusion of SOC has negligible influence on the qualitative temperature dependence of the gap. The y-axis is given in dimensionless units.

distinctly different topological structure, displaying a Chern number of -7, in contrast to the value of $C = 1$ carried by a 2D, single-band p-wave state [184]. It has been argued that, for a chiral superconducting state with Chern number $C = 1$, the topological edge current will carry the full orbital angular momentum of the condensate (of the order $N\hbar/2$) as discussed in Section 4.1.2 [108, 109, 207, 209]. However, values of $|C| > 1$ do not enforce topological currents of this magnitude, and a large suppression of the edge magnetisation is expected [109, 207, 209].

Qualitatively, the results obtained from this extended pairing model are very similary to those displayed for the 3D model in Section 4.3.1. The large reduction observed in the moment here gives a value of approximately 40 mG at 0 K, but this does not bring the itinerant magnetisation below experimental resolution and the issue of whether this result can be reconciled with experiment remains paramount. However, taking into account again the presence of Meissner screening currents, and the inclusion of local bulk fields, it becomes more feasible that this structure would produce an edge current which would not be visible to scanning SQUID magnetometers. Given that Meissner screening is expected to reduce the edge magnetisation by approximately an order

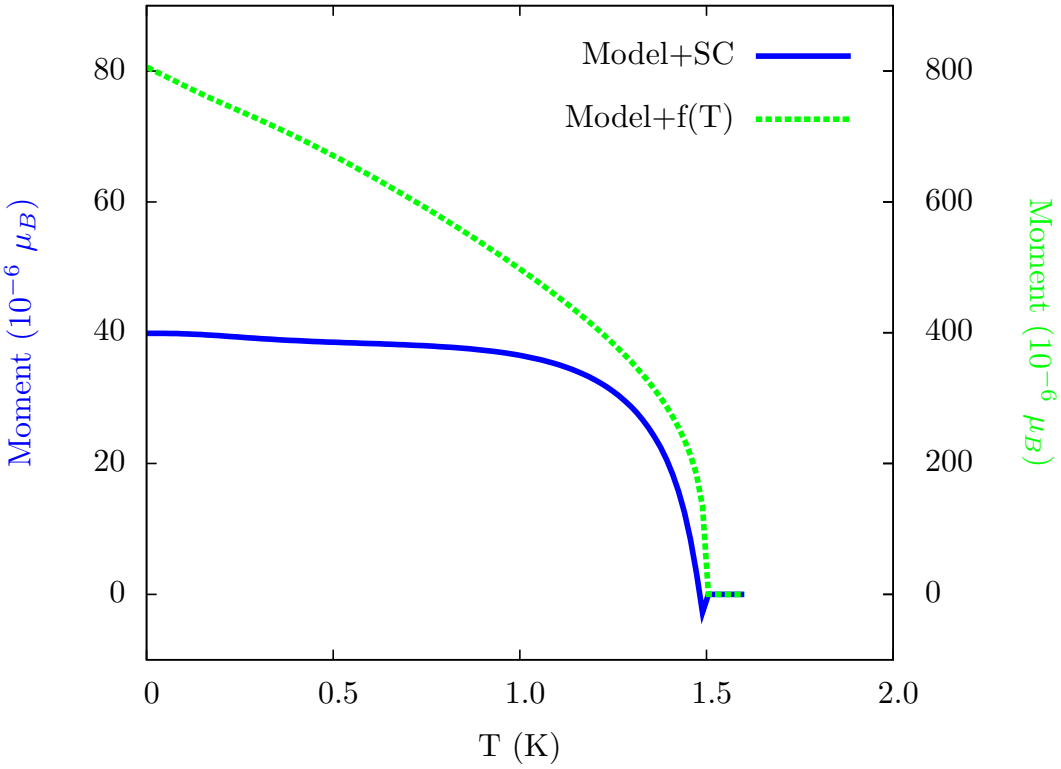

FIGURE 4.8. Sum of the itinerant contributions to the orbital magnetic moment for the two-dimensional model in the extended pairing regime. The y-axis on the left-hand side corresponds to the moment per unit cell obtained in the self-consistent calculation, which is represented by the blue, unbroken curve. The green, dashed line gives the result from the fitted gap magnitudes with approximate temperature-dependence $f(T) = \Delta(0)\sqrt{1 - T/T_c}$, and has a different scale given by the y-axis on the right-hand side. Both curves are given in units of Bohr magneton.

of magnitude [107], an itinerant magnetisation of roughly 4 mG is obtained. The proportion of this which is restricted to the bulk unit cells is difficult to estimate, but it is easy to speculate that the visible edge magnetisation reported here could be below the experimental resolution of 2.5 mG.

Figs. 4.8 and 4.9 also starkly highlight the inaccuracy of the fitted temperature-dependence $f(T)$. Despite the fact that this approach appears to give the correct nodal structure in the low-temperature region, the orbital moment now shows no correlation with the evolution of the gap parameters with respect to temperature. Furthermore, this estimation gives an itinerant orbital moment which is an order of magnitude larger than the self-consistent results. Nevertheless, the most promising avenue for progress with this model is to adjust the zero temperature parameters to recreate the gap magnitudes of the renormalised fit used in this approach, and then solve for the temperature-dependence self-consistently via the Bogoliubov-de Gennes equations.

The spin magnetic moment for the extended pairing model is plotted in 4.10. Both the spin and

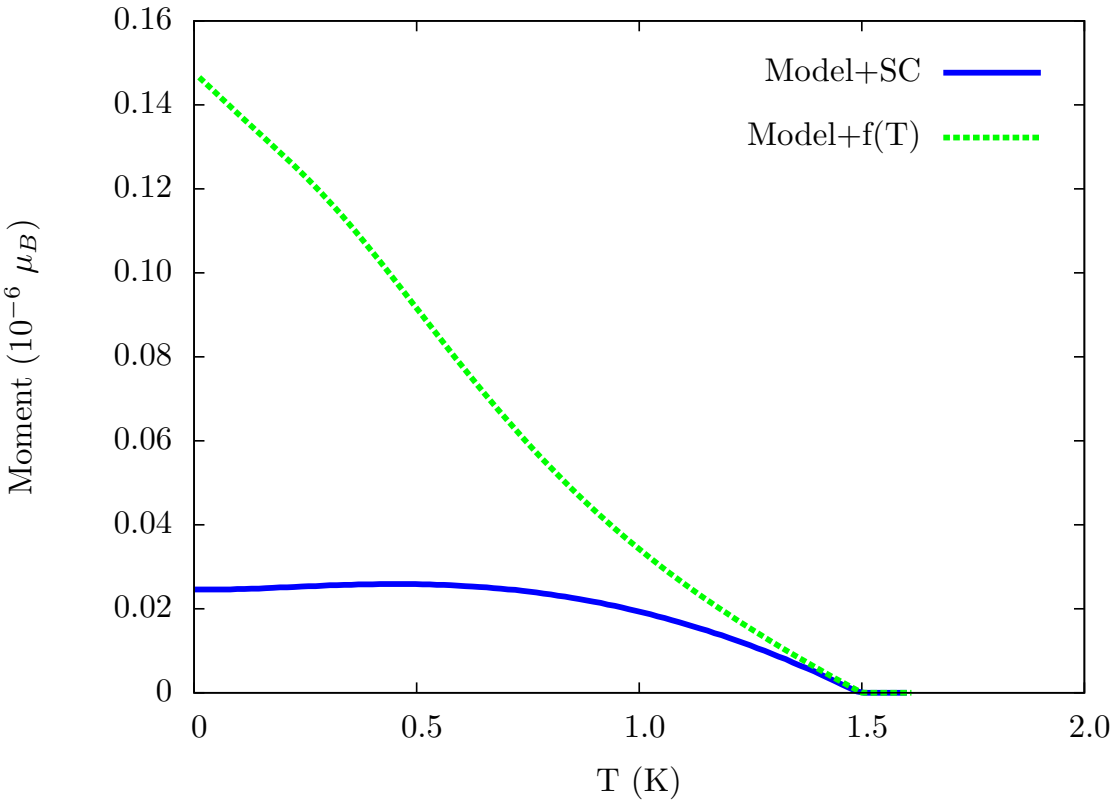

FIGURE 4.9. The on-site contribution to the orbital magnetic moment for the two-dimensional model in the extended pairing regime, calculated via the self-consistent approach and the renormalised fit with approximate temperature-dependence.

on-site orbital moment curves are of very similar order of magnitude and qualitative temperature dependence, again highlighting the close connection between spin magnetisation and the on-site orbital magnetisation. However, the spin magnetisation is larger than $\mathbf{M}_{\mathrm{LC}}^{(2)}$ in this case, likely as a result of the enhanced inter-orbital hybridisation of the band-gaps arising due to the larger number of pairing channels, facilitating a large transfer of magnetic moment from the orbital to the spin part. It would be interesting to observe the dependence of this component in potential future studies if a different spin-orbit coupling parameter is enforced in order to obtain the correct low-temperature nodal structure. The results obtained through the 3D model calculations would suggest that $\langle \hat{S}_z \rangle$ should decrease with λ.

To summarise the results presented thus far, the orbital moment was calculated for both the multi-band 3D model and the 2D model with extended pairing. The magnitude of the computed moments are significantly smaller than that predicted through single-band models, and the qualitative temperature-dependence of the moment agrees well with μSR and Kerr effect signals. A further insight into the interplay between the spin and orbital magnetisation via the spin-orbit interaction has also been highlighted. However, the outstanding issue of the existence of edge

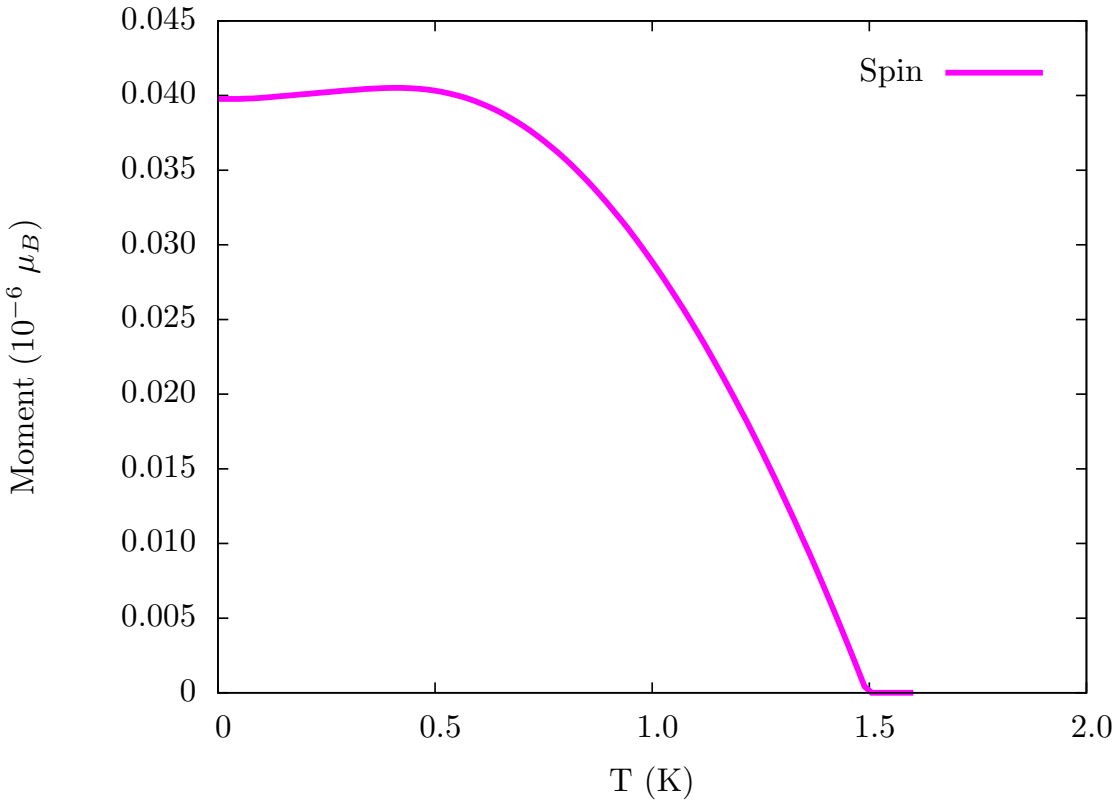

FIGURE 4.10. The spin magnetic moment for the two-dimensional model in the extended pairing regime, calculated via the self-consistent approach.

currents in Sr_2RuO_4 has not been resolved, although the problem of the surface magnetisation is difficult to study comprehensively with the current formalism as it a fundamentally bulk calculation.

4.3.3 Finite Sample Investigation

Following the initial derivation of a Bloch-dependent set of equations to determine the orbital magnetisation in a periodic insulator, the authors sought to verify their formalism through comparison with a direct computation of the orbital angular momentum operator $\hat{\mathbf{l}}$ in a small, finite-sized sample [114]. For a finite sample, the expectation value of the circulation operator can be evaluated explicitly with respect to a set of position-dependent wavefunctions. By performing the operation for a sample with a defined boundary, the position operator becomes localised and the problems arising in the Bloch-dependent case are negated.

For a relatively small sample, the computed orbital magnetisation will be strongly-dependent on the number of atoms in the calculation. A finite-size analysis can be performed to extrapolate the bulk orbital moment from the real-space calculations. This should then be a reasonable approximation of the value calculated through the periodic lattice formalism given by equation

(4.4). For a square lattice of dimension $N \times N$, the total moment approximately varies with sample size via

$$M(N) = M + \frac{a}{N} + \frac{b}{N^2}, \tag{4.64}$$

where M is the bulk quantity. The parameters a and b account for the contributions to $M(N)$ arising from lattice cells along the edge of the sample and the corners respectively. This approach demonstrated perfect agreement with the results obtained for the bulk contribution to the itinerant magnetisation computed via the Brillouin zone integration [113, 114].

It would be natural to hope that this same approach could be used to verify that the generalisation of the orbital moment theory to the superconducting state had been performed correctly. Outlined below will be the preliminary real-space results obtained through a finite-size replica of the chiral p-wave model of Sr_2RuO_4. Unfortunately, this endeavour was ultimately unsuccessful as no consistency between the real-space and Bloch calculations was found. A discussion of the likely reasons for this is presented here, and a suggestion for an alternative approach which may be able to resolve this issue in future investigations is given.

Preliminary calculations were performed with a 2D square sample with a modified bandstructure, taking only the circular γ band and enforcing a gap with the p-wave order parameter (3.30). To study the effects of the gap on a finite-size structure, the self-consistent Bogliubov-de Gennes framework must be converted from the $\mathbf{k}$-dependent framework used in 3.2 to the position basis. The lattice tight-binding Hamiltonian is constructed by taking [161, 162]

$$H_{ii\prime} = \left[\epsilon_0 \delta_{ii\prime} + t\left(\delta_{i(i\prime\pm\hat{\mathbf{x}})} + \delta_{i(i\prime\pm\hat{\mathbf{y}})}\right) + t'\left(\delta_{i(i\prime\pm(\hat{\mathbf{x}},\hat{\mathbf{y}}))} + \delta_{i(i\prime\pm(\hat{\mathbf{x}},-\hat{\mathbf{y}}))}\right)\right] c_i^\dagger c_{i\prime}, \tag{4.65}$$

where i, i' sum over all atoms in the sample, $\hat{\mathbf{x}}, \hat{\mathbf{y}}$ are lattice vectors, and the lattice spacing has been set to 1. The on-site and hopping parameters are taken directly from Table 3.1 for the purpose of preliminary calculations. Enforcing only the 2D order parameter (3.30), the pairing interaction takes the form

$$\Delta_{ii\prime} = \left[\Delta_0\left(\delta_{i(i\prime\pm\hat{\mathbf{x}})} + \mathrm{i}\delta_{i(i\prime\pm\hat{\mathbf{y}})}\right)\right] c_i^\dagger c_{i\prime}. \tag{4.66}$$

To calculate the orbital angular momentum, the velocity operator must be evaluated. This is achieved by inserting the lattice Hamiltonian (4.65) into the standard relationship (4.14). The orbital moment is then computed by evaluating (4.9) with respect to wavefunctions given by solutions of the BdG equation,

$$\begin{pmatrix} \underline{H} & \underline{\Delta} \\ \underline{\Delta}^\dagger & -\underline{H}^* \end{pmatrix} \begin{pmatrix} u(\mathbf{r}) \\ v(\mathbf{r}) \end{pmatrix} = E \begin{pmatrix} u(\mathbf{r}) \\ v(\mathbf{r}) \end{pmatrix}. \tag{4.67}$$

The self-consistent calculations yielded values of Δ_0 of the order 0.1 meV at zero temperature (see Fig. 3.11). It has been shown previously, however, that it is not possible to resolve gap sizes this small through a finite-size sample of a reasonable dimension [242]. The result is that the energy eigenvalues E will not converge with respect to N for gap values of this size.

The factor which most likely places this restriction on the gap size is the associated coherence length. A binding energy on the scale of the physical system corresponds to a pair condensate with a coherence length approximately 1000 Å in magnitude, greatly exceeding the size of the sample considered here. This can be counteracted by arbitrarily increasing the magnitude of the gap by a factor of 1000, making it possible to qualitatively study the behaviour of the velocity matrix elements in a finite-sized sample. The value of the orbital moment obtained in this approach converges smoothly as N approaches 10. An estimate for the bulk magnetic moment was then found by fitting this converged curve to (4.64), generating fitted values of M with an accuracy within 0.1%. However, by taking Δ_0 as an adjustable parameter, and comparing with the equivalent calculations with the Bloch-dependent equations, an agreement between the two was not found.

It was observed that the magnitude of M increased linearly with Δ_0 in the reciprocal-space results. This would be expected intuitively as the total moment is a direct consequence of the energy gap corresponding to the formation of Cooper pairs carrying an orbital magnetic moment. Comparison with the theoretical studies of the intrinsic moment in ^{3}He would also fit this result. As outlined in Section 4.1.2, the moment is generally given as being proportional to $(|\Delta|/\epsilon_f)^\gamma$, where the exponent γ has been deduced to be either 0 [108, 109, 207, 209], 1 [69], or 2 [232]. Comparison with Fig. 4.7 also affirms this as the moment computed through the 3D model excluding SOC evolved with temperature as $|\Delta(T)/\Delta(0)|$.

In contrast, it was found in real-space calculations that the magnitude of the orbital moment would decrease with respect to gap size. This behaviour is certainly not intuitive, and it can only be concluded that the inverse dependence arises from finite-size effects which are not accounted for in the fitting curve (4.64). To try to gain an understanding of the origin of this discrepancy, it is beneficial to study the evolution of the velocity matrix elements with gap size. In Fig. 4.11, a position-resolved plot of the electron velocity for the finite sample is displayed with a finite gap. Clearly observed is a smooth edge current, with no net velocity terms within the bulk of the sample. The behaviour of the velocity elements with respect to the gap is interesting, however. While the magnitudes of the velocities do indeed increase with gap as would be expected, it was observed that the direction of these terms would veer drastically from the smooth path resulting in a highly corrugated edge current (see Fig. 4.12). It appears that these strong surface effects are dominating the total computed moment, resulting in the decrease of moment with increasing gap, and thus the behaviour of the bulk-dependent reciprocal-space calculation is not recreated.

Solutions to this limitation of the finite-size approach are not immediately obvious, as it appears that an unattinably large sample would be required in order to mask the observed

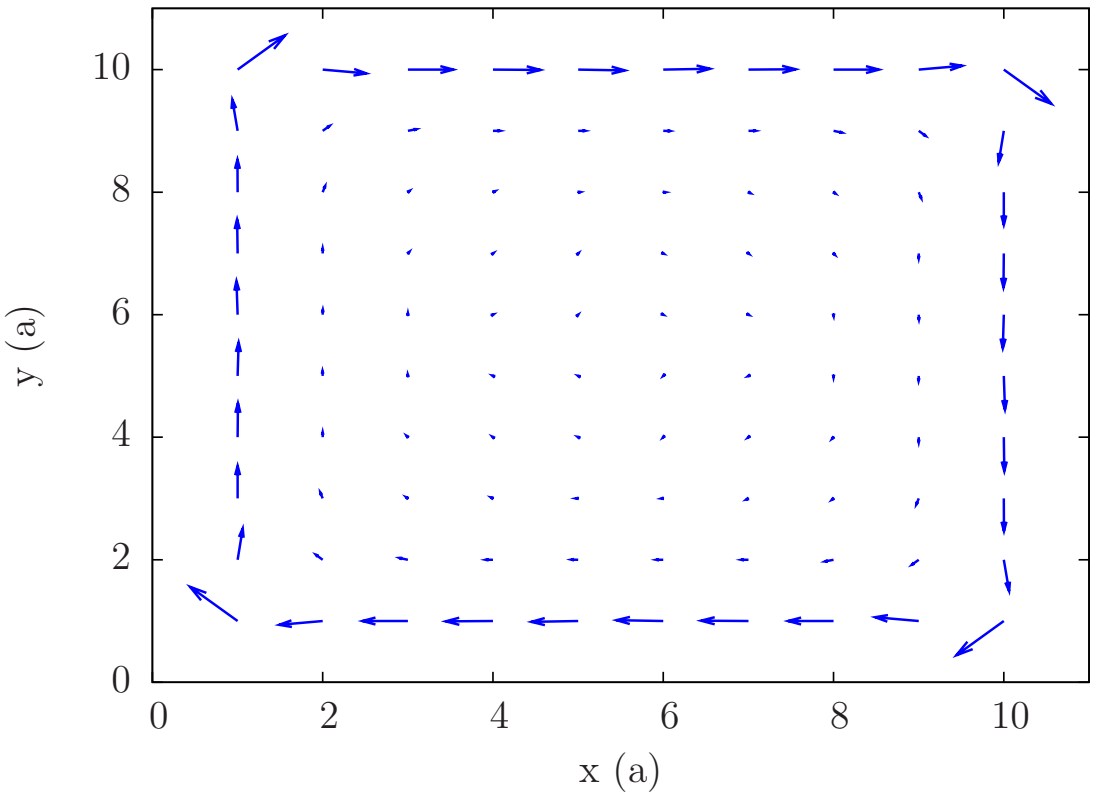

FIGURE 4.11. A two-dimensional plot of the velocity matrix elements for the simplified finite-size model, with gap multiplied by a factor 1000. The axes are given in units of the lattice parameter $a = 0.3862$ nm.

surface effects. However, it is possible that a different set of boundary conditions would provide an avenue for future work. Previous work using a real space model of Sr_2RuO_4 demonstrated that the edge currents vanish when imposing periodic boundary conditions in the x and y-directions [242]. This result is believed to be a consequence of the cancellation of orbital currents due to the relative motion of Cooper pairs. In contrast, open boundary conditions did yield a finite edge current due to the incomplete cancellation of the orbital currents near to the boundary. This approach coincides with the real-space calculations made to validate the formulae for an insulator [114].

In the work presented here, open boundary conditions were enforced in both directions. An alternative approach would be to apply open conditions along one axis and a periodic boundary on the other, thus approximating an infinite width strip. It is possible that the complete cancellation of the fully periodic approach would not occur in this geometry, and that the removal of a surface in one direction may facilitate quick convergence with cluster size. Whether this approach would accurately recreate the bulk orbital moment obtained through reciprocal-space calculations remains an open question. An accurate calculation of the coherence length associated with the

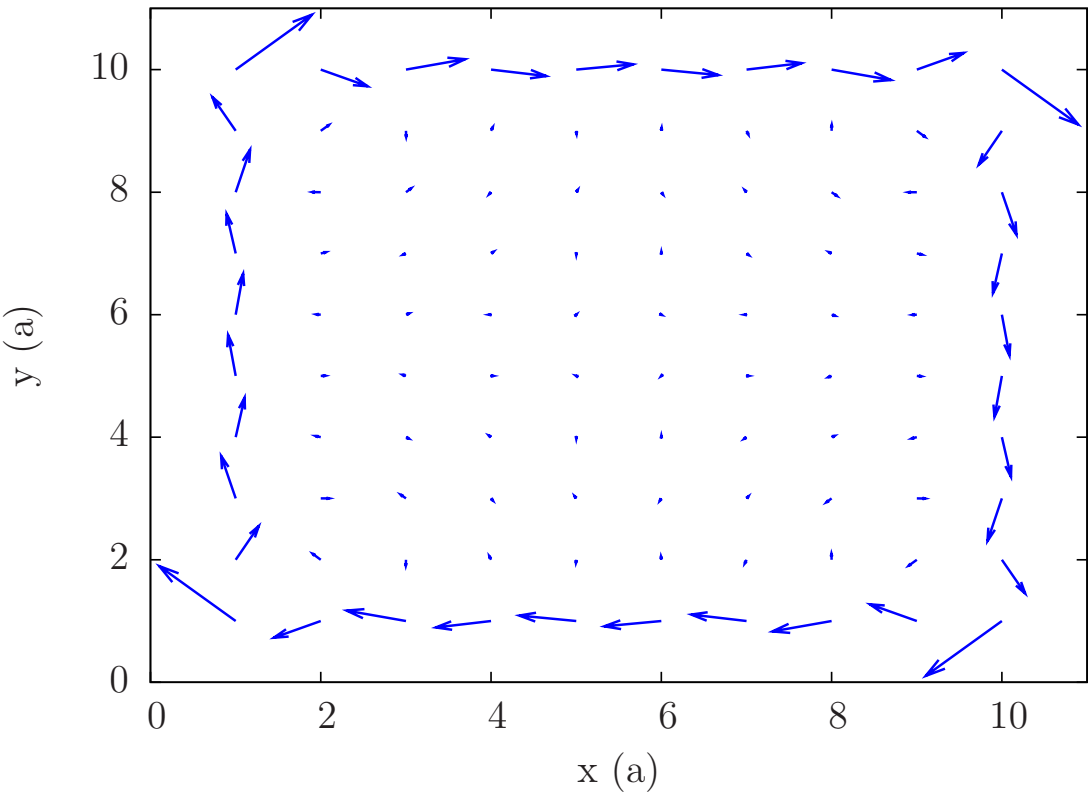

FIGURE 4.12. A two-dimensional plot of the velocity matrix elements for the simplified finite-size model, with gap multiplied by a factor 5000. The axes are given in units of the lattice parameter $a = 0.3862$ nm.

magnified gap size would also be beneficial in future investigations. Comparison of the coherence lengths with the lattice spacing for the two gap magnitudes used here may serve to elucidate the origin of the finite-size effects.

This section concludes Chapter 4. In summary, the key result presented here is the derivation of a general set of equations to calculate the orbital magnetisation in a superconductor. The equations are written in a Bloch-dependent framework suitable for the study of infinite lattices. The identification of a bulk-dependent formalism to describe the orbital magnetisation in a state including edge currents marks a significant achievement. Furthermore, performing a tight-binding expansion revealed the purely on-site magnetisation. Application of these equations to the two p-wave models of Sr_2RuO_4 demonstrates that the inclusion of inter-band pairing and multiple gaps leads to a suppression of the total moment relative to single-band quasi-classical approximations. No finite conclusions regarding the nature of edge currents in a p-wave configuration of Sr_2RuO_4 can be drawn from these results, but it has been starkly highlighted that a distinction must be drawn when considering the bulk and surface contributions to the total magnetisation. Also outstanding is the issue of corroborating the derived equations against

an equivalent real-space calculation, as calculations made via a finite-size sample with open boundary conditions were dominated by surface effects.

CHAPTER 5

ANOMALOUS HALL EFFECT

The appearance of a transverse conductivity in response to an applied voltage, in the absence of an externally applied magnetic field or magnetic impurities, indicates that a state has intrinsically broken time-reversal or inversion symmetry. Such a property is the driving mechanism for a number of novel and anomalous phenomena. In this chapter, results from calculations of the anomalous Hall conductivity for the p-wave models of Sr_2RuO_4 are presented. A direct consequence of an anomalous Hall conductivity is the Kerr effect, an optical phenomenon causing a rotation in the plane of polarisation of a reflected beam of radiation. Also presented here are the results of model calculations of the Kerr effect in Sr_2RuO_4.

5.1 Spontaneous Hall Conductivity

The conventional Hall effect is a well known phenomenon arising in metals and semiconductors under the application of an external magnetic field. In 1879, Hall discovered that the charge carriers in a current-carrying wire within a magnetic field are deflected in the transverse direction due to the Lorentz force [243]. The transverse voltage generated through this process is dependent on the density of charge carriers in the wire, and thus the Hall effect provides a simple method with which to investigate the concentration of conduction electrons in a given material. Additional applications include solid state devices such as magnetometers, which are used to detect magnetic fields by placing a probe in close proximity to a sample and measuring the induced Hall voltage.

Shortly after the discovery of the Hall effect, it was observed that the Hall voltage generated in a ferromagnet is an order of magnitude larger than in a normal metal [244]. An additional contribution to the Hall conductivity arises from the intrinsic magnetisation in such a material. The transverse motion induced by the internal magnetic field was dubbed an “anomalous velocity”

[171], and this effect is now known as the anomalous Hall effect (AHE). Spontaneous Hall voltages have been identified in a number of unconventional superconductors, but the exact origin of the anomalous velocity in this class of materials remains a source of debate [115]. This controversy provides a key motivation for the work presented here.

Before tackling the debate concerning the origin of the AHE, it is necessary to clarify some fine points regarding the nomenclature in this topic. An anomalous Hall conductivity specifically refers to any contribution to the Hall voltage arising from internal magnetic fields. This contribution may be generated via two distinct responses. For a paramagnetic material, the application of an external magnetic field induces an internal magnetisation, which will then generate an anomalous Hall conductivity in addition to the conventional effect arising from the applied field. This can be referred to as an induced AHE. In this thesis, the focus is rather placed on a spontaneous anomalous Hall conductivity arising from ferromagnetic materials in the absence of an applied magnetic field. Henceforth, any remark on the AHE will refer specifically to the spontaneous mechanism unless otherwise stated. It should also be highlighted that the focus is restricted to transverse conductivities generated by the breaking of time-reversal symmetry, which are distinct from those arising from inversion symmetry breaking as the former produce an antisymmetric response ($\sigma_{xy} = -\sigma_{yx}$), while the latter is symmetric ($\sigma_{xy} = \sigma_{yx}$).

5.1.1 Origins of the Anomalous Hall Effect

In the literature, there are three mechanisms which are typically referred to as the driving sources behind an anomalous Hall conductivity: “intrinsic”, “skew-scattering” and “side-jump”. Both skew-scattering [236, 237] and side-jump [238] processes originate from coupling between the charge carriers and lattice impurities through interactions such as SOC. These can be deemed extrinsic sources of AHE as they rely on disorder in the lattice. The focus of the work reported here is rather on the intrinsic mechanism, arising in states which have a finite Berry curvature [218]. Time-reversal symmetry breaking, in conjunction with a non-zero Berry curvature in the bandstructure, leads to an intrinsic transverse conductivity.

A theory for the intrinsic mechanism of the AHE was first developed in 1954 by Karplus and Luttinger [171], through a mechanism which is now referred to as the KL theory. The authors showed that the group velocity of itinerant electrons in the presence of an electric field includes an additional term which had not previously been noted. It was then shown that, by summing over all the bands in a periodic crystal, this anomalous velocity generally cancels to zero, but is finite in a ferromagnet leading to an anomalous Hall conductivity. This mechanism is purely reliant on the crystal bandstructure and is present even in the absence of disorder, in contrast to the skew-scattering and side-jump approaches. In this picture the longitudinal conductivity (σ_{xx}) will be infinite due to the lack impurities, while a finite transverse conductivity is maintained. However, early experiments on a series of high-purity transition-metal samples revealed that the transverse conductivity is linearly-dependent on σ_{xx} in such materials, indicating that disorder

plays a key role in the anomalous transprt [245]. As a result, the KL theory was highly-contested in the years following its development [115].

It was later found that the intrinsic contribution is indeed present in transition-metal ferromagnets, but that the AHE in the high-conductivity regime is dominated by the skew-scattering mechanism [115]. At moderate levels of impurity concentration, the intrinsic mechanism dominates and the anomalous Hall voltage is scattering-independent [246]. The intrinsic anomalous velocity is in fact directly related to the Berry phase of an electron in momentum-space [247, 248]. Interestingly, the introduction of KL theory pre-dated the discovery of the Berry phase by three decades [234], but was ultimately extremely influential in demonstrating the importance of Berry phase effects on electric transport properties [218]. It is for this reason that the sources of contributions to the Berry curvature of the bandstructure within the model must be strongly taken into consideration when determining whether an intrinsic source of the AHE is present. A detailed discussion of the origins of Berry phase effects in periodic lattices is presented in Section 5.1.2 below.

The intrinsic contribution to the AHE is defined microscopically as the d.c. limit of the inter-band conductivity [115]. This is a consequence of the fact the Berry curvature in a lattice arises from inter-orbital coupling [218], meaning that a finite anomalous Hall conductivity can only be recreated theoretically in a multi-band model. For the case of a normal state ferromagnet, the spin-orbit interaction is essential in order to recover the AHE for the reasons outlined in Section 5.1.2. In the superconducting model used here, however, the chiral symmetry breaking associated with the order parameter is sufficient to recover the effect, as demonstrated in refs. [129, 165, 205], while inter-orbital pairing terms provide an additional source of Berry curvature [163]. The addition of SOC to the p-wave models of Sr_2RuO_4 provides a platform on which to investigate the interplay between these various sources of anomalous transport in a chiral superconductor, and the results of this are discussed in Sections 5.1.4 and 5.1.5.

5.1.2 Berry Phase Effects

In this section, the connection between the intrinsic AHE and the Berry phase is formalised. In the groundbreaking report by Berry, it was demonstrated that certain parameter-dependent eigenstates gain a phase if the parameter is varied adiabatically in a closed loop in the parameter space [234]. This phase is a gauge-invariant, observable quantity commonly referred to as the "Berry phase" or the "geometric phase". The dependence of the phase change on the geometric properties of the parameter space has been shown to be a fundamentally unifying concept, linking the fields of quantum mechanics, topology and the electronic properties of many-body states.

The Berry phase (γ_n) does not depend on the rate of change of the parameter, as long as the change remains adiabatic. It is dependent, however, on the closed path taken in the parameter space. In this sense, a Berry phase is not a fundamentally useful quantity in defining the magnetic and topological properties of a particular eigenstate. A related quantity which does uniquely

capture these properties is the Berry curvature ($\mathbf{\Omega}_n$), a local property related to the Berry phase via

$$\gamma_n = \int_S \mathbf{\Omega}_n(\mathbf{R}) \cdot \mathrm{d}S\,, \tag{5.1}$$

where $\mathbf{R}$ is the variable parameter and S is the area in parameter space mapped out by the closed loop. This definition allows one to intuitively picture $\mathbf{\Omega}_n$ as a magnetic field in the parameter space, with the phase obtained via a closed loop path analogous to the magnetic flux passing through the loop.

A natural platform on which to study Berry phase effects is provided by the energy states of electrons in crystalline solids. The wavefunction of such an electron is described by a Bloch state, which is parametrised by the Bloch wavevector $\mathbf{k}$. Applying a magnetic field to a solid induces cyclotron orbits which map out closed loops in $\mathbf{k}$-space. If the bandstructure of the lattice displays a finite Berry curvature, an electron eigenstate gains a phase factor upon completing the orbit. This phenomenon has a significant impact on, for example, the energy quantisation of Landau levels [121], and the shift caused by the Berry phase ($\gamma = \pi$) in graphene has been observed experimentally through the quantum Hall effect [249].

The Berry curvature of a Bloch band is defined formally by [218, 235, 250]

$$\mathbf{\Omega}_n(\mathbf{k}) = \nabla_{\mathbf{k}} \times \langle u_{n\mathbf{k}} | \mathrm{i}\nabla_{\mathbf{k}} | u_{n\mathbf{k}} \rangle\,, \tag{5.2}$$

where the states $|u_{n\mathbf{k}}\rangle$ here refer to the cell-periodic components of single-electron Bloch wavefunctions for a general normal state Hamiltonian. The Dirac notation refers in this case to an inner product computed via a real space integral over the unit cell only. By making the relevant symmetry considerations of the basis set, it is possible to deduce immediately the configurations in which the Berry curvature is non-zero. The inversion operator ($\hat{\mathrm{I}}$) transforms real and reciprocal space parameters via

$$\hat{\mathrm{I}}\mathbf{r} = -\mathbf{r}, \quad \hat{\mathrm{I}}\dot{\mathbf{r}} = -\dot{\mathbf{r}}, \quad \hat{\mathrm{I}}\mathbf{k} = -\mathbf{k}, \quad \hat{\mathrm{I}}\dot{\mathbf{k}} = -\dot{\mathbf{k}}. \tag{5.3}$$

According to (5.2), if inversion symmetry holds, the Berry curvature transforms as $\hat{\mathrm{I}}\mathbf{\Omega}_n(\mathbf{k}) = \mathbf{\Omega}_n(-\mathbf{k})$. Performing a time-reversal operation ($\hat{T}$), on the other hand, transforms the parameters as

$$\hat{\mathrm{T}}\mathbf{r} = \mathbf{r}, \quad \hat{\mathrm{T}}\dot{\mathbf{r}} = -\dot{\mathbf{r}}, \quad \hat{\mathrm{T}}\mathbf{k} = -\mathbf{k}, \quad \hat{\mathrm{T}}\dot{\mathbf{k}} = \dot{\mathbf{k}}. \tag{5.4}$$

The resulting transformation of $\mathbf{\Omega}_n$ incurs a sign change, meaning that $\hat{\mathrm{T}}\mathbf{\Omega}_n(\mathbf{k}) = -\mathbf{\Omega}_n(-\mathbf{k})$ if TRS is present. Thus, the Berry curvature vanishes for any non-degenerate state which

is simultaneously time-reversal symmetric and centrosymmetric. In addition, the factor i in equation (5.2) highlights that, for a normal state Hamiltonian, the inclusion of a spin-orbit perturbation is required. Without SOC, the Hamiltonian and wavefunctions are real and the Berry curvature is zero.

Extending to the superconducting state, the Berry curvature must be defined in terms of Bloch-type quasiparticle eigenstates of the BdG equation. To maintain consistency with the notation used thus far, the eigenstates are written as two-component vectors $\boldsymbol{\psi}_{n\mathbf{k}}$. The definition of the Berry curvature requires the use of the cell-periodic components of the superconducting states, however, which will be referred to via

$$\boldsymbol{\theta}_{n\mathbf{k}}(\mathbf{r}) = \mathrm{e}^{-\mathrm{i}\mathbf{k}\cdot\mathbf{r}}\boldsymbol{\psi}_{n\mathbf{k}}(\mathbf{r}) = \begin{pmatrix} u_{n\mathbf{k}}(\mathbf{r}) \\ v_{n\mathbf{k}}(\mathbf{r}) \end{pmatrix}. \tag{5.5}$$

The cell-periodic quasiparticle states are then solutions of $\mathbf{k}$-dependent BdG equation,

$$\begin{gathered} \underline{H}_{\mathbf{k}}(\mathbf{r})\boldsymbol{\theta}_{n\mathbf{k}}(\mathbf{r}) = \epsilon_{n\mathbf{k}}\boldsymbol{\theta}_{n\mathbf{k}}(\mathbf{r}) \\ \begin{pmatrix} \hat{H}_{\mathbf{k}}(\mathbf{r}) & \Delta(\mathbf{r}) \\ \Delta^{\dagger}(\mathbf{r}) & -\hat{H}^{*}_{-\mathbf{k}}(\mathbf{r}) \end{pmatrix} \begin{pmatrix} u_{n\mathbf{k}}(\mathbf{r}) \\ v_{n\mathbf{k}}(\mathbf{r}) \end{pmatrix} = \epsilon_{n\mathbf{k}} \begin{pmatrix} u_{n\mathbf{k}}(\mathbf{r}) \\ v_{n\mathbf{k}}(\mathbf{r}) \end{pmatrix}, \end{gathered} \tag{5.6}$$

where $\hat{H}_{\mathbf{k}}(\mathbf{r}) = \mathrm{e}^{-\mathrm{i}\mathbf{k}\cdot\mathbf{r}}\hat{H}(\mathbf{r})\mathrm{e}^{\mathrm{i}\mathbf{k}\cdot\mathbf{r}}$.

The Berry curvature of the superconducting state can be defined by replacing the functions $u_{n\mathbf{k}}$ in (5.2) with $\boldsymbol{\theta}_{n\mathbf{k}}$. The $\mathbf{k}$-derivatives of these states are then replaced with a $\mathbf{k}$-derivative of the Hamiltonian operator (as demonstrated in equations (4.57)-(4.58)), resulting in an equation for the Berry curvature written in terms of the BdG Hamiltonian [163],

$$\boldsymbol{\Omega}_{n}(\mathbf{k}) = \mathrm{i}\sum_{n\neq n\prime} \frac{\langle\boldsymbol{\theta}_{n\mathbf{k}}|\nabla_{\mathbf{k}}\underline{H}_{\mathbf{k}}|\boldsymbol{\theta}_{n\prime\mathbf{k}}\rangle \times \langle\boldsymbol{\theta}_{n\prime\mathbf{k}}|\nabla_{\mathbf{k}}\underline{H}_{\mathbf{k}}|\boldsymbol{\theta}_{n\mathbf{k}}\rangle}{(\epsilon_{n\mathbf{k}} - \epsilon_{n\prime\mathbf{k}})^{2}}. \tag{5.7}$$

Equation (5.7) elucidates the various sources of Berry curvature within a particular band-structure, assuming that either time-reversal symmetry or inversion symmetry have been broken as discussed above. The gradient of the Hamiltonian taken with respect to the Bloch wavevector is directly related to the velocity operator. Given that the sum is restricted to non-equal bands, this reveals the reliance of the curvature on finite inter-band velocity matrix elements. The requirement for a multi-band structure with inter-orbital coupling is clearly highlighted here.

Furthermore, the denominator indicates that the curvature diverges at band degeneracies. The vector components are strongly enhanced, however, by inter-band transitions which occur at near-degeneracies in the bandstructure. Introducing a spin-orbit coupling matrix thus plays a key role in the study of anomalous transport phenomena. The spin-orbit interaction induces splitting and avoided crossings at points in the dispersion which would otherwise be degeneracies,

as demonstrated in Figs. (3.6)-(3.9), which can result in a significant enhancement of the Berry curvature.

The link between the Berry curvature and the anomalous Hall conductivity can be written explicitly through the Hall sum rule or the Kramers-Kronig transformation. Formally, the two properties in the normal state have been demonstrated to be related via [230]

$$\int_0^\infty \mathrm{d}\omega \frac{\mathrm{Im}[\sigma_{xy}(\omega)]}{\omega} = -\frac{\pi e^2}{2\hbar} \sum_n \int_{BZ} \frac{\mathrm{d}\mathbf{k}}{(2\pi)^3} [\mathbf{\Omega}_n(\mathbf{k})]_{\hat{z}} f_{n\mathbf{k}}\,, \tag{5.8}$$

where ω is the frequency of the applied field which induces the conductivity. It has been verified that this equation holds for a Berry curvature arising from Bloch quasiparticles in a general superconducting state [163]. While equation (5.8) is not implemented here to compute either the Hall conductivity or Berry curvature, it serves as a potent demonstration of the reliance of anomalous transport properties on Berry phase effects in the quasiparticle bandstructure for a superconducting state.

Equation (5.8) also demonstrates that the enhancement of the Berry curvature does not necessarily lead to an increased Hall conductivity, as the two properties are related via a sum rule. This would be expected intuitively in the case of a normal state ferromagnet. In that scenario, the influence of SOC is required to generate an anomalous Hall response, yet equation (5.7) indicates that the Berry curvature is maximised by infinitesimally small avoided crossings, which would be associated with a negligibly small SOC. The sum rule (5.8) shows that the contribution to the Hall conductivity arising from this would be negligible when integrated across the Brillouin zone.

A further link between the Berry curvature and anomalous transport phenomena can be made by formalising the origin of the edge current in a TRS breaking system. The anomalous velocity introduced by KL theory relates to the Berry curvature by $\mathbf{v}_A \propto \mathbf{F} \times \mathbf{\Omega}$ [218]. In the case of the Hall effect, the force exerted on the charge carriers is given by $q\mathbf{E}$, where $\mathbf{E}$ is the electric field associated with an applied voltage. Consider instead the surface of a sample. A finite-size lattice is bounded by a potential $V(\mathbf{r})$, which is 0 in the bulk of the material, but goes to infinity at the boundary. This potential exerts a force on charge carriers near to the boundary ($\mathbf{F} = \nabla V(\mathbf{r})$), which points perpendicularly to the surface. An anomalous velocity is thus generated parallel to the surface if the Berry curvature is non-zero, resulting in the net edge current expected in a multi-band chiral superconductor.

5.1.3 Calculating the Anomalous Hall Conductivity

Intrinsic contributions to the Hall conductivity can be computed by considering the linear response of a stationary state to an external perturbation. For a normal metal, the appropriate expression is derived from a general form of the Kubo formula [115]. The generalisation of the equation to a superconducting state is outlined below, having originally been performed by

Capelle *et al* [251, 252]. Their approach derives the Hall conductivity arising in the specific case in which the perturbation is generated by the absorption of an incident, circularly polarised photon, which is appropriate for study of the Kerr effect (as discussed further in Section 5.2).

The electrical power generated in a material under a general, time-dependent perturbation is given by

$$P = \sum_{i,i\prime} (E_{i'} - E_i) f_i (1 - f_{i'}) w_{i \to i\prime}, \tag{5.9}$$

where i and i' denote the states before and after the perturbtation and w is the transition probability rate. The transition rate is defined through Fermi's golden rule for first-order time-dependent perturbations [36]. For a transition corresponding to the absorption of a photon with energy $\hbar\omega$, this takes the form

$$w_{n \to n\prime} = \frac{2\pi}{\hbar} \left| \langle \boldsymbol{\psi}_{n\prime\mathbf{k}} | \delta \underline{H}^{\dagger}(\mathbf{r}, t) | \boldsymbol{\psi}_{n\mathbf{k}} \rangle \right|^2 \delta(\epsilon_{n\prime\mathbf{k}} - \epsilon_{n\mathbf{k}} - \hbar\omega), \tag{5.10}$$

where $\delta\underline{H}$ is the perturbation matrix associated with incident radiation. The perturbation matrix must be conformed to the particle-hole symmetry of the BdG framework. Assuming that the absorbed photon does not perturb the pair potential, the perturbing matrix is given in the electron-hole basis by

$$\delta \underline{H}(\mathbf{r}, t) = \begin{pmatrix} \delta h(\mathbf{r}, t) & 0 \\ 0 & -(\delta h(\mathbf{r}, t))^* \end{pmatrix}, \tag{5.11}$$

where δh describes the interaction of a particle with the incident photon. This interaction is defined by

$$\delta h(\mathbf{r}, t) = \frac{\mathrm{i}e}{2m} \frac{E_0}{\omega} \mathrm{e}^{\mathrm{i}(\omega t - \mathbf{q}\cdot\mathbf{r})} \boldsymbol{\epsilon} \cdot \hat{\mathbf{p}}, \tag{5.12}$$

where e is the electric charge, E_0 is the amplitude of the incident radiation, $\mathbf{q}$ is the propagation direction and $\boldsymbol{\epsilon}$ is the polarisation.

For circularly polarised light, the polarisation vectors are

$$\boldsymbol{\epsilon}_L = \frac{1}{\sqrt{2}} \begin{pmatrix} 1 \\ \mathrm{i} \\ 0 \end{pmatrix}, \quad \boldsymbol{\epsilon}_R = \frac{1}{\sqrt{2}} \begin{pmatrix} 1 \\ -\mathrm{i} \\ 0 \end{pmatrix}, \tag{5.13}$$

where L and R denote left and right-handed orientations respectively. Inserting equations (5.10)-(5.13) into (5.9), the power absorption as a function of photon frequency and polarisation can be obtained,

$$P(\omega,\boldsymbol{\epsilon}_{L/R}) = \frac{\pi^2 e^2 {E_0}^2}{2\omega} \sum_{n,n\prime,\mathbf{k}} f_{n\mathbf{k}}\left(1-f_{n\prime\mathbf{k}}\right)\left|\langle\boldsymbol{\psi}_{n\prime\mathbf{k}}\left|\underline{H}_I(\boldsymbol{\epsilon}_{L/R})\right|\boldsymbol{\psi}_{n\mathbf{k}}\rangle\right|^2 \delta(\epsilon_{n\prime\mathbf{k}}-\epsilon_{n\mathbf{k}}-\hbar\omega), \tag{5.14a}$$

$$\underline{H}_I(\boldsymbol{\epsilon}_{L/R}) = -\mathrm{i}\begin{pmatrix} \boldsymbol{\epsilon}_{L/R}\cdot\hat{\mathbf{p}} & 0 \\ 0 & \boldsymbol{\epsilon}_{L/R}\cdot\hat{\mathbf{p}} \end{pmatrix}, \tag{5.14b}$$

where $\underline{H}_I(\epsilon_{L/R})$ is the Hamiltonian describing the interaction with a left/right-handed photon.

The real and imaginary components of the optical Hall conductivity are directly related to the power absorption via [253]

$$\begin{aligned}\mathrm{Im}\left[\sigma_{xy}(\omega)\right] &= \frac{1}{V{E_0}^2}[P(\omega,\epsilon_L)-P(\omega,\epsilon_R)] \\ &= \frac{\pi^2 e^2}{2\omega V m^2}\sum_{n,n\prime,\mathbf{k}} f(\epsilon_n(\mathbf{k}))[1-f(\epsilon_{n\prime}(\mathbf{k})]\delta(\epsilon_n(\mathbf{k})-\epsilon_{n\prime}(\mathbf{k})-\hbar\omega) \\ &\qquad \times\left(\left|\langle\boldsymbol{\psi}_{n\prime\mathbf{k}}\left|\underline{H}_I(\epsilon_L)\right|\boldsymbol{\psi}_{n\mathbf{k}}\rangle\right|^2-\left|\langle\boldsymbol{\psi}_{n\prime\mathbf{k}}\left|\underline{H}_I(\epsilon_R)\right|\boldsymbol{\psi}_{n\mathbf{k}}\rangle\right|^2\right),\end{aligned} \tag{5.15}$$

$$\begin{aligned}\mathrm{Re}\left[\sigma_{xy}(\omega)\right] &= \frac{1}{V{E_0}^2}[P(\omega,\epsilon_L)+P(\omega,\epsilon_R)] \\ &= \frac{e^2\hbar}{Vm^2}\sum_{n,n\prime,\mathbf{k}} f(E_n(\mathbf{k}))\left[1-f(E_{n\prime}(\mathbf{k})\right] \\ &\qquad \times\frac{\left(\left|\langle\boldsymbol{\psi}_{n\prime\mathbf{k}}\left|\underline{H}_I(\epsilon_L)\right|\boldsymbol{\psi}_{n\mathbf{k}}\rangle\right|^2-\left|\langle\boldsymbol{\psi}_{n\prime\mathbf{k}}\left|\underline{H}_I(\epsilon_R)\right|\boldsymbol{\psi}_{n\mathbf{k}}\rangle\right|^2\right)}{\left(\epsilon_n(\mathbf{k})-\epsilon_{n\prime}(\mathbf{k})\right)^2-(\hbar\omega)^2}.\end{aligned} \tag{5.16}$$

The matrix elements of the interaction Hamiltonian must be written in terms of the tight-binding solutions. This conversion is performed by expanding the particle-hole wavefunctions in the tight-binding basis, via the method outlined in equations (3.22)-(3.25).

The following identities and conditions are utilised in order to obtain the matrix elements. Firstly, the momentum operator is related to the lattice Hamiltonian via

$$\hat{\mathbf{p}} = \frac{-\mathrm{i}m}{\hbar}\left(\hat{\mathbf{r}}\hat{H}(\mathbf{r})-\hat{H}(\mathbf{r})\hat{\mathbf{r}}\right). \tag{5.17}$$

Note that this relationship was introduced in (4.14), but the constants m and $\hbar$ were set to 1 for the purpose of the derivation in Section .. , while here they will be considered explicitly. Inserting (5.17) into the interaction operator, the assumption of a vanishing dipole moment can be implemented using

$$\int \mathrm{d}\mathbf{r}\,\phi^*_{j\prime}(\mathbf{r}-\mathbf{R}'_i)\hat{\mathbf{r}}\phi_j(\mathbf{r}-\mathbf{R}_i) = \mathbf{R}\delta_{ii\prime}\delta_{jj\prime}, \tag{5.18}$$

where j refers to the orbital and spin components of the wavefunction (d,α). Performing the tight-binding expansion, the interaction matrices become

$$\langle \boldsymbol{\theta}_{n'\mathbf{k}} \left| \underline{H}_I(\epsilon_{L/R}) \right| \boldsymbol{\theta}_{n\mathbf{k}} \rangle = \frac{m\epsilon^*_{L/R}}{\mathrm{i}\hbar} \begin{pmatrix} \mathbf{u}_{n'}(\mathbf{k}) \\ \mathbf{v}_{n'}(\mathbf{k}) \end{pmatrix}^\dagger \begin{pmatrix} \nabla_{\mathbf{k}} \underline{H}(\mathbf{k}) & 0 \\ 0 & \nabla_{\mathbf{k}} \underline{H}(\mathbf{k}) \end{pmatrix} \begin{pmatrix} \mathbf{u}_n(\mathbf{k}) \\ \mathbf{v}_n(\mathbf{k}) \end{pmatrix}, \tag{5.19}$$

where the relation $\nabla_{\mathbf{k}} H_{jj'}(\mathbf{k}) = \mathrm{i}\mathbf{R} H_{jj'}(\mathbf{k})$ obtained from equation (3.24) has been applied. A full set of orbitals has also been inserted to obtain this result via the completeness relation

$$\sum_{j,\mathbf{R}} \phi_j(\mathbf{r}-\mathbf{R}) \phi_j^*(\mathbf{r}'-\mathbf{R}) = \delta(\mathbf{r}-\mathbf{r}'). \tag{5.20}$$

By solving the BdG equation self-consistently, the optical Hall conductivity was computed for a given photon frequency. Given that contributions arise from inter-band coupling, the natural frequency range in which to investigate this property is set by the energy scale of the inter-orbital gap in the pairing structure and any inter-band near-degeneracies in the bandstructure near to the Fermi level. This is a low-frequency regime of around 0-0.1 eV, given by the gap interaction parameters, the energies of the band splitting induced by the addition of SOC (see Fig. 3.8) and the inter-orbital hopping terms (see Tables 3.1 and 3.2) [129]. Inter-orbital transitions in this range are most prominent at the [110] region on the Fermi surface where all three bands cross the Fermi energy in close proximity in $\mathbf{k}$-space.

5.1.4 Model Calculations: 3D

The results of the calculations of the transverse conductivity for the 3D multi-band, chiral p-wave model of Sr_2RuO_4 are presented below. This extends the results presented previously for this model excluding spin-orbit coupling [129, 165]. In the normal state, SOC is essential to generate an AHE, and must be present in conjunction with multi-band ferromagnetism. Multi-band, unconventional superconductivity, however, provides a mechanism to induce a transverse conductivity without the need for SOC as the Cooper pairs have an intrinsic orbital magnetisation. As discussed in Chapter 4, the introduction of SOC appears to facilitate a transfer of magnetic moment from the orbital to spin component, and therefore the results presented below provide an interesting insight into the influence that the interplay of spin and orbital magnetisation have on the anomalous transport phenomena appearing in a superconducting state.

Figs. 5.1 and 5.2 depict the computed values of the real and imaginary components of the optical Hall conductivity in the low-frequency regime, for the model with and without the inclusion of SOC. The addition of a spin-orbit interaction clearly has a severe impact on the conductivity, revealing rich structure below 0.1 eV. In both components, the signal remains negligible below the onset of around 10 meV, even in the presence of SOC. The transport here appears to be strictly

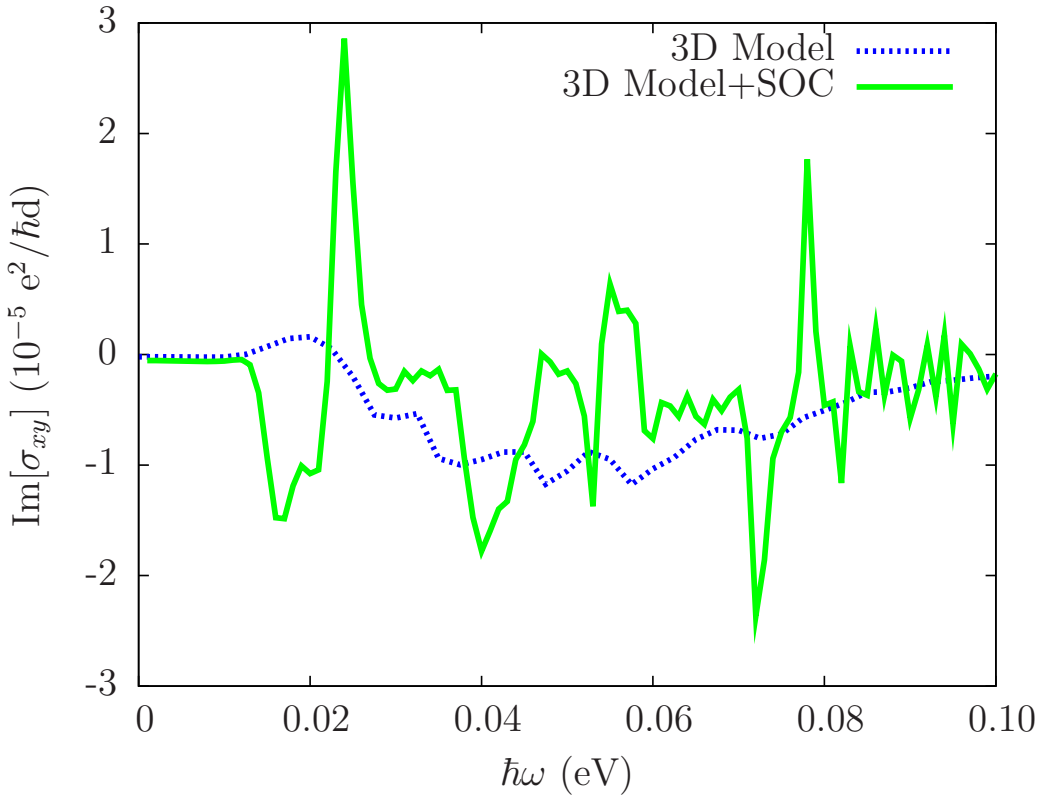

FIGURE 5.1. The imaginary component of the Hall conductivity generated by an incident photon in the low-frequency regime at $T = 0$, for the 3D, p-wave model with and without SOC included.

limited to incident energies exceeding the inter-orbital hopping energy t'_{bc}. Sharp features are introduced in the range 0.01-0.1 eV by the inclusion of the spin-orbit interaction.

As a further demonstration of the relation between the Hall conductivity and Berry curvature, heat maps of the contributions to σ_{xy} throughout the Brillouin zone are depicted in Fig. 5.3. The calculations are performed at zero frequency, where only the real component is finite, and at zero temperature. Evidently, the contributions to the Hall conductivity stem from rather distinct regions in the Brillouin zone when compared with the onset of the heat capacity (see Fig. 3.14). Peaks appear around the near degeneracies along the [110] directions, where SOC induces a stronger band mixing as well as further avoided crossings. It has been demonstrated previously that these are indeed the regions of the Brillouin zone which drive the Berry curvature for this particular model in the absence of SOC [163]. In contrast, the heat capacity is driven primarily by the nodes and minima in the bandstructure, which are largely independent of the spin-orbit interaction.

The upper plot of Fig. 5.3 reveals that the anomalous Hall response occurs only in the α and β bands when spin-orbit coupling is absent. A vital impact of the addition of the spin-orbit interaction is that contributions from the predominantly d_{xy} band become clearly evident (see

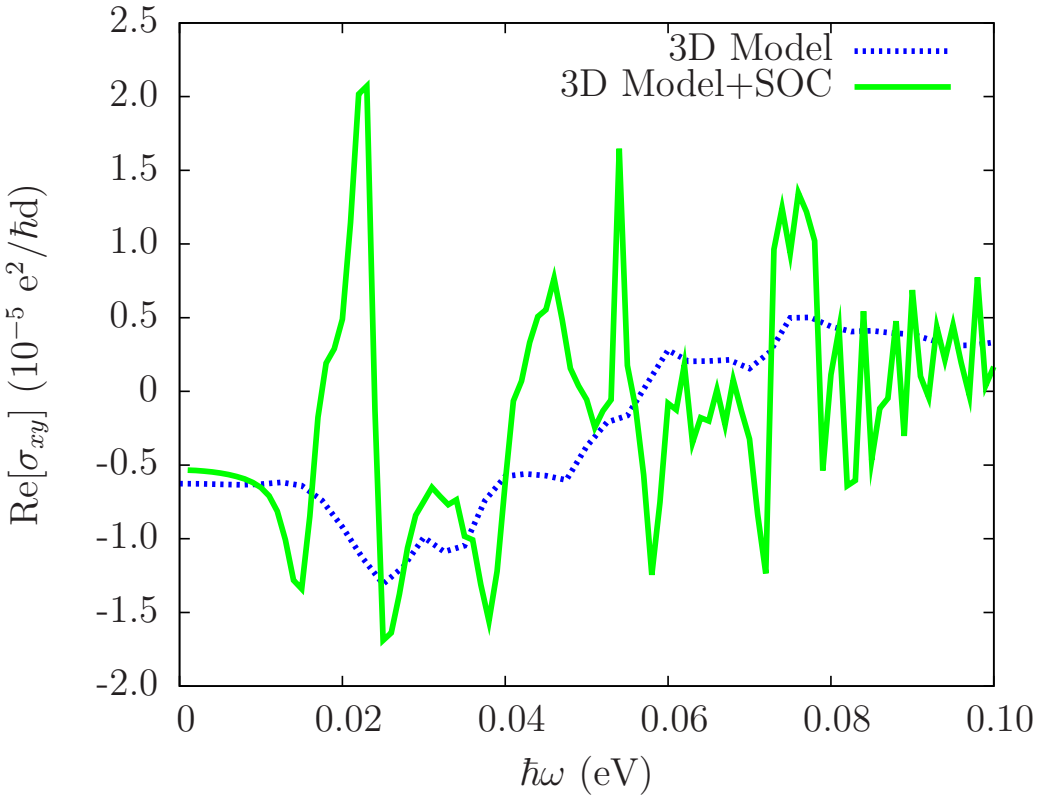

FIGURE 5.2. The real component of the Hall conductivity generated by an incident photon in the low-frequency regime at $T = 0$, for the 3D p-wave model with and without SOC included.

the lower plot of Fig. 5.3). The γ band is now active in the AHE due to the additional orbital character mixing shown in Fig. 3.9. However, this band contributes to the Hall conductivity with the opposite sign with respect to contributions from the hybridised 1D-bands, which creates much more fine structure throughout the Brillouin zone. This response is very similar to that seen in the spin magnetic moment following the addition of SOC, where the γ band contributes with opposite sign to the α and β bands (see Fig. 4.6). The additional inter-orbital mixing thus generates fine structure in the otherwise very localized contributions. This is the likely cause of the sharp oscillations observed in the frequency-resolved plots in comparison to the relatively smooth curves obtained in the absence of SOC (see Figs. 5.1 and 5.2).

5.1.5 Model Calculations: 2D

The Hall conductivity calculations were repeated through the two-dimensional model with extended pairing. Results are compared from the self-consistent approach (see Fig. 5.4) to the model using the renormalised fit (Fig. 5.5). As can be observed, the qualitative behaviour of the Hall conductivity with respect to frequency remains similar for both gap configurations. However,

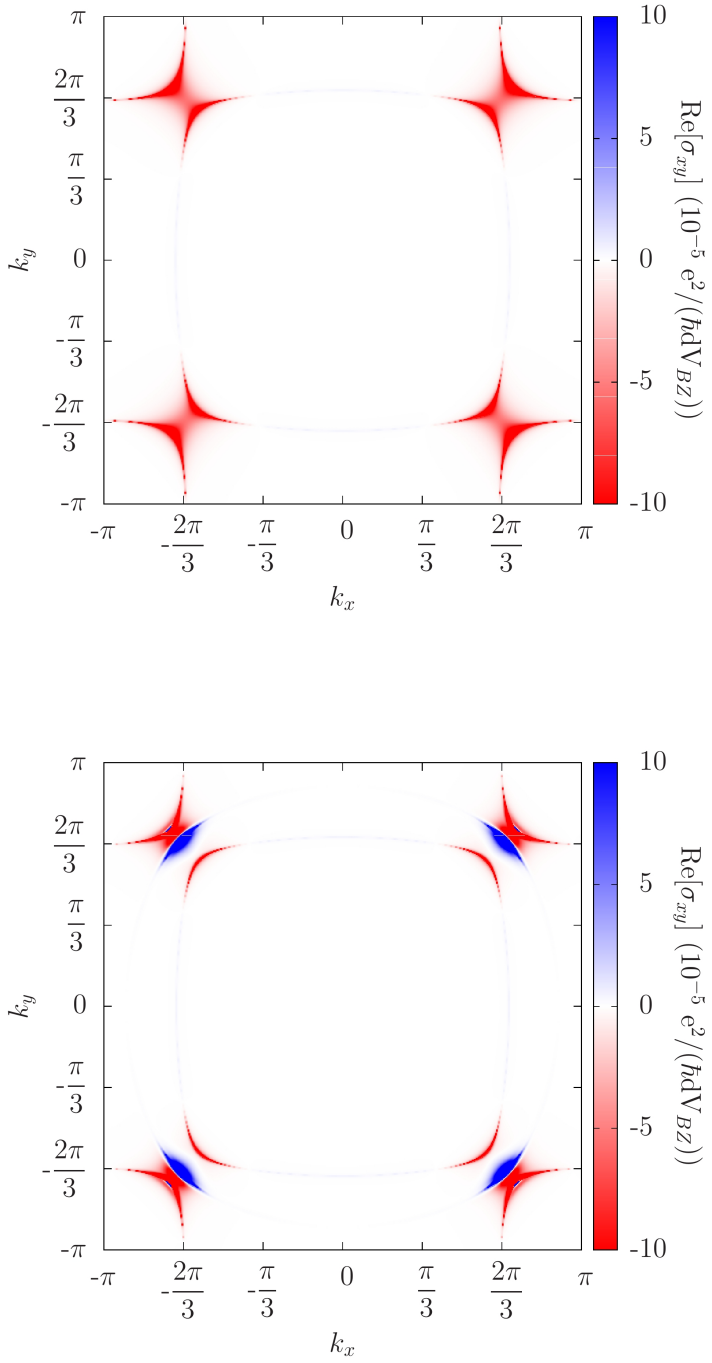

FIGURE 5.3. The k_x-k_y resolved optical conductivity at $k_z = 0$ and temperature $T = 0$. The plots show the contributions without (top) and with (bottom) the inclusion of SOC. The contributions come predominantly from a small area along the [110] direction where the band mixing is most prevalent.

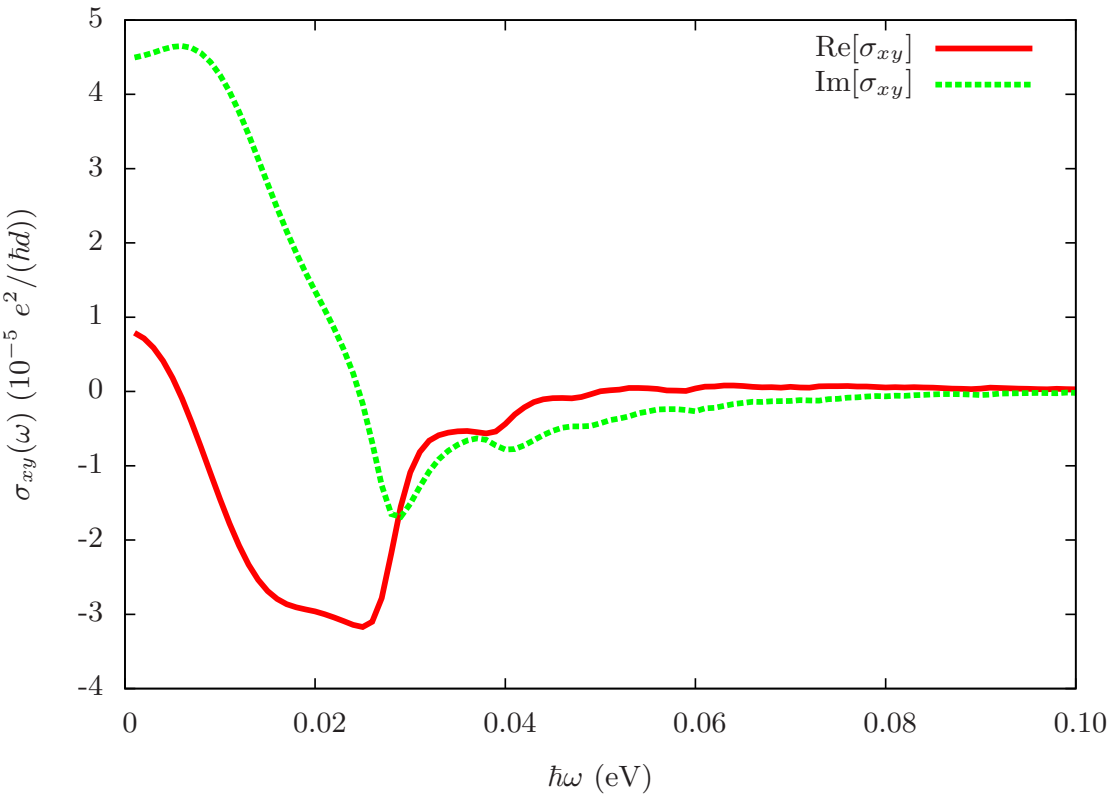

FIGURE 5.4. The real and imaginary components of the Hall conductivity generated by an incident photon in the low-frequency regime at $T = 0$, for the model computed self-consistently through the BdG framework.

the magnitude of the computed effect is vastly different. It is interesting to note here that the imaginary component now becomes non-zero at zero frequency. This is most likely a result of the distinctly different topological structure of the extended superconducting order parameter.

The large enhancement of the conductivity observed with the gap magnitudes taken from the renormalised fit is similar to the difference observed in the magnetic moment for the two approaches (as displayed in Section 4.3). These results are likely driven by the fact that the renormalised fit displays deep minima on all three bands, which is not observed at low temperature in the self-consistent approach. The gap minima on the γ and α bands appear in close proximity in $\mathbf{k}$-space (see Fig. 3.17), leading to further inter-band near-degeneracies in the quasiparticle bandstructure. The behaviour of the two nodal structures also displays little qualitative difference in the Brillouin zone resolved plot of the real component at zero frequency (Fig. 5.6). It can be seen, however, that there is no longer the stark contrast in the sign of the contributions from the different bands that was seen in the 3D model (Fig. 5.3). This results in the considerably smoother frequency-resolved plots observed here, and also contributes to the enhanced net Hall conductivity.

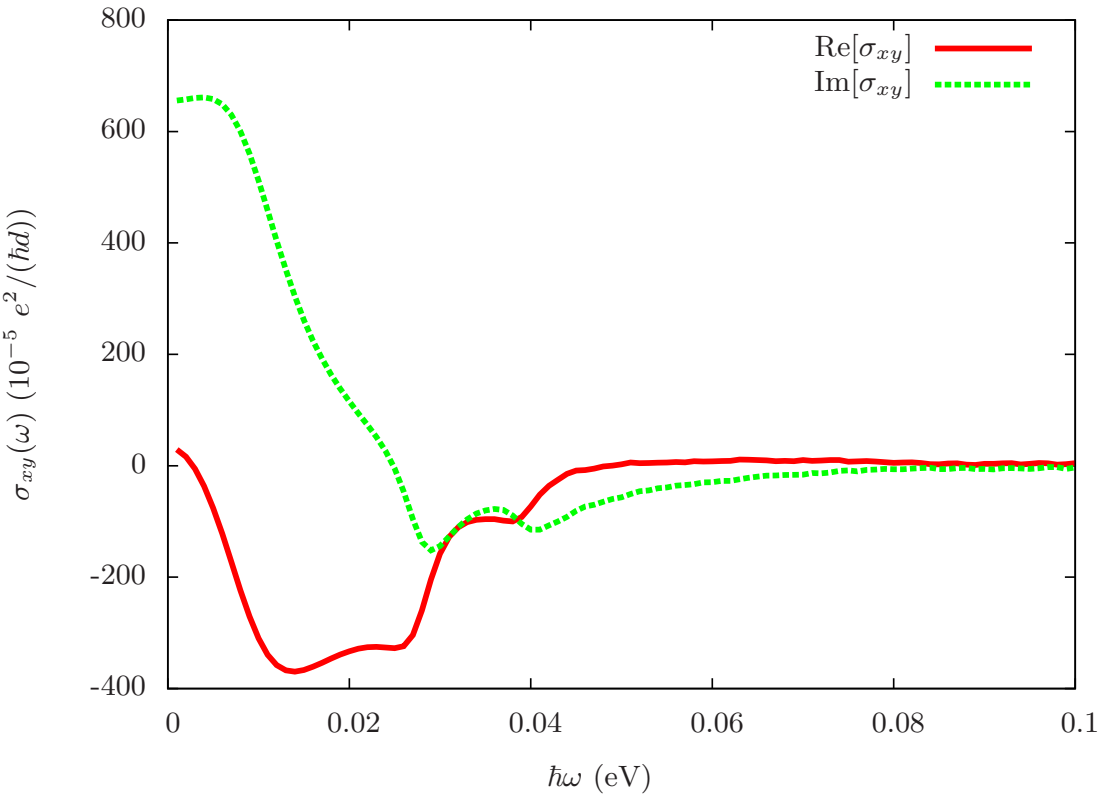

FIGURE 5.5. The real and imaginary components of the Hall conductivity generated by an incident photon in the low-frequency regime at $T = 0$, for the model obtained from renormalised fitting parameters.

The results from this section verify that it is possible to generate an anomalous Hall effect through an intrinsic mechanism for a multi-band p-wave model of Sr_2RuO_4. Highlighted is the dominant influence of the spin-orbit interaction on the spontaneous Hall voltage in the low-frequency range. The avoided crossings and band mixing induced by SOC have a significant impact on the inter-band velocity matrix elements, leading to much more fine structure in the Berry curvature throughout the Brillouin zone for the 3D model. In addition, comparison with the results obtained from the extended pairing model highlight the influence of minima in the gap structure and the distinct topological properties of this order parameter.

Direct experimental measurement of the anomalous transport properties of general superconductors is restricted by the influence of Meissner screening, as discussed in Section 4.1. However, a consequence of the appearance of an anomalous Hall conductivity is the optical phenomenon referred to as the Kerr effect. This provides an alternative method with which to identify an AHE in a chiral superconductor. In the following section, the results presented here are benchmarked with respect to the experimental identification of the AHE made through the observation of the polar Kerr effect in Sr_2RuO_4 [102].

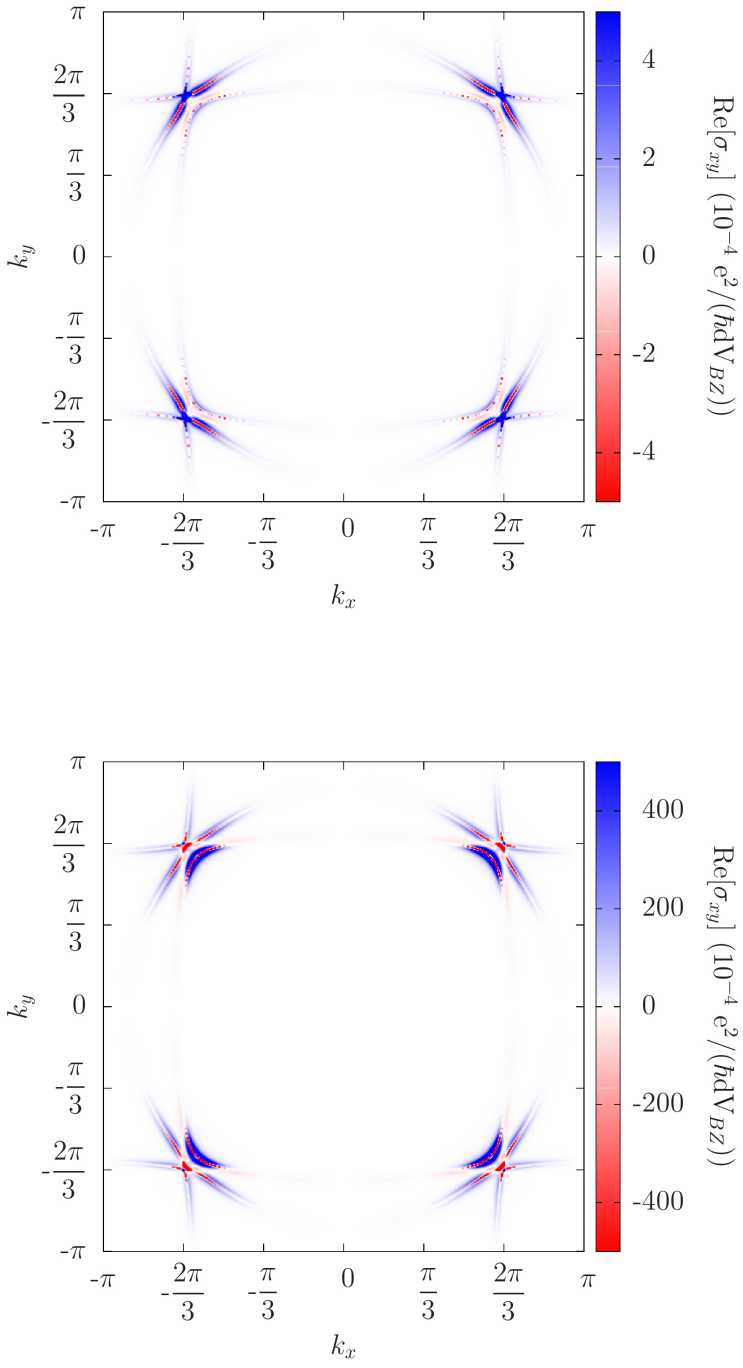

FIGURE 5.6. The k_x-k_y resolved optical conductivity at $k_z = 0$ and temperature $T = 0$. The plots show the contributions to the real part of the conductivity in the self-consistent solutions (upper) and renormalised fit (lower). The contributions come predominantly from a small area along the [110] direction where the band mixing is enhanced.

5.2 Polar Kerr Effect

A consequence of broken time-reversal symmetry in a general state is the occurrence of magnetic circular dichroism [254, 255]. This is the phenomenon in which a material will interact differently with incident circularly polarised light depending on its handedness. A quantifiable measure of dichroism can be attained by considering a beam of linearly polarised light falling onto a TRS-breaking surface. Such a beam can be equated with the sum of two circularly polarised beams of identical intensity but opposite handedness. Due to the dichroism of the surface, the reflectivity of right and left-handed photons is different and the plane of polarisation of the beam experiences a phase shift upon reflection (see Fig. 1.5). This phenomenon is known as the Kerr effect. The polar Kerr effect (PKE) refers to the specific case in which the magnetisation of the state is perpendicular to the plane of reflection.

Given that Meissner screening inhibits the study of the internal magnetisation in unconventional superconducting states, the Kerr effect was proposed as a possible alternative approach to determining the time-reversal properties of a state [98, 251, 252]. However, the magnitude of the Kerr shift is relatively small, and a very precise apparatus is required to detect the effect. In Sections 5.2.1 and 5.2.2 below, an outline of the experimental procedure and observations of the Kerr effect in superconductors is given, followed by an investigation into the effect observed through the p-wave models of Sr_2RuO_4 in 5.2.3.

5.2.1 Experimental Details

The first experimental observation of circular dichroism in a superconducting material was made in 1996 [256, 257]. Magnetotransmission measurements on $YBa_2Cu_3O_7$ (YBCO) thin films demonstrated that the intensity of transmitted infrared beams varies between left and right-circularly polarised light. In the following years, however, a Kerr signal was not reported in any high-T_c materials due to the limitations of the available apparatus. Observation of Kerr shifts smaller than 100 nrad has been made possible in recent years by the advancement of the Sagnac interferometer (see Fig. 5.7).

The interferometer obtains Kerr measurements via the following process [33]. Two linearly polarised beams are transmitted by a polarisation maintaining optical fiber, such that their polarisations are aligned perpendicularly. The beams pass through a quarter-wave plate oriented at 45°, causing them to be converted into right and left-circular polarisations respectively. While the two beams are circularly polarised, they reflect from the sample surface and return to the detector along the same path, meaning that their path lengths are identical. The relative phase shift between the beams at the detector is then equal to twice the Kerr angle.

It should be noted that this set up refers specifically to a zero-area Sagnac interferometer, as the two beams follow the same path. The conventional Sagnac interferometer is set up such that the beams are split and follow separate paths, thus enclosing a finite loop. Although the

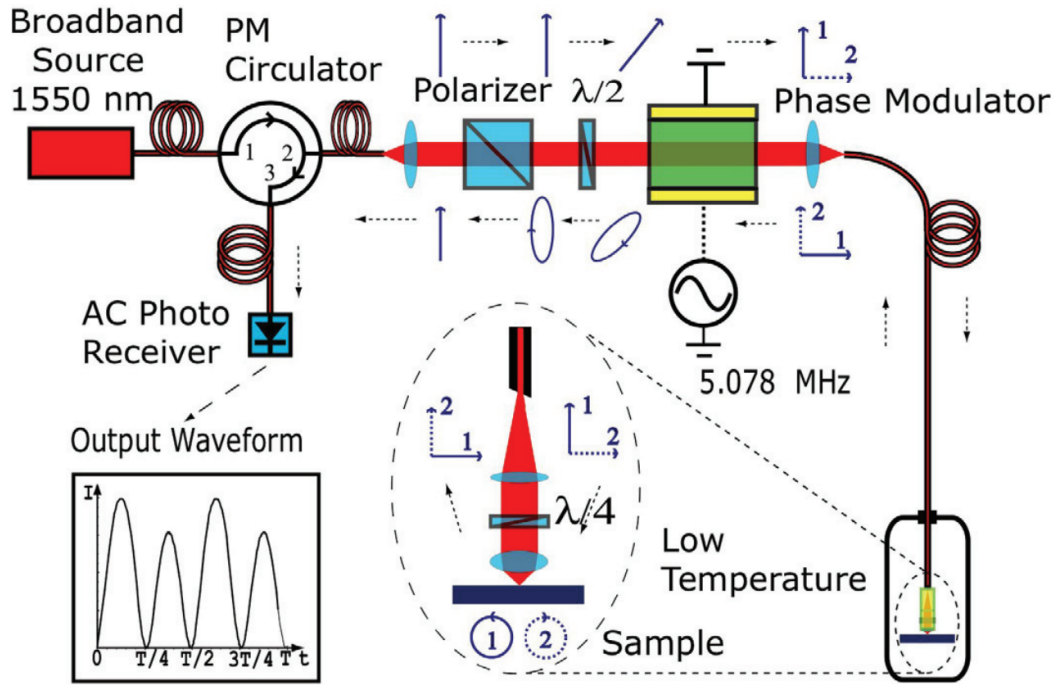

FIGURE 5.7. Apparatus set up for the zero-area Sagnac interferometer. Labels 1 and 2 denote the two polarised beams and the arrows describe the polarisation state at each point along the optical path. Figure recreated from ref. [33].

finite-area set up can be used to measure a Kerr shift [258], it was initially proposed to detect small gyroscopic rotations [259]. The advantage of the zero-area method is that it is sensitive only to TRS-breaking mechanisms, and so any rotation of the platform on which the apparatus is placed will not affect the Kerr measurement [260].

A finite Kerr signal was observed in Sr_2RuO_4 in 2006, the first such measurement of the effect in a superconductor [102]. The Kerr angle measured here reached 65 nrad at temperatures approaching 0 K. Studying both even and odd harmonics in the signal from the detector, it was possible to verify that the onset of a Kerr response coincides precisely with the formation of a superconducting state. Odd harmonics are proportional to the Kerr angle while even harmonics are proportional to the intensity of the reflected beam. The even harmonics can be used to monitor phase transitions, as any TRS-breaking transition will result in a shift in the reflectivity of the surface.

In addition to the identification of a Kerr shift, the authors demonstrated that it is possible to "train" the sample into which of the two chiralities it chooses at T_c (see Fig. 5.8). Fields of ±47 Oe were applied as the sample was cooled, with the resulting Kerr shift being equal in magnitude but opposite in direction depending on the direction of the external field. Application of an external TRS-breaking field during the transition thus fixes the direction of the local magnetic moment

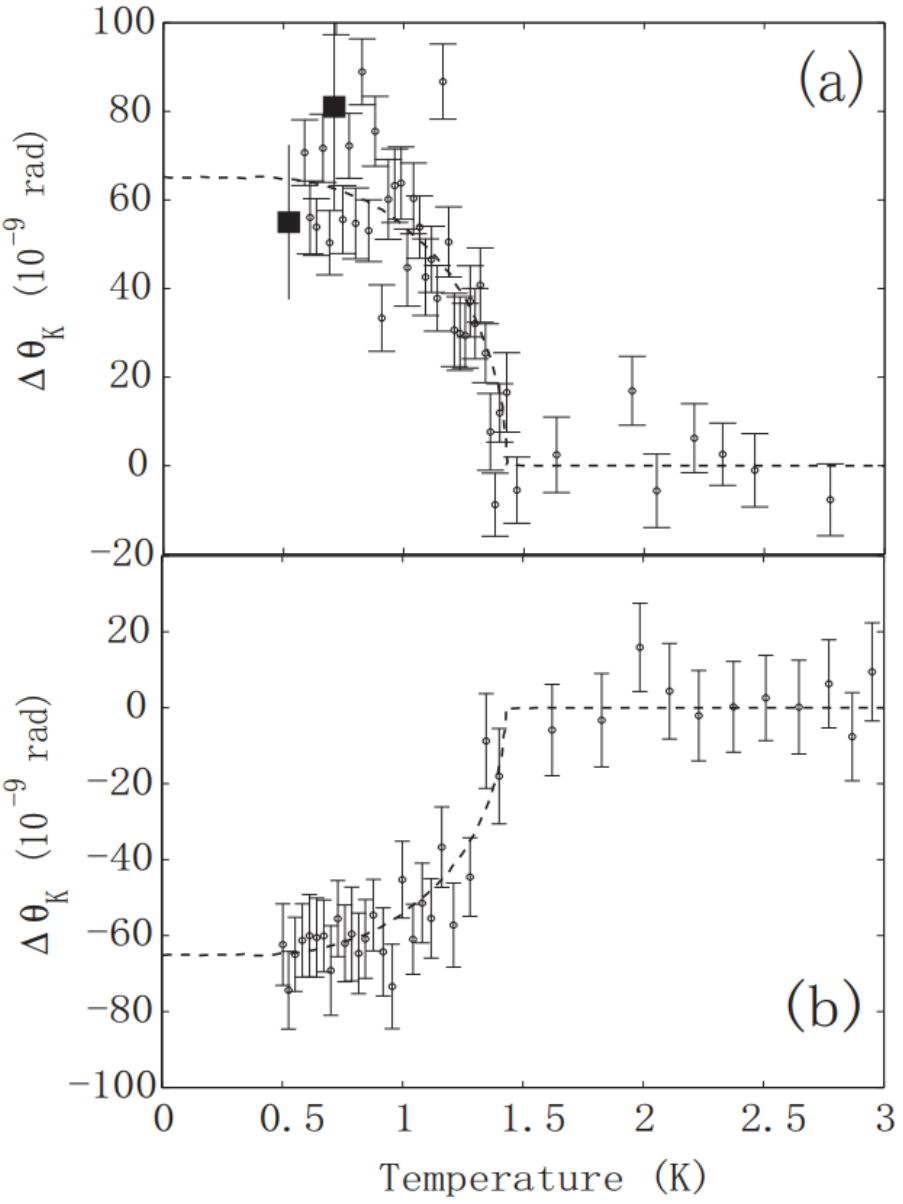

FIGURE 5.8. Field-cooled Kerr angle measurements on Sr_2RuO_4, demonstrating a dichroic response at the superconducting transition. a) An external magnetic field of 47 Oe is applied as the sample is cooled through 1.5 K. b) Repeat measurements with the field applied in the opposite direction. Figure recreated from ref. [102].

associated with the chiral Cooper pairs formed at 1.5 K. The same effect was demonstrated through measurements of the Kerr effect in the heavy-fermion compound UPt_3 [86].

Through repeat measurements in zero-field, it was demonstrated that the magnitude of the Kerr effect is generally constant, altering only in phase depending on the handedness chosen at T_c. One particular measurement, however, reported a significantly reduced Kerr shift which changed in direction upon increasing temperature. This establishes that the domain size is likely a few times larger than the beam size, with the latter measurement occurring when the beam fell over a domain wall. It was estimated that the lower bound for the domain size of the superconducting state in Sr_2RuO_4 is approximately 50 μm [102]. This is of vital importance when comparing with the studies made in search of edge currents, outlined in Section 4.1.3. Domains of 50 μm would be well within the resolution of magnetometry measurements and the local edge magnetisation should therefore be visible experimentally.

A further noteworthy comment is that the anomalous Hall transport driving the Kerr effect in Sr_2RuO_4 appears to be entirely spontaneous. Measurements of the Kerr effect made in the presence of a magnetic field were compared with zero-field measurements, and both approaches give shifts of the same order of magnitude [102]. This is not a trivial observation given that the Kerr effect is dominated by the surface-region, meaning the effect likely includes contributions from domains within the penetration depth of the sample. There appears however to be no paramagnetic response of the local orbital moments to the external field in this region, and thus any induced contribution to the AHE is negligible.

The same group of experimentalists repeated the Kerr effect measurements in 2008 on the cuprate YBCO, with much larger Kerr shifts of up to 0.8 μrad reported [33, 118]. An interesting difference here was that training required exceedingly large fields of approximately 3 T. The conclusion drawn from this observation was that the TRS-breaking mechanism occurred at much higher temperatures than the Kerr transition. In this case, it would not be possible to train the signal through the transition with an arbitrarily small symmetry-breaking field as the system has already chosen a chirality. Measurements of the cuprate $La_{2-x}Ba_xCuO_4$ (LBCO) showed similar results, with Kerr shifts of the same order of magnitude [119] and an equivalent resistance to field-training [261]. The onset of the signal in the cuprates also differs from Sr_2RuO_4 in that it coincides with the pseudogap phase, rather than the superconducting transition, which fits with the idea that the pseudogap corresponds to the preformation of Cooper pairs carrying an internal structure [90, 91].

5.2.2 Theoretical Results

Many theoretical models of Sr_2RuO_4 were proposed following the Kerr effect experiment in attempts to describe an intrinsic origin of the optical effect [262–265]. These works focused predominantly on single-band pictures and were unable to produce a quantitative prediction of the Kerr angle in the superconducting state. Subsequently, it was argued that the intrinsic effect

must vanish by symmetry in a spatially homogeneous system [17, 117, 266] and that the source of the Kerr rotation may be extrinsic, i.e., due to impurity scattering [116, 239–241]. However, these investigations were unable to produce an estimate of a Kerr angle to a similar order of magnitude as experiment.

As has been discussed at great length already over the course of this chapter, the intrinsic mechanism can produce a finite AHE, but a multi-band configuration is essential to recover the effect. The reason for this is that the Kerr effect is a direct consequence of the existence of a finite optical Hall conductivity, as given by equation (5.15). Anomalous Hall transport requires a finite Berry curvature [163], for which contributions arise at near degeneracies and avoided crossings of different bands. The curvature, and consequently the Kerr shift, are thus zero when only a single band is considered. This requirement for a multi-band structure is reiterated by observations that gaps of similar magnitude occur on all three Fermi sheets in Sr_2RuO_4 [157, 191, 192, 210].

It has been shown previously that multi-gap models can reproduce a reasonable estimate of the Kerr shift in the absence of SOC. This has been achieved using the three-band 3D model introduced in Chapter 3 [129, 165], and also through a two-band model in which gaps are enforced on the α and β sheets only [205]. The results presented in this section demonstrate the influence of the spin-orbit interaction on the Kerr effect, through calculations made with the 3D model including SOC, in addition to the Kerr shift obtained in the extended pairing regime of the 2D model.

The Kerr angle is directly related to the optical Hall conductivity by [267]

$$\theta_K(\omega) = \frac{1}{\epsilon_0 \omega} \mathrm{Im}\left[\frac{\sigma_{xy}(\omega)}{n(\omega)[n^2(\omega)-1]}\right], \tag{5.21}$$

where $n(\omega)$ is the complex refractive index. Estimating the refractive index for Sr_2RuO_4 provides a serious obstacle to accurate computation of the Kerr shift. This property is the square of the permittivity, which is given by

$$n^2(\omega) = \epsilon(\omega) = \epsilon_\infty + \frac{\mathrm{i}\sigma_{xx}(\omega)}{\omega \epsilon_0}, \tag{5.22}$$

leaving unknown quantities ϵ_∞ and the longitudinal conductivity σ_{xx}.

The required values can be derived directly from empirical data. Given that ϵ_∞ is a real constant, the imaginary part of the permittivity according to (5.22) is

$$\mathrm{Im}[\epsilon(\omega)] = \frac{\mathrm{Re}[\sigma_{xx}(\omega)]}{\omega \epsilon_0}. \tag{5.23}$$

The real part of the longitudinal conductivity can be taken from the literature [268]. At the experimental frequency of 0.8 eV, this has a value of 800 Ω^{-1} cm^{-1}, giving $\mathrm{Im}[\epsilon(0.8)] = 7.43$. The

real part of the refractive index can then be calculated through the relation to the reflectivity, where

$$R(\omega) = \left| \frac{n(\omega) - 1}{n(\omega) + 1} \right|^2 . \tag{5.24}$$

The reflectivity has been measured to be 0.6 at 0.8 eV [268]. Inserting the imaginary component, the real part of the permittivity is deduced to be $\mathrm{Re}[\epsilon(0.8)] = -6.09$. The required permittivity is thus $\epsilon(0.8) = -6.09 + 7.43\mathrm{i}$, and the complex refractive index is obtained by inserting this into (5.22).

5.2.3 Model Calculations

Model calculations have previously demonstrated that a finite Kerr effect can be found intrinsically in the superconducting state [129, 165]. In these investigations, the 3D multi-band model including inter-plane pairing was used and the estimated refractive index of $n(0.8) = \sqrt{-6.09 + 7.43\mathrm{i}}$ was taken. In the most recent of these approaches, taking the 3D model including inter-plane pairing but excluding SOC, a Kerr shift of 12 nrad was computed, in comparison to the experimental measurements of 60-90 nrad. Obtaining a value within an order of magnitude of the observed shifts represented significant progress when benchmarked with respect to the null results obtained through single-band calculations. This provides substantial support to the idea that the Kerr shift in this material is driven by Berry phase effects in the bandstructure, rather than disorder in the lattice.

The results presented here highlight the role that SOC plays in the Kerr effect. Inserting the computed Hall conductivity into (5.22), an estimated Kerr angle of 6.3 nrad at 0.8 eV is obtained for the model including spin-orbit coupling. The computed values of the Kerr angle are displayed in Fig. 5.9 for the model with and without SOC in the experimental frequency range. It is clear that the inclusion of a spin-orbit interaction inhibits the overall AHE, leading to a suppression of the estimated Kerr shift by a similar order of magnitude to that presented in the orbital moment in Section 4.3. This reinforces the arguments made concerning the shared origin of the orbital moment and the Kerr effect arising from the Berry curvature in the bandstructure.

It should be stressed that the computed values are calculated taking the rough estimation of the complex refractive index $n(\omega)$ outlined above. The close proximity of the experimental frequency to the plasmon frequency of the system exacerbates any error in the estimation of the refractive index, and so the computed value may vary considerably. However, the demonstration that a Kerr effect is possible through an intrinsic mechanism is in itself a key result, given the literature cited in Section 5.2.1 which demonstrated that the Kerr shift is very small in impurity-based models [116, 239–241].

In addition, it is worth again emphasising that extrinsic mechanisms tend to be the key driving force of the AHE in normal state ferromagnets. Although previous studies have suggested that

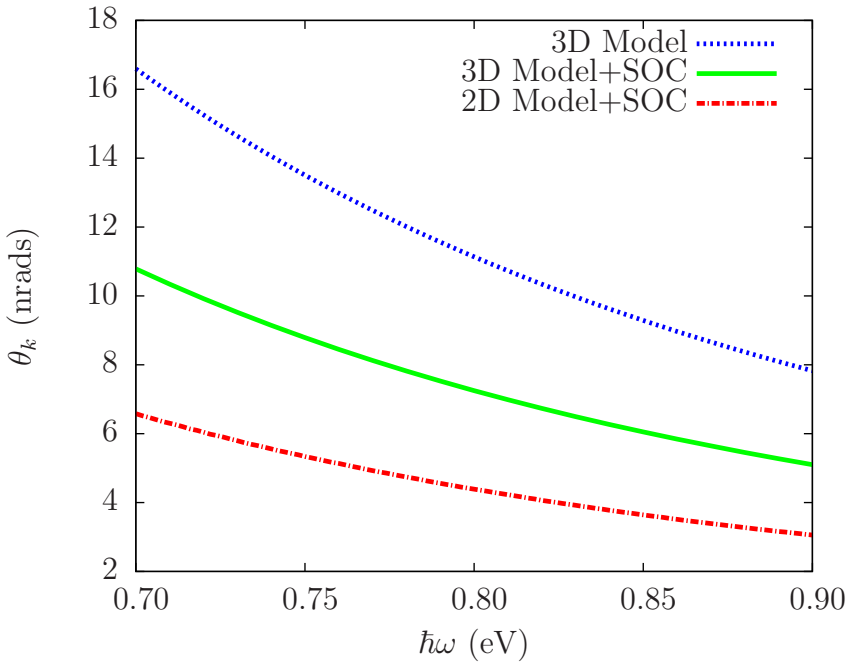

FIGURE 5.9. Estimated Kerr angle in the high-frequency regime for the 3D model, with and without SOC, and the 2D model in the renormalised fit.

disorder-based mechanisms alone can not be responsible for the Kerr effect in Sr_2RuO_4 [116, 239–241], the interplay between impurity-scattering and the Berry curvature driven mechanism has not been investigated. It is easy to speculate that the presence of impurities, in addition to SOC, may well enhance the optical Hall conductivity arising from the intrinsic bandstructure.

The enhancement of itinerant currents by disorder has in fact been highlighted in recent theoretical work. A finite sample calculation demonstrated that the presence of a muon in the otherwise clean lattice results in a large increase in the local spontaneous current [215]. This was proposed as an explanation as to why the seemingly large currents found in μSR measurements did not coincide with a visible edge current. The result highlights the potent influence that the coexistence of SOC and impurities can have on Berry phase effects generated by the intrinsic bandstructure.

The computed Kerr shift for the 2D model with extended pairing terms is smaller than in the 3D model. It should be stressed that this is calculated in the experimental frequency range, where the influence of inter-band near-degeneracies is negligible. This makes it difficult to quantify the exact cause of the suppressed moment in the extended pairing model relative to the 3D approach. However, given that the experimental frequency corresponds to photons with energy of the order of the bandwidth, it could be speculated that this reduction is simply a product of the reduced

bandwidth obtained in the 2D tight-binding Hamiltonian (see Tables 3.1 and 3.2). It is interesting to note, however, that the reduced Kerr shift observed here coincides with a reduction in the total computed orbital moment. This provides an interesting outlook as to whether the relatively large Kerr shift observed in Sr_2RuO_4 can be reconciled with extremely small orbital magnetisation implied by the lack of observed edge currents.

Included in Fig. 5.9 is the Kerr angle angle obtained from calculations using the renormalised fit 2D gap structure at $T = 0$. The self-consistent approach gave values an order of magnitude smaller here, which do not compare satisfactorily with experiment. However, as stressed in Section 3.2.3, results obtained in this temperature region for the self-consistent 2D model should be taken tentatively as the correct nodal structure is not enforced.

To conclude this final results chapter, the Kerr angle was computed for both multi-band p-wave models of Sr_2RuO_4. The results compare reasonably well with experiment, particularly when benchmarked against single-band and impurity-based approaches, but remain around an order of magnitude smaller. Calculations made via the 3D model compare most favourably with experiment, but the 2D model results must be taken tentatively as further work is required to gain the correct nodal structure for this regime. The influence of SOC here is shown to be congruent with that seen in the calculations of orbital moment, as the spin-orbit interaction inhibits both phenomena to a similar degree. This again emphasises the shared origin of these anomalous transport properties.

CHAPTER 6

CONCLUSIONS AND OUTLOOK

In this final chapter, the results displayed over the course of this thesis are summarised, followed by a discussion of the possible investigations which could be carried out to further the progress made here. Key among the results which have been reported is the derivation of a generalised set of equations to calculate the total orbital magnetisation carried by a superconducting state in an extended periodic lattice. An immediate impact of this new formalism has been demonstrated through an investigation of the possible order parameters in the proposed chiral p-wave superconductor Sr_2RuO_4, while its implications for the study of magnetic and transport properties in other chiral superconductors and superfluids is extensive. Further results regard the anomalous Hall conductivity, the Kerr effect, and structure of the superconducting gap in Sr_2RuO_4.

6.1 Orbital Moment

The orbital moment was computed and contrasted for two distinct gap configurations in Sr_2RuO_4, as outlined in Chapter 4. Results obtained reveal a number of interesting facets of the magnetic properties of the chiral state. It has been shown that the addition of multiple pairing channels in the presence of strong inter-orbital hybridisation leads to a significant suppression of the total moment (see Figs. 4.3 and 4.4). The inclusion of longer-range pairing terms appears to incur further reduction in the total moment and cuts the calculated itinerant magnetisation down to a similar magnitude to that of the current experimental resolution [112] (Figs. 4.8 and 4.9). Despite this progress, however, it is not possible to irrefutably reconcile a p-wave symmetry with the lack of observed edge currents in Sr_2RuO_4 [110–112, 233]. The moment computed for both models is larger than would be inferred from the null experimental observations,

but it should be emphasised that the computed value is a bulk-dependent quantity, which incorporates contributions from intra-cell movement of electrons, which would not appear in the edge magnetisation, and neglects surface effects. Meissner screening currents, not accounted for here, further inhibit the visible magnetic moment at the surface of a finite sample. Given these considerations, it is certainly feasible that the edge currents associated with the two gap configurations studied here would be sufficiently small as to not be detected through current experimental techniques.

A key aspect of the results presented here is the influence that the spin-orbit interaction plays in the anomalous phenomena associated with a chiral order parameter. Figs. 4.3 and 4.4 demonstrate that the additional hybridisation incurred by SOC results in further suppression of the computed moment. A finite spin magnetisation also appears in response to the inclusion of a spin-orbit interaction (Fig. 4.5). Given that the moment in this chiral superconducting state arises entirely from the orbital angular momentum carried by the Cooper pairs (which have total spin $S_z = 0$), it can be inferred that SOC mediates a transfer of magnetic moment from the orbital channel to the spin degree of freedom. This provides a fascinating insight into the influence of the spin-orbit interaction on states in which time-reversal symmetry is intrinsically broken, and presents a clear analogue of the origin of the anomalous Hall conductivity in spin ferromagnets (as discussed in Section 5.1) [171].

Aside from the search for edge currents in Sr_2RuO_4, there are a number of other motivations for studying the intrinsic orbital magnetic moment in chiral superconductors, and a wide range of potential materials which provide an ideal platform for the emergence of this phenomenon. Various derivatives of the moment have been shown to be directly related to anomalous phenomena such as NMR [223], orbital magnetoelectric coupling and response [224, 225], and the spin Hall conductivity [226]. Additionally, the impact of different topological configurations on the intrinsic moment has been displayed, through comparison of the results obtained from the two distinct models of Sr_2RuO_4 in Section 4.3. The potential of chiral superconductors for applications in quantum computation devices has driven a surge of interest within the current community into the topological properties of unconventional superconductors [21–23]. Longer-range pairing in the 2D model leads to a distinctly different topology [184, 185]. It has been estimated that the modified Chern number asssociated with the extended order parameter used here should reduce the total edge current by a factor of 20 [184], which compares reasonably well the reduction in the orbital moment observed in model calculations presented here.

An outstanding issue remaining is to theoretically verify that the derived reciprocal-space formalism for the orbital moment accurately replicates the circulation operator in the position basis (see Section 4.3.3). Correspondence between the two can only be confirmed through comparison of the bulk moment computed through equations (4.41) with that obtained from calculations with a finite-size sample [114]. An investigation of this nature was performed but found it was not possible to accurately reproduce the effects of a superconducting gap with a sample size of

the order 10×10 unit cells due to strong surface effects (see Figs. 4.11 and 4.12). It is possible that this problem could be resolved by instead implementing a sample which approximates an infinite-width strip, but it remains to be seen whether this can negate the surface-dependent problems which were observed when performing calculations under open boundary conditions.

6.2 Anomalous Hall and Kerr Effects

Following the comprehensive study of the orbital moment, the general formalism for computing the anomalous Hall conductivity and the resulting Kerr effect is presented in Chapter 5. Figs. 5.1, 5.2 and 5.9 display model calculations made through the 3D, multi-band model of Sr_2RuO_4 including spin-orbit coupling. This work expands upon previous results which demonstrated that the inclusion of inter-plane pairing results in a gap structure capable of producing a reasonable estimate of the Kerr angle, even in the absence of SOC [129]. The necessity for a multi-band structure with inter-band pairing to generate an AHE intrinsically is clearly highlighted here, and **k**-resolved plots of the Brillouin zone support this observation by demonstrating that the Hall conductivity is driven by regions of near-degeneracy at the Fermi surface (Fig. 5.3).

The calculations were reproduced through the alternative 2D model approach with extended pairing (see Section 5.1.5), and a Kerr shift of a similar order of magnitude was obtained (Fig. 5.9). However, the results obtained through the 2D model do not compare as favourably with experiment as the 3D approach, most likely due to the enhanced influence of SOC here. An interesting prospect for further study would be to ascertain the analogous out-of-plane terms for the extended pairing structure by generalising to three dimensions. Careful consideration would have to made here regarding the topological structure of the gap configuration upon the introduction of inter-plane pairing. The presence of symmetry-imposed line nodes associated with the inter-plane order parameter may result in a different total Chern number for the multi-band structure, which would have a significant impact on the magnitude of the computed orbital moment and the temperature dependence of the heat capacity below T_c.

Again, the influence of SOC on the anomalous phenomenon of the Kerr effect has been studied extensively. A suppression of the computed Kerr shift relative to the model excluding SOC occurs, and is of a similar order of magnitude to that observed in the orbital moment (Fig. 5.9). The reliance of both phenomena on the Berry curvature arising from inter-band hybridisation is clearly highlighted here (see Section 5.1.2 for a discussion on the link to Berry phase effects). This also supports the idea that the intrinsic anomalous Hall effect is a direct result of the presence of a finite orbital magnetisation, and is not possible through time-reversal symmetry breaking in the spin channel alone, supporting the KL theory of the anomalous velocity in ferromagnets [171].

The computed Kerr shift for the 3D model including SOC is approximately 5 times smaller than experiment, and so a key question remains regarding the origin of this discrepancy. A

potential indicator could be the presence of impurities in the lattice, which have been neglected here. It would be interesting to investigate the influence of disorder on model calculations of the Kerr effect through both the inter-plane and extended pairing models. Coupling of the bandstructure to impurities can generate an anomalous Hall voltage through the extrinsic side-jump and skew scattering process [116, 239–241], which would hypothetically enhance the computed Kerr signal originating from the intrinsic bandstructure and account for part of the reduction relative to experiment.

6.3 Gap Structure of Sr_2RuO_4

A deep contrast is observed in the properties of the 3D and 2D pairing models used here to evaluate a p-wave structure in the tetragonal Sr_2RuO_4 lattice (Section 3.2). The inclusion of inter-plane pairing terms enforces line nodes in the gap configuration for the 3D model, and the heat capacity is clearly recreated as a result (Fig. 3.13). The 2D model is slightly more problematic, however, as there are no symmetry-enforced nodes and so the power law dependence of the thermal properties below T_c must be recreated by enforcing sufficiently deep minima on all three band gaps simultaneously. Self-consistent solutions were obtained which produced a single transition at 1.5 K for the distinct pairing channels (Fig. 3.15), but evidently this did not produce small enough minima below 0.5 K and the state appeared to be fully gapped in this region (Fig. 3.16). Further work is required in order to obtain the correct nodal structure in the extended pairing regime in the low-temperature region. Until such time, the results for the orbital moment and Kerr effect obtained through this model must be taken tentatively.

With this provision in mind, it can still be observed that the 2D model appears to roughly reduce the total moment by an order of magnitude relative to the 3D approach. This supports the idea that the itinerant magnetisation is strongly dependent on the topological properties of the gap structure. The result for the orbital moment seems to favour the 2D model for this reason, yet the Kerr effect calculations contrastingly give preferable values for the 3D model. To attempt to reconcile these possibly contradictory observations, it is vital to obtain the correct low-temperature nodal structure for the extended pairing regime and observe the impact this has on the moment and the Kerr shift.

There are a number of possible avenues for further work on the extended pairing model which may result in the correct nodal properties. Firstly, the relative magnitudes of the distinct gaps in this approach is strongly dependent on the magnitude of the spin-orbit interaction included in the normal state Hamiltonian. A significant suppression of the γ band gap would hypothetically reproduce the deep minima required on all three Fermi sheets. Future investigations could therefore focus on reproducing the electronic structure calculations outlined for this model in Chapter 3 with a reduced SOC parameter λ. A new set of superconducting interaction constants would then need to be devised in order to tune the various components of the gap to the single

transition temperature. It is difficult to gauge at this point the magnitude that λ would have to be reduced by in order to recreate the correct nodal structure in the low-temperature region. The value of 10.9 meV used in the 2D calculations made here is smaller than the 12.5 meV estimated through comparison with first-principles calculations, which is in itself 4 times smaller than that predicted by *ab initio* methods. Suppression of λ by a large order of magnitude to produce sufficiently small gap minima would therefore seem difficult to reconcile with *ab initio* and experimental results.

The second avenue would be to keep λ fixed and instead tune the interaction constants such that the zero temperature magnitudes for each component of the gap are closer in magnitude to those obtained through renormalisation group calculations. The constants used in the calculations made here are designed such that the 5 band gaps all reach a T_c of 1.5 K with a smooth temperature evolution (Fig. 3.15). This may not be completely necessary in order to replicate the smooth band gap evolution required, however, due to strong inter-orbital hybridisation in this structure. It may be possible to obtain the low-temperature deep minima required on all three bands by enforcing kinks in the low-temperature regions of the orbitally-resolved gap parameters.

6.4 Outlook

The general formalism for the orbital moment developed here is applicable to a number of proposed chiral superconductors, such as the heavy-fermion compound UPt_3 [86], for which the exact form of the order parameter remains controversial. Study of the influence of different superconducting symmetries on the magnetic properties in this material will provide an additional insight into its possible gap configurations. The cuprate class of superconductors also provide an avenue for further exploration [88]. It would be particularly interesting to study the magnetic properties of the distinct pseudogap and superconducting transitions in such a material, as it is proposed that the pseudogap phase corresponds to the preformation of non-s-wave Cooper pairs [90, 91]. The issue of the orbital angular momentum carried by the chiral p-wave state of superfluid ^{3}He also remains heavily debated, with estimates ranging by 6 orders of magnitude [69, 109, 207, 209, 232], and the formalism presented here is equally valid for a superfluid.

A wide range of unconventional superconductors have displayed a Kerr signal experimentally [33, 86, 102, 118, 119, 261], and so the general formalism presented here provides a further avenue with which to verify tight-binding models of these lattices. It would be of particular interest to ascertain whether the much larger signal of 0.8 μrad observed in the cuprate YBCO could be recreated through a multi-band model [33, 118], given that current estimations for Sr_2RuO_4 give shifts smaller than experiment. It would also be of significance in the study of potential mechanisms for the formation of the pseudogap phase, as the onset of the Kerr effect here coincides with the pseudogap transition.

Finally, laid out here is an introduction to the anomalous Nernst effect, which is closely

related to the orbital moment and AHE, and lacks an appropriate theory for study in a superconducting state [269]. The Nernst effect is analogous to the Hall effect, being instead related to the transverse electric conductivity generated when a thermal gradient is applied to a sample to induce a current, rather than the applied voltage required to incur a Hall conductivity. An anomalous Nernst effect therefore describes the spontaneous transverse conductivity obtained when a sample with broken TRS conducts a thermal current in the absence of an external magnetic field.

It has been shown that the appearance of a Nernst conductivity (α_{xy}) is directly related to the intrinsic orbital moment of a system at finite temperatures [219]. The current associated with the Nernst effect is given by

$$\mathbf{j} = \nabla \times \mathbf{M}_T \,, \tag{6.1}$$

where $\mathbf{M}_T$ is the finite temperature correction to the ortbial magentisation. This current is then related to the Nernst conductucitivity by $j_x = \alpha_{xy}(-\nabla_y T)$. The formalism developed in Chapter 4 is technically a zero temperature approach, and is thus not appropriate for the discussion of the anomalous Nernst effect. A normal state framework has been derived to describe the finite temperature correction to the orbital magnetisation described by equations (4.4) [219, 270],

$$\mathbf{M}_T = \frac{k_B T e}{\hbar} \int_{BZ} \frac{\mathrm{d}\mathbf{k}}{(2\pi)^3} \sum_n \mathbf{\Omega}_n(\mathbf{k}) \log\left[1 + \exp\left(\frac{-\epsilon_{n\mathbf{k}}}{k_B T}\right)\right], \tag{6.2}$$

where k_B is the Boltzmann constant and $\mathbf{\Omega}_n(\mathbf{k})$ is the Berry curvature. To generalise this formalism for study in a superconductor, the single-particle wavefunctions used in the derivation laid out in ref. [270] must again be transformed to the required particle-hole basis. This process is distinct from the derivation applied to derive the zero temperature orbital moment as it utilises the perturbation of the wavefunctions with respect to an external field, rather than a transformation to a localised basis.

To conclude, the framework to study a number of anomalous phenomena present in chiral superconductors has been formally presented. This formalism has then been used to investigate the intriguing state of Sr_2RuO_4, generating key insights into the possible order parameters which may be able to describe the distinct experimental properties of the material. It is believed that the work presented here will find far-reaching applications in the study of transport and topological properties of unconventional superconductors and superfluids, and the hope is that this will ultimately be influential in laying the groundwork for a wide range of applications from these unique and fascinating materials.

APPENDIX A

QUANTUM MECHANICS NOMENCLATURE

Brief appendices clarifying the notation used in the quantum mechanical terms throughout the derivations presented in this thesis. The reader is referred to textbooks such as refs. [26, 36] for detailed derivations of this formalism.

A.1 Pairing Configurations

Consider a state consisting of a pair of identical particles, located at positions $\mathbf{r}_1$ and $\mathbf{r}_2$ respectively. Under the exchange of these particles in position space, the probability density of the state must be constant,

$$|\psi(\mathbf{r}_1,\mathbf{r}_2)|^2 = |\psi(\mathbf{r}_2,\mathbf{r}_1)|^2 . \tag{A.1}$$

Condition (A.1) can be satisfied if a phase change of the wavefunction is incurred by permutation of the two particles. It has been found experimentally that the exchange of particles is symmetric if they are bosonic, but antisymmetric for fermions [26],

$$\hat{P}\psi(\mathbf{r}_1,\mathbf{r}_2) = \begin{cases} \psi(\mathbf{r}_1,\mathbf{r}_2), & \text{bosons} \quad (s = 0,1,2,..) \\ -\psi(\mathbf{r}_1,\mathbf{r}_2), & \text{fermions} \quad (s = 1/2,3/2,..) \end{cases} . \tag{A.2}$$

The paired particles individually occupy single-particle wavefunctions, which are quantised in terms of a set of quantum numbers n. Bosonic and fermionic pair wavefunctions can be written such that condition (A.2) is satisfied via products of the single-particle states,

$$\psi_B(\mathbf{r}_1,\mathbf{r}_2) = \frac{1}{\sqrt{2}}\left[\psi_n(\mathbf{r}_1)\psi_{n'}(\mathbf{r}_2) + \psi_n(\mathbf{r}_2)\psi_{n'}(\mathbf{r}_1)\right] \tag{A.3}$$

$$\psi_F(\mathbf{r}_1,\mathbf{r}_2) = \frac{1}{\sqrt{2}}\left[\psi_n(\mathbf{r}_1)\psi_{n'}(\mathbf{r}_2) - \psi_n(\mathbf{r}_2)\psi_{n'}(\mathbf{r}_1)\right], \tag{A.4}$$

where B and F refer to bosons and fermions respectively. This construction elucidates the origin Pauli's exclusion principle, as ψ_F vanishes for $n = n'$, establishing that no two fermions in the same system can display the same quantum numbers.

Focussing now on the fermionic case, the spatial part of the wavefunction can be constructed in two distinct configurations. Writing the spin part of the wavefunction explicitly,

$$\psi_F(\mathbf{r}_1,\mathbf{r}_2) = \psi(\mathbf{r}_1,\mathbf{r}_2)\,\chi(s_1,s_2), \tag{A.5}$$

where s_1 and s_2 are the spin quantum numbers. If χ is antisymmetric under particle exchange, then ψ must be symmetric to satisfy (A.4), giving

$$\psi(\mathbf{r}_1,\mathbf{r}_2) = \frac{1}{\sqrt{2}}\left[\psi_n(\mathbf{r}_1)\psi_{n'}(\mathbf{r}_2) + \psi_n(\mathbf{r}_2)\psi_{n'}(\mathbf{r}_1)\right], \tag{A.6a}$$

$$\chi(s_1,s_2) = \frac{1}{\sqrt{2}}\left[\begin{pmatrix}1\\0\end{pmatrix}^{(1)}\begin{pmatrix}0\\1\end{pmatrix}^{(2)} - \begin{pmatrix}0\\1\end{pmatrix}^{(1)}\begin{pmatrix}1\\0\end{pmatrix}^{(2)}\right]. \tag{A.6b}$$

This is referred to as the singlet pairing configuration, and it corresponds to even-parity pairs, where the total spin quantum number is 0 and the orbital quantum number is even.

Alternatively, a pair of fermions may be bound in an odd-parity pair. The spin wavefunction is symmetric in this case, which means that the total spin $S = 1$. This can correspond to three possible spin projections,

$$\psi(\mathbf{r}_1,\mathbf{r}_2) = \frac{1}{\sqrt{2}}\left[\psi_n(\mathbf{r}_1)\psi_{n'}(\mathbf{r}_2) + \psi_n(\mathbf{r}_2)\psi_{n'}(\mathbf{r}_1)\right], \tag{A.7a}$$

$$\chi(s_1,s_2) = \begin{cases} \begin{pmatrix}1\\0\end{pmatrix}^{(1)}\begin{pmatrix}1\\0\end{pmatrix}^{(2)} \\ \dfrac{1}{\sqrt{2}}\left[\begin{pmatrix}1\\0\end{pmatrix}^{(1)}\begin{pmatrix}0\\1\end{pmatrix}^{(2)} + \begin{pmatrix}0\\1\end{pmatrix}^{(1)}\begin{pmatrix}1\\0\end{pmatrix}^{(2)}\right] \\ \begin{pmatrix}0\\1\end{pmatrix}^{(1)}\begin{pmatrix}0\\1\end{pmatrix}^{(2)}. \end{cases} \tag{A.7b}$$

This is known as a spin triplet pair.

A.2 Second Quantised Notation

The language of "second quantisation", or more accurately the "occupation number representation" refers to the formulation of many-body quantum states through number operators. In this approach, a wavefunction is an ensemble of single-particle states, and is parametrised through the number of those states which are occupied.

A general wavefunction in this representation can be written in the Dirac form as $|N_i\rangle$, where the index i runs over all possible single-particle states and N_i is 0 or 1 depending on whether the state is occupied or not. Taking an ensemble of fermions, the index runs over the full set of quantum numbers. A particle is added or removed from a particular state through the fermion creation and annihilation operators, denoted $\hat{a}_i^\dagger$ and $\hat{a}_i$ respectively,

$$\hat{a}_i^\dagger|0_i\rangle = |1_i\rangle, \quad \hat{a}_i|1_i\rangle = |0_i\rangle\,. \tag{A.8}$$

The operator $\hat{N}_i = \hat{a}_i^\dagger\hat{a}_i$ is thus referred to as the fermion number operator, as $\hat{N}_i|N_i\rangle = N_i$.

In order to abide by the antisymmetric requirement of a many-body state of identical fermions (as outlined in App. A.1), the fermion operators must obey the anti-commutation rules,

$$\hat{a}_i\hat{a}_{i\prime} + \hat{a}_{i\prime}\hat{a}_i = \hat{a}_i^\dagger\hat{a}_{i\prime}^\dagger + \hat{a}_{i\prime}^\dagger\hat{a}_i^\dagger = 0\,, \tag{A.9a}$$

$$\hat{a}_{i\prime}\hat{a}_i^\dagger + \hat{a}_i^\dagger\hat{a}_{i\prime} = \delta_{ii\prime}\,. \tag{A.9b}$$

Rather than Dirac states of the form $|N_i\rangle$, it will be beneficial in the work presented here to use wavefunctions defined in the real-space representation. An equivalent set of Fermi field creation and annihilation operators $\hat{\psi}^\dagger(\mathbf{r})$ and $\hat{\psi}(\mathbf{r})$ are required to do this. These are defined by taking an expansion of the single-particle operators, which is typically achieved via

$$\psi^\dagger(\mathbf{r}) = \sum_i \phi_i^*(\mathbf{r})\hat{a}_i^\dagger\,, \tag{A.10a}$$

$$\psi(\mathbf{r}) = \sum_i \phi_i(\mathbf{r})\hat{a}_i\,. \tag{A.10b}$$

The Fermi field operators must then obey an equivalent set of anti-commutation relations,

$$\hat{\psi}_\alpha(\mathbf{r})\hat{\psi}_\beta(\mathbf{r}') + \hat{\psi}_\beta(\mathbf{r}')\hat{\psi}_\alpha(\mathbf{r}) = 0\,, \tag{A.11a}$$

$$\hat{\psi}_\alpha^\dagger(\mathbf{r})\hat{\psi}_\beta(\mathbf{r}') + \hat{\psi}_\beta(\mathbf{r}')\hat{\psi}_\alpha^\dagger(\mathbf{r}) = \delta_{\alpha\beta}\delta^{(3)}(\mathbf{r}-\mathbf{r}')\,. \tag{A.11b}$$

A.3 Angular Momentum Operators

The intrinsic orbital angular momentum of an electron is parametrised by the azimuthal (l) and magnetic (m_l) quantum numbers. In Dirac form, such a state is written as $|l, m_l\rangle$. For an electron

which has angular momentum quantised along the z-axis, the z-component of the orbital angular momentum operator acts on the Dirac state via

$$\hat{l}_z |l, m_l\rangle = \hbar m_l |l, m_l\rangle . \tag{A.12}$$

It is possible to introduce a pair of "ladder operators", which are defined for the given state by $\hat{l}_+ = \hat{l}_x + \mathrm{i}\hat{l}_y$ and $\hat{l}_- = \hat{l}_x - \mathrm{i}\hat{l}_y$. Given that the components of angular momentum operator commute via $[\hat{l}_i, \hat{l}_j] = \mathrm{i}\hbar\epsilon_{ijk}\hat{l}_k$ [36], it is found that the ladder operators obey the following relations,

$$[\hat{l}_z, \hat{l}_\pm] = \pm\hbar\hat{l}_\pm , \tag{A.13a}$$

$$[\hat{l}_+, \hat{l}_-] = 2\hbar\hat{l}_z . \tag{A.13b}$$

Applying these relations, it can be shown that

$$\hat{l}_z\hat{l}_\pm |l, m_l\rangle = \hbar(m_l \pm 1)\hat{l}_\pm |l, m_l\rangle . \tag{A.14}$$

The term $\hbar(m_l \pm 1)$ is equal to the eigenvalue obtained when $\hat{l}_z$ acts on a state $|l, (m_l \pm 1)\rangle$. It is thus inferred that the ladder operators are analogous to the creation and annihilation operators introduced in App. A.2, but rather than incrementing the number of particles in a state they increase or decrease the magnetic quantum number of a particular particle. The eigenvalues of the ladder operators are deduced by considering the operation of $\hat{l}_+\hat{l}_-$ on a general state, as outlined in textbooks such as ref. [36]. The ladder operations are found to display the form

$$\hat{l}_+ |l, m_l\rangle = \hbar\sqrt{l(l+1) - m_l(m_l+1)}\, |l, (m_l+1)\rangle , \tag{A.15a}$$

$$\hat{l}_- |l, m_l\rangle = \hbar\sqrt{l(l+1) - m_l(m_l-1)}\, |l, (m_l-1)\rangle . \tag{A.15b}$$

APPENDIX B

NUMERICS

Further technical details on the numerical calculations performed in this project. Equations to compute the Fermi surface, heat capacity and Bloch-spectral functions are given. Also discussed are the units used for calculations and the conversion to SI.

B.1 Electronic Structure Formulae

The electronic bandstructure is calculated by solving the Schrödinger equation (3.11), while the quasiparticle dispersion is obtained through diagonalisation of the tight-binding Bogoliubov-de Gennes equation given in (3.23). To produce the Fermi surface plot in Fig. 3.5, the approach is to compute the **k**-resolved density of states for the normal state dispersion (as the Fermi surface vanishes upon the appearance of a superconducting gap). The density of states (D) at a given energy is

$$D(\epsilon) = \sum_{n,\mathbf{k}} \delta(\epsilon - \epsilon_{n\mathbf{k}}), \tag{B.1}$$

where δ is the Dirac-delta function and $\epsilon_{n\mathbf{k}}$ is the band dispersion. Implementation of a Dirac-delta function numerically is not viable, however, as the function would be required to converge on infitesimally narrow points. Instead, the delta can be replaced with a bell-shaped distribution, such as a Gaussian or Lorentzian function. A Lorentzian was implemented here, defined by

$$\delta(\epsilon) = \lim_{\sigma \to 0} \frac{1}{\pi} \frac{\sigma}{\sigma^2 + \epsilon^2}, \tag{B.2}$$

where the width of the distribution decreases on increasing σ.

The Fermi surface is defined by evaluating $D(\epsilon_F)$, where ϵ_F is the Fermi energy. In the calculations performed here, the Fermi energy has been set to zero. The **k**-resolved density of states at the Fermi energy is thus

$$D(\epsilon_F, \mathbf{k}) = \sum_n \frac{1}{\pi} \frac{\sigma}{\sigma^2 + {\epsilon_{n\mathbf{k}}}^2}. \tag{B.3}$$

Fig. 3.5 was obtained with $\sigma = 0.0075$.

To compute the orbitally-resolved Bloch spectra displayed in Fig. 3.9, the individual contributions of each orbital character to the Fermi surface density of states were extracted via

$$D_d(\epsilon_F, \mathbf{k}) = \sum_{n,\alpha} \delta(\epsilon_{n\mathbf{k}}) \left(|u^\alpha_{nd}|^2 + |v^\alpha_{nd}|^2 \right). \tag{B.4}$$

The heat capacity is defined as the rate of change of the internal energy with respect to temperature. The total internal energy of a system is given by

$$U = \int_{BZ} \frac{\mathrm{d}\mathbf{k}}{(2\pi)^3} \sum_n \epsilon_{n\mathbf{k}} f_{n\mathbf{k}}, \tag{B.5}$$

where $f_{n\mathbf{k}}$ is the Fermi factor, as defined in (2.34). The heat capacity for constant volume is then related by

$$C_v = \frac{\partial U}{\partial T} = \int_{BZ} \frac{\mathrm{d}\mathbf{k}}{(2\pi)^3} \sum_n \epsilon_{n\mathbf{k}} f_{n\mathbf{k}} \left(1 - f_{n\mathbf{k}}\right) \left[\frac{\epsilon_{n\mathbf{k}}}{T^2} - \frac{1}{T} \frac{\partial \epsilon_{n\mathbf{k}}}{\partial T} \right]. \tag{B.6}$$

The derivative of the energy with respect to temperature was approximated by storing the bandstructure for the previous temperature increment and taking

$$\frac{\partial \epsilon_{n\mathbf{k}}}{\partial T} = \frac{\Delta \epsilon_{n\mathbf{k}}}{\Delta T}. \tag{B.7}$$

B.2 Units

Calculations are performed in atomic units, with the reduced Planck constant $\hbar = 1.054 \times 10^{-34}$ J s, the electronic mass $m = 9.11 \times 10^{-31}$ kg and the lattice constant $a = 0.3862$ nm set to 1. Energy and temperature are taken in units of eV, meaning that the temperature must be divided by the Boltzmann constant ($k_B = 8.62 \times 10^{-5}$ eV K^{-1}) to convert to Kelvin.

The heat capacity is plotted in units of mJ K^{-2} (mol)$^{-1}$. The conversion from atomic units thus requires a factor $q(1 \times 10^3) k_B^2 N_A = 0.716$ eV^2 K^{-2} (mol)$^{-1}$, where q is the electric charge constant (1.6×10^{-19}) and N_A is Avogadro's number (6.02×10^{23} (mol)$^{-1}$).

Special care must be taken when converting the distinct components of the orbital magnetisation to SI units. The on-site contribution $\mathbf{M}_{\mathrm{LC}}^{(2)}$ is computed by directly evaluating the angular momentum operator $\hat{l}_z$. The integration in equation (4.60) is thus dimensionless, as the unit of orbital angular momentum $\hbar$ has been taken out. The factor $\gamma\hbar$ preceding the integral in (4.60) generates the magnetic moment per unit cell, where $\gamma = -e/(2m)$ and e is the fundamental electric charge (1.6×10^{-19} C).

Conversion of the on-site magnetisation to magnetic field (in units of T) is performed by multiplying the value obtained from equation (4.60) by μ_0/V_c, where μ_0 is the vacuum permeability (1.257×10^{-6} T m A^{-1}) and V_c is the unit cell volume of Sr_2RuO_4 (9.49×10^{-29} m^3). The conversion of the integral computed in atomic units to SI thus incurs a total factor $\gamma\hbar\mu_0/V_c = 0.1226$ T. The electrostatic unit of magnetic field is Gauss (G), which is related to Tesla by 1 T = 10^4 G.

In contrast to the on-site component, the itinerant magnetisation is approached by considering $\langle \mathbf{r} \times \mathbf{v} \rangle$, resulting in the requirement for the factor $(\gamma m/\hbar)$ in equations (4.47) and (4.50) to generate the moment per unit cell. The integrations in (4.47) and (4.50) contain the Hamiltonian, which is constructed in eV, and the $\mathbf{k}$-derivatives $|\partial_{\mathbf{k}} u_{n\mathbf{k}}\rangle$, which are given in units of a. Converting to the magnetic moment from atomic units thus requires an additional factor $a^2 q$. The conversion from the computed integration in this case incurs a total factor of $a^2 q(\gamma m/\hbar)\mu_0/V_c = 0.240$ T.

BIBLIOGRAPHY

[1] H. Kamerlingh Onnes and J. Clay.
Comm. Phys. Lab. Univ. Leiden, 95d, 1906.

[2] H. Kamerlingh Onnes.
Comm. Phys. Lab. Univ. Leiden, 119b, 1911.

[3] J. Dewar and J. A. Fleming.
Philos. Mag., 34:205–209, 1892.

[4] K. Gavroglu.
James dewar and the vanishing electrical resistance at absolute zero temperature.
Ann. Phys., 524(3-4):61–64, 2012.

[5] H. Kamerlingh Onnes.
The resistance of pure mercury at helium temperatures.
Comm. Phys. Lab. Univ. Leiden, 120b:1479–1481, 1991.

[6] H. Kamerlingh Onnes.
The disappearance of the resistivity of mercury.
Comm. Phys. Lab. Univ. Leiden, 122b:81–83, 1911.

[7] H. Kamerlingh Onnes.
On the sudden change in the rate at which the resistance of mercury disappears.
Comm. Phys. Lab. Univ. Leiden, 124c:799–802, 1911.

[8] H. Kamerlingh Onnes.
Comm. Phys. Lab. Univ. Leiden, 140c, 1914.

[9] H. Kamerlingh Onnes.
Comm. Phys. Lab. Univ. Leiden, 139f, 1914.

[10] W. Meissner and R. Ochsenfeld.
Ein neuer effekt bei eintritt der supraleitfähigkeit.
Naturwissenschaften, 21(44):787–788, 1933.

[11] J. Eisenstein.
Superconducting elements.
Rev. Mod. Phys., 26(3), 1954.

[12] B. T. Matthias and J. K. Hulm.
A search for new superconducting compounds.
Phys. Rev., 87(5):799–806, 1952.

[13] B. T. Matthias, T. H. Geballe, and V. B. Compton.
Superconductivity.
Rev. Mod. Phys., 35(1), 1963.

[14] P. J. Ford and G. A. Saunders.
The Rise of the Superconductors.
CRC Press, 2005.

[15] A. P. Schnyder, S. Ryu, A. Furusaki, and A. W. W. Ludwig.
Classification of topological insulators and superconductors in three spatial dimensions.
Phys. Rev. B, 78(19):195125, 2008.

[16] A. Kitaev.
Periodic table for topological insulators and superconductors.
AIP Conf. Proc., 1134(1):22–30, 2009.

[17] N. Read and D. Green.
Paired states of fermions in two dimensions with breaking of parity and time-reversal symmetries and the fractional quantum Hall effect.
Phys. Rev. B, 61(15):10267–10297, 2000.

[18] A. Y. Kitaev.
Unpaired Majorana fermions in quantum wires.
Phys.-Usp., 44:131, 2001.

[19] M. Sato.
Non-Abelian statistics of axion strings.
Phys. Lett. B, 575(1-2):126–130, 2003.

[20] M. Sato and Y. Ando.
Topological superconductors: a review.
Rep. Prog. Phys., 80(7), 2017.

[21] B. Schumacher.
Quantum coding.
Phys. Rev. A: At., Mol., Opt. Phys., 51(4):2738, 1995.

[22] M. H. Devoret, A. Wallraff, and J. M. Martinis.
Superconducting qubits: A short review.
arXiv:cond-mat/0411174.

[23] D. Aasen, M. Hell, R. V. Mishmash, A. Higginbotham, J. Danon, M. Leijnse, T. S. Jespersen, J. A. Folk, C. M. Marcus, K. Flensberg, and J. Alicea.
Milestones Toward Majorana-Based Quantum Computing.
Phys. Rev. X, 6:031016, 2016.

[24] F. London and H. London.
The electromagnetic equations of the supraconductor.
Proc. Royal Soc. A, 149(866):71–88, 1935.

[25] F. S. Henyey.
Distinction between a perfect conductor and a superconductor.
Phys. Rev. Lett., 49(6):416, 1982.

[26] S. N. Ketterson, J. B.; Song.
Superconductivity.
Cambridge University Press, 1999.

[27] J. Bardeen, L. N. Cooper, and J. R. Schrieffer.
Theory of Superconductivity.
Phys. Rev., 108(5):1175–1204, 1957.

[28] J. Bardeen, L. N. Cooper, and J. R. Schrieffer.
Microscopic Theory of Superconductivity.
Phys. Rev., 106(1):162–164, 1957.

[29] M. Sigrist and K. Ueda.
Phenomenological theory of unconventional superconductivity.
Rev. Mod. Phys., 63(2):239, 1991.

[30] V. P. Mineev and K. V. Samokhin.
Introduction to Unconventional Superconductivity.
Gordon and Breach Science, 1999.

[31] G. R. Stewart.
Unconventional superconductivity.
Adv. Phys., 66(2):75–196, 2017.

[32] C. Kallin and J. Berlinksy.
Chiral superconductors.
Rep. Prog. Phys., 79(5):054502, 2016.

[33] A. Kapitulnik, J. Xia, E. Schemm, and A. Palevski.
Polar Kerr effect as probe for time-reversal symmetry breaking in unconventional superconductors.
New Journal of Physics, 11:055060, 2009.

[34] T. Sauer.
Einstein and the early theory of superconductivity, 1919-1922.
Archive for History of Exact Sciences, 61(2):159–211, 2007.

[35] D. Goodstein and J. Goodstein.
Richard feynman and the history of superconductivity.
Physics in Perspective, 2(1):30–47, 2000.

[36] E. Merzbacher.
Quantum Mechanics.
John Wiley & Sons, Inc., third edition, 1998.

[37] M. Wolfke and W. H. Keesom.
Comm. Phys. Lab. Univ. Leiden, 190b, 1927.

[38] W. H. Keesom and K. Clusius.
Comm. Phys. Lab. Univ. Leiden, 219e, 1932.

[39] P. Kapitza.
Viscosity of Liquid Helium below the λ-Point.
Nature, 141(3558):74, 1938.

[40] J. F. Allen and A. D. Misener.
Flow Phenomena in Liquid Helium II.
Nature, 142(3597):643–644, 1938.

[41] A. Einstein.
Quantentheorie des einatomigen idealen Gases.
Sitzunber. Preuss. Akad. Wiss., 1(3), 1925.

[42] F. London.
The λ-phenomenon of liquid helium and the bose-einstein degeneracy.
Nature, 141:643–644, 1938.

[43] F. London.
On the Bose-Einstein Condensation.
Phys. Rev., 154:947–954, 1938.

[44] L. Tisza.
Transport Phenomena in Helium II.
Nature, page 913, 1938.

[45] L. Tisza.
C. R. Acad. Sci., 207:1035, 1938.

[46] F. London.
On the problem of the molecular theory of superconductivity.
Phys. Rev., 74(5):562–573, 1948.

[47] R. A. Ogg Jr.
Bose-Einstein Condensation of Trapped Electron Pairs. Phase Separation and Superconductivity of Metal-Ammonia Solutions.
Phys. Rev., 69(5-6):243–244, 1946.

[48] N. N. Bogoliubov.
On the theory of superfluidity.
J. Phys. (U.S.S.R.), 11(1):23–32, 1947.

[49] L. D. Landau.
On the theory of superfluidity.
Phys. Rev., 75(5):884–885, 1949.

[50] L. N. Cooper.
Bound Electron Pairs in a Degenerate Fermi Gas.
Phys. Rev., 104(4):1189–1190, 1956.

[51] A. M. Kadin.
Spatial structure of the cooper pair.
J. Supercond. Nov. Magn., 20(4):285–292, 2007.

[52] A. B. Pippard.
An experimental and theoretical study of the relation between magnetic field and current in a superconductor.
Proc. Royal Soc. A, 216(1127):547–568, 1953.

[53] N. N. Bogoliubov.
A new method in the theory of superconductivity i.
J. Exptl. Theoret. Phys. (U.S.S.R.), 34(1):41–46, 1958.

[54] V. V. Tolmachev and S. V. Tiablikov.
A new method in the theory of superconductivity ii.
J. Exptl. Theoret. Phys. (U.S.S.R.), 34(1):46–50, 1958.

[55] L. P. Gor'kov.
Zh. Eksp. Teor. Fiz., 36(1918), 1959.

[56] G. M. Eliashberg.
Zh. Eksp. Teor. Fiz., 38(966), 1960.

[57] G. M. Eliashberg.
Zh. Eksp. Teor. Fiz., 39(1437), 1960.

[58] H. Fröhlich.
Theory of the Superconducting State. I. The Ground State at the Absolute Zero of Temperature.
Phys. Rev., 79(5):845–856, 1950.

[59] W. L. McMillan.
Transition temperature of strong-coupled superconductors.
Phys. Rev., 167(2):331, 1968.

[60] J. Bardeen.
Electron-Vibration Interactions and Superconductivity.
Rev. Mod. Phys., 23(3):261, 1951.

[61] J. Bardeen.
Theory of the Meissner Effect in Superconductors.
Phys. Rev., 97(6):1724–1725, 1956.

[62] E. Maxwell.
Isotope effect in the superconductivity of mercury.
Phys. Rev., 78(4):477, 1950.

[63] C. A. Reynolds, B. Serin, W. H. Wright, and L. B. Nesbitt.
Superconductivity of isotopes of mercury.
Phys. Rev., 78(4):487, 1950.

[64] E. Dagotto.
Correlated electrons in high-temperature superconductors.
Rev. Mod. Phys., 66(3):763, 1994.

[65] A. P. Drozdov, M. I. Eremets, I. A. Troyan, Ksenofontov V., and S. I. Shylin.
Conventional superconductivity at 203 kelvin at high pressures in the sulfur hydride system.
Nature, 525:73–76, 2015.

[66] F. London.
Superfluids I.
Wiley and Sons, 1950.

[67] D. W. Osborne, B. Weinstock, and B. M. Abraham.
Comparison of the Flow of Iostopically Pure Liquid He^3 and He^4.
Phys. Rev., 75(6):988, 1949.

[68] K. A. Brueckner, T. Soda, P. W. Anderson, and P. Morel.
Level Structure of Nuclear Matter artd Liquid ^{3}He.
Phys. Rev., 118(5):1442, 1960.

[69] P. W. Anderson and P. Morel.
Generalized Bardeen-Cooper-Schrieffer States and the Proposed Low-Temperature Phase of Liquid ^{3}He.
Phys. Rev., 123(6):1911, 1961.

[70] R. Balian and N. R. Werthamer.
Superconductivity with Pairs in a Relative **p** Wave.
Phys. Rev., 131(4):1553, 1963.

[71] D. D. Oscheroff, R. C. Richardson, and D. M. Lee.
Evidence for a New Phase of Solid He^3.
Phys. Rev. Lett., 28(14):885, 1972.

[72] D. M. Lee.
The extraordinary phases of liquid ^{3}He.
Rev. Mod. Phys., 69(3):645–665, 1997.

[73] J. C. Wheatley.
Experimental properties of superfluid ^{3}He.
Rev. Mod. Phys., 47(2):415, 1975.

[74] A. J. Leggett.
A theoretical description of the new phases of liquid ^{3}He.
Rev. Mod. Phys., 47(2):331, 1975.

[75] P. W. Anderson and W. F. Brinkman.
Anisotropic Superfluidity in ^{3}He: A Possible Interpretation of Its Stability as a Spin-Fluctuation Effect.
Phys. Rev. Lett., 30(22):1108, 1973.

[76] W. F. Brinkman and P. W. Anderson.

Anisotropic superfluidity in ^{3}He: Consequences of the spin-fluctuation model.
Phys. Rev. A: At., Mol., Opt. Phys., 8(5):2732, 1973.

[77] F. Steglich, J. Aarts, C. D. Bredl, W. Lieke, D. Meschede, W. Franz, and Schäfer.
Superconductivity in the Presence of Strong Pauli Paramagnetism: $CeCu_2Si_2$.
Phys. Rev. Lett., 43(25):1892–1896, 1979.

[78] W. Franz, A. Grießel, F. Steglich, and D. Wohlleben.
Transport properties of $LaCu_2Si_2$ and $CeCu_2Si_2$ between 1.5K and 300K.
Z. Phys. B. Con. Mat., 31(1):7–17, 1978.

[79] G. R. Stewart.
Heavy-fermion systems.
Rev. Mod. Phys., 56(4):755, 1984.

[80] C. Pfleiderer.
Superconducting phases of f-electron compounds.
Rev. Mod. Phys., 81(4):1551, 2009.

[81] L. Taillefer, J. Flouquet, and G. G. Lonzarich.
Normal and superconducting phases of heavy fermions.
Physica B, 169(1-4):257–270, 1991.

[82] P. W. Anderson.
Heavy-electron superconductors, spin fluctuations, and triplet pairing.
Phys. Rev. B, 30(3):1549, 1984.

[83] R. Joynt and L. Taillefer.
The superconducting phases of UPt_3.
Rev. Mod. Phys., 74(1):235, 2002.

[84] J. W. Chen, S. E. Lambert, M. B. Maple, Z. Fisk, J. L. Smith, G. R. Stewart, and J. O. Willis.
Upper critical magnetic field of the heavy-fermion superconductor UPt_3.
Phys. Rev. B, 1984.

[85] J. A. Sauls.
A theory for the superconducting phases of UPt^3.
J. Low Temp. Phys., 95(1-2):153–168, 1994.

[86] E. R. Schemm, W. J. Gannon, C. M. Wishne, W. P. Halperin, and A. Kapitulnik.
Observation of broken time-reversal symmetry in the heavy-fermion superconductor UPt_3.
Science, 345(6193):190–193, 2014.

[87] J. G. Bednorz and K. A. Muller.
Possible High-Tc Superconductivity in the Ba-La-Cu-O System.
Z. Phys. B. Con. Mat., 64(2):189–193, 1986.

[88] P. A. Lee, N. Nagaosa, and X. G. Wen.
Doping a Mott insulator: Physics of high-temperature superconductivity.
Rev. Mod. Phys., 78(1):17–85, 2006.

[89] A. Schilling, M. Cantoni, J. D. Guo, and H. R. Ott.
Superconductivity above 130-K in the Hg-Ba-Ca-Cu-O system.
Nature, 363(6424):56–58, 1993.

[90] T. Timusk and B. Statt.
The pseudogap in high-temperature superconductors: An experimental survey.
Rep. Prog. Phys., 62(1):61–122, 1999.

[91] Y. J. Uemura, G. M. Luke, B. J. Sternlieb, J. H. Brewer, J. F. Carolan, W. N. Hardy, R. Kadano, J. R. Kempton, R. F. Kiefl, S. R. Kreitzman, P. Mulhern, T. M. Riseman, D. Ll. Williams, B. X. Yang, S. Uchida, H. Takagi, J. Gopalakrishnan, A. W. Sleight, M. A. Subramanian, C. L. Chien, M. Z. Zieplak, Xiao Gang, V. Y. Lee, B. W. Statt, C. E. Stornach, W. J. Kossler, and X. H. Yu.
Universal Correlations between T_c and n_s/m^* (Carrier Density over Effective Mass) in High-T_c Cuprate Superconductors.
Phys. Rev. Lett., 62(19):2317, 1989.

[92] R. Mankowsky, A. Subedi, M. Först, S. O. Mariager, M. Chollet, H. T. Lemke, J. S. Robinson, J. M. Glownia, M. P. Minitti, A. Frano, M. Fechner, N. A. Spaldin, T. Loew, B. Keimer, A. Georges, and A. Cavalleri.
Nonlinear lattice dynamics as a basis for enhanced superconductivity in $YBa_2Cu_3O_{6.5}$.
Nature, 516:71–73, 2014.

[93] L. Walz and F. Lichtenberg.
Refinement of the Structure of Sr_2RuO_4 with 100 and 295 K X-Ray Data.
Acta Crystallogr., Sect. C: Cryst. Struct. Commun., 49:1268–1270, 1993.

[94] Q. Huang, J. L. Soubeyroux, O. Chmaissem, I. Natali Sora, A. Santoro, R. J. Cava, J. J. Krajewski, and W. F. Peck, Jr.
Neutron powder diffraction study of the crystal structures of Sr_2RuO_4 and Sr_2IrO_4 at room temperature and at 10 k.
J. Solid State Chem., 112(2):355–361, 1994.

[95] J. L. Martínez, C. Prieto, J. Rodríguez-Carvajal, A. de Andrés, M. Vallet-Regí, and J. M. González-Calbet.

Structural and magnetic properties of Sr_2RuO_4-type oxides.
J. Magn. Magn. Mater., 140-144:179–180, 1995.

[96] Y. Maeno, H. Hashimoto, K. Yoshida, S. Nishikazi, T. Fujita, J. G. Bednorz, and F. Lichtenberg.
Superconductivity in a layered perovskite without copper.
Nature, 372(6506):532–534, 1994.

[97] K. Ishida, H. Mukuda, Y. Kitaoka, Z. Q. Mao, Y. Mori, and Y. Maeno.
Anisotropic Superconducting Gap in the Spin-Triplet Superconductor Sr_2RuO_4: Evidence from a Ru-NQR Study.
Phys. Rev. Lett., 84(23):5387, 2000.

[98] G. M. Luke, Y. Fudamoto, K. M. Kojima, M. I. Larkin, J. Merrin, B. Nachumi, Y. J. Uemura, Y. Maeno, Z. Q. Mao, Y. Mori, H. Nakamura, and M. Sigrist.
Time-reversal symmetry-breaking superconductivity in Sr_2RuO_4.
Nature, 394(6693):558–561, 1998.

[99] T. M. Riseman, P. G. Kealey, E. M. Forgan, A. P. Mackenzie, L. M. Galvin, A. W. Tyler, S. L. Lee, C. Ager, D. McK. Paul, C. M. Aegerter, R. Cubitt, Z. Q. Mao, T. Akima, and Y. Maeno.
Observation of a square flux-line lattice in the unconventional superconductor Sr_2RuO_4.
Nature, 396:242–245, 1998.

[100] T. M. Riseman, P. G. Kealey, E. M. Forgan, A. P. Mackenzie, L. M. Galvin, A. W. Tyler, S. L. Lee, C. Ager, D. McK. Paul, C. M. Aegerter, R. Cubitt, Z. Q. Mao, T. Akima, and Y. Maeno.
Correction: Observation of a square flux-line lattice in the unconventional superconductor Sr_2RuO_4.
Nature, 404:629, 2000.

[101] P. G. Kealey, T. M. Riseman, E. M. Forgan, L. M. Galvin, A. P. Mackenzie, S. L. Lee, D. M. Paul, R. Cubitt, D. F. Agterberg, R. Heeb, Z. Q. Mao, and Y. Maeno.
Reconstruction from small-angle neutron scattering measurements of the real space magnetic field distribution in the mixed state of Sr_2RuO_4.
Phys. Rev. Lett., 84(26):6094, 2000.

[102] J. Xia, Y. Maeno, P. T. Beyersdorf, M. M. Fejer, and A. Kapitulnik.
High resolution polar Kerr effect measurements of Sr_2RuO_4: Evidence for broken time-reversal symmetry in the superconducting state.
Phys. Rev. Lett., 97(16)(167002), October 2006.

[103] T. M. Rice and M. Sigrist.
Sr_2RuO_4: An electronic analogue of ^{3}He?
J. Phys.: Condens. Matter, 7(47):643, 1995.

[104] G. Baskaran.
Why is Sr_2RuO_4 not a high T_c superconductor? Electron correlation, Hund's coupling and p-wave instability.
Physica B, 223-224:490–495, 1996.

[105] K. Ishida, H. Mukuda, Y. Kitaoka, K. Asayama, Z. Q. Mao, Y. Mori, and Y. Maeno.
Spin-triplet superconductivity in Sr_2RuO_4 identified by ^{17}O Knight shift.
Nature, 396(6712):658–660, 1998.

[106] A. P. Mackenzie and Y. Maeno.
The superconductivity of Sr_2RuO_4 and the physics of spin-triplet pairing.
Rev. Mod. Phys., 75(2):657–712, 2003.

[107] M. Matsumoto and M. Sigrist.
Quasiparticle states near the surface and the domain wall in a $p_x \pm ip_y$-wave superconductor.
J. Phys. Soc. Jpn., 68(3):994, 1999.

[108] M. Stone and R. Roy.
Edge modes, edge currents, and gauge invariance in px+ipy superfluids and superconductors.
Phys. Rev. B, 69(18):184511, 2004.

[109] W. Huang, S. Lederer, E. Taylor, and C. Kallin.
Non-topological nature of the edge current in a chiral p-wave superconductor.
Phys. Rev. B, 91(9):094507, 2015.

[110] J. R. Kirtley, C. Kallin, C. W. Hicks, E.-A. Kim, Y. Liu, K. A. Moler, Y. Maeno, and K. D. Nelson.
Upper limit on spontaneous supercurrents in Sr_2RuO_4.
Phys. Rev. B, 76(1):014526, 2007.

[111] C. W. Hicks, J. R. Kirtley, T. M. Lippman, N. C. Koshnick, M. E. Huber, Y. Maeno, W. M. Yuhasz, M. B. Maple, and K. A. Moler.
Limits on superconductivity-related magnetization in Sr_2RuO_4 and $PrOs_4Sb_{12}$ from scanning SQUID microscopy.
Phys. Rev. B, 81(21):214501, 2010.

[112] P. J. Curran, S. J. Bending, W. M. Desoky, A. S. Gibbs, S. L. Lee, and A. P. Mackenzie.
Search for spontaneous edge currents and vortex imaging in Sr_2RuO_4 mesostructures.
Phys. Rev. B, 89(14):144504, 2014.

[113] T. Thonhauser, D. Ceresoli, D. Vanderbilt, and R. Resta.
Orbital magnetization in periodic insulators.
Phys. Rev. Lett., 95(13):137205, 2005.

[114] D. Ceresoli, T. Thonhauser, D. Vanderbilt, and R. Resta.
Orbital magnetization in crystalline solids: Multi-band insulators, Chern insulators, and metals.
Phys. Rev. B, 74(2):024408, 2006.

[115] N. Nagaosa, J. Sinova, S. Onoda, A. H. MacDonald, and N. P. Ong.
Anomalous hall effect.
Rev. Mod. Phys., 82(2):1539, 2010.

[116] J. Goryo.
Intrinsic and extrinsic origins of the polar Kerr effect in a chiral p-wave superconductor.
Mod. Phys. Lett. B, 24(29):2831–2836, 2010.

[117] V. P. Mineev.
Whether there is the intrinsic Hall effect in a multi-band superconductor?
J. Phys. Soc. Jpn., 81(9):093703, 2012.

[118] J. Xia, E. Schemm, G. Deutscher, S. A. Kivelson, D. A. Bonn, W. N. Hardy, R. Liang, W. Siemons, G. Koster, M. M. Fejer, and A. Kapitulnik.
Polar Kerr-effect measurements of the high-temperature $YBa_2Cu_3O_{6+x}$ superconductor: Evidence for broken symmetry near the pseudogap temperature.
Phys. Rev. Lett., 100(12)(127002), March 2008.

[119] H. Karapetyan, J. Xia, M. Hucker, G. D. Gu, J. M. Tranquada, M. M. Fejer, and A. Kapitulnik.
Evidence of chiral order in the charge-ordered phase of superconducting $La_{1.875}Ba_{0.125}CuO_4$ single crystals using polar Kerr-effect measurements.
Phys. Rev. Lett., 112(4):047003, 2014.

[120] C. L. Kane and E. J. Mele.
Z_2 Topological Order and the Quantum Spin Hall Effect.
Phys. Rev. Lett., 95(14):146802, 2005.

[121] F. D. M. Haldane.

Model for a quantum Hall effect without Landau levels: Condensed-matter realization of the “parity anomaly”.
Phys. Rev. Lett., 61(18):2015, 1988.

[122] X. Chen, Z. C. Gu, and X. G. Wen.
Classification of gapped symmetric phases in one-dimensional spin systems.
Phys. Rev. B, 83(3):035107, 2011.

[123] M. H. Freedman, A. Kitaev, M. J. Larsen, and Z. Wang.
Topological quantum computation.
Bull. Amer. Math. Soc., 40:31–38, 2002.

[124] M. König, S. Wiedmann, C. Brüne, A. Roth, H. Buhmann, L. W. Molenkamp, X. L. Qi, and S. C. Zhang.
Quantum Spin Hall Insulator State in HgTe Quantum Wells.
Science, 318(5851):766–770, 2007.

[125] P. Hohenberg and W. Kohn.
Inhomogeneous electron gas.
Phys. Rev., 136(3B):864, 1964.

[126] W. Kohn and L. J. Sham.
Self-consistent equations including exchange and correlation effects.
Phys. Rev., 140(4A):1133, 1965.

[127] F. Bloch.
Z. Phys., 52:555, 1928.

[128] J. C. Slater and G. F. Koster.
Simplified LCAO Method for the Periodic Potential Problem.
Phys. Rev., 94(6):1498, 1954.

[129] M. Gradhand, K. I. Wysokiǹski, J. F. Annett, and B. L. Györffy.
Kerr rotation in the unconventional superconductor Sr_2RuO_4.
Phys. Rev. B., 88(9):094504, 2013.

[130] N. N. Bogoliubov, V. V. Tolmachev, and D. V. Shirkov.
A new method in the theory of superconductivity.
Fortschr. Phys., 6(11-12):605–682, 1958.

[131] N. N. Bogoliubov.
On a new method in the theory of superconductivity.
Il Nuovo Cimento, 7(6):794–805, 1958.

[132] P. G. de Gennes.
Superconductivity of Metals and Alloys.
W. A. Benjamin, New York, 1966.

[133] J. G. Valatin.
Comments on the theory of superconductivity.
Il Nuovo Cimento, 7(6):843–857, 1958.

[134] G. C. Wick.
The evaluation of the collision matrix.
Phys. Rev., 80(2):268, 1950.

[135] L. P. Gor'kov.
On the energy spectrum of superconductors.
J. Exp. Theor. Phys., 34(7)(3):505–508, 1958.

[136] M. H. Cohen.
Generalized self-consistent-field theory: Gor'kov factorization.
Phys. Rev., 137(2A):497–507, 1965.

[137] T. Oguchi.
Electronic band structure of the superconductor Sr_2RuO_4.
Phys. Rev. B, 51(2):R1385, 1995.

[138] R. J. Cava, B. Batlogg, K. Kiyono, H. Takagi, J. J. Krajewski, W. F. Peck, Jr., L. W. Rupp, Jr., and C. H. Chen.
Localized-to-itinerant electron transition in $Sr_2Ir_{1-x}Ru_xO_4$.
Phys. Rev. B, 49(17):11890, 1994.

[139] M. Braden, A. H. Moudden, S. Nishizaki, Y. Maeno, and T. Fujita.
Structural analysis of Sr_2RuO_4.
Physica C, 273(3-4):248–254, 1997.

[140] J. S. Gardner, G. Balakrishnan, and D. McK. Paul.
Neutron powder diffraction studies of Sr_2RuO_4 and $SrRuO_3$.
Physica C, 252(3-4):303–307, 1995.

[141] J. S. Gardner, G. Balakrishnan, D. McK. Paul, and C. Haworth.
Neutron diffraction and magnetisation studies of Sr_2RuO_4 below 2 K.
Physica C, 265(3-4):251–257, 1996.

[142] T. Vogt and D. J. Buttrey.
Low-temperature structural behavior of Sr_2RuO_4.
Phys. Rev. B, 52(14):R9843, 1995.

[143] O. Chmaissem, J. D. Jorgensen, H. Shaked, S. Ikeda, and Y. Maeno.
Thermal expansion and compressibility of Sr_2RuO_4.
Phys. Rev. B, 57(9):5067, 1998.

[144] J. J. Neumeier, M. F. Hundley, M. G. Smith, J. D. Thompson, C. Allgeier, H. Xie, W. Yelon, and J. S. Kim.
Magnetic, thermal, transport, and structural properties of $Sr_2RuO_{4+\delta}$: Enhanced charge-carrier mass in a nearly metallic oxide.
Phys. Rev. B, 50(24):17910, 1994.

[145] C. Bergemann, A. P. Mackenzie, S. R. Julian, D. Forsythe, and E. Ohmichi.
Quasi-two-dimensional fermi liquid properties of the unconventional superconductor Sr_2RuO_4.
Adv. Phys., 52(7):639–725, 2003.

[146] A. P. Mackenzie, S. R. Julian, A. J. Diver, G. J. McMullan, M. P. Ray, G. G. Lonzarich, Y. Maeno, S. Nishizaki, and T. Fujita.
Quantum oscillations in the layered perovskite superconductor Sr_2RuO_4.
Phys. Rev. Lett., 76(20):3786, 1996.

[147] D. J. Singh.
Relationship of Sr_2RuO_4 to the superconducting layered cuprates.
Phys. Rev. B, 52(2):1358, 1995.

[148] I. Hase and Y. Nishihara.
Electronic structures of Sr_2RuO_4 and Sr_2RhO_4.
J. Phys. Soc. Jpn., 65(12):3957–3963, 1996.

[149] G. J. McMullan, M. P. Ray, and R. J. Needs.
Comparison of the calculated and observed fermi surfaces of Sr_2RuO_4.
Physica B, 223-224:529–531, 1996.

[150] Y. Yoshida, R. Settai, Ōnuki. Y., H. Takei, K. Betsuyaku, and H. Harima.
Fermi surface and yamaji effect in Sr_2RuO_4.
J. Phys. Soc. Jpn., 67(5):1677–1681, 1998.

[151] C. Noce and M. Cuoco.
Energy bands and fermi surface of Sr_2RuO_4.
Phys. Rev. B, 59(4):2659, 1999.

[152] A. Pérez-Navarro, J. Costa-Quintana, and F. López-Aguilar.
Electronic structure of Sr_2RuO_4 by means of local-density approximation plus strong correlation effects.

Phys. Rev. B, 61(15):10125, 2000.

[153] C. Bergemann, S. R. Julian, A. P. Mackenzie, S. Nishizaki, and Y. Maeno.
Detailed topography of the fermi surface of Sr_2RuO_4.
Phys. Rev. Lett., 84(12):2662–2665, 2000.

[154] A. P. Mackenzie, S. R. Julian, A. J. Diver, G. J. McMullan, G. G. Lonzarich, Y. Maeno, S. Nishizaki, and T. Fujita.
Observation of quantum oscillations in Sr_2RuO_4.
In Z. Fisk, L. Gor'kov, D. Meltzer, and R. Schrieffer, editors, *Proceedings of the 2nd Conference on Physical Phenomena at High Magnetic Fields*, page 537. World Scientific, Singapore, 1996.

[155] S. Nishizaki, Y. Maeno, S. Farner, S. Ikeda, and T. Fujita.
Evidence for unconventional superconductivity of Sr_2RuO_4 from specific-heat measurements.
J. Phys. Soc. Jpn., 67(2):560–563, 1998.

[156] S. Nishizaki, Y. Maeno, and Z. Mao.
Effect of impurities on the specific heat of the spin-triplet superconductor Sr_2RuO_4.
J. Low Temp. Phys., 117(5-6):1581–1585, 1999.

[157] S. Nishizaki, Y. Maeno, and Z. Mao.
Changes in the superconducting state of Sr_2RuO_4 under magnetic fields probed by specific heat.
J. Phys. Soc. Jpn., 69(2):572, 2000.

[158] C. Langhammer, F. Steglich, M. Lang, and T. Sasaki.
Low-temperature specific heat of Sr_2RuO_4.
Eur. Phys. J. B, 26(4):413–416, 2002.

[159] Y. Hasegawa, K. Machida, and M. Ozaki.
Spin-Triplet Superconductivity with Line Nodes in Sr_2RuO_4.
J. Phys. Soc. Jpn., 69(2):336, 2000.

[160] J. F. Annett, B. L. Györffy, and K. I. Wysokiǹski.
Orbital magnetic moment of a chiral p-wave superconductor.
New Journal of Physics, 11:055063, 2009.

[161] J. F. Annett, B. L. Györffy, and K. I. Wysokiǹski.
Interlayer coupling and p-wave pairing in strontium ruthenate.
Phys. Rev. B, 66(13):134514, 2002.

[162] J. F. Annett, B. L. Györffy, G. Litak, and K. I. Wysokiǹski.
Gap nodes and time reversal symmetry breaking in strontium ruthenate.
Eur. Phys. J. B, 36(3):301–312, 2003.

[163] M. Gradhand and J. F. Annett.
The Berry curvature of the Bogoliubov quasiparticle Bloch states in the unconventional superconductor Sr_2RuO_4.
J. Phys.: Condens. Matter, 26(27):274205, 2014.

[164] J. Robbins, J. F. Annett, and M. Gradhand.
Effect of spin-orbit coupling on the polar Kerr effect in Sr_2RuO_4.
Phys. Rev. B, 96(14):144503, 2017.

[165] K. I. Wysokiǹski, J. F. Annett, and B. L. Györffy.
Intrinsic optical dichroism in the chiral superconducting state of Sr_2RuO_4.
Phys. Rev. Lett., 108(7):077004, 2012.

[166] K. I. Wysokiǹski, G. Litak, J. F. Annett, and B. L. Györffy.
Spin triplet superconductivity in Sr_2RuO_4.
Phys. Status Solidi B, 236(2):325–331, 2003.

[167] T. Yokoya, A. Chainani, T. Takahashi, H. Ding, J. C. Campuzano, H. Katayama-Yoshida, M. Kasai, and Y. Tokura.
Angle-resolved photoemission study of Sr_2RuO_4.
Phys. Rev. B, 54(18):13311, 1996.

[168] V. B. Zabolotnyy, D. V. Evtushinsky, A. A. Kordyuk, T. K. Kim, E. Carleschi, B. P. Doyle, R. Fittipaldi, M. Cuoco, A. Vecchione, and S. V. Borisenko.
Renormalized band structure of Sr_2RuO_4: A quasiparticle tight-binding approach.
J. Electron Spectrosc. Relat. Phenom., 191:48, 2013.

[169] A. P. Mackenzie, S.-I. Ikeda, Y. Maeno, T. Fujita, S. R. Julian, and G. G. Lonzarich.
The Fermi surface topography of Sr_2RuO_4.
J. Phys. Soc. Jpn., 67(2):385, 1998.

[170] N. Iwahara and L. F. Chibotaru.
Orbital disproportionation of electronic density - a universal feature of alkali-doped fullerides.
Nat. Commun., 7(13093), 2016.

[171] R. Karplus and J. M. Luttinger.
Hall Effect in Ferromagnetics.
Phys. Rev., 95(5):1154, 1954.

[172] T. Jungwirth, Q. Niu, and A. H. MacDonald.
Anomalous hall effect in ferromagnetic semiconductors.
Phys. Rev. Lett., 88(20):207208, 2002.

[173] J. Robbins, J. F. Annett, and M. Gradhand.
Modern theory for the orbital moment in a superconductor.
arXiv:1802.10533, 2018.

[174] T. Tanaka, H. Kontania, M. Naitoa, D. S. Hirashima, K. Yamadab, and J. Inouec.
Spin Hall effect in Sr_2RuO_4 and transition metals (Nb,Ta).
J. Phys. Chem. Solids, 69(12):3250–3252, 2008.

[175] C. D. H. Chisholm.
Group theoretical techniques in quantum chemistry.
Academic Press, New York, 1976.

[176] Y. Yanase, S. Takamatsu, and M. Udagawa.
Spin-Orbit Coupling and Multiple phases in Spin-Triplet Superconductor Sr_2RuO_4.
J. Phys. Soc. Jpn., 83(6):061019, 2014.

[177] Y. Yanase and M. Ogata.
Microscopic Identification of the D-vector in Triplet Superconductor Sr_2RuO_4.
J. Phys. Soc. Jpn., 72(3):673, 2003.

[178] C. G. Fatuzzo, M. Dantz, S. Fatale, P. Olalde-Velasco, N. E. Shaik, B. Dalla Piazza, S. Toth, J. Pelliciari, R. Fittipaldi, A. Vecchione, N. Kikugawa, J. S. Brooks, H. M. Rønnow, M. Grioni, Ch. Rüegg, T. Schmitt, and J. Chang.
Spin-orbit-induced orbital excitations in Sr_2RuO_4 and Ca_2RuO_4: A resonant inelastic x-ray scattering study.
Phys. Rev. B, 91(15):155104, 2015.

[179] I. I. Mazin, D. A. Papaconstantopoulos, and D. J. Singh.
Tight-binding hamiltonians for sr-filled ruthenates: Application to the gap anisotropy and hall coefficient in Sr_2RuO_4.
Phys. Rev. B, 61(8):5223, 2000.

[180] T. Mishonov and E. Penev.
Tight-binding modelling of the electronic band structure of layered superconducting perovskites.
J. Phys.: Condens. Matter, 12(2):143,Äì159, 2000.

[181] P. K. de Boer and R. A. de Groot.
Electronic structure of magnetic Sr_2RuO_4.

Phys. Rev. B, 59(15):9894, 1999.

[182] M. W. Haverkort, I. S. Elfimov, L. H. Tjeng, G. A. Sawatzky, and A. Damascelli.
Strong spin-orbit coupling effects on the Fermi surface of Sr_2RuO_4 and Sr_2RhO_4.
Phys. Rev. Lett., 101(2):026406, 2008.

[183] T. Oguchi.
Spin-Orbit Effects on the Ru-*d* Orbital Hybridization and Fermi Surface in $Ca_{2-x}Sr_xRuO_4$.
J. Phys. Soc. Jpn., 78(4):044702, 2009.

[184] T. Scaffidi and S. H. Simon.
Large Chern number and edge currents in Sr_2RuO_4.
Phys. Rev. Lett., 115(8):087003, 2015.

[185] T. Scaffidi, J. C. Romers, and S. H. Simon.
Pairing symmetry and dominant band in Sr_2RuO_4.
Phys. Rev. B, 89(22):220510(R), 2014.

[186] A. P. Mackenzie, R. K. W. Haselwimmer, A. W. Tyler, G. G. Lonzarich, Y. Mori, S. Nishizaki, and Y. Maeno.
Extremely strong dependence of superconductivity on disorder in Sr_2RuO_4.
Phys. Rev. Lett., 80(1):161, 1998.

[187] A. P. Mackenzie, R. K. W. Haselwimmer, A. W. Tyler, G. G. Lonzarich, Y. Mori, S. Nishizaki, and Y. Maeno.
Erratum: Extremely strong dependence of superconductivity on disorder in Sr_2RuO_4 [phys. rev. lett. 80, 161 (1998)].
Phys. Rev. Lett., 80(17):3890, 1998.

[188] P. W. Anderson.
Knight Shift in Superconductors.
Phys. Rev. Lett., 3(7):325, 1959.

[189] E. Hassinger, P. Bourgeois-Hope, H. Taniguchi, S. René de Cotret, G. Grissonnanche, M. S. Anwar, Y. Maeno, N. Doiron-Leyraud, and L. Taillefer.
Vertical line nodes in the superconducting gap structure of Sr_2RuO_4.
Phys. Rev. X, 2017.

[190] M. E. Zhitomirsky and T. M. Rice.
Interband proximity effect and nodes of superconducting gap in Sr_2RuO_4.
Phys. Rev. Lett., 87(5):057001, 2001.

[191] K. Deguchi, Z. Q. Mao, and Y. Maeno.

Determination of the superconducting gap structure in all bands of the spin-triplet superconductor Sr_2RuO_4.
J. Phys. Soc. Jpn., 73(5):1313–1321, 2004.

[192] K. Deguchi, Z. Q. Mao, H. Yaguchi, and Y. Maeno.
Gap structure of the spin-triplet superconductor Sr_2RuO_4 determined from the field-orientation dependence of the specific heat.
Phys. Rev. Lett., 92(4):047002, 2004.

[193] I. Bonalde, B. D. Yanoff, M. B. Salamon, D. J. Van Harlingen, E. M. E. Chia, Z. Q. Mao, and Y. Maeno.
Temperature dependence of the penetration depth in Sr_2RuO_4: Evidence for nodes in the gap function.
Phys. Rev. Lett., 85(22):4775, 2000.

[194] M. A. Hein, Ormeno R. J., and C. E. Gough.
The microwave surface impedance of ultra-pure superconducting metals.
J. Phys.: Condens. Matter, 13(4):L65, 2001.

[195] H. Suderow, J. P. Brison, J. Flouquet, A. W. Tyler, and Y. Maeno.
Very low temperature thermal conductivity in the layered perovskite superconductor Sr_2RuO_4.
Journal of Physics: Condensed Matter, 10(34):L597, 1998.

[196] K. Izawa, H. Takahashi, H. Yamaguchi, Y. Matsuda, M. Suzuki, T. Sasaki, T. Fukase, Y. Yoshida, R. Settai, and Y. Onuki.
Superconducting gap structure of spin-triplet superconductor Sr_2RuO_4 studied by thermal conductivity.
Phys. Rev. Lett., 86(12):2653, 2001.

[197] M. A. Tanatar, M. Suzuki, S. Nagai, Z. Q. Mao, Y. Maeno, and T. Ishiguro.
Anisotropy of magnetothermal conductivity in Sr_2RuO_4.
Phys. Rev. Lett., 86(12):2649, 2001.

[198] M. A. Tanatar, S. Nagai, Z. Q. Mao, Y. Maeno, and T. Ishiguro.
Thermal conductivity of superconducting Sr_2RuO_4 in oriented magnetic fields.
Phys. Rev. B, 63(6):064505, 2001.

[199] M. Takigawa, M. Ichioka, K. Machida, and M. Sigrist.
Vortex structure in chiral p-wave superconductors.
Phys. Rev. B, 65(1):014508, 2001.

[200] D. F. Agterberg.
Vortex lattice structures of Sr_2RuO_4.
Phys. Rev. Lett., 80(23):5184, 1998.

[201] J. A. Duffy, S. M. Hayden, Y. Maeno, Z. Mao, J. Kulda, and G. J. McIntyre.
Polarized-neutron scattering study of the Cooper-pair moment in Sr_2RuO_4.
Phys. Rev. Lett., 85(25):5412, 2000.

[202] J. F. Annett, G. Litak, B. L. Györffy, and K. I. Wysokiǹski.
Spin-orbit coupling and symmetry of the order parameter in strontium ruthenate.
Phys. Rev. B, 73(13):134501, 2006.

[203] S. Nakajima.
Paramagnon Effect on the BCS Transition in He^3.
Progr. Theor. Phys., 50(4):1101–1109, 1973.

[204] D. F. Agterberg, T. M. Rice, and M. Sigrist.
Orbital dependent superconductivity in Sr_2RuO_4.
Phys. Rev. Lett., 78(17):3374, 1997.

[205] E. Taylor and C. Kallin.
Intrinsic Hall effect in a multiband chiral superconductor in the absence of an external magnetic field.
Phys. Rev. Lett., 108(15):157001, 2012.

[206] K. Kuroki, M. Ogata, R. Arita, and H. Aoki.
Crib-shaped triplet-pairing gap function for an orthogonal pair of quasi-one-dimensional fermi surfaces in Sr_2RuO_4.
Phys. Rev. B, 63(6):060506, 2001.

[207] Y. Tada, W. Nie, and M. Oshikawa.
Orbital angular momentum and spectral flow in two-dimensional chiral superfluids.
Phys. Rev. Lett., 114(19):195301, 2015.

[208] G. E. Volovik.
Orbital momentum of chiral superfluids and the spectral asymmetry of edge states.
JETP Lett., 100(11):742–745, 2015.

[209] W. Huang, E. Taylor, and C. Kallin.
Vanishing edge currents in non-p-wave topological chiral superconductors.
Phys. Rev. B, 90(22):224519, 2014.

[210] I. A. Firmo, S. Lederer, C. Lupien, A. P. Mackenzie, J. C. Davis, and S. A. Kivelson.

Evidence from tunneling spectroscopy for a quasi-one-dimensional origin of superconductivity in Sr_2RuO_4.
Phys. Rev. B, 88(13):134521, 2013.

[211] S. Raghu, S. A. Kivelson, and D. J. Scalapino.
Superconductivity in the repulsive Hubbard model: An asymptotically exact weak-coupling solution.
Phys. Rev. B, 81(22):224505, 2010.

[212] A. J. P. Meyer and G. Asch.
Experimental g' and g Values of Fe, Co, Ni, and Their Alloys.
J. Appl. Phys., 32(3):S330, 1961.

[213] A. Einstein and W. J. de Haas.
Experimental proof of the existence of ampère's molecular currents.
KNAW, Proceedings, 18 I:696–711, 1915.

[214] S. J. Barnett.
Magnetization by Rotation.
Phys. Rev., 6(4):239, 1915.

[215] K. Miyake and A. Tsuruta.
Theory for Intrinsic Magnetic Field in Chiral Superconductor Measured by μSR: Case of Sr_2RuO_4.
arXiv, 2017.

[216] S. Qiao, A. Kimura, H. Adachi, K. Iori, K. Miyamoto, T. Xie, H. Namatame, M. Taniguchi, A. Tanaka, T. Muro, S. Imada, and S. Suga.
Direct evidence of ferromagnetism without net magnetization observed by x-ray magnetic circular dichroism.
Phys. Rev. B, 70(13):134418, 2004.

[217] J. W. Taylor, J. A. Duffy, A. M. Bebb, M. R. Lees, L. Bouchenoire, S. D. Brown, and M. J. Cooper.
Temperature dependence of the spin and orbital magnetization density in $Sm_{0.982}Gd_{0.018}Al_2$ around the spin-orbital compensation point.
Phys. Rev. B, 66(16):161319, 2002.

[218] D. Xiao, M.-C. Chang, and Q. Niu.
Berry phase effects on electronic properties.
Rev. Mod. Phys., 82(3):1959, 2010.

[219] D. Xiao, Y. Yao, Z. Fang, and Q. Niu.
Berry-Phase Effect in Anomalous Thermoelectric Transport.
Phys. Rev. Lett., 97(2):026603, 2006.

[220] D. Xiao, W. Yao, and Q. Niu.
Valley-Contrasting Physics in Graphene: Magnetic Moment and Topological Transport.
Phys. Rev. Lett., 99(23):236809, 2007.

[221] F. Mauri and S. G. Louie.
Magnetic Susceptibility of Insulators from First Principles.
Phys. Rev. Lett., 76(22):4246, 1996.

[222] C. J. Pickard and F. Mauri.
First-Principles Theory of the EPR g Tensor in Solids: Defects in Quartz.
Phys. Rev. Lett., 88(8):086403, 2002.

[223] T. Thonhauser, D. Ceresoli, A. A. Mostofi, N. Marzari, R. Resta, and D. Vanderbilt.
A converse approach to the calculation of NMR shielding tensors.
J. Chem. Phys., 131(10):101101, 2009.

[224] A. M. Essin, J. E. Moore, and D. Vanderbilt.
Magnetoelectric Polarizability and Axion Electrodynamics in Crystalline Insulators.
Phys. Rev. Lett., 102(14):146805, 2009.

[225] A. M. Essin, A. M. Turner, J. E. Moore, and D. Vanderbilt.
Orbital magnetoelectric coupling in band insulators.
Phys. Rev. B, 81(20):205104, 2010.

[226] S. Murakami.
Quantum Spin Hall Effect and Enhanced Magnetic Response by Spin-Orbit Coupling.
Phys. Rev. Lett., 97(23):236805, 2006.

[227] R. D. King-Smith and D. Vanderbilt.
Theory of polarization of crystalline solids.
Phys. Rev. B, 47(3):1651, 1993.

[228] R. Resta.
Macroscopic polarization in crystalline dielectrics: the geometric phase approach.
Rev. Mod. Phys., 66(3):941, 1994.

[229] N. Marzari, A. A. Mostofi, J. R. Yates, I. Souza, and D. Vanderbilt.
Maximally localized Wannier functions: Theory and applications.
Rev. Mod. Phys., 84(4):1419, 2012.

[230] I. Souza and D. Vanderbilt.
Dichroic f-sum rule and the orbital magnetization of crystals.
Phys. Rev. B, 77(5):054438, 2008.

[231] M. Ishikawa.
Orbital Angular Momentum of Anisotropic Superfluid.
Prog. Theor. Phys, 57(6):1836, 1976.

[232] M. C. Cross.
A generalized Ginzburg-Landau approach to the superfluidity of helium 3.
J. Low Temp. Phys., 21(5-6):525–534, 1975.

[233] J. Jang, D. G. Ferguson, V. Vakaryuk, R. Budakian, S. B. Chung, P. M. Goldbart, and Y. Maeno.
Observation of Half-Height Magnetization Steps in Sr_2RuO_4.
Science, 331(6014):186–188, 2011.

[234] M. V. Berry.
Quantal phase factors accompanying adiabatic changes.
Proc. Roy. Soc. London, 392:45–57, 1984.

[235] M. Gradhand, D. V. Fedorov, F. Pientka, P. Zahn, I. Mertig, and B. L. Györffy.
First-principle calculations of the berry curvature of bloch states for charge and spin transport of electrons.
J. Phys.: Condens. Matter, 24(21):213202, 2012.

[236] J. Smit.
The spontaneous Hall effect in ferromagnetics I.
Physica, 21(6-10):877–887, 1955.

[237] J. Smit.
The spontaneous Hall effect in ferromagnetics II.
Physica, 24(1-5):39–51, 1958.

[238] L. Berger.
Influence of spin-orbit interaction on the transport processes in ferromagnetic nickel alloys, in the presence of a degeneracy of the 3d band.
Physica, 30(6):1141–1159, 1964.

[239] W. Kim, F. Marsiglio, and C. S. Ting.
Hall conductivity of a spin-triplet superconductor.
Phys. Rev. Lett., 100(22):227003, 2008.

[240] R. M. Lutchyn, P. Nagornykh, and V. M. Yakovenko.
Frequency and temperature dependence of the anomalous ac Hall conductivity in a chiral $p_x + ip_y$ superconductor with impurities.
Phys. Rev. B, 80(10):104508, 2009.

[241] J. Goryo.
Impurity-induced polar Kerr effect in a chiral p-wave superconductor.
Phys. Rev. B, 78(6):060501(R), 2008.

[242] A. Tsuruta, S. Yukawa, and K. Miyake.
Intrinsic Angular Momentum and Intrinsic Magnetic Moment of Chiral Superconductor on Two-Dimensional Square Lattice.
J. Phys. Soc. Jpn., 84(9):094712, 2015.

[243] E. H. Hall.
On a new action of the magnet on electric currents.
Amer. J. Math., 2:287–292, 1879.

[244] E. H. Hall.
On the "Rotational Coefficient" in nickel and cobalt.
Philos. Mag., 12(74):157–172, 1881.

[245] A. K. Majumdar and L. Berger.
Hall Effect and Magnetoresistance in Pure Iron, Lead, Fe-Co, and Fe-Cr Dilute Alloys.
Phys. Rev. B, 7(9):4203, 1973.

[246] T. Miyasato, N. Abe, T. Fujii, A. Asamitsu, S. Onoda, Y. Onose, N. Nagaosa, and Y. Tokura.
Crossover Behavior of the Anomalous Hall Effect and Anomalous Nernst Effect in Itinerant Ferromagnets.
Phys. Rev. Lett., 99(8):086602, 2007.

[247] M.-C. Chang and Q. Niu.
Berry phase, hyperorbits, and the hofstadter spectrum.
Phys. Rev. Lett., 75(7):1348, 1995.

[248] M.-C. Chang and Q. Niu.
Berry phase, hyperorbits, and the hofstadter spectrum: Semiclassical dynamics in magnetic bloch bands.
Phys. Rev. B, 1996.

[249] Y. Zhang, Y.-W. Tan, H. L. Stormer, and P. Kim.
Experimental observation of the quantum Hall effect and Berry's phase in graphene.
Nature, 438:201–204, 2005.

[250] P. Ghosh, J. D. Sau, S. Tewari, and S. Das Sarma.
Non-abelian topological order in noncentrosymmetric superconductors with broken time-reversal symmetry.
Phys. Rev. B, 82(18):184525, 2010.

[251] K. Capelle, E. K. U. Gross, and B. L. Györffy.
Theory of dichroism in the electromagnetic response of superconductors.
Phys. Rev. Lett., 78(19):3753–3756, 1997.

[252] K. Capelle, E. K. U. Gross, and B. L. Györffy.
Analysis of dichroism in the electromagnetic response of superconductors.
Phys. Rev. B., 58(1):473–489, 1998.

[253] H. S. Bennett and E. A. Stern.
Faraday effect in solids.
Phys. Rev., 137(2A):448–461, 1965.

[254] S. K. Yip and J. A. Sauls.
Circular-dichroism and birefringence in unconventional superconductors.
J. Low Temp. Phys., 86:257–290, 1992.

[255] Q. P. Li and R. Joynt.
Theory of dichroism in high-temperature superconductors.
Phys. Rev. B., 44(9):4720–4723, September 1991.

[256] H. T. S. Lihn, S. Wu, H. D. Drew, S. Kaplan, Q. P. Li, and D. B. Fenner.
Measurement of the far-infrared magnetoconductivity tensor of superconducting $YBa_2Cu_3O_{7-\delta}$ thin films.
Phys. Rev. Lett., 76(20):3810–3813, 1996.

[257] S. Wu, S. G. Kaplan, H. T. S. Lihn, H. D. Drew, S. Y. Hou, J. M. Phillips, J. C. Barbour, E. L. Venturini, Q. Li, and D. B. Fenner.
Temperature dependence of the far-infrared magnetotransmission of $YBa_2Cu_3O_{7-\delta}$ films.
Phys. Rev. B., 54(18):13343, 1996.

[258] J. S. Dodge, L. Klein, M. M. Fejer, and A. Kapitulnik.
Symmetry of the magneto-optic response of the Sagnac interferometer.
J. Appl. Phys., 79(8):6186–6188, 1996.

[259] B. Culshaw.
The optical fibre Sagnac interferometer: An overview of its principles and applications.
Meas. Sci. Technol., 17(1):R1–R16, 2006.

[260] A. D. Fried.
Relationship of time-reversal symmetry breaking to optical Kerr rotation.
Phys. Rev. B, 90(12):121112, 2014.

[261] H. Karapetyan, M. Hucker, G. D. Gu, J. M. Tranquada, M. M. Fejer, J. Xia, and A. Kapitulnik.
Magneto-optical measurements of a cascade of transitions in superconducting $La_{1.875}Ba_{0.125}CuO_4$ single crystals.
Phys. Rev. Lett., 109(14):147001, 2012.

[262] V. M. Yakovenko.
Theory of the high-frequency chiral optical response of a $p_x + ip_y$ superconductor.
Phys. Rev. Lett., 98(8):087003, 2007.

[263] V. P. Mineev.
Broken time-reversal symmetry in the superconducting state of Sr_2RuO_4.
Phys. Rev. B., 76(21):212501, 2007.

[264] R. Roy and C. Kallin.
Collective modes and electromagnetic response of a chiral superconductor.
Phys. Rev. B., 77(17):174513, 2008.

[265] References [262] and [263] produced reasonable estimates of the Kerr angle. However, the equations used by these authors were later shown in Ref. [264] to be inaccurate in the superconducting state.

[266] R. M. Lutchyn, P. Nagornykh, and V. M. Yakovenko.
Gauge-invariant electromagnetic response of a chiral $p_x + ip_y$ superconductor.
Phys. Rev. B, 77(14):144516, 2008.

[267] R. M. White and T. Geballe.
Long Range Order in Solids.
Academic Press, New York, 1979.

[268] T. Katsufuji, M. Kasai, and Y. Tokura.
In-plane and out-of-plane optical spectra of Sr_2RuO_4.
Phys. Rev. Lett., 76(1):126, 1996.

[269] K. Behnia and H. Aubin.
Nernst effect in metals and superconductors: a review of concepts and experiments.
Rep. Prog. Phys., 79(4), 2016.

[270] J. Shi, G. Vignale, D. Xiao, and Q. Niu.

Quantum Theory of Orbital Magnetization and Its Generalization to Interacting Systems. *Phys. Rev. Lett.*, 99(19):197202, 2007.